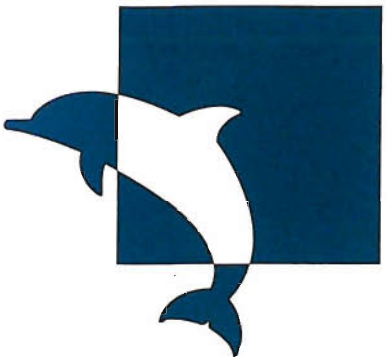

University of Southampton

Modelling of Combined Roughness and Plasticity Induced Closure Effects in High Strength Al-Alloys

A thesis submitted for the degree of Doctor of Philosophy

By

Konjengbam Darunkumar Singh

Materials Research Group
School of Engineering Sciences
University of Southampton

to the Lord

to my dearest parents

Brajabidhu and Sijakhombi

UNIVERSITY OF SOUTHAMPTON

ABSTRACT

SCHOOL OF ENGINEERING SCIENCES

Doctor of Philosophy

MODELLING OF COMBINED ROUGHNESS AND PLASTICITY INDUCED CLOSURE EFFECTS IN HIGH STRENGTH AL-ALLOYS

By Konjengbam Darunkumar Singh

An investigation of plasticity induced crack closure (PICC) and roughness induced crack closure (RICC) behaviour using finite element (FE) methods is presented for cracks subjected to small scale yielding (SSY) conditions. For constant amplitude (CA) undeflected cracks have been examined under both plane strain and plane stress conditions, whilst plane strain analyses have been particularly considered for deflected cracks. A previous two dimensional analytical treatment of RICC (2D CA-RICC) [Parry, 2000] has been extended to produce a 'continuous' closure model matching the FE findings. The model is further modified to address three dimensional effects and compared to detailed experimental findings. Results shows the increase in closure levels with increasing twist angle (ϕ) are less significant compared to that with increasing tilt angle (θ).

Further FE modelling of PICC and RICC for cracks subjected to single overloads is presented. A single overload analytical model of PICC proposed by Parry has been modified following similar arguments to the CA-RICC model. The analytical model has further been modified to address RICC effects during single overloads. Effects of L/r_p ratios on deflected cracks during overloads are seen to be functionally similar to RICC under constant amplitude loading (particularly in the 'saturation' of RICC influence for $L/r_{p(OL)} \geq 1$), where L, r_p and $r_{p(OL)}$ are deflected crack length, baseline plastic zone size and overload plastic zone size respectively. Competitive influences of PICC and RICC effects during single overloads are identified in both the FE and simplified analytical models. A modified 'strip yield' analytical model of the 'FASTRAN'-type [Xu, 2001] has also been used to study PICC effects during single overloads. Comparisons of models and experimental closure and growth rate studies are presented. Investigations have then been extended to consider both double and multiple overload conditions. In particular, attempts are made to study the effects of overload spacing on closure levels and growth rates. It appears to exist a maximum overload interaction zone for double overloads which severity of overload closure effect is at its greatest.

Overall it is found that key functional aspects of the various FE models are reproducible in simple analytical representations of RICC and PICC efforts. Whilst some fitting is involved, good correlation of the present analytical models and experimental data is shown, opening a potential route to improve, computationally efficient, multimechanistic fatigue lifing methods involving crack closure.

Contents

Acknowledgements v

Nomenclature vii

1 Introduction 1

1.1 Objectives 5

1.2 Thesis organisation 6

2 Review of literature 7

2.1 Introduction 7

2.2 Aluminium alloys for airframe applications 7

2.2.1 Heat-treatable alloys 8

2.2.2 Precipitates in heat-treatable aluminium alloys 8

2.2.3 Age hardening in Aluminium alloys 9

2.2.4 Aluminium alloy 2024-T351 alloy 10

2.3 Fatigue crack growth 11

2.3.1 Background 11

2.3.2 Fatigue crack closure 12

2.3.3 Mechanisms of fatigue crack closure 14

2.3.3.1 Plasticity induced crack closure (PICC) 14

2.3.3.2 Roughness induced crack closure (RICC) 17

2.3.4 Theoretical models of fatigue crack closure 19

2.3.4.1 Plasticity induced crack closure 19

2.3.4.2 Roughness induced crack closure 23

2.3.5 Finite element modelling of closure 24

2.3.5.1 Element type and Mesh refinement 25

2.3.5.2 Stabilisation of crack closure 29

2.3.5.3 Crack-tip node release scheme 30

2.3.5.4 Effect of constitutive model 32

2.3.5.5 Effect of specimen geometry 33

2.3.5.6 Plain strain and plane stress modelling of PICC 34

2.3.5.7 Monitoring crack closure 35

2.3.5.8 Numerical modelling of crack deflection 37

2.4 Fatigue crack growth behaviour under variable amplitude loading **39**

2.4.1 Introduction 39

2.4.2 Transient post-overload effects 40

2.4.2.1 Plasticity induced crack closure 41

2.4.2.2 Crack tip blunting 43

2.4.2.3 Residual stresses 43

2.4.2.4 Crack deflection and branching 44

2.4.2.5 Activation of near-threshold mechanisms 45

2.4.2.6 Strain hardening 46

2.4.3 Experimental trends and its rationalisation 47

2.4.4 FE modelling of overload-induced crack closure 49

3 Basic modelling configuration and assessment of constant amplitude loading **59**

3.1 Introduction **59**

3.2 Problem description **61**

3.3 FE model formulation **62**

3.4 Crack propagation algorithms **63**

3.5 Closure determination **64**

3.6 Results and discussion **65**

3.6.1 Undeflected cracks 65

3.6.1.1 Direct comparison with previous work 65

3.6.1.2 Plane strain crack behaviour 66

3.6.1.3 Plane stress crack behaviour 74

3.6.2 Deflected cracks 78

3.6.2.1 Comparison with previous work 78

3.6.2.2 Asperity size effects 79

3.6.2.3 Analytical modelling 80

3.7 Conclusions **89**

4 Modelling of RICC and PICC under single overload loading **121**

4.1 Introduction **121**

4.2 FE modelling of undeleted cracks **123**

4.2.1 Crack profiles 123

4.2.1.1 Effect of overload conditions 123
4.2.1.2 Effect of baseline loading level 125
4.2.2 Crack closure 125
4.2.2.1 Effect of overload ratio 128
4.2.2.2 Effect of baseline loading level 129
4.3 Simple analytical modelling of OL effects on undeflected cracks 130
4.3.1 Model formulation 130
4.3.2 Results 132
4.4 Strip-yield modelling of undeflected cracks 134
4.4.1 Model formulation 134
4.4.2 Governing equations 136
4.4.3 Plastic-zone size approximations 139
4.4.4 Results 140
4.5 FE modelling of deflected cracks 141
4.5.1 Effect of overload ratio 142
4.5.2 Effect of asperity length 143
4.6 Normalised asperity size analysis 143
4.6.1 FE modelling 143
4.6.2 Analytical modelling 145
4.7 Comparison with experimental data 150
4.7.1 Crack closure levels 150
4.7.2 Growth rate comparisons (*da/dN*) 153
4.7.2.1 Comparison with Parry's result 154
4.7.2.2 Comparison with Xu's experimental results 155
4.8 Conclusions 159
5 Finite element analyses of closure due to double/multiple overloads 197
5.1 Introduction 197
5.2 Double overloads 198
5.2.1 FE modelling 198
5.2.1.1 Crack profiles 199
5.2.1.2 Crack closure - overload spacing effects 199
5.2.1.3 Crack closure - OL ratio effects 200
5.2.1.4 Crack closure - $\Delta K_{(BL)}$ ratio effects 201

5.2.2 Strip yield modelling 201
5.2.2.1 Crack closure – overload spacing effects 201
5.2.2.2 Crack closure - $\Delta K_{(BL)}$ ratio effects 202
5.2.3 Analytical modelling – dual overloads 202
5.2.3.1 Crack closure – overload spacing effects 203
5.2.3.2 Crack closure - $\Delta K_{(BL)}$ ratio effects 204
5.2.4 Comparison of FE, strip yield type and Analytical modelling 204
5.2.5 Growth rate interaction 204
5.3 **Multiple overloads** 206
5.3.1 Strip yield type modelling 208
5.3.2 Analytical modelling 209
5.3.3 FE modelling 209
5.3.4 Growth rate predictions: Airbus test data 212
5.4 Conclusions 213
6 Summary and conclusions **239**
7 Recommendations for future work **242**
References **243**
Appendix A Fracture mechanics concepts **274**
A.1 The Energy balance concept **274**
A.2 Stress intensity factors **275**
A.3 Small scale yielding condition **276**
A.4 The Plastic zone **277**
A.5 Crack tip opening displacement **282**
A.6 The *J* integral and elastic-plastic fracture mechanics **283**
A.6.1 Hutchinson-Rice-Rosengran (HRR) fields 284
A.6.2 Regions of K and J dominance 285
A.6.3 Mixed mode fracture aspects 286
Appendix B Input preparation of the FE model **291**
B.1 Loads and boundary conditions **291**
B.2 Material properties **292**
B.3 Element properties **292**
B.4 Typical ABAQUS input files **296**

Acknowledgements

In my endeavour for this research project, I have been scrupulously trained and moulded by my supervisor Dr. Ian Sinclair for which I have been truly fortunate. Every discussion with him has always been a pleasure, enlightening and educative, considering his wide knowledge and expertise in the subject. I express my warm and sincere heartfelt thanks for the confidence he had shown, absolute freedom he had given and the vast amount of patience he had with me.

I would like to express my gratitude to Airbus UK and EPSRC UK for the financial support that this project has received. I wish to acknowledge Dr. Richard Collins (Airbus, UK) for his valuable interest in this project. I would like to thank Dr. Jean-Christophe Ehrstrom (Alcan, France) for the useful discussions.

I am indepted to Dr. Julian Boselli (Alcan, France), Dr. Mathew Parry (Airbus, UK), Dr Yigeng Xu (Airbus, UK), Dr Nicolas Kamp (Manchester University) and Dr. Fabein Lefebvre (INSA, France) for the initial stage of this work.

A word of deep appreciation to Dr. Phillipa Reed for her valuable and timely help. I am thankful to Ms Gwyneth Skiller for her kindly help.

Thanks are due to other researchers viz. Dr. Martin Browne, Dr. Nong Gao, Dr. Mark Joyce, Dr. Au Seong Wong, Dr. Keng Soong Tan, Dr. Sebastian Morris, Dr. Hamdi Habbab, Dr. Jonathan Jeffers, Dr Jian Liu, Dr. Mathew Mwanza, Dr. Vishwanath Kotta, Dr. Vinu Palissery, Mr. Kern Hauw Khor, Mr. Jun Sun, Mr. Mohamed Azlam Suhot, Mr. Imran Khan, Mr. Muhammed Safraz Ali, Mr. Mark Miller, Mr. Andrew Moffett, Mr. Thilo Morgeneyer, Mr. Narasimhan Sampathkumar, Mr Ramkumar Penchaliah, Mr. Krishnan Lakshmi Narasimhan, Ms. Katerina Fragaki, Ms. Charlene Squires, Ms. Louise Venning, Ms. Polly Sinnett-Jones, Ms. Vandana Bhattacharya, ... for their warm and thoughtful company throughout this work..

A truly unbounded work of thanks to my parents, brothers and sister in Manipur for their affection, constant encouragement, well being and forbearance.

A word of thanks to all my teachers, friends and colleagues whose names are not mentioned but nevertheless encouraged and helped me in many ways.

To all these wonderful people I am pleased to express my gratitude.

Nomenclature

$\%OL$	overload ratio
2D	2-dimension
3D	3-dimension
A	monotonic strength coefficient
ASTM	American Society of Testing an Materials
a	crack length
a^*	distance of the crack tip from the last asperity point
a'	increment of crack extension separating two overloads
a'_{min}	distance to the minimum crack growth from OL location
a_o	initial crack length
a_d	delay distance
a_{eff}	affected distance
a_{uhalf}	crack growth from OL position to rise U from U_{min} by $0.5U_{ret}$
a_{umin}	crack growth from OL position to U_{min}
b_k	dimensions for partially loaded crack, $k = 1,2$
B	specimen thickness
BF	back-face (displacement gauge location)
C	Paris law scaling constant
C	compressive spring
CA	Constant amplitude
CCT	centre cracked tension (panel)
CA-RICC	constant amplitude – roughness induced crack closure
CM	crack mouth
COD	crack opening displacement
CPU	central processing unit
CRSS	critical resolved shear stress
CST	constant strain triangle (elements)
CT	compact tension (panel)
$CTOD$	crack tip opening displacement
$CTOD_{res(OL)}$	residual crack tip opening displacement due to baseline loading
$CTOD_{res(OL)}$	residual crack tip opening displacement due to overload
$CTSD_{(OL)}$	crack tip sliding displacement due to overload

$CTSD_{res}$	residual crack tip sliding displacement
$CTSD_{IIIres}$	mode III residual crack tip sliding displacement
d	half of crack length plus tensile plastic zone
da/dN	crack growth rate
DOL	double/dual overload
D	size of K-dominated region
dP	load
ds	length increment
$d\Delta$	change in crack flank displacement
E	Young's modulus
E'	$E/(1-\nu^2)$
F	geometry correction factor for stress intensity factor
FASTRAN	Fatigue crack growth structural analysis (code)
FD	finite difference
FE	finite element
f_{ij}	dimensional function
G	elastic energy release rate; shear modulus
G_{IC}	critical energy rate
H	slope of plastic portion of stress-strain curve
h	effective residual displacement of the asperity tip
h_{III}	mode III effective residual displacement of the asperity tip
h'	effective fraction of h expressed as a function of a^*
h_{rw}	residual wedge height
h'_{rw}	effective fraction of h_{rw} expressed as a function of a^*
$h_{rw(max)}$	maximum residual wedge height
h_o	notch height
HRR	Hutchinson-Rice-Rosengren (crack tip field)
I_n	integration constant
IH	isotropic hardening
J	J-integral
K	stress intensity factor
K_c	critical stress intensity factor
K_{cl}	closure stress intensity factor

K_{cont}	contact/closure stress intensity factor
$[K_{cl}/K_{max}]_{DOL\text{-}max}$	maximum closure level following double overload conditions
$[K_{cl}/K_{max}]_{SOL\text{-}max}$	maximum closure level following single overload conditions
K_o	stress intensity factor due to flow stress
K_I	mode I stress intensity factor
k_I	local mode I stress intensity factor
$K_{I(max)}$	maximum mode I stress intensity factor
K_{II}	mode II stress intensity factor
K_{III}	mode III stress intensity factor
K_{max}	maximum stress intensity factor
$K_{max(BL)}$	maximum stress intensity factor due to baseline load
K_{min}	maximum stress intensity factor
K_{OL}	overload stress intensity factor
K_{op}	opening stress intensity factor
K_M^p	mixed mode plastic stress intensity factor
KH	kinematic hardening
l	distance behind crack tip
L	crack deflection length; characteristic length
L'	specimen length
L_e	element size
L_j	element length
$L_j^{(k)}$	length of element j at k^{th} iteration
LDU	loading-debonding-unloading
LDULU	loading-debonding-unloading-loading-unloading
LEFM	linear elastic fracture mechanics
M^e	far-field elastic mixity
M^p	near-tip plastic mixity
m'	dimensionless constant
N	number of cycles
NTE	normalised transient effect
N^*_D	retarded cycles in a single overload test
NTL	near-tip-left (displacement gauge location)
NTR	near-tip-right (displacement gauge location)

n	strain hardening exponent
N_d	number of delay cycles
OL	overload
OL_1	first overload
OL_2	second overload
P	load
PICC	plasticity induced crack closure
PP	perfectly plastic
Q4	4-noded quadrilateral element
Q8	8-noded quadrilateral element
r	polar co-ordinate
R	ratio of minimum to maximum applied stress intensity factor
R'	crack resistance
r_c	cyclic plasticity zone size
RICC	roughness induced crack closure
RICC-OL	roughness induced crack closure - overload
r_p	monotonic plastic zone size
$r_{p(BL)}$	baseline plastic zone size
$r_{p(OL)}$	overload plastic zone size
R_{eff}	effective R ratio
RSFZ	residual stretch free zone
RSZ	residual stretch zone
SENB	single edge notched bend specimen
SOL	single overload
S	applied stress
S_{max}	applied maximum stress
S_{open}	crack opening stress
T	non-singular 'T-stress'
T	tensile spring
TPZ	turning point controlled zone
T_{max}	maximum T-stress
U	ratio of effective to applied stress intensity factor range
U_{min}	minimum U

U_{ret}	change in U as a result of retardation
U_{BL}	U due to baseline loading
U_{OL}	U due to overload loading
u_x	mode II displacement of fracture surfaces
U_x	transverse displacement along crack growth direction
u_y	mode I displacement of fracture surfaces
v	displacement geometry correction factor
VA	variable amplitude
V_j	crack surface opening displacement at point j
$V_j^{(k)}$	crack surface opening displacement at point j at k^{th} iteration
w	strain energy density
W'	specimen width
WCZ	wedge controlled closure zone
WTPZ	wedge and turning point control zone
x_i	x co-ordinate of the centre of element i
X-FEM	extended finite element method
Δa	crack growth increment
Δa_s	separation distance between two overloads
$\Delta CTOD$	change in cyclic crack tip opening displacement
$\Delta CTSD$	change in cyclic crack tip sliding displacement
$\Delta CTSD_{(BL)}$	change in cyclic crack tip sliding displacement due to baseline load
ΔK	stress intensity factor range
ΔK_I	mode I stress intensity factor range
$\Delta K_{(BL)}$	baseline stress intensity factor range
ΔK_{app}	applied stress intensity factor range
ΔK_{eff}	effective stress intensity factor range
$\Delta\delta$	cyclic CTOD
$\Delta\varepsilon^{pl}_{xx}$	change in plastic strain in x-direction
$\Delta\varepsilon^{e}_{zz}$	change in elastic strain in z-direction (ε^{e}_{zz})
$\Delta\varepsilon^{pl}_{zz}$	change in plastic strain in z-direction (ε^{pl}_{zz})
Γ	curve enclosing a crack tip
α	constraint factor

α'	ratio of the reverse plastic zone for growing crack to that of stationary crack
α_g	global constraint factor (ratio of average normal stress in the plastically deformed material to the flow stress)
$\alpha_{SOL\text{-}max}$	measure of peak closure level due to double overload as compared to that of single overload condition
β	scaling factor
β_I	β due to mode I loading
β_{II}	β due to mode II loading
β_{III}	β due to mode III loading
δ	crack opening displacement
δ_o	crack tip opening displacement
δ_{cl}	closure crack displacement
δ_{max}	maximum crack displacement
η	material constant, $\eta = 0$ for plane stress and $\eta = \nu$ for plane strain
δ_R	plastic stretch
ε^e_{zz}	elastic strain in z-direction
ε^{pl}_{zz}	plastic strain in z-direction
κ	elastic constant
λ	fraction of the plastic zone
ν	Poisson's ratio
θ	polar co-ordinate; mode II crack deflection angle
σ	remote uniaxial stress
σ_o	flow stress
σ_i	stress on segment of crack surface
σ_j	stress on element j
$\sigma_j^{(k)}$	stress on element j at k^{th} iteration
σ_y	yield stress
σ'_y	cyclic yield stress
σ_{ij}	stress tensor/component
σ_{max}	maximum stress in load cycle

$\tilde{\sigma}_{ij}$	dimensionless function
σ_{UTS}	ultimate tensile strength
ξ	$K_{max(OL)}/K_{max(BL)}$
υ	dimensionless constant
ϕ	mode III crack deflection angle
χ	ratio of mode I to mode II displacement which occurs during unloading

Chapter 1

1 Introduction

Failure events in the first commercial jet aircraft, (the de Havilland Comet) that mysteriously disintegrated mid-air on May 1953, January 1954 and April 1954 provide a tragic but intriguing insight into the importance of 'fracture and fatigue' theory. In one of the most extensive post-mortem studies in engineering history, the Comet's failure was investigated by full-scale de/pressurisation cycles (to simulate typical fluctuating flight cycles) of a retired-aircraft in a massive water tank by the Royal Aircraft Establishment (RAE), Farnborough. The RAE tests led to the conclusion that the most probable cause of the aforementioned Comet accidents was 'fatigue cracking', with cracks spreading from the square edges of the windows in the passenger cabin (after Suresh, 1998, Aerospaceweb, 2003, Roylance, 2001, BBC, 1954). Three other fatigue accidents and subsequent investigations involving a General Dynamics F-111 (1969), Dan Air Boeing 707-321C (1977) and Aloha Airlines Boeing 737-200 (1988) have significantly influenced the design approaches to aircraft 'airworthiness', vis-à-vis structural safety (after Schijve, 1994, Wanhill, 2002).

Before and during the early Comet generation, aircrafts were designed on 'safe-life' principles. Safe-life means that the structure has been evaluated to be able to withstand fatigue loads expected during its service life without detectable damage/cracks. However, the Comet accidents and other similar ill-fated experiences showed earlier occurrences of cracks than anticipated, suggesting that the safe-life approach could not sufficiently guarantee structural safety. To deal with the shortcomings of safe-life, 'fail-safe' design principles were proposed in the late 1950s. In the fail-safe approach the structure is designed to assure that catastrophic failure is a remote possibility after fatigue failure or obvious partial failure of a single, principal structural element. Fail-safe design necessitates regular inspections so that flaws are identified for prompt repair or replacement so that structural safety is not compromised. In the following fatigue research to ensure aircraft structural safety, the United States Air Force (USAF) suggested and mandated new guidelines which were later referred to as the 'damage tolerance' philosophy. Damage tolerance considers

the structure be evaluated to assure that in the event of serious damage within the operational life, the structure can withstand reasonable loads without excessive deformation until the damage is detected. While considerations associated with fail-safe design are understood to be included in the damage tolerance philosophy it differs in two aspects:

1. the probability of an initial flaw in the structure is assumed and
2. structural damage may be inspectable or non-insepectable in the design service life.

One of the key considerations under this philosophy is that after the initiation of cracks, the materials and stress levels must provide a controlled slow rate of crack propagation where a critical defect size to cause failure cannot occur between inspections (non-inspectable structures may still be regarded as damage tolerant should crack growth occur, provided it does not cause any threat to the structure during the design life). 'Damage tolerance requirements' were incorporated into USAF Military Specification 83444 in 1974 and remain the favoured design philosophy to date for many aspects of aircraft engineering (after Schijve, 1994, Wanhill, 2002, FAA, 1997, Schutz, 1996, Suresh, 1998).

With the introduction of the damage tolerant design philosophy there arose a paradigm shift in the design of aircraft structures, demanding an understanding of fatigue crack propagation rates in general. The demand for fatigue resistant materials and structures has therefore increased as improvements are sought in aircraft performance, maintenance requirements and total service life. As such an understanding of the factors affecting fatigue crack growth rates in aerospace alloys (e.g. the established damage tolerant aluminium alloys formulation, AA2024) is therefore vital in the optimisation of alloys, their selection and the design of lifing algorithms. It has been recognised that fatigue failures are complex and multimechanistic in character [Sinclair and Gregson, 1998], where several competitive and synergistic interactions arise from aspects such as applied stress conditions (including stress history, stress state, mean stress levels), crack length, geometrical conditions and environment (e.g. temperature and, chemical). Overall, microstructural and mechanical influences on crack growth behaviour may be related to;

1. intrinsic factors, regarding the actual process of crack advance at its tip, which have relevance to characteristic microstructural features such as grain size, secondary phase particle shearability, and dislocation cell size; that may vary with basic alloy condition, environment and length scale of crack tip deformation,
2. extrinsic factors, which reflects the sensitivity to 'shielding' processes that tend to attenuate the crack driving force due to influences in the crack wake (e.g. fracture surface asperity, corrosion products) or ahead of the crack tip (e.g. reverse plastic deformation).

The dissociation of extrinsic and intrinsic effects has been a major thrust of fatigue research for the last few decades, with shielding mechanisms ('crack closure' in particular) have being used to rationalise various microstructual and mechanical influences on crack growth behaviour. Crack closure is particularly identified as the premature contact of crack faces at positive load levels due to factors such as plastic deformation, crack surface asperities, oxides *etc.* [Sinclair and Gregson, 1998, Parry, 2000, Suresh, 1988], limiting the cyclic loads/displacements experienced at the actual crack tip, and hence the fatigue crack driving force.

Since the initial demonstration of the role of crack closure in fatigue crack growth in the early research of Elber [1970, 1971], extensive efforts has gone into the influence of fatigue crack closure on crack propagation, although there is an apparent lack of consensus regarding the accurate, meaningful and non-subjective measurement of crack closure (e.g. in terms of apparent differences in near-tip and global closure measurements, and location of contact points). The relative importance of crack closure has also been questioned by Vasudevan and co-workers [Lout *et al.*, 1993 and Vasudevan *et al.*, 1994], however extensive evidence (both experimental and theoretical) exists to support a central role of crack closure in many aspects of fatigue crack growth [Ritchie, 1988 and Sinclair and Gregson, 1998].

The practical requirement for accurate and reliable fatigue crack growth prediction under complex load spectra (or 'variable amplitude' load conditions) for the prompt and economical scrutiny of airframe structures is well established [e.g. Molent and Aktepe, 2000]. A plethora of experimental, analytical and numerical investigations

have been reported to study fatigue crack growth under such conditions. Despite the fact that there may be many processes (e.g. plasticity induced crack closure (PICC), roughness induced crack closure (RICC), residual stress ahead of the crack tip, static tearing, crack deflection, *etc.*) that are known to influence variable amplitude (VA) fatigue response [Sinclair and Gregson, 1998, Xu, 2000], the published modelling approaches are known to be of limited accuracy [Collins, 2001], even in relatively simple loading conditions. Two points that can be linked to this limited precision are:

- simplified single mechanism treatment of VA effects,
- the difficulty associated with interpreting real closure results for the validation and/or calibration of any given modelling approach.

Of late Parry [2000] extended the modelling concepts of Newman and Armen [1975] and conducted finite element (FE) modelling of crack closure arising from the combined effects of crack deflection and prior plastic deformation in long fatigue cracks in aerospace aluminium alloys under constant and basic variable amplitude (single tensile overload) loading under small scale yielding. It was observed that crack roughness (and slip band simulations) led to a significant increasing effect on closure levels for crack subjected to constant amplitude loading. To the author's knowledge, this work represents the first explicit treatment of PICC and RICC in combination, [Parry *et al.*, 1999, 2000, 2000a, 2000b, 2000c] representing a critical development in clearly linking of RICC to residual strains in the crack wake. This is an important shift in understanding, making RICC more amenable to analytical representation in computationaly efficient forms that may be usable for engineering design.

As Parry conducted limited FE modelling on the effects of single overloads on RICC, the work was not clear on the competitive influences for RICC and PICC effects with varying load conditions. Furthermore, due to the scarcity of consistent, comparable single overload experimental results for a range of fracture surface asperity geometries it is not possible to derive conclusive response of surface roughness due to overloads. Hence it is particularly pertinent to explore through FE modelling possible RICC-PICC interaction due to single overloads, with the potential then existing to model analytically the understanding gained from the FE studies.

Whilst the study of the effects of single overloads on crack growth rate is indispensable in understanding the fundamental mechanisms responsible for crack growth retardation under variable amplitude loading, it is clearly valuable to address the issues of load transient interactions that may arise in more complex/realistic spectra. Although several experimental reports have been provided since the early studies of Jonas and Wei [1971], there exist experimental difficulties in monitoring growth rates (in relation to the separation distances) when overloads are applied very closely [Khor, 2004]. Using numerical models (e.g. FE methods) may then provide a valuable tool to obtain qualitative and quantitative understanding of the effects of interacting periodic overloads. To the best of author's knowledge there are various attempts using FE methods to model the of periodic overloads effects on plane stress cracks [e.g. Blom and Holm, 1987, Park and Song, 1999, Heper and Vardar, 2003], however there is a lack of studies on plane strain crack behaviour. As such efforts in this work are directed to investigate plane strain cracks under periodic overloads.

1.1 Objectives

The current project represents a direct follow-up of the experimental and theoretical crack closure studies of Parry, Xu and co-workers [see Parry 2000, Xu, 2001]. Overall, the project aims to extend the findings of their work on PICC and RICC effects in fatigue of airframe alloys, particularly in relation to more complex load transients and the development of detailed, computationally efficient analytical approaches for crack growth analysis that may be realistically integrated into future design processes.

Key objectives are then threefold:

1. To review the concepts of fracture mechanics, fatigue crack closure and its relevant literature.
2. To analyse crack closure arising for undeflected and deflected cracks under constant amplitude loading using the finite element (FE) technique. Effort has been particularly made in establishing model confidence by assessing and extending load cases reported by Parry [2000], and the investigation of various basic model parameters for their influences on apparent closure behaviour.

3. To extend the initial single overload studies of undeflected and deflected cracks by Parry and Xu to clarify RICC interactions relevant to realistic aerospace load conditions and the possible effects of multiple load transients.

1.2 Thesis organisation

The material presented in this thesis is split into seven chapters.

- An introduction to the work and the main objectives is given in Chapter 1.
- In Chapter 2, the relevant work reported by various investigators regarding concepts of metal fatigue and fatigue crack closure is mainly addressed.
- Following the work of Parry [2000], FE and simplified analytical analyses are reported to analyse crack closure affects arising for undeflected and deflected cracks under constant amplitude loading conditions in Chapter 3. Detailed comparisons with experimental results are also presented.
- In Chapter 4, results from FE, strip yield model [Xu, 2001] and simplified analytical models for single overload effects on PICC and RICC are discussed. Experimental closure and growth rate variations are compared with the model results.
- Effects of dual and periodic multiple overloads on PICC are studied using FE and strip yield models in Chapter 5. Simplified analytical models are proposed to simulate the FE and strip yield results. Models results are compared for some experimental results.
- Chapter 6 draw briefly the summarised main conclusions.
- Recommendations for possible future research directions in this field are highlighted in Chapter 7.

Chapter 2

2 Review of Literature

2.1 Introduction

From the published reports, investigations on metal fatigue date back to the early nineteenth century. Since the study by Albert [1838] [after Suresh, 1998], many efforts have been made to understand the fatigue behaviour of metals. The reader is directed elsewhere for further background, such as the reports of Miller [1991, 1993], Schutz [1996], Paris [1998], Rice [1967], Laird [1979], Suresh [1998], and Lawson *et al.,* [1999]. The works of Gangloff *et al.,* [1994], Swift [1996] and Sinclair and Gregson [1998] can be referred to for an overview of the application of fatigue-based research to the design of alloys used in aerospace structures.

Given the many reviews and texts available on fracture mechanics, the present review will, of brevity, focus on fatigue aspects, with the underlying fracture mechanic principles and equations being provided in Appendix A. Given the specific interests, a brief summary of the main metallurgical features of these materials are also provided here. Apologies are made to those whose vital contributions have unintentionally been overlooked, and to those whose affirmations of historical precedence have inevitably been missed, particularly in non-English language papers.

2.2 Aluminium alloys for airframe applications

Whilst the present thesis emphasis the modelling of fatigue processes, the physical parameters for modelling and experimental validation has been closely based on standard airframe materials. As such, the following section provides a general review of these materials and associated physical metallurgy of high strength aluminium alloys. For further details the reader is directed to more extensive reference materials,

such as Polmear [1995], Vasudevan and Doherty [1989], and ASM Speciality Handbook, [1994].

2.2.1 Heat-treatable alloys

Aluminium alloys (Al-alloys) can be broadly classified into heat-treatable and non-heat-treatable depending on whether or not they respond to precipitation hardening. The main heat-treatable classes of wrought aluminium alloys are designated by the following International Alloy Designation Series (IADS): 2xxx (Al-Cu and Al-Cu-Mg), 6xxx (Al-Mg-Si) and 7xxx (Al-Zn-Mg and Al-Zn-Mg-Cu). 7xxx and 2xxx series are the two major heat-treatable Al-alloys for structural aerospace applications. 7xxx series are generally used for high-strength applications, whilst 2xxx series alloys are mainly used as damage-tolerant applications due to their good crack growth resistance, e.g. see Xu, 2001.

2.2.2 Precipitates in heat-treatable aluminium alloys

Whilst age hardening precipitates are perhaps most critical to alloy performance, the secondary phase particles that are present in commercial alloys should be considered in terms of three separate basic classes:

1. Constituent particles (coarse intermetallics), typically 0.5 – 10 μm in size
2. Dispersoids (submicron particles), typically 0.05 – 0.5 μm in size
3. Strengthening precipitates (fine precipitates), up to 0.1 μm in size

- *Constituent particles*

Consituent particles may be divided into two groups: the first consists of virtually insoluble compounds; predominantly formed from the impurities in the aluminium, e.g. $Al_6(Fe,Mn)$, Al_3Fe, $\alpha Al(Fe,Mn,Si)$ and Al_7Cu_2Fe, which form interdendritically during solidification and are only altered by subsequent mechanical working, whilst the second group is made up of soluble compounds formed from the major alloying

elements; e.g. Al_2Cu, Al_2CuMg, Mg_2Si. Both these constituent particles form as lacy networks around grain boundaries during casting. They normally do not perform any useful function, except the soluble particles may be dissolved by subsequent treatment/processing, thereby contributing to strength.

- *Dispersoids*

Dispersoids are formed in the homogenisation of cast ingots by solid-state precipitation. These are usually formed from transition elements that have low solubility in aluminium. The dispersoids resist dissolution or coarsening due to low diffusivity of the associated elements (phases include $Al_{20}Mn_3Cu_2$, $Al_{12}Mg_2Cr$ and Al_3Zr). Dispersoids help in controlling grain growth, retarding recrystallisation during thermomechanical deformation processes. They also tend to homogenise slip in the final material, by blocking dislocation motion. The dispersoids may be either coherent (Al_3Zr), or semi coherent/incoherent ($Al_{12}Mg_2Cr$ and $Al_{20}Mn_3Cu_2$); with coherent dispersoids being thought to have a greater effect in controlling grain size during deformation.

- Strengthening precipitates

Strengthening precipitates are formed during the ageing treatment in heat treatable alloys, described further below. Strengthening phases associated with commercial Al-alloys include S' (Al_2CuMg) in 2xxx alloys, and η' (Mg_2Zn) in 7xxx alloys.

2.2.3 Age hardening in Aluminium alloys

Age hardening in aluminium alloys consists of three main stages: solution treatment, followed by quenching to develop a super saturated solid solution (SSSS) of solutes and vacancies, and then controlled decomposition of the SSSS. Solution treatment involves heating the alloy to a single phase region in the phase diagram, to temperatures typically around 500°C for 2xxx materials. It is important that the temperature remains below the solidus temperature to avoid local melting, which may have an effect on mechanical properties. Quenching is designed to maintain the

maximum supersaturation of alloying elements. In thin sheets, quenching may produce distortion, whilst in thicker gauges, it may introduce residual stresses. Reducing cooling rates can reduce the stresses introduced in quenching, however it may slow down the response of the alloy to subsequent ageing, as there is a lower percentage of alloying elements in solid solution. Such 'quench sensitivity' may be increased by the presence of dispersoids, as they can act as nucleation sites for coarse precipitates during cooling.

Decomposition of the SSSS is a complex process involving several stages that depend on the temperature at which it is carried out. The first stage in usually the decomposition is the formation of Guinier-Preston (GP) zones. Such zones are coherent and finely dispersed within the matrix; they are ordered, solute-rich clusters of atoms which may be one or two atom planes in thickness with densities as high as 10^{17} to 10^{18} cm^{-3}. They are the major strengthening precipitates for naturally aged materials. The next stage of decomposition is the formation of the intermediate precipitate. These are normally larger than GP zones and may nucleate homogeneously, or heterogeneously at vacancy clusters, GP zones, dislocations, or sub-boundaries. Intermediate precipitates are typically partially coherent. Following the formation of intermediate precipitates is the formation of equilibrium precipitates, which are generally larger still and more widely spaced, and they may be formed by transformation of intermediate precipitates. Equilibrium precipitates can also nucleate at dislocations and at interfaces such as grain boundaries and sub-grain boundaries, and at the interfaces between other particles and the matrix. They occur at relatively high ageing temperatures/times and are largely incoherent with the matrix.

Overall the decomposition sequence may be identified as:

SSSS → clusters → intermediate precipitate → equilibrium precipitates

For Al-Cu-Mg alloys the sequence is typically given as:

SSSS → GPB[1] zone (Al-Cu-Mg zones) → semi-coherent S' (Al_2CuMg) → incoherent S (Al_2CuMg)

[1] GPB (Ginier-Preston-Baragaskii) zone is the Cu and Mg containing GP zone

It may be noted that the very early stages of decomposition are still the subject of debate, with advanced imaging techniques such as 3D atom probe microscopy (3DAP) providing valuable insights [Starink *et al.*, 2004].

2.2.4 Aluminium alloy 2024-T351 alloy

2xxx series alloys represent the 'original' heat-treatable aluminium alloys, based on the binary Al-Cu system. Such alloys respond to natural ageing and with the discovery that the degree and rate of ageing could be improved by addition of Mg, led to the development of the Duralumin composition type.

Natural ageing in 2024-type alloys is generally attributable to GP zone formation. In spite of the fact that the rate and extent of natural ageing vary from one alloy to another, most of the strengthening occurs during the first day, and stability is reached after about four days. Whilst the maximum strength cannot normally be realised during natural ageing, many 2xxx series alloys are used in the natural ageing tempers such as T3 (represented by solutionised, cold work and natural ageing) and T4 (solutionised and natural ageing) due to their good combination of ductility, strength, fracture toughness and fatigue resistance. The 2024 alloy is commonly used (in the naturally aged temper) in the aerospace industry for lower wing structures and other damage tolerant applications. Typical mechanical properties of the alloy are shown in Table 2.1, whilst Table 2.2 shows composition details for standard 2024 and the advanced variant, 2027.

2.3 Fatigue Crack Growth

2.3.1 Background

The work reported by Paris *et al.*, [1961] is widely considered to reveal a key role of stress intensity factors in fatigue crack growth particularly for physical large cracks. A wider and general acceptance of the idea followed from the 1963 publication of Paris

and Erdogan [1963] based on empirical observations. Paris and Erdogan [1963] reported fatigue crack growth data from different load conditions, showing they could be consolidated via ΔK, the cyclic stress intensity factor. The result essentially established the relation that is now commonly known as the Paris law, as given by;

$$\frac{da}{dN} = C\Delta K^m \tag{2.1}$$

where C and m are experimentally determined materials constants and da/dN is the crack growth increment per cycle (a being the crack length and N the number of load cycles). For a wide range of ΔK values however, Equation 2.1 cannot be used to correlate experimental data effectively. A plot of $\log da/dN$ and $\log \Delta K$ for fatigue crack growth in typical metals shows a sigmoidal curve containing three distinct regions, as illustrated in Figure 2.1. The curve is broadly linear at intermediate values of ΔK (i.e. following the Paris law), however crack growth rates deviate from linear behaviour at both high and low ΔK values. Beyond the linear region, the crack growth rates accelerate as K_{max} approaches K_C, the fracture toughness of the material, here crack growth may be accelerated by quasi-static failure mechanisms. At the other extreme, da/dN is generally seen to approach zero asymptotically at a threshold ΔK value, ΔK_{th}. Many researchers [e.g. Weertman, 1966, Foreman *et al.,* 1967 , Klesnil and Lukas, 1972, Donahue *et al.,* 1972, McEvily 1988] have attempted to develop empirical and theoretical equations which model all or part of the sigmoidal curve using the ΔK concept. However, it is widely believed that any direct relationship between ΔK and crack growth rates must take into account not only those phenomena occurring at a particular crack tip due to applied loads, but also micromechanical phenomena occurring behind and around the crack tip: in particular the incidence of crack flank contact during the load cycle or 'crack closure'.

2.3.2 Fatigue crack closure

Fatigue crack closure phenomena are widely considered to cause a reduction in the range of cyclic loading experienced at a fatigue crack tip due to the contact of crack faces at positive load levels. Elber [1970, 1971] is commonly identified as the first to

observe the crack closure phenomenon. Elber reported his experimental observation on the changes of compliance in thin sheets of cracked 2024-T3 aluminum alloy. At high loads, fatigue crack compliances ($d\Delta / dP$, where Δ is crack flank displacement and P is load) agreed well with known formulae for cracked bodies; however, at low loads, compliance levels were closer to those of uncracked specimens. Elber reasoned that the change in compliance was due to the contact between crack faces (i.e. crack closure), occurring at low but positive loads. This was linked to the presence of residual tensile strains in the fatigue crack *wake*. As such, reduction in the apparent driving force for fatigue crack advance occurs as the crack tip does not experience the full unloading associated with the normal applied load cycle (crack advance can only arise from cyclic plastic deformation at the tip).

Elber put forward the idea that the decrease in the fatigue crack growth rate due to crack closure was due to a reduction in *effective stress intensity factor range*. The closure concept is illustrated schematically in the Figure 2.2; indicating that crack propagation can only take place during the portion of the loading cycle in which the crack is fully open, Elber defined the *effective stress intensity factor range* as;

$$\Delta K_{eff} = K_{max} - K_{cl} \tag{2.2}$$

where K_{cl} is the stress intensity factor at which contact of crack faces occurs. Elber then proposed a modified Paris equation (Equation 2.3)

$$\frac{da}{dN} = C\left(\Delta K_{eff}\right)^m \tag{2.3}$$

In this approach, the crack tip is considered to be isolated from the applied stress changes on the point of first contact of the crack faces during unloading. Numerous experimental and modelling reports have been published on the incidence of crack closure (e.g. see Newman and Elber, 1988, McClung and Newman, 1999), with a wide variety of fatigue phenomena being related to its occurrence (e.g. microstructural influences on fatigue and the behaviour of small fatigue cracks).

The incidence of crack closure due to residual plastic strain in the crack wake, as noted by Elber is commonly referred to as 'plasticity induced crack closure' (PICC)

[Ritchie *et al.,* 1980, Suresh *et al.*, 1981 and Suresh and Ritchie, 1982a, 1982b]. Ritchie [1988] has further summarised the various related mechanisms by which the effective crack-driving force experienced at a crack tip is locally reduced. Such mechanisms are commonly described as 'crack shielding processes', and may be broadly categorised into the following groups:

- crack deflection and meandering, whereby the mode I 'crack driving force' is reduced by crack path deviations from the plane of maximum tensile loading,
- contact shielding, involving physical contact between mating crack surfaces. This may occur directly, through the presence of surface asperities, or via fibres in a composite, or through the presence of an external medium, such as corrosion debris or the entry of a viscous fluid in to a crack. Roughness induced crack closure (RICC) results from interference between crack surfaces asperities arising from deflected crack growth.
- zone shielding from 'inelastic or dilated zones' surrounding the crack wake, for example due to transformation toughening, microcrack toughening, crack field void formation, crack wake plasticity (resulting in plasticity induced crack closure, PICC), or residual stress fields.

For the fatigue of aerospace aluminium alloys, RICC and PICC are generally considered to be of greatest importance (depending on the alloy and loading conditions) [Parry *et al.,* 2000, 2000a, 200b, Xu, 2001]. The following section will consider some of the mechanisms featured in the literature to explain PICC and RICC.

2.3.3 Mechanisms of fatigue crack closure

2.3.3.1 Plasticity induced crack closure (PICC)

During fatigue crack propagation in ductile materials, material at the crack tip undergoes tensile plastic strains which are not fully reversed during unloading. When the crack propagates it leaves behind a wake of such residual tensile displacements in the direction perpendicular to the crack. However, this plastically deformed region is constrained by the surrounding elastic material, which attempts to return to its original position. The resulting compressive stresses lead to contact of crack faces in the wake

under a far-field tensile fatigue load, causing a possibility of premature crack closure, known as plasticity induced crack closure [Elber, 1971, McClung *et al.,* 1991]. Figure 2.3 shows schematically the developed plastic zone envelope for a fatigue crack which propagates under a constant ΔK magnitude.

Under plane stress conditions, a potential mechanism for the development of an 'extra material' wedge in the crack wake is the transfer of material from the thickness direction to the axial direction (i.e. from the original surface to subsurface region), as the volume of material must be conserved during plastic deformation. This causes the specimen to become thinner and longer in vicinity of the crack tip, and subsequently, the crack wake [McClung *et al.,* 1991, Pippan *et al.,* 1994, Sehitoglu and Sun, 1991, Minakawa *et al.,* 1986]. However the mechanism of material transfer in the out-of-plane direction postulated for plane stress is not admissible for plane strain by definition. Various experimental [Lindley and Richards, 1974, Minakawa *et al.,* 1986], numerical and analytical [Fleck and Newman, 1988] studies have come to this conclusion for a steady state growing fatigue crack (i.e. excepting transient or overload effects). But there are also experimental [Dawicke *et al.,* 1990a,b, Pitonaik *et al.,* 1974, Mills and Hertzberg, 1975, Ewalds and Furnee, 1978, Mahulikar *et al.,* 1979, Fleck and Smith, 1982] and numerical [Chermahini and Blom, 1991, McClung, 1991, Blom and Holm, 1985, Chermahini *et al.,* 1988] investigations which support the phenomenon of PICC under plane strain conditions. Thus the issue of the occurrence of plain strain PICC is still debatable. Nevertheless, various mechanisms by which PICC could occur in plain strain have been suggested in the literature:

- Fleck and Newman [1988] proposed that in plane strain, the residual *plastic* strain in the thickness (z-) direction is not equal to zero i.e. $\Delta\varepsilon_{zz} = 0$ with $\Delta\varepsilon^{pl}_{zz} = -\Delta\varepsilon^{e}_{zz} \neq 0$ (where ε^{pl}_{zz} and ε^{e}_{zz} are the plastic and elastic strain components of the strain ε_{zz} in the z-direction) and provides material to crack surfaces due to the tensile strain in the loading direction resulting from the Poisson effect on the elastic and plastic deformation. Residual material is then considered to come from the compressive $\Delta\varepsilon^{pl}_{zz}$ component. Sehitoglu and Sun [1991] put forward that, depending on the stress levels in the x, y and z axes at unloading, the elastic strain component ($\Delta\varepsilon^{e}_{zz}$) could be compressive and the plastic

component ($\Delta\varepsilon^{pl}_{zz}$) may be tensile instead of compressive. They found that for R = -1, 0 and 0.3, $\Delta\varepsilon^{pl}_{zz}$ was positive at minimum load when the maximum applied load was above 30% of the limit load[2]. If $\Delta\varepsilon^{pl}_{zz}$ is tensile the corresponding residual displacements may not induce any appreciable crack closure. However, they observed that $\Delta\varepsilon^{pl}_{xx}$ (i.e. parallel to the crack direction) was compressive in all the cases of R (= -1, 0 and 0.3) considered and suggested that it could supply residual material to crack surface during crack advance leading to closure (discussed in the following paragraph).

- Sehitoglu and Sun [1989, 1991] put forward a model analogous to the plane stress case involving the progressive lateral contraction of the material ahead of the crack tip along the crack growth direction. The ligament size ahead of the crack is decreased due to the compressive nature of the transverse residual strain $\Delta\varepsilon^{pl}_{xx}$ (the direction of crack propagation). This contraction occurs progressively as the crack propagates and $\Delta\varepsilon^{pl}_{xx}$ increases in the opposite direction to that of crack advance. Closure is then achieved by the competition of crack blunting and transverse motion of material in the –ve crack growth direction as illustrated in Figure 2.4. The left arrow shows the motion of movement of material in the +ve x-direction immediately behind the crack tip from in the blunting of crack surfaces in the crack wake. The right arrow depicts motion to crack surfaces in the –ve x-direction. Closure is considered to take place as a result of the sum of material movement in the +ve and –ve x-directions.
- Riemelmoser and Pippan [1998a,b] similarly suggested that plane strain closure is due to the in-plane transport of material from the wake to the crack tip but emphasise this as an elastic effect caused by the matrix surrounding the plastic wake, see Figure 2.5. The transported material produces a wedge (of the same scale as the plastic zone) which 'follows' the crack tip. However it does not leave a stretch layer of residual deformation on the crack flanks in contrast to the plane stress condition. Similarities may be seen in the deformation patterns identified by Sehitoglu and Sun [1989, 1991] in Figure 2.4, although the sense of the critical deformation is reversed.

[2] the maximum load which an elastic-perfectly plastic solid can sustain without collapsing is generally termed as 'limit load'. For CCP specimen the limit load is shown to be twice the yield stress in shear on the uncracked ligament (i.e. net section) [see Anderson, 1995] .

- Pippan *et al.,* [1994] presented a model for the plastically induced contact for meandering and branching fatigue cracks under plane strain conditions as shown in Figure 2.6. Here, plastic deformation changes the shape of crack flanks and causes a residual deformation on parts of the crack flanks. If the crack tip is near a deflection point and the plastic zone size is of the same order of magnitude or larger than the deflected length a plastic flow forward and backwards along the loading direction take place, reducing the triaxiality stress state in the vicinity of the crack tip, thus forming cavity at the deflected parts of the crack (Figure 2.6). It is interesting to note that this convolution with crack path deflections can be seen as a roughness induced crack closure processes (next section) with the implication that the efficacy of the mechanism, as shown in Figure 2.6, relies on crack tip plastic deformation being of the same order as the local deformation dimensions (for effective 'drawing up' of the material from asperity flanks to the asperity tops). As an RICC mechanism, this then has the counter-intuitive requirement for crack deflections to be small to cause RICC.

Sehitoglu and Sun [1991] discussed the relative applicability of the first three models and suggested the transverse transport of material in the crack wake is most significant through FE study.

2.3.3.2 Roughness induced crack closure (RICC)

It may be seen that when a crack is grown along a deflected (zigzag) crack path and is subjected to any permanent shear deformation (i.e. in mode II), there is a possibility that this will cause a mis-match between the crack face asperities, leading to premature contact during unloading. This type of closure, caused by virtue of crack surface roughness, is generally known as RICC. This mechanism is illustrated in Figure 2.7, with Walker and Beevers [1979] reporting for the first time the possibility of premature crack closure caused by crack surface roughness while studying fatigue crack growth in titanium samples. Discrete contacts were particularly seen in the crack flanks whilst PICC effects were apparently found to be absent. Studies of RICC in aluminium alloys for example provided by Nowack *et al.,* [1979], Halliday and

Beevers [1981], Minakawa and McEvily [1981], Ritchie and Suresh [1982, 1982a, 1982b], Bolm *et al.,* [1983].

Near the threshold crack growth condition, the maximum plastic zone size can be smaller than characteristic microstructural dimensions such as the grain size, which may then lead to a crystallographic fracture pattern where the crack growth is controlled by a 'stage I type' mechanism (crack growth may occur predominantly by single shear, in the direction of the primary slip system [Forsyth, 1953, 1962]). This results in a highly serrated or faceted fracture morphology widely identified with and an elevation in crack closure stress via the above mechanism [Minakawa and McEvily, 1981, Asaro *et al.,* 1981, Ritchie and Suresh, 1982]. The enhancement of slip irreversibility due to environmental interactions under such conditions has also been suggested to favour crack closure (enhancing irreversible mode II displacements) [Carter *et al.,* 1984, Suresh, 1998]. Various studies have pointed out the influence of RICC on near threshold crack propagation for different ageing conditions of high strength Al-alloys [Lafarie-Frenot and Gasc, 1983, Petit *et al.*, 1982, Suresh *et al.,* 1984, Carter *et al.,* 1984]. The underaged condition in particular is characterised by a crystallographic mode of failure (i.e. stage I type) with a higher resistant to crack growth, whilst the overaged condition exhibits comparatively flat fracture surfaces and higher crack growth rates. In this case shearability of the strengthening precipitates in underaged microstructures may be particularly linked to a highly inhomogeneous slip distributions and crystallographic crack growth in the underaged alloys, whilst in the overage condition, large, incoherent and non-shearable precipitates are present, inducing a more homogenous plastic deformation mode and and a flatter crack growth path, reducing RICC effects [Hornbogen and Zum Ghar, 1976 and Lindigkeit *et al.,* 1981].

2.3.4 Theoretical models of fatigue crack closure

2.3.4.1 Plasticity induced crack closure (PICC)

Having qualitatively introduced crack closure processes, important insight may of course be gained from the associated theoretical treatments. The model of PICC developed by Budiansky and Hutchison [1978] is probably the earliest. They employed an ideal plastic Dugdale [1960] model to consider the steady state growth of a long crack under small scale yielding conditions. Consistent with the Dugdale model, plane stress conditions were considered. The essence of their model is contained in two sets of assumptions. First, it is assumed that the crack line displacements at K_{max} are the same as in the ordinary Dugdale model, except that a wake of plastically stretched material remains appended to the upper and lower faces of the crack. The second set of assumptions relate to the state at K_{min}, particularly:

1. the plastically stretched crack wake surfaces are in contact all along their length,
2. ahead of the crack tip there is a region which has undergone reverse plastic flow, and
3. the plastic stretch that existed at K_{max} remains unchanged beyond this region.

Figure 2.8 shows the Dugdale model for a stationary crack, and the Budiansky and Hutchinson model for a growing crack. The nominal plastic-yielding zone size is given by,

$$r_p = \frac{\pi}{8}\left(\frac{K}{\sigma_y}\right)^2 \tag{2.4}$$

The crack tip opening displacement is given by,

$$\delta_o = \frac{K^2}{E\sigma_y} = \frac{8\sigma_y r_p}{\pi E} \tag{2.5}$$

The plastic stretch variation in the interval $(0, r_p)$ is given by,

$$\frac{\delta}{\delta_o} = g\left(\frac{x}{r_p}\right) \tag{2.6}$$

where

$$g(\xi) = \sqrt{1-\xi} - \frac{\xi}{2}\log\left|\frac{1+\sqrt{1-\xi}}{1-\sqrt{1-\xi}}\right| \tag{2.7}$$

For $x < 0$, the same expression provides the crack opening displacement. On unloading to $K = K_{min} = 0$, reverse plastic flow occurs under compressive stresses $\sigma_y = -\sigma_y$ in the interval $(0, r_p/4)$, while the plastic stretch, δ_{max} due to K_{max} in the remainder of the zone is unchanged. The residual plastic stretch in this interval $(0, r_p/4)$ can be shown as:

$$\frac{\delta}{\delta_o} = g\left(\frac{x}{r_p}\right) - \frac{1}{2}g\left(\frac{4x}{r_p}\right) \tag{2.8}$$

For the steady-state propagating crack problem, the modifications of the stationary crack result in the integral equations,

$$\frac{\delta_R}{\delta_o} = \frac{\pi^2\alpha'}{4} - \int_{\alpha'}^{1}\left(\frac{\xi-\alpha'}{\xi}\right)^{\frac{1}{2}} g'(\xi)d\xi \tag{2.9}$$

$$\frac{\delta_R}{\delta_o} = -\frac{\pi^2\alpha'}{4} - \int_{\alpha'}^{1}\left(\frac{\xi}{\xi-\alpha'}\right)^{\frac{1}{2}} g'(\xi)d\xi \tag{2.10}$$

where

$$g'(\xi) = \frac{1}{2}\log\left(\frac{1+\sqrt{1-\xi}}{1-\sqrt{1-\xi}}\right) \tag{2.11}$$

and α' denotes the ratio the reverse plastic zone size for the growing crack to that of the stationary crack, and δ_R is the thickness of the stretched material 'attached' to the crack flanks. Solving Equation 2.9 numerically, it is found that $\alpha' = 0.09$. Thus, in contrast to the stationary crack where reverse plastic yielding occurs in a quarter of the forward plastic zone, the growing crack experiences reverse yielding in less than 10 percent of the zone. The residual crack tip stretch may be found to be 86 percent of the maximum stretched value, whilst in the stationary crack case it was 50 percent.

Upon unloading, first contact of the crack flank is found to occur at $K_{cl}/K_{max} = 0.48$. As the load is further reduced, the size of the contact zone along the crack wake increases until complete closure occurs at $K = 0$. On reloading the contact region moves progressively towards the crack tip until it vanishes at $K_{op}/K_{max} = 0.56$ (K_{op} corresponds the stress intensity factor at which the crack opens). Calculated values of K_{cl} and K_{op} as a function of R compare favourably with Elber's result, as given by:

$$K_{op}/K_{max} = 0.5 + 0.1R + 0.4R^2 \qquad (2.12)$$

The Budiansky and Hutchison model suffers from three deficiencies. Firstly, cyclic crack growth is not explicitly included in their analysis. Secondly, plane strain conditions were not analysed. And thirdly, their work is limited to constant amplitude cyclic loading, although Lo [1980] has extended the approach to assess the effects of step changes in loading.

Newman [1981] developed a model also based on the Dugdale approach, modified to leave plastically deformed material in the wake of a growing crack. In the Newman model the plastic region near the crack tip and the residual plastic deformation region along the crack surfaces were considered to be composed of rigid-perfectly plastic bar elements with a flow stress σ_o, which is the average between the yield stress (σ_y) and the ultimate tensile strength (σ_{UTS}). When stress is applied, the bar elements are either intact (in the plastic zone) or broken (residual plastic deformation), with broken elements only being able to carry compressive loads (when they are in contact). Elements that are not in contact do not affect the calculation of crack-surface displacements. The crack opening stresses are computed numerically by solving the boundary value problem. A constraint factor, α, is used to elevate the crack tip flow stress $(\alpha\sigma_o)$ to notionally account for the influence of stress state on plastic-zone size and crack-surface displacements. For plane stress conditions α is equal to unity (original Dugdale model), but equal to 3 for simulated plane strain conditions. Based on 3D FE analyses Newman *et al.*, [1993] found that the 'global constraint factor', α_g (defined as the ratio of average normal stress in the plastically deformed material to the flow stress) rapidly drops as K levels increase (plastic zone size increases) and approaches a value near the plane stress limit (~1.0). The performance of such models in practice is found to depend on the correct estimation of α, in effect becomes a

fitting parameter as explicit descriptions of, mixed stress states and α_g are not available. Different crack tip stress states have a significant effect on α, hence a reliable model needs to address the gradual change of the crack-tip stress conditions with crack propagation (especially for variable loading conditions). To model variable amplitude loading conditions Wang and Blom [1991] and McMaster and Smith [2001] for example adopted variable constraint method where α is varied with a normalised stress intensity factor range ($\Delta K/(\sigma_o \sqrt{B})$) where B is the plate thickness; and plastic zone size and plate thickness respectively. The strip yield model does not model the yield zone shape correctly (particularly for plane strain conditions), however, with a high constraint factor it may be shown to produce crack-surface displacements and crack opening stresses of the correct order to those calculated from three-dimensional, elastic-plastic, finite element analyses of crack growth and closure for finite thickness plates [Blom *et al.,* 1990]. The model is used within the "FASTRAN" computer programme, currently at Version 3.0 [Newman, 1999]. Reasonable predictions of crack growth rates under complex loading histories can be obtained particularly when fitting via selection of the constraint factor is carried out [Newman, 1997, 1998, Harter, 1999], although problems have been identified in this approach e.g. see Zapatero *et al.,* 1997. A major disadvantage of the FASTRAN model is that it does not make any allowance for the influence of other mechanisms of closure; e.g. oxide induced crack closure and roughness induced crack closure. Nakamura and Kobayashi [1988] extended Newman's approach to investigate crack closure characteristics caused by asperities by increasing the length of some of the elements, under constant amplitude loading for plane stress conditions, however the imposed blocky crack paths are physically unrealistic and the mixed mode mechanism of RICC identified by most authors are essentially ignored. Xu [2001] further extended Newman's *FASTRAN* model by introducing an 'effective surface roughness' stretch to crack wake elements, designed to evaluate combined effects of PICC, RICC, and oxide-induced crack closure under both constant amplitude (CA) and variable amplitude (VA) loading conditions, however an essentially empirical approach was adopted to account for these other closure mechanisms and baseline (CA) crack closure effects were ignored. More reviews on modified strip yield models are presented by Newman [1998b].

2.3.4.2 Roughness induced crack closure

Significant literature exists on modelling RICC [Beever *et al.,* 1984, Carlson and Beevers, 1985, Evans and Hutchinson 1989, Ravinchandran 1990, Li *et al.,* 1992, Mendelsohn *et al.,* 1995, Chen *et al.,* 1996, Gracia and Sehitoglu, 1997, Sehitoglu and Gracia, 1997, Wang *et al.,* 1998]. A notable early analytical study was by Suresh and Ritchie [1982a]. They modelled crack closure induced by fracture surface roughness as a two-dimensional problem by imposing both mode I and mode II crack surface displacements. Figure 2.9 represents schematically fatigue crack closure associated with their model. Idealising the fracture roughness as triangular asperities they derived an expression for the closure stress intensity factor as,

$$\frac{K_{cl}}{K_{\max}} = \sqrt{\frac{\delta_{cl}}{\delta_{\max}}} = \sqrt{\frac{\chi \tan\theta}{1+\chi \tan\theta}} \tag{2.13}$$

where δ_{cl} is the closure crack displacement, δ_{max} is the peak displacement at $K = K_{max}$, θ is the crack deflection angle and χ is the ratio of mode II to mode I displacement that occurs during unloading. The model predicts that the extent of crack closure, defined in terms of the ratio of K_{cl}/K_{max}, is a function of the angle of surface asperities and the relative mode II crack displacements, but takes no account of absolute asperity size, and χ is an unknown fitting parameter.

Adopting an empirical approach Wasen *et al.,* [1988] proposed a relationship between K_{cl} and the standard deviation of fracture surface asperity heights based on experimental observations of ferritic steels, with deflection angles not being considered important. Wang *et al.,* [1998] pointed out that the empirical relationship of Wasen *et al.,* [1988] includes no information on the asperity shape and applied load, and the geometric model of Suresh and Ritchie [1982a] is very simplified. They proposed a dislocation-based model to estimate fracture surface mismatch. A key drawback of all these models is the need to fit unknown proportionality constants to experimental results. Parry [2000] however suggested an analytical modelling based on the micromechanical understanding obtained through FE analysis of deflected cracks for both CA and VA loading conditions, considering a description of the opening behaviour of the final deflected crack tip section and the residual deformation of asperities in the crack wake. Further discussion will be presented in Section 3.6.2.2

of this thesis. Newman *et al.,* [2003] developed an analytical model to study closure due to roughness, oxide and plasticity by combining both continuum and crack-tip dislocation concepts by relating crack displacements to crack-tip loads. The model evaluates closure as a competition of contact at the crack tip and the asperity nearest to the tip using geometric criteria. However, their model is unable to address the asperity tip deformation obtained through elastic-plastic FE analyses reported by Parry [2000].

2.3.5 Finite element modelling of crack closure

- *Introduction*

Initial attempts in finite element modelling of fatigue crack growth were reported by Miyamoto *et al.,* [1973] and Miyamoto [1974]. Comparision was made of cyclic and monotonic loading with a particular focus on changes in strain and stress distributions, and crack opening displacements upon release of the crack tip node (i.e. extension of the crack). Premature contact of the crack surfaces (i.e. crack closure) was observed during unloading in a tension-tension cycle. Ohji *et al.,* [1974] studied closing and opening behaviour, as well as stress and strain around the crack tip, for a growing crack using kinematic hardening theory under plane stress conditions. The crack was made to extend incrementally at every loading cycle, starting from a given crack length. Under a stepped program load, they observed a very high value of the effective stress intensity factor range just after the stress amplitude is raised, followed by a gradual decrease to a certain stable value, agreeing with the experimental results of Elber [1971]. Newman and Armen [1975] modified an existing finite element code to account for changing boundary conditions, crack growth and intermittent contact of crack faces under constant amplitude and simple block loading. Although a simple FE model was adopted, the calculated crack opening stresses under either constant or simple block programme loading were found to be qualitatively comparable with experimental observations. It was observed that for higher values of R (~ 0.45) under constant amplitude loading crack opening levels were lower than the minimum applied stress levels, consistent the experimental results by Katcher [1973]. Calculated crack growth using Elber's crack growth equation (see Equation 2.12)

from FE based opening levels gave qualitatively consistent agreement with experimental observations [Mathews *et al.,* 1971], i.e. crack growth retardation following a high block loading and acceleration following a low block loading. Ohji *et al.,* [1975] analysed stress and strain fields of a propagating fatigue crack and the resulting crack opening and closing behaviour, finding that the strain range value in the vicinity of the crack tip is closely related to the effective stress intensity range determined on the basis of the modelled crack opening and closing behaviour at the tip. Numerous other finite element study of the crack closure phenomenon under different loading conditions, stress states and geometries have in fact been reported in the literature, including Newman [1976, 1977], Ogura *et al.,* [1977a,b], Nakagaki and Atluri [1979, 1980] , Nakamura *et al.,* [1983], Blom and Holm [1985], Fleck [1986], Ritchie *et al.,* [1987], Lalor and Sehitoglo [1988], Fleck and Newman [1988], Chermahini *et al.*, [1988], Nicholas *et al.,* [1988], McClung and Sehitoglu [1989, 1989a], Llorca and Sanchez-Galvez [1990], McClung *et al.*, [1991], McClung and Davidson [1991], Sehitoglu and Sun [1991], Biner *et al.*, [1994], McClung [1994], Ashbaugh *et al.*, [1997], Zhang and Bowen [1998], Wei and James [2000], Parry *et al.,* [2000a, 2000b, 2000c], Anderson *et al.*, 2001, 2004, Solanki *et al.,* [2003, 2003a], Roychowdhury and Dodds [2003, 2003a], Antunes *et al.*, 2004, Kibey *et al.*, 2004. As may be found from the finite element studies in the literature, that for a consistent and reliable result, careful attention needs to be given to a series of decisions on mesh refinement, crack advance technique and attainment of a steady-state crack closure level. Further, it has been cautioned by McClung [1999] that it may not be best to place too much emphasis on the exact computed numerical values of closure or opening levels, rather focus should be to study the effects of various physical parameters on crack closure levels upon the attainment of a stable numerical model. In the following sections, a brief description of these issues affecting FE modelling is given.

2.3.5.1 Element type and mesh refinement

It is generally considered that higher order elements perform better in capturing the stress and strain fields near the crack tip. However, due to the computational cost demanded by higher order elements (from higher bandwidth requirement), non-linearity analysis needing many load steps and possibly easier meshing, early (e.g.

Miyamoto *et al.,* 1973, Ohji *et al.,* 1974, 1975, Ogura *et al.,* 1974, 1977a, 1977b, Newman and Armen, 1975, Newman, 1976, 1977, Socie, 1977) and some recent investigators (e.g. Nicholas *et al.*, 1988, Anquez and Bauding, 1988, Wei and James, 2000) adopted constant-strain triangle (CST) elements to study fatigue crack propagation. It has been put forward that their results might not give an accurate result due to lack of mesh refinement and potential plane strain locking [Nagtegaal, *et al.,* 1974] of the elements [Solanki *et al.,* 2003]. When locking occurs the stresses oscillate wildly from one element to another. To meet the incompressibility requirement associated with large plastic strains with such CST elements, Fleck and Newman [1988] adopted a 'union-jack' mesh configuration (i.e. the CST elements are arranged to form a series of squares and their diagonals) as suggested by Nagtegaal *et al.,* Later workers (e.g. Lalor and Sehitoglu, 1988, McClung and Sehitoglu, 1989, McClung *et al.*, 1991, Ashbaugh *et al.,* 1997, Dougherty *et al.,* 1997, Parry, 2000, Wang *et al.*, 2002, Solanki *et al.,* 2003, Andersson *et al.*, 2001,2004, Zhao *et al.*, 2004, Kibey, *et al.*, 2004] used predominantly 4-noded (Q4) linear strain elements. McClung and Sehitoglu [1989] found that Q4 elements predicted comparatively higher opening levels, apparently due to a better ability to capture the crack singularity leading to larger residual deformations. Recently, Solanki *et al.,* [2003] reported a mesh convergence study of various elements *viz.* CST, CST with 'union jack' configuration, Q4 and Q4 with the reduced integration method (considered to be helpful for avoiding plane strain locking [Nagtegaal *et al.,* 1977]) for both the CCT (center crack tension) and CT (compact tension) test specimen geometries. It was observed that for the CCT geometry under plane strain condition, the steady-state opening stresses (steady-state opening stress values were obtained after the crack had grown approximately twice the initial forward plastic zone size) converged as the mesh was refined. However for the CT geometry, the opening values did not converge (opening values were seen to decrease) with mesh refinement indicating that PICC is negligible or does not exist under plane strain conditions whilst for plane stress, convergence in opening values were seen readily for both CCT and CT geometries with Q4 elements. Parry [2000] adopted Q4 elements which use the selectively reduced-integration technique, (whereby reduced integration was used for volumetric strain, and full integration for deviatoric strain [ABAQUS, 1998]). Parry specifically verified that these elements could model the incompressible material behaviour under plane strain. Attempts have also been reported using higher order elements viz.,

triangular elements of cubic base functions (e.g. Ritchie *et al.,* 1987) and Q8 (8-noded quadrilateral) elements (e.g. Dougherty *et al.,* 1997, Pommier and Bompard, 2000, Wang *et al.,* 2002, Antunes *et al.*, 2004). Dougherty *et al.,* [1997] conducted a comparison of Q4 and Q8 (8-noded quadrilateral) elements. A sinusoidal residual stress pattern, with corner nodes in compression and mid-side nodes in tension was observed in the crack wake when Q8 elements were used. Refining the mesh reduced the amplitude of sinusoidal pattern, but failed to eliminate the compression-tension-compression residual stress pattern along the edge of the element. The behaviour is attributable due to the displacement functions used for Q8 elements, resulting in non-uniform stiffness along the element edge. However, for Q4 elements, mesh refinement, reduced the amplitude of the saw-tooth pattern of stresses to an acceptably low magnitude.

Meshing along the crack line must be sufficiently refined to capture the severe stress concentration at the crack tip and to simulate 'real' crack growth. However, extreme mesh refinement would lead to a large stiffness matrix bandwidth and many degrees of freedom demanding long run times. Furthermore many increments of crack growth would be required for crack propagation studies. Optimising with these two constraints is required for a computational cost effective and reliable result. Newman [1976] studied three meshes composed of constant strain triangles of different sizes on the crack line and identified critical mesh spacing for dependable solutions at different stresses. McClung and Sehitoglu [1989] observed opening levels for different meshes for a wide range of stress levels and two stress ratios. They found that above a certain stress level at each R-ratio, the meshes considered ($L_e/W = 0.002$ and $L_e/W = 0.004$, where W is the half plate width, and L_e is the element size along the crack line) gave reasonably similar results, with a consistent tendency for the finer mesh to yield higher opening levels. At intermediate maximum stress values, normalised opening levels (S_{open}/S_{max}) sharply increased and then sharply decreased with S_{max}/σ_y, where S denotes remotely applied stress and σ_y is the yield stress. They suggested this to be a 'false peak', i.e. an artefact of the modelling process, noting that at low loads the mesh is not sufficiently fine to capture reversed yielding upon unloading. They suggested a simple criterion for mesh sufficiency based on the ratio of the element

size along the crack line to the forward plastic zone size (r_p). They recommended that a value of $L_e/r_p \leq 0.05$ is good enough for reliable results with Newman's constant strain elements, whilst for first order quadrilateral elements (Q4), a criterion of $L_e/r_p \leq 0.10$ seems to be sufficient for $R = 0$, and $L_e/r_p \leq 0.15$ for $R = -1$. In a later study McClung *et al.*, [1991] observed the criterion to be slightly over conservative for plane strain where plastic zones widths along the crack propagation line are smaller and the near-tip has severe strain gradients, and suggested $L_e/r_p \leq 0.20$ be satisfied. However, mesh refinement studies on CCT and CT geometries by Dougherty *et al.*, [1997] under plain strain suggested that the mesh density ahead of the crack should satisfy $L_e/r_p \leq 0.10$. Park *et al.*, [1997] suggested from their FE study on the CCT geometry with Q4 elements that, a unique, most-appropriate mesh size exists for a given loading condition that will give good numerical results with close accord with the experimental results. The value of the most-appropriate mesh size was found to be nearly constant, ranging from 0.77 to 0.91 times the reversed plastic zone size (r_c), however in terms of the monotonic plastic zone size it was seen to decrease with increasing K_{max}, for the ranges of R (0-0.3) considered; suggesting that r_c may relate better for estimating appropriate mesh size. However Solanki *et al.*, [2003] argued that this method is flawed as various techniques [e.g. Blandford *et al.*, 2002, Dawicke *et al.*, 1990a, Allision and Pompetzki, 1988, Ray and Grandt, 1988, Donald, 1988] give inconsistent results in measuring the opening loads. It has been suggested by Solanki *et al.*, [2003] that an adequate mesh (Q4 elements) refinement is one which contains 3-4 elements in the reversed plastic zone. However, a slightly coarser element of about 0.5-1.0 r_c was suggested by Antunes *et al.*, [2004] using Q8 elements. Antunes *et al.*, found that elements that are too large give reduced closure levels because of the inability of the elements to capture the crack tip elasto-plastic behaviour, whilst very small size elements also tend to give lower closure levels. In a recent 3D small scale yielding fatigue crack growth study, it has been reported that computed opening loads showed an independence of mesh refinement when a) the plastic zone at peak load encloses more than 10 eight-noded brick elements, b) at least two elements are contained in the reversed plastic zone, and c) the half-thickness has at least five element layers [Roychowdhury and Dodds, 2003]. Thus from the findings of Solanki *et al.*, [2003]

and Roychowdhury and Dodds [2003], about 20 elements in the forward plastic zone is suggested for simulating fatigue crack closure using FE method. However, in the studies by Parry [2000], it has been observed that mesh refinement of $L_e = r_p/30$ resulted in slightly lower crack opening profiles in the region away from the near-tip, and higher opening profiles in the near-tip region as compared to that of $L_e = r_p/15$ refinement, suggesting that mesh refinement may have an influence in the closure determination. Nevertheless, when exact quantitative corroboration between experimental and FE results is inherently difficult considering the idealised nature of FE models, and for long fatigue crack growth simulation wherein the computational cost is expensive, a mesh refinement of a minimum of about $L_e = r_p/10$ (as adopted by many researchers e.g., Nicholas, 1988, Dougherty *et al.*, 1997, Wang *et al.*, 2002, Andersson *et al.*, 2004, Kibey, *et al.*, 2004) is expected to give fairly good understanding of the closure phenomena. Whilst most the aforementioned criteria on mesh refinement requirement are expressed in terms of the element length along the crack plane (L_e), Dougherty *et al.*, [1997] found that an aspect ratio (H_e/L_e, where H_e is element height) of 2 significantly reduced the amplitude of saw tooth residual stress pattern along the crack wake, and this consideration is adopted by Andersson *et al.*, [2004]. Although they attributed the benefit of using an aspect ratio of 2 to the bending resistance of the crack plane element immediately ahead of the tip, it may be mentioned that elements $H_e/L_e \rightarrow 1.0$ (i.e. square element) are considered a better choice and help in minimising interpolation errors (Antunes *et al.*, 2004).

2.3.5.2 Stabilisation of crack closure

In many cases, cracks progressing from an initial length are reported to reach a constant closure level [e.g. McClung and Sehitoglu, 1989, Kibey *et al.*, 2004]. To attain this stabilisation, the crack must grow far enough to develop a significant plastic wake and the crack tip should be outside the stress field of the initial defect or pre-crack. Park *et al.*, [1997] and Antunes *et al.*, [2004] observed stabilised closure levels after a crack has propagated ahead of the monotonic plastic zone of the first cycle. However, Fleck and Newman [1988] and Wu and Ellyin [1996] reported non-stabilised crack opening values even after the crack has propagated through the initial forward plastic zone. Ward-Close and Ritchie [1988] observed that a steady-state closure level will typically be obtained when a crack has propagated through three or

four overload plastic zone sizes flowing a transient. McClung and Sehitoglu [1989] suggested that a modelled crack should be allowed to grow beyond the region of material which experiences significant plastic deformation on the first cycle of loading. A large amount of crack growth and sufficiently high applied stress have been found to show an initial stabilisation followed by a subsequent decrease in crack opening levels due to the loss of elastic constraints resulting from extensive yielding around the crack tip [McClung, 1991a]. A similar observation on decaying opening levels when the remaining ligament becomes small has also been reported [Daniewicz and Bloom, 1996]

2.3.5.3 Crack-tip node release scheme

There is no clear consensus on the appropriate FE 'mechanisms' for crack advance, with various schemes being reported in the literature. Again, none of the reported approaches can be assumed to represent the fatigue process where, according to slip models of striation formation, crack propagation is a progressive process occurring during the entire loading cycle (Wei and James, 2000, Antunes *et al.*, 2004). Attempts have been made to develop crack advance schemes using critical damage criteria, such as Miyamoto *et al.*, [1973] and Miyamoto's [1974] critical cumulative plastic work near the tip, Newman's [1977] critical strain criterion, Nakagaki and Atluri's [1979] critical crack opening stress, and the critical energy rate criterion of Zhang *et al.*, [1992]. Other reported crack propagation schemes include moving mesh methods [e.g. Nakagaki and Atluri, 1980], cohesive element methods (crack propagation is regarded as a gradual process in which separation between incipient material surfaces is resisted by cohesive forces) [Nguyen *et al.*, 2001, Roe *et al.*, 2001] and X-FEM (extended FE method, where discontinuous and 2D asymptotic crack tip displacement fields are added to the FE approximation to account for the crack, thus enabling the domain to be modelled with no explicit crack surface meshing) [Sukumar *et al.*, 2003]. However most numerical models adopt the technique of releasing a model node (e.g. extension of one element) on every cycle for efficiency [e.g. McClung, 1999, Kibey, *et al.*, 2004] and few have tried releasing more than one node per cycle (e.g., Pommier and Bompard, 2000, Antunes *et al.*, 2004, Kibey, *et al.*, 2004). Antunes *et al.*, [2004] found that releasing nodes at every cycle resulted in 'smoother' crack profiles. Newman and Armen [1975], Newman [1976, 1977], Blom and Holm

[1985], Fleck [1984, 1986, 1988], Lalor and Sehitoglu, 1988, Sun and Sehitoglu [1991], Chermahini and Newman [1988], Solanki *et al.,* [2003], Zhang *et al.,* [1992], Zhang and Bowen, 1998, Parry [2000], Wei and James [2000], Zhao *et al.*, [2004] and Antunes *et al.*, [2004] have adopted the release of the crack tip node at maximum load in each cycle to simulate crack growth. Ohiji *et al.,* [1974, 1975], Ogura *et al.,* [1974, 1977a, 1977b], Nakamura *et al.,* [1983], McClung *et al.,* [1991], Park *et al.*, 1997, Park and Song [1999] and Solanki *et al.,* [2003] alternatively released the crack tip node at the minimum load in each fatigue cycle. Newman [1997] contented the rationality behind propagating a crack at a minimum load cycle, as the crack tip would obviously be subjected to compressive stress field. Nakagaki and Atluri [1979, 1980] use a scheme of releasing the crack tip node at different points along the forward loading excursion, and observing from their formulation that the apparent crack closing levels were dependent on the 'timing' of the node release. Palazotto and Bendnarz [1989] and Palazotto and Mercer [1990] suggested a criterion of extending the crack at 98% of the maximum load. Lalor *et al.,* [1986], Lalor and Sehitoglu [1988] and Kibey, *et al.*, 2004 considered a node release scheme in which the crack tip was allowed to propagate immediately after the point of maximum load, during the first increment of unloading. Nicholas *et al.,* [1988] employed the gradual release of the crack tip node during unloading, beginning at the maximum load. However, studies on three-dimensional semi-circular fatigue crack by Zhang and Bowen [1998] suggested that node releases at 10%, 50% and 100% of the maximum load resulted in very little effect both on the surface and in the interior of the specimen.

There are further reports of observed differences when using either the maximum or minimum load node release scheme [e.g. McClung and Sehitoglu, 1989, Wu and Ellyin, 1996, Park *et al.*, 1997]. McClung and Sehitoglu [1989] compared three schemes *viz.* node release at maximum load with stabilisation (after Newman), node release at minimum load (after Ogura *et al.*), node release immediately after maximum loading (after Lalor), and observed that the differences in the three schemes were not significant, especially at higher stresses. However, Wu and Ellyin [1996] found some variation in the crack opening values under the minimum and maximum loading node advance schemes. Park *et al.*, [1997] observed that releasing the node at maximum load on every cycle produces higher opening levels as compared to closing

levels (similar finding can be found in the work of Newman [1976] and Wei and James [2000]), which is generally contradictory to experimental results; on the other hand the reverse is found to be true when nodes are released at the minimum load on every cycle. Solanki *et al.,* [2003a] suggested that the differences may be due to the insufficient discretisation of the reversed plastic zone size. McClung *et al.,* [1991] revisited their earlier work [McClung and Sehitoglu, 1989] after truss elements (used to imposed the changing boundary condition) were removed. When the boundary conditions on the crack line nodes were imposed directly, they observed that both the maximum and minimum node release schemes gave similar crack opening levels for nearly all the cases that were examined. Recently Solanki *et al.,* [2003, 2003a] showed that both the minimum and maximum load node release schemes agree well when a suitably refined mesh is used. Whilst it is now generally evident that node releases at maximum or minimum does not substantially affect numerical results concerned, releasing at maximum load cycle may appear to be closer to a realistic physical process; with crack propagation at minimum load generally been carried out to avoid numerical solution difficulties [Antunes, 2004].

2.3.5.4 Effect of constitutive model

The majority of finite element studies of crack closure in the literature have employed bilinear hardening stress-strain relationships due to the simplicity in numerical implementation (e.g. Fleck and Newman, 1988, McClung *et al.*, 1991, Ashbaugh *et al.*, 1997, Andersson *et al.*, 2004, Kibey, *et al.*, 2004). However such relationships do not accurately represents the constitutive response of many real materials (although, some materials like medium carbon steels, may be reasonably well represented in response to cyclic loading [Landgraf, 1979]). McClung and Sehitoglu [1989a] made an attempt to accurately simulate rounding of the stress strain curve on each load reversal following significant plastic deformation, based on the Ramberg-Osgood power-law formulation. Although this model is more sophisticated, it has its own limitations. The implementation in numerical analysis is more involved than a bilinear model, and accurate calibration of the material behaviour is required. The power-law may be able to represent well a cyclically stable stress-strain relationship, and is probably therefore a better descriptor of near-tip behaviour. It is seen that under different loading conditions and for different materials, both forms of material model

may compare well with experimental results. For instance, the closure levels obtained from the experiments of Elber [1970] taken at relatively low maximum stress levels agree well with bilinear model results, whereas power-law hardening model results compare well with the experimental results of Lankford *et al.*, [1984] for higher maximum stress levels. Ritchie *et al.*, [1987] and Dougherty *et al.*, [1997] have used multi-linear stress-strain curves by explicitly defining the dependence of yield stress on increasing plastic strain. However there appears to be a lack of detailed comparison between closure levels obtained using this approach and using a bilinear model. Antunes *et al.*, [2004] studied isotropic and kinematic models (for plane stress conditions) and found that isotropic hardening predicted higher closure levels as compared to that of kinematic hardening models, attributing more significant plastic deformation with isotropic hardening model; however predicted closure levels using kinematic hardening models were found to be closer to experimental results. Parry [2000] reported for higher strength Al-alloy modelling in SSY that there was no significant difference in crack opening displacements using kinematic, isotropic and elastic-perfectly plastic material behaviour, suggesting that strain hardening effects and hardening may not be a primary factor in crack closure, at least for materials of interest here.

2.3.5.5 Effect of specimen geometry

The influence of fatigue specimen geometry upon closure response was studied by Fleck [1986] and Fleck and Newman [1988], conducting plain strain analyses for CCT and single edge notched bend (SENB) specimens. At a load ratio of 0, crack closure was observed for centre-cracked panels but not for bend specimens. Closure was not observed for CCT specimens for $R \geq 0.3$. For a transient period of crack growth, as the crack evolved from the state of a stationary crack to the steady state of a growing fatigue crack, closure was enhanced for the CCT specimen format. They explained the influence of crack specimen geometry upon closure in terms of the T-stress (see Appendix A2). A decrease in closure levels has been particularly observed for increasing T-stress (T_{max}/σ_y is lower for CCT than SENB specimen) which would appeal, on first inspection at least, consistent with decreasing plastic zone dimensions as T rises. McClung [1994] also studied specimen geometry effects on fatigue closure. Elastic-plastic finite element analysis was conducted for CCT, single-edge-cracked

plate (tension), and single-edge-cracked plate (bend), at different crack length to width to ratios. It was observed that the maximum stress to flow stress ratio, S_{max}/σ_o, which successfully describes closure in many CCT configurations, does not correlate with the different geometries. It was seen that the normalised stress intensity parameter, K_{max}/K_o, where $K_o = \sigma_y\sqrt{\pi a}$, can correlate crack opening stresses for different geometries and crack lengths better. The quality of correlation was found to be good at small K_{max}/K_o, and gradually degenerated as $K_{\max}/K_o$ increase beyond the small-scale yielding regime. K of course becomes less effective in characterising the crack tip deformation and stress fields at progressively higher stresses, consistent with a diminishing correlation with LEFM criteria (i.e. 'K' based).

2.3.5.6 Plain strain and plain stress modelling of PICC

It is generally agreed that 'extra' material behind the crack tip may resist reverse deformation during unloading causing a reduction in the crack growth rate. For plane stress conditions, a specimen may become thinner near the tip of a crack as material is transported to the crack flanks from the free surfaces of the sample. Each crack growth increment produces a part of the 'extra' material which eventually extends over the entire crack length [Reimelmoser and Pippan, 1998a,b]. Models by Budiansky and Hutchinson [1978] and Fuhring and Seeger [1979] are able to describe this situation. As noted earlier, out-of-plane flow for plane strain conditions is not allowed, and there is no volume change of the material under plastic deformation by definition, hence various researchers are of the view that PICC cannot occur under these conditions [Minakawa *et al.,* 1986 and Louat *et al.,* 1993]. However, both experimental [Fleck and Smith, 1982, Bray *et al.,* 1992] and numerical [Ogura *et al.,* 1977 and Blom and Holm, 1985] studies have been reported to suggest that PICC can occur under plane strain. Stabilised FE modelled closure levels were observed by Blom and Holm [1985] which were identified to agree well with results for experiments on Al 2024. However, mesh refinement criteria of McClung and Sehitoglu [1989] would not be met for the analysis performed by Ogura *et al.,* [1977], hence the reliability of some results may be questionable. Investigations by Reimelmoser and Pippan [1996, 1998a] suggests that plastic deformation left in the crack wake during fatigue crack propagation close the crack, near the tip, in spite of

the volume constancy during plastic deformation, as a rotation of material occurs parallel to the growth direction (i.e. as in Figure 2.5). Two dimensional finite element analysis reported by Fleck [1986] and Fleck and Newman [1988] concluded, in general, that crack closure did not occur under steady-state plane strain conditions. Fleck and Newman [1988] indicated that PICC in plane strain was due to an 'artificial wedge' of material formed near the initial crack tip used in the modelling. It was put forward that PICC in plane strain exists only for a transient period due to the unrepresentative residual strains at the initial crack tip and its effect would diminish as the crack was allowed to propagate away from the wedge. These results are somewhat in contradiction to the later works of Llorca and Sanchez-Galvez [1990], McClung *et al.,* [1991], Sehitoglu and Sun [1991] and Wei and James [2000], where closure levels of the order of 20% to 30% of K_{max} are found, at a zero load ratio, under small scale yielding. Even at a higher load ratio of 0.5, closure has been reported in plane strain for 20% of the loading cycle [Blom, 1984, Blom and Holm, 1985, Ritchie *et al.,* 1989]. Three dimensional investigation reported by Chermahini *et al.*, [1988] has shown that a crack front may first close on a free surface (exterior) plane on the specimen, and closes last on the interior plane, depicting that fully three dimensional closure behaviour corresponds to a continuous variation between two dimensional behaviour for plane stress on the specimen surface, and plane strain in the mid-plane.

2.3.5.7 Monitoring crack closure

Of the various ways of monitoring crack closure in FE models the following may be identified as relatively simple and direct approaches: *viz.* 1) observing the point in the unloading cycle at which the displacement of a crack wake node becomes zero [e.g. Newman and Armen, 1975, Fleck and Newman, 1988], 2) assessing the crack tip stress [e.g. Wu and Ellyin, 1996], 3) assessing the stress of the nodes behind the crack tip [e.g. Lalor and Sehitoglu, 1988, McClung and Sehitoglu, 1989, Solanki, *et al.,* 2003, Kibey *et al.*, 2004] and 4) examining changes in specimen compliance [e.g. Socie, 1977 and Nakamura *et al.,* 1983]. Newman and Armen [1975] and Fleck and Newman [1988] have monitored the closure of the first node behind the crack tip; however it has been observed that, in plane strain, the first node behind the tip nearly may even close during the first unloading increment. As noted earlier McClung and Sehitoglu [1989] suggested that it might be due to the in-complete redistribution of

loads and plastic strains immediately upon node release. To circumvent this, they assessed closure by the behaviour of the second node behind the crack tip, while opening levels were based on the behaviour of the first node behind the crack tip. However, in a later paper [Sehitoglu and Sun 1991, Kibey, *et al.*, 2004], returned to using closure of first node to examine closure. Solanki *et al.*, [2003] assessed crack opening values based on the contact stress distribution at minimum load using superposition principle, and hence cannot be valid for large stress distribution. Wu and Ellyin [1996] assessed crack closure values based on the crack tip stress, employing the assumption that when the tensile stress borne by the crack tip node changed to compression, a crack can be considered close. However, this method depends on the accuracy of the crack tip stress where the stress gradients are at their most severe. Further, Sun and Sehitoglu [1992] propounded that Wu and Ellyin's method may confuse the role of crack-tip residual stresses in fatigue crack growth (which are related to closure), as the presence of residual stresses at the tip does not imply crack closure. Antunes *et al.*, [2004] observed that closure definition based on crack-tip stress reversal (from tension to compression) gives higher values of crack closure/opening stresses as compared to the conventional definitions based on first contact of the crack flank because a compressive stress state must exist for crack flank contact. Further it was argued that contact of the first node behind the current tip does not indicate that the crack is fully open but that the crack is open between this node and the current crack tip. However, mesh convergence studies reported by Anquez and Baudin [1988] showed apparent merging of the results based on both definitions. James *et al.*, [2003] alternatively reported that definitions based on first node contact gave a better fit to the experimental results based on compliance change. Parry *et al.*, [2000, 2000a] have determined closure points by neglecting the first node behind the crack tip and compared the results with closure points obtained using an offset compliance method, finding the results comparable, suggesting that either of the two methods could be used. Overall it may be noted that significant ambiguity remains in monitoring the behaviour of near-tip nodes and relating the results to real closure processes.

2.3.5.8 Numerical modelling of crack deflection

Roughness induced crack closure was first modelled numerically by Llorca [1992] using finite difference (FD) techniques. It was assumed that the functional dependence of the displacements in time and space can be dissociated, giving rise to independent semi-discretizations for both time and space. The mesh of the continuum is made up of constant strain triangles and the computation is broken down into a number of time steps. Isotropic hardening and bilinear stress-strain curve were chosen. In the FD technique the continuum (elastic-plastic solid) is analysed based on the conservation of momentum and the constitutive behaviour of the material. The masses of the elements are assumed to be lumped at the nodes. In each time step, the forces acting at each node are used to calculate its acceleration which is integrated to yield its velocity and displacements. These nodal displacements produce forces which results from: 1) relative displacements within each triangle giving rise to strains that cause the corresponding stresses through material properties, and 2) the contact between different surfaces. These forces, together with body forces and the external loads, give rise to the resultant force acting at each node. This completes one computational cycle and the process is continued until the final time step. Displacement boundary conditions are imposed by eliminating the equations of the nodes whose displacements are known. In order to effectively uncouple the equations of motion, the time increment between two time steps is made less than the time required for the information to travel between the two nearest nodes in a mesh (based on the pressure wave speed). To satisfy this criteria, the numerical simulations were carried out at about 5000 Hz, which is comparatively large compared to the standard fatigue test frequencies (below 100Hz). Dynamic effects are claimed to be small and do not perturb the results. In Llorca's model of RICC, it is stated that as the attention was focussed on modelling of RICC and the effects of plasticity were largely neglected: the source of crack closure was suggested to be in the displacements of the crack surfaces in the crack wake. Modelling criteria for PICC [McClung, R.C. and Sehitoglu, 1989, Llorca and Sanchenz-Galvez, 1989], particularly the element size in the crack path being smaller than one-tenth of the plastic zone size, was not followed, and it was assumed that a ratio of crack branch length to element size of about four was reasonable. For the problem considered the maximum plastic zone size was about

1 μm, giving the ratio of element size to plastic zone size of about 10:1 (which is much larger than suggested for PICC modelling, as discussed previously). It was observed that RICC closure was discontinuous and concentrated at points where the crack changes its direction of propagation. The main controlling factor of RICC was seen to be the deflection angle between the crack branches and the average direction of crack propagation. When the deflection angle was kept constant, crack closure took place in the last crack kink, and closure levels increase with the deflection angle (consistent with the geometrical model of Suresh and Ritchie [1982a]), with no effect of the crack length for the range studied. However, when the deflection angle was allowed to change during crack propagation, significant amounts of closure were developed, the crack being closed during the greater part of the fatigue cycle. The results were indentified to agree with high closure loads measured experimentally in 2124-T351 aluminium alloy [Ritchie *et al.,* 1987]. The main mechanism of RICC was suggested to be when the mode I and mode II displacement ratio in the crack wake is different during loading and unloading steps. The proposed mechanism has been criticised on two points by Parry [2000] from a physical standpoint. First, the change in the mode I/ mode II displacements from loading to unloading during real crack propagation can be expected to be very small as, in a near threshold condition, the increment of crack growth becomes infinitesimal. Second, the mechanism would lead to residual deformation of a purely elastic crack, which cannot be realistic - permanent deformation of the crack faces and hence RICC can only occur from *plastic* deformation.

Parry *et al* [2000,a,b,c] investigated crack closure arising from crack deflection and plasticity using finite element modelling in a long fatigue crack in a notional aerospace aluminium alloy. The approach is an extension of Newman and Armen's [1975] modelling concepts. The FE mesh consisted of four-noded quadrilateral elements and bilinear kinematic hardening model was used. The element length along the crack propagation direction was set so that McClung and Sehitoglu's [1989] mesh sufficiency criteria was met. An incremental crack propagation scheme was used along the lines of Newman and Armen [1975] and Fleck and Newman [1988]. Friction effects along the crack surface were not considered. Plane slip bands ahead of the crack tip were also simulated by restraining nodes in shear with rigid-perfectly

plastic truss elements. By controlling the yield stress of the truss elements, the effective critical resolved shear stress (CRSS) along the crack propagation direction was varied. Based on both overall specimen compliance and node behaviour along the crack path, the results showed: 1) an increasing effect of crack deflection angle on RICC levels, consistent with the simple analytical model of Suresh and Ritchie [1982a] and FD model of Llorca [1992], 2) strong dependence of closure on the residual plastic strains in the wake, rather than global shear displacements of the fracture surface due to mixed mode behaviour at the crack tip, and 3) low closure levels compared to experimental data, suggested to be consistent with the absence of environmental irreversibility in the FE models and the 2D idealisation of crack path. Slip band simulations showed a particular increase in closure levels at high deflection angles, improving the apparent accuracy of the modelling in relation to experimental data. The findings of this work are considered in considerable detail in Chapter 3.

2.4 Fatigue crack growth behaviour growth under variable amplitude loading

2.4.1 Introduction

In the preceding sections, issues pertaining to fatigue crack growth behaviour under constant amplitude loading have been particularly addressed. The study of constant amplitude (CA) fatigue behaviour imparts useful insights into the fundamental mechanisms of fatigue crack growth behaviour. However, for most engineering components/structures, variable amplitude loading (VA) is more relevant than constant amplitude loading. The ability to understand the phenomenon of load interaction under VA loading is therefore significant in residual life assessments and damage tolerant design. Given the importance of VA loading, various intensive investigations have been made over the years (e.g. Schijve and Broek, 1962, von Euw et al., 1972, Jones, 1973, Arkema and Schijve, 1976 Bernard *et al.*, 1976, Vecchio *et al.*, 1984, Shin and Fleck, 1987, Alexander and Knott, 1987, Shin and Hsu, 1993, Wheatley *et al.*, 1999, Borrego *et al.*, 2003). As real time loading spectra are potentially highly complex, much research has been focussed on understanding the simplest case of a single overload or underload inserted in a constant amplitude

loading schedule, with the general conclusion that crack growth retardation and acceleration occurs respectively for each case. Whilst retardation of fatigue crack growth associated with an overload is clearly beneficial for fatigue life extension, the technique is not widely used, perhaps due to the lack understanding of its underlying mechanisms [Shin and Hsu, 1993]. When overloads are applied periodically, interaction between them may occur with the importance of load interaction effects for periodic overloads being established in several of studies [e.g. Wei *et al.,* 1973, Mills and Hertzberg, 1976, Tur and Varder, 1996, Hammouda *et al.,* 1998], identifying an optimum spacing between two individual overloads for maximum growth rate retardation. Load sequence effect have been studied by Zhang *et al.,* [1987] by considering underload-overload and overload-overload situations, with a reduction of post-overload retardation being clearly identified when an underload is followed by an overload, as compared to the situation where overload is followed by another overload, emphasising the presence of strong load sequence effects.

2.4.2 Transients post overload effects

It is well documented that the application of a single tensile overload in a constant amplitude load schedule will generally lead to transient crack growth retardation or sometimes even crack arrest. For most ductile materials, the transient crack growth response for a mode I crack following a single tensile overload entails an initial brief crack growth acceleration (immediately after the overload), followed by a period of prolonged retardation leading either to crack arrest, or growth rates eventually returning to their baseline (pre-overload) levels [e.g. Corlby and Packman, 1973, Ward-Close and Ritchie, 1988, Venkateshwara Rao and Ritchie, 1988,a, Von Euw, 1972], as shown schematically in Figure 2.10. However, there are also reports which suggest the absence of initial acceleration in crack growth rates [e.g. Paris and Herman, 1982, Goel and Chand, 1994]. Shin and Hsu [1993] and Tsukunda *et al.,* [1996] have for example reported that for higher load ratios (e.g. 0.5, 0.7), post-overload growth rates show: 1) no indication of initial brief acceleration, 2) an acceleration phase following the retardation where the crack growth rate is greater than the stable baseline rate, and 3) relatively short lengths of transient post-overload retardation. The magnitude of the delay following an overload may be quantified in a number of ways, for example either in terms of delay distance (a_d), or affected

distance (a_{aff}), or number of delay cycles (N_d) (see Figure 2.10). Delay behaviour is typically a function of the baseline stress intensity range ($\Delta K_{(BL)}$), load ratio (R), overload ratio, $\%OL$ (defined as $\frac{K_{OL} - K_{\max}}{K_{\max}} \times 100\%$, where K_{OL} is the maximum value of K during the overload cycle), sequence of loading and specimen thickness, for a given material, microstructure and environment. The occurrence of a minimum in crack growth rate some distance *after* the application of a tensile overload is generally termed as 'delayed retardation'. Von Euw [1972] reported that the distance of delayed retardation from the overload location is approximately one-eight to one-quarter of the overload plastic zone size. Variation in post-overload crack growth response has also been reported in terms of crack front position in thick specimens [Bernard *et al.*, 1976, 1977]. At the surface of thick specimens (where conditions are closest to plane stress), crack growth retardation behaviour is similar to that of thin specimens, where plane stress conditions apply. However, at the centre of the specimen, where plane strain conditions exist, retardation of crack growth occurs for a shorter distance compared to measurements made at the surface. It has also been observed that the minimum crack growth condition may be obtained at the centre of a thick specimen almost immediately after application of overload [Bernard *et al.*, 1976,1977, Bathias and Vancon, 1978, Suresh, 1983, de Castro and Park, 1982, Fleck *et al.*, 1983].

In the literature, various mechanisms have been proposed to account for experimentally observed post-overload fatigue behaviour in ductile alloys. However, precise mechanistic origins remain open to discussion [Venkateshwara Rao and Ritchie, 1988]. In general it is considered that no single mechanism can rationalise the complex phenomena of crack acceleration and retardation during VA amplitude loading, and that several concurrent, and potentially competing mechanistic processes govern behaviour [Suresh, 1988]. Several critical reviews on the various mechanisms have been made [e.g. Suresh, 1983, 1983a, 1988, Fleck, 1988, Shin and Hsu, 1993, Skorupa, 1998, 1999]. The following subsections will discuss the proposed mechanisms to explain the post-overload fatigue behaviour.

2.4.2.1 Plasticity induced crack closure

The discussion presented in Section 2.3.2.1 considered the mechanism by which PICC may retard fatigue crack growth under constant amplitude loading. It has been identified that PICC may also account for post-overload transient retardation phenomena [Elber, 1970, 1971]. Subsequent reports (e.g. Shin and Fleck, 1987, Fleck, 1988, Tokaji *et al.*, 1984, Fleck *et al.*, 1983, Tanaka *et al.*, 1981, Shin and Fleck, 1989, McEvily and Ishihara, 2002, Borrego *et al.*, 2003] have supported Elber's argument. The application of an overload induces immediate, local crack blunting (e.g. Bichler and Pippan, 1999). Extensive tensile deformation is caused ahead of the crack tip, with the potential to reduce crack closure levels as near-tip crack opening levels are increased during subsequent crack propagation. The effective stress intensity range, ΔK_{eff} (= K_{max} - K_{cl}) is increased by crack blunting, causing the initial acceleration in crack growth rate, but as the crack advances closure levels are rapidly increased due to the wedging action of the overload stretched material passing into the crack wake. The increase in closure levels leads to a reduction in ΔK_{eff}, thus decreasing the crack growth rate. When the crack grows away from the zone of plastically stretched overload material, its effect on the near tip strain field, and hence the crack growth rate can be expected to decay back to pre-overload levels. Experimental work [e.g. Von Euw, 1972, Ward-Close and Ritchie, 1988, Kumai and Higo, 1996] suggests that enhanced levels of PICC and the subsequent increase in frictional contact between crack surfaces and abrasion in the post-overload region can be seen in the obliteration of fracture surface marking such as striations. Enhanced post-overload closure levels are also reported by Fleck [1988] particularly using a specialised push-rod compliance gauge to access plane strain behaviour in thick specimens. It has been noted that crack closure via wedging is not relevant in mode III fatigue cracks (anti plane shear) situations, where opposite behaviour (i.e. accelerations in crack growth rate) are reported following a single overload [Nayeb-Hashemi *et al.*, 1983]. In terms of mode I plane stress behaviour it has also been observed that, in contrast to baseline loading where higher closure levels are expected compared to plane strain because of comparatively larger plastic zone sizes and availability of through-thickness contraction, enhanced post overload retardation effects have been shown for some materials in plane strain compared to plane stress [Suresh, 1983]. Despite the fact that there are various experiments [e.g. Elber, 1970, Himmelein and Hillberry, 1976] to support the role of PICC in influencing crack

growth retardation effects, many inconsistencies have been reported, with the experimental results suggesting that PICC alone is not sufficient to explain all the observed retardation phenomena (e.g. Robin *et al.,* 1983, de Castro and Parks, 1982, Chanani and Mays, 1971, Shih and Wei, 1974, Wei and Shih, 1974, Wei *et al.*, 1980, Gan and Weeterman, 1981, Brown and Weeterman, 1981, Kim and Shin, 1999). However, Fleck [1988] also notes that some of the controversies may be influenced by: 1) the use of insensitive closure measuring equipment, and 2) different responses to an overload in the bulk of a thick specimen and at the surface.

2.4.2.2 Crack tip blunting

Christensen [1959] and Rice [1967] have argued that on application of an overload, a previously sharp crack will become blunted, and it can remain blunted even during post overload crack growth, leading to crack growth retardation. Retardation is then linked to the crack behaving like a notch with finite tip curvature with a less stress concentration than the original sharp crack tip. Furthermore a finite number of cycles may be required to re-initiate and propagate from this notch. Blunting following an overload has been observed in polymeric materials such as polycarbonate [Banasaik *et al.,* 1977] and in several metal alloys (e.g. Lankford and Davidson, 1981). Based on experimental evidence [Taylor and Knott, 1982] cited by Fleck [1988] it is suggested that blunting only causes retardation at extremely high overload ratios. On the other hand, temporary arrest following an overload has been observed for an apparently sharp crack tip by Lankford and Davidson [1976]. It also has been observed that both crack growth acceleration under spike underloads and crack growth retardation under spike overloads are accompanied by crack tip blunting [Fleck, 1985, Halliday *et al.,* 1997], hence the contribution of crack blunting to immediate retardation is not clear rather than causing non-closure of the crack tip upon application of overload, leading to a brief increase in fatigue crack growth rates just after the application of overload [Mille, 1979, Robin *et al.,* 1983, Shih and Hsu, 1993, Ward-Close *et al.,* 1989, Ngangga and James, 1996, Venkateshwara Rao and Ritchie, 1988].

2.4.2.3 Residual stresses

A residual compressive stress zone is produced at a fatigue crack under positive tensile loading due to constraint of the surrounding elastic material of the previously

yielded zone [Rice, 1967]. X-ray measurements have shown that upon application of an overload, the residual compressive zone is enlarged compared to the baseline loading [Allison, 1979, Taira and Tanaka, 1979] and that the magnitude of the residual stress may be of the order of the yield stress [Davidson, 1988]. When an overload induced compressive residual stress is superimposed on the applied stresses, a reduction of the local tip stress is predicted which might be expected to generate retardation of crack growth rates [Schijve and Broek, 1962]. Classical empirical models of variable amplitude fatigue based on this concept has been proposed by Willenborg *et al.,* [1971] and Wheeler [1972]. The importance of residual stresses has however been questioned by Fleck [1988, 1985] and Suresh [1998]. Fleck [1988, 1985] argued that due to mean stress relaxation the material immediately ahead of the crack tip probably experiences fully reversed loading regardless of the residual stress. Thus the residual compressive stress ahead of an overloaded crack tip can at most account for the initial retardation phase and cannot account for the total retardation transient. Shin and Fleck [1987] compared overload induced retardation effects in both cracked and notched specimens. No significant difference in overload transient behaviour was found, although residual compressive stresses from specimens could be expected to be different. It may also be mentioned that the extent of crack growth retardation is often much larger than the overload reversed plastic zone size [Suresh, 1982, 1983, 1988, Jones, 1973, Bernerd *et al.,* 1976, Fleck *et al.,* 1983, Robin *et al.,* 1983, Wei *et al.,* 1980, Powell *et al.,* 1981] suggesting further that residual stresses cannot be the only factor affecting transient post-overload crack growth.

2.4.2.4 Crack deflection and branching

Post-overload crack deflection and/or branching from a nominal Mode I crack growth plane has been observed by various researchers [Lankford and Davidson, 1981, Schijve, 1974, Suresh, 1983, Shuter and Geary, 1996, Bray *et al.,* 1992, Venkateshawara Rao and Ritchie, 1988, Ward-Close and Ritchie, 1988, Brown and Weeterman, 1978, Vecchio *et al.,* 1984, Bucci *et al.,* 1980]. Suresh [1983] proposed that overload induced crack path deflection or branching can lower the actual local crack driving force with a possibility of activating near-threshold growth mechanisms, promoting local mode II displacements. Consequently RICC mechanisms (due to crystallographic propagation) are activated even though the global loading pertains to Stage II crack growth. As the local, near tip stress intensity factor which controls the

propagation of a deflected or branched crack can be considerably less than that of a straight crack of the same projected length [Kitagawa *et al.,* 1975, Lo, 1978, Bilby *et al.,* 1977, Palaniswamy and Knauss, 1978], immediate crack retardation is implied [Walker and Beevers, 1979]. However, it has been put forward that an immediate brief acceleration of crack growth rather than retardation during post overload can occur because of the reduced crack growth resistance along a deflected path (crack deflection occurs preferentially along a path of weak fracture resistance). Thus there is a lack of agreement over the ability of crack deflection to explain post overload retardation. Experimental work on 7075-T6, 2024-T4 and 6061-T6 aluminium alloys showed that post overload crack tip deflection leads to an initial acceleration in crack growth rate with retardation only occurring after the influence of the deflection is passed and the crack re-oriented back to its previous direction [Lankford and Davidson, 1981]. It may be suggested that enhanced RICC via surface asperity contact after such crack deflection may still account for some element of growth retardation. Similar observations have been made by Venkatesh Rao and Ritchie [1988] where greater post overload retardation in growth rate has been observed for the aluminium-lithium alloy 2090-T8E41, as compared to the conventional 2124-T351 and 7150-T651 alloys, attributed primarily due to the crack deflection and resulting RICC arising from highly tortuous crack path morphologies in the Al-Li materials. Powell *et al.,* [1981] also suggested the incidence of increased post-overload fracture surface roughness in an Aluminium-Zinc-Magnesium alloy (but not in an En 58B stainless steel). It has however also been argued that on the basis of stress relief treatments the *primary* cause in post overload retardation in aluminium alloys cannot be the increase in crack surface irregularities [Fleck, 1988]. Similar observations have also been noted by Shin and Fleck [1987], suggesting that crack deflection may be a secondary cause for the post overload retardation. Nevertheless, it may still be believed that crack surface irregularities may have a role in post overload retardation in the near-threshold regime where roughness induced crack closure and oxide induced crack closure mechanisms may be most effective.

2.4.2.5 Activation of near-threshold mechanisms

On the basis of that post tensile overload fatigue cracks may be subjected to enhanced levels of PICC, residual compressive stresses and/or crack deflection/branching resulting in low post-overload effective stress intensity ranges, it may be seen that

stress intensity ranges approaching near-threshold conditions may induce a change in crack growth mode, as is indeed often seen in practise. For many alloys, this may then induce additional retardation mechanisms involving Stage I crack growth as well as RICC and oxide induced crack closure [Suresh, 1983]. Suresh [1998] particularly put forward that the activation of near-threshold mechanisms following an overload helps prolong post-overload retardation but may not be the primary cause of retardation. It is argued that the near-tip ΔK should first be lowered to near-threshold levels by other processes before the near-threshold mechanisms are invoked to influence the post overload failure. Experiments in 2xxx and 7xxx aluminium alloys, indicated that, in the Paris regime, the pre-overload crack growth rates are found to decrease in the sequence: under-aged, peak-aged and over-aged condition, opposite to trends observed in the threshold range [Suresh, 1983, 1998]. Under post-overload conditions, crack growth retardation increases are reported in the sequence: over-aged, peak aged, and under-aged [Knott and Packard, 1977, Bucci *et al.,* 1979], supporting a role of near-threshold growth behaviour in post-overload response [e.g. Hertzberg and Mills, 1976, Hopkins *et al.,* 1976, Nowack *et al.,* 1979, Suresh and Vasudevan, 1984].

2.4.2.6 Strain hardening

Jones [1973] suggested that excessive plastic straining on an overloaded crack tip may lead to strengthening of the material in the crack tip vicinity which might then have some effect on growth retardation. This has been supported by Knott and Pickard [1977] from their experiments on an Al-4.5Zn-2.5Mg alloy in the under-aged, peak-aged, and over-aged conditions. It has been noted that higher crack tip flow stress after cyclic hardening would cause smaller subsequent crack tip plastic strain causing greater retardation in an under-aged alloy. However, other experimental studies on Ti-6Al-4V titanium alloy, 2024-T3 aluminium alloy, and SAE 1010 steel (Jones, 1973, Schijve, 1976, Legris *et al.,* 1981) showed that cracks grew faster through prestrained/strain-hardened material than through the as-received material. Shijve [1976] put forward the idea that tensile pre-straining raised the yield strength leading to two interrelated consequences for crack growth: 1) reduction in the amount of crack closure and higher effective stress intensity range at the crack tip due to reduced plastic deformation in the crack wake, and 2) higher stresses at the crack tip zone, leading to enhanced crack closure. Chaki and Li [1984] observed post overload

retardation effects for the metallic glass Metglas 2705X which lacks strain hardening, clearly suggesting that strain hardening alone cannot account for retardation following an overload. In comparing the crack growth retardation responses, it has been found that for a cyclic strain softening steel and cyclic strain hardening 2024-T3 aluminium alloy, observed differences are not significant [Mills *et al.,* 1977]. Petit *et al.,* [1988] observed that at low baseline loading, post overload fatigue crack growth retardation in an under-aged 7075 aluminium alloy (which displays reasonably high strain hardening) is greater than that seen in over-aged 7075 with lower strain hardening. However this may be related to crystallographic paths leading to RICC following an overload for the underaged alloy [see Suresh and Vasudevan, 1984, Knott and Pickard, 1977].

2.4.3 Experimental trends and rationalisation

In the preceding sections mechanisms related to the general post overload retardation behaviour of a single tensile overload have been discussed. However it has been observed by various investigators that fatigue growth rate following a single tensile overload will depend on various aspects of the mechanical and microstructural conditions. It has been observed that the higher the *%OL*, the larger is the retardation effect [e.g. Robin *et al.,* 1983, Venkateshwara Rao and Ritchie, 1988, 1988a, Ward-Close and Ritchie, 1988, Shin and Shu, 1993, Xu, 2001, Borrego *et al.,* 2003]. Typically, with increasing *%OL*, there is an increase of delay cycles (N_d) and affected distance (a_{eff}). On the contrary, increasing R, tends to gradually decrease post-overload crack growth transients which are seen at lower R [Skorupa, 1999, Borrego, *et al.,* 2003]. The distance between overload location and the minimum *da/dN* is found to decrease with increasing R [Damri and Knott, 1991, Tsukuda *et al.,* 1995]. For $R \geq 0.65$, immediate crack retardations in crack growth rate have been seen, unlike at low R values where an initial brief acceleration in growth was observed (no crack closure detected before the overload application) [Shin and Hsu, 1993]. Several authors reported that for a number of aluminium alloys [Vecchio *et al.,* 1983, 1984, Venkateshwara Rao and Ritchie, 1988, McEvily and Yang, 1990, Chanani, 1977] and titanium alloys [Ward-Close and Ritchie, 1988] that the number of delay cycles (N_d) and delay distance (a_d) following an overload results in a characteristic U-shaped

curve when considered as a function of $\Delta K_{(BL)}$ level (see Figure 2.11). The degree of retardation (expressed in terms of N_d or a_d) is observed to increase (from a minimum at an intermediate $\Delta K_{(BL)}$), with increasing $\Delta K_{(BL)}$ toward instability, and with decreasing $\Delta K_{(BL)}$ toward threshold. However, an inverted U-shape curve is reported to be obtained for AISI 304 steel [Shin and Shu, 1993]. The results of Shutter and Geary [1996] for BS4360 steel show an increase in N_d with decreasing $\Delta K_{(BL)}$.

Combinations of the factors discussed in Section 2.4.2 may of course be used to rationalise the experimentally observed retardation trends. However, the significance of *PICC* to account quantitatively for crack growth retardations following an overload has been asserted by various researchers [e.g. Tokaji *et al.*, 1984, Fleck *et al.*, 1983, Tanaka *et al.*, 1981, Paris and Herman, 1982, Fleck, 1988] as discussed in Section 2.4.2.1. The PICC effect could be expected to decrease with increasing R as the increase in residual wedge (see Budiansky and Hutchinson, 1978) would be expected to be smaller than the increase in crack opening [Parry, 2000]. This PICC mechanism is consistent with the experimentally observed decrease in delay cycles, retardation magnitude, and distance between overload location and minimum *da/dN* location with increasing R.

The influence $\Delta K_{(BL)}$ on retardation behaviour represented in most cases by the characteristic U-shaped curve (mentioned above) has been explained by Venkateshwara Rao and Ritchie [1988], Ward-Close and Ritchie [1988], Ward-Close *et al.*, [1989] and McEvily and Yang [1990] based on closure concepts. Venkateshwara Rao and Ritchie [1988], Ward-Close and Ritchie [1988], Ward-Close *et al.*, [1989] proposed that the retardation behaviour is a consequence of competition between various mechanisms, as shown in Figure 2.11. They argued that at high $\Delta K_{(BL)}$, the crack tip residual stress field (and hence the PICC magnitude) is related to the plastic zone size, provided it does not become large enough such that the surrounding elastic material constraint is removed (i.e. as the net section stresses approach the yield value). Apparently PICC then dominates leading to an increase in retardation effect with increasing $\Delta K_{(BL)}$. Conversely at low $\Delta K_{(BL)}$ where CTOD levels are small, the dominant closure mechanisms are associated with wedge/contact shielding processes, where the CTOD and roughness is comparable. Thus RICC is

considered to have a significant effect at low $\Delta K_{(BL)}$. Also, changes in closure levels are considered to have a proportionately larger effect at lower $\Delta K_{(BL)}$. However, McEvily and Yang [1990] proposed that the U-shaped curve is entirely due to PICC effects. They put forward that the increase in N_d at lower $\Delta K_{(BL)}$ (near threshold) is due to the high sensitivity of crack growth rates to small changes in ΔK_{eff} (steep gradient region in the *da/dN* vs ΔK_{eff} plot). The increase in N_d as $\Delta K_{(BL)}$ approaches the unstable fracture region is then due to an increasing development of plane stress PICC effects as plastic zone size grows in relation to the specimen thickness.

2.4.4 FE modelling of overload-induced crack closure

Early attempts at FE modelling of PICC under variable amplitude loading were made by Ohji *et al.*, [1974, 1975] and Newman and Armen [1975] considering simple high-low and low-high block loading histories under plane stress conditions. Their results showed qualitative agreement with experimental results although the FE meshes used were coarse and do not satisfy mesh refinement criteria discussed in Section 2.3.5.1, and the crack growth lengths with the models were small. In the recent years, many reports have been put forward to understand single overload transients using both 2D [e.g. Fleck and Shercliff, 1989, Shercliff and Fleck, 1990, Zhang *et al.*, 1992, Dougherty *et al.*, 1997, Ellyin and Wu, 1999, Pommier and Bompard, 2000, Parry, 2000] and 3D [e.g. Chermahani *et al.*, 1988, Zhang, 1999] FE models. FE studies for cracks subjected to double and periodic tensile overloads have been reported by Hammouda *et al.*, [1998] and Heper and Vardar [2003]. Fleck and Shercliff [1989] and Shercliff and Fleck [1990] studied the effect of an overload on crack closure following a tensile overload for CCT and bend (SENB) specimens under both plane stress and plane strain conditions using FE methods. Under plane stress condition, the specimen geometry was found to have little influence on the closure transient, whilst under plane strain condition a stronger closure transient was observed in the CCT than Bend geometry, consistent with larger overload plastic zone size seen in the CCT geometry compared to that in bend (specimen geometry was not found to have significant influence on overload plastic zone under plane stress). From the crack opening profiles, discontinuous closure was observed, with crack opening near the tip

region, and contact near the overload location once the crack has advanced some way beyond the overload location, for both plane strain and plane stress conditions, consistent with the experimental observed 'discontinuous closure' phenomenon [e.g. Fleck *et al.,* 1983, Fleck, 1988, Shin and Hsu, 1993]. In the plane strain case, the CCT geometry showed a longer contact zone (near the overload location) in agreement with the larger overload plastic zone as compared with the Bend specimen. Fleck [1988] put forward that underestimation of predicted crack growth rates based on ΔK_{eff} (due to discontinuous contact near the overload location) as compared to the measured values in the overload transient zone is due to the fact that ΔK_{eff} experienced by the crack tip is larger than that suggested by the closure measurement. Following the reasonable agreement in closure transients following an overload for both experimental (on BS4360 50B / BS EN 10025 S355JR steel) and FE predicted results, Fleck and Shercliff [1989] put forward that overload retardation is due to PICC effects. Dougherty *et al.,* [1997] observed that FE modelling resulted in increased post-overload closure levels over a larger distance than experimentally measured. It is suggested that the over-prediction of the FE model is due to the over estimation of overload plastic zone, as the overload strain (well in excess of previous cyclic strain) moves into the inbuilt strain softening behaviour in the FE model. This entails an understanding of the effect of overload on the stress-strain curve, which needs to be determined experimentally. Pommier and Bompard [2000] observed that cyclic plastic material behaviour (Bauschinger effects in particular) has some effect on the post-overload crack behaviour. They found that material which displays a Bauschinger effect may display a lower 'resistance' to VA loading as compared with a material with isotropic hardening behaviour. The effect is linked to hardening in the overload crack tip plastic zone, which produces retarded transient effects that are not observed in the perfectly-plastic material, where the effect of the overload is due to the residual strain fields only and not due to the plastic history of the material. Using the definition of crack closing and opening in terms of the sign of the crack tip node stress (rather than the nodes behind the tip, avoiding discontinuous closure away from the tip), Wu and Ellyin [1996] pointed out the importance of the residual stress and strain distribution on the closing stress levels. A large residual tensile deformation (stretched material) ahead of the crack tip followed by a corresponding large compressive residual stress decreases ΔK_{eff} which may then lead to post-overload

retardation in growth rate. The analysis (with $R = 0$) also indicated an increase in crack growth rate above the baseline rate following retardation prior to attaining the stable baseline growth (in agreement with experimental result at a higher R of 0.7 [Tsukuda *et al.,* 1996]). However, there are many experimental reports [e.g. Ward-Close and Ritchie, 1988, Venkateshwara Rao and Ritchie, 1988] as mentioned in Section 2.4.2 which shows the absence in a post-retardation rise in crack growth rates above the stable baseline value. It was argued by Wu and Ellyin that a crack would not necessarily 'close' if the crack tip carries a tensile stress, even though a part of the crack may close in the wake (similar to the closure near the overload location), and a conversely crack may not be considered to be open if the crack tip carries a compressive stress, even though the crack wake is fully opened. Further it is commented that even though the node immediately behind the crack tip is opened, it would not guarantee that the zone between this node and the tip be opened. Alternatively, the importance of cyclic strain in the crack tip process zone as a crack driving force (being the primary physical cause of crack advance) has been put forward by Laird [1979] and Rice [1967], thus monitoring tip stresses alone may not give a true micromechanical understanding of crack driving force. It may also be noted that the near-tip (between the crack tip and its immediate node in the wake) can be checked for local contact through mesh refinement to some degree, albeit very fine refinement may induce associated numerical problems. Ultimately, the stress singularity implied near the tip, cannot be well captured as the elements exhibit predetermined stress variations and hence, not be particularly meaningful to monitor the stress sign at the very crack tip. Overall it may be seen that both experimental and theoretical understanding of load transient behaviour (particularly simple effects such as single transients) is quite well developed, but debate remains in a number of aspects. It may be noted, that to the best of the author's knowledge, no FE treatment of VA RICC effects appears to have been published, beyond the initial work of Parry , as discussed in Chapter 4.

Temper	Yield strength (MPa)	Tensile strength (MPa)	Elongation (% in 50 mm)
0	186	76	20
T3	324	469	18
T4, T351	345	483	20
T6	395	475	10
T8	450	480	6

Table 2.1: Typical mechanical properties for 2024 in different tempers.

Alloy	Si	Fe	Cu	Mg	Mn	Zr
2024	0.121	0.203	4.065	1.36	0.537	-
2024A	0.049	0.16	4.51	1.44	0.33	-
2027-ReX(8)	0.05	0.09	4.3	1.3	0.65	0.10
2027-ReX(55)	0.045	0.092	4.005	1.365	0.59	0.0997
2027-ReX(100)	0.046	0.085	4.075	1.347	0.64	0.096

Table 2.2: Composition specification of Pechiney supplied 2024 Al alloy, and the advanced variant, 2027 (expressed in % maximum by weight unless shown as a range or a minimum) (after Khor, 2004).

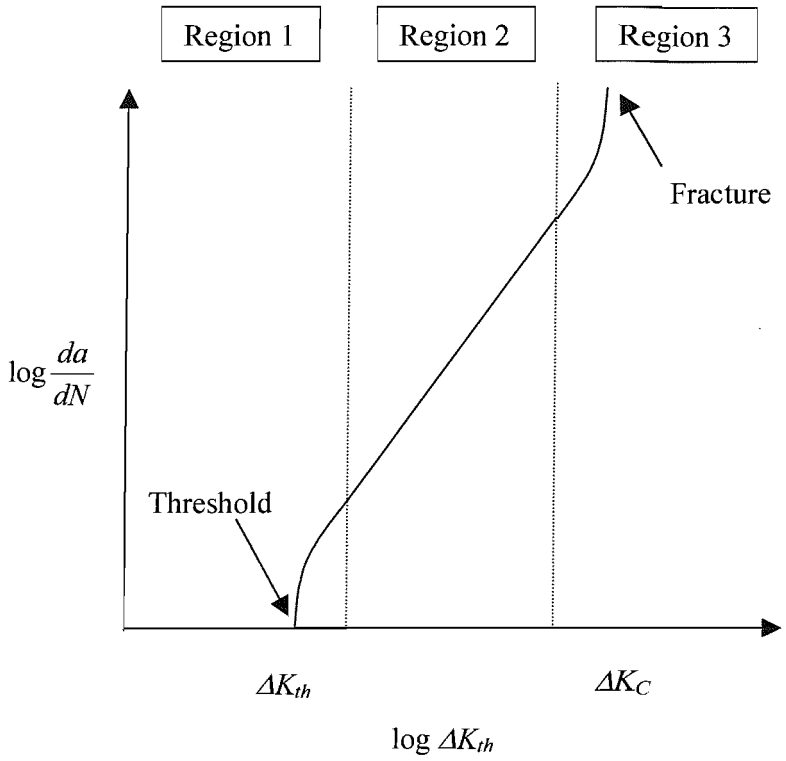

Figure 2.1: Typical fatigue crack growth behaviour for ductile metals.

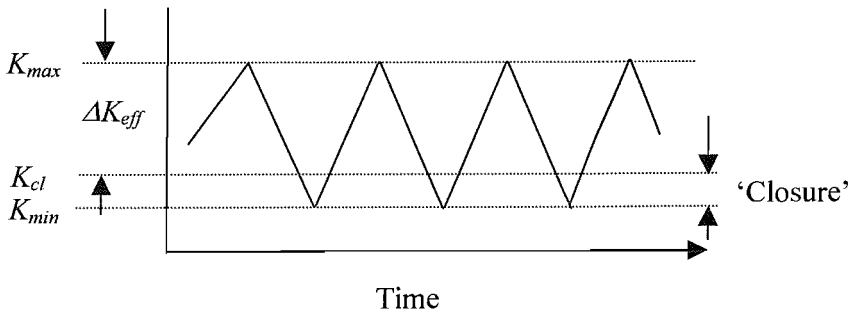

Figure 2.2: Definition of the effective stress intensity factor (ΔK_{eff}).

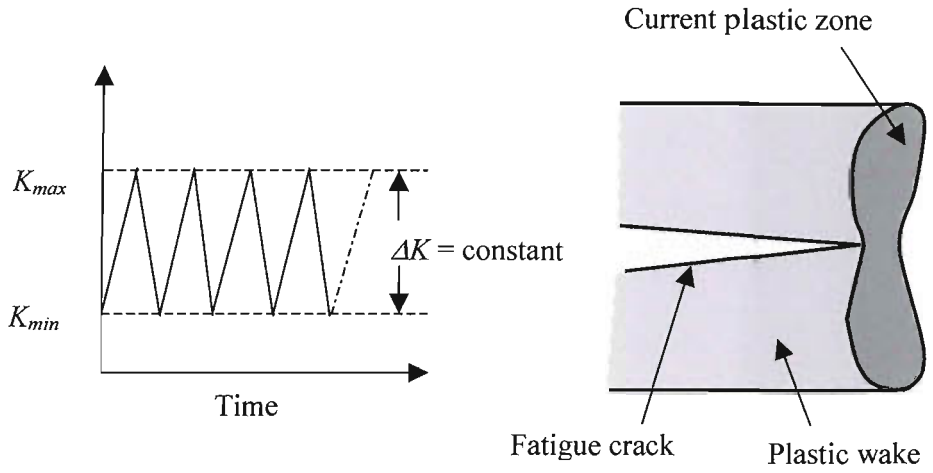

Figure 2.3: Schematic illustration of the developed plastic zone envelope for a propagating fatigue crack [after Anderson, 1995].

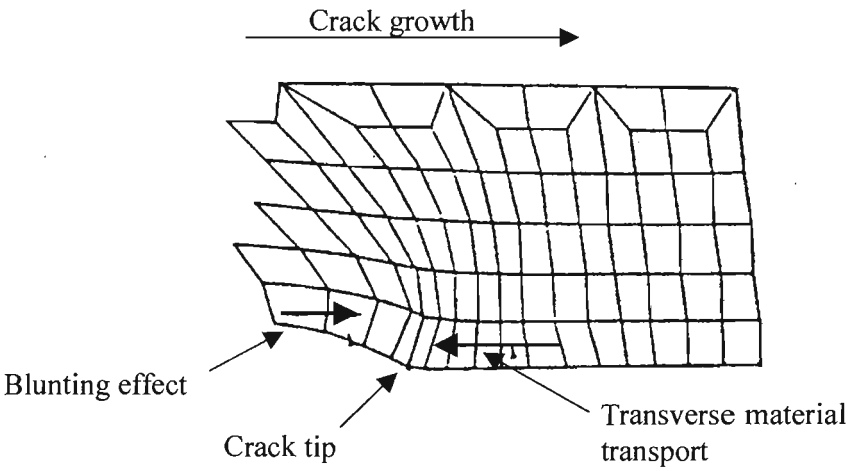

Figure 2.4. Deformed FE mesh showing the direction of transverse material transport and blunting effect [Sehitoglu and Sun, 1991].

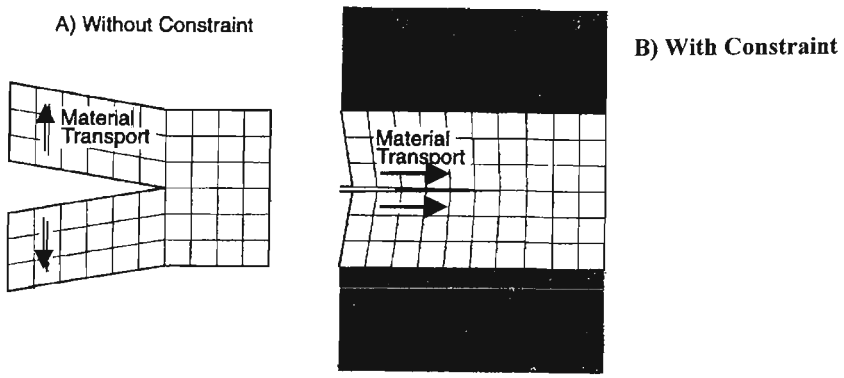

Figure 2.5. PICC caused by plastic shear deformation in the wake of a fatigue crack. Deformation is without constraint in (A). In (B) deformation is constrained by an elastic material leading to the transport of material in the direction of crack growth, thereby inducing closure [Riemelmoser and Pippan, 1998].

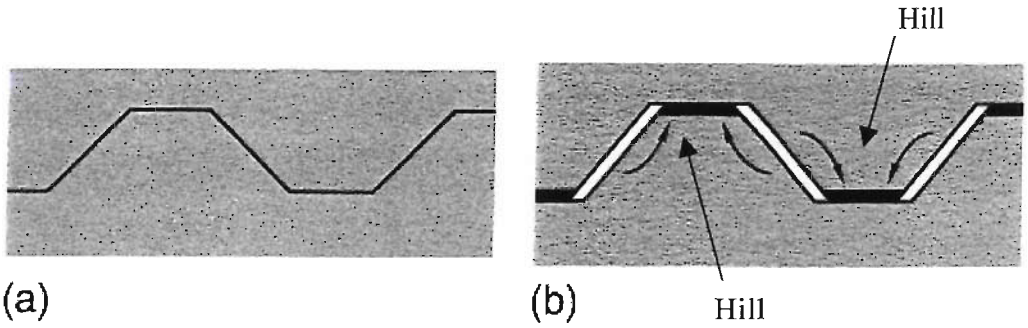

Figure 2.6. Schematic representation of a deflected crack with periodic tilts: (a) shows the perfect fitting of a crack flanks in the absence of plasticity, (b) illustrates the crack flanks where a reduction of the width of the 'hills' (convex part) and an increase in their height, is caused by plastic deformation leading to closure [Pippan and Riemelmoser, 1998].

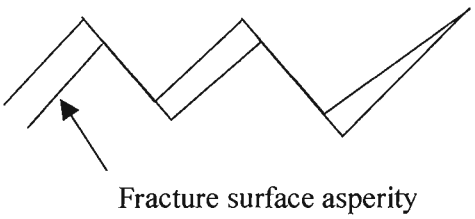

Figure 2.7. Schematic illustration of roughness induced closure (RICC) [after Suresh, 1991].

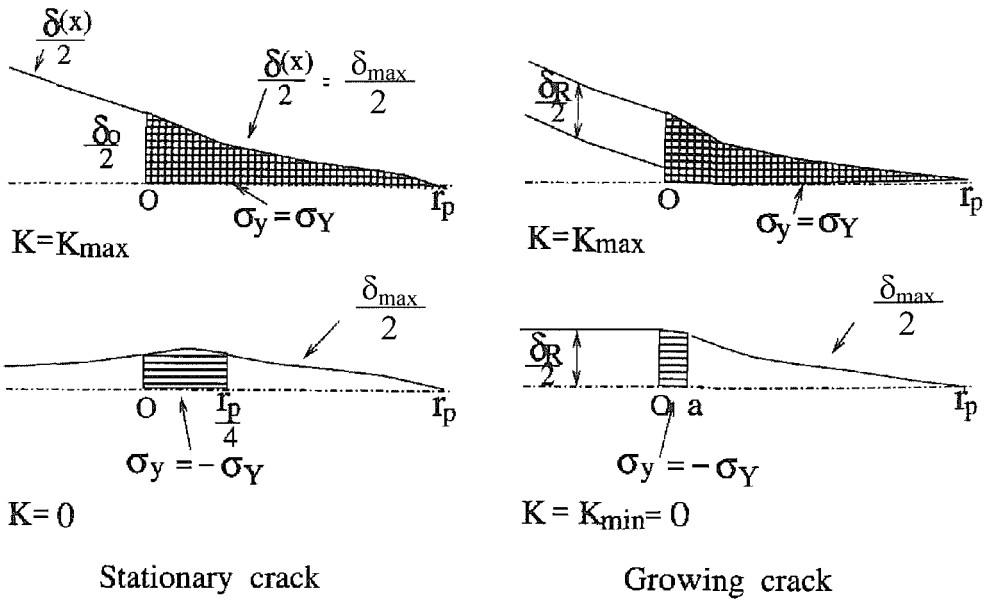

Figure 2.8: Crack profiles and plasticity according to Dugdale (stationary crack) and Budiansky and Hutchinson (growing crack). The crack shape is shown for the upper crack face with the hatched regions identifying plasticity at the crack tip.

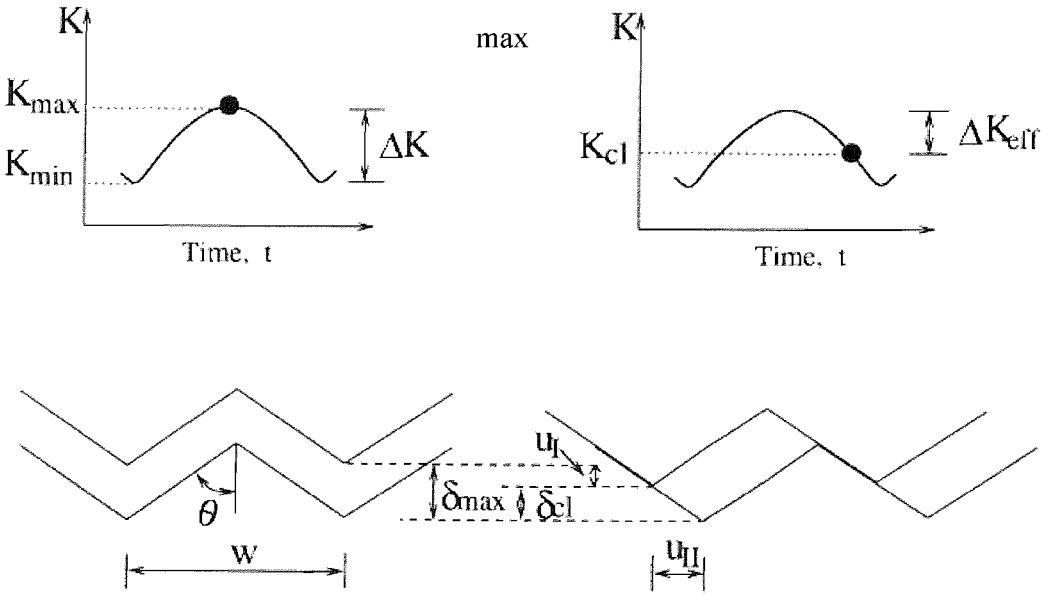

Figure 2.9: Schematic illustration of fatigue crack closure induced by surface roughness [after Suresh and Ritchie, 1982].

(a)

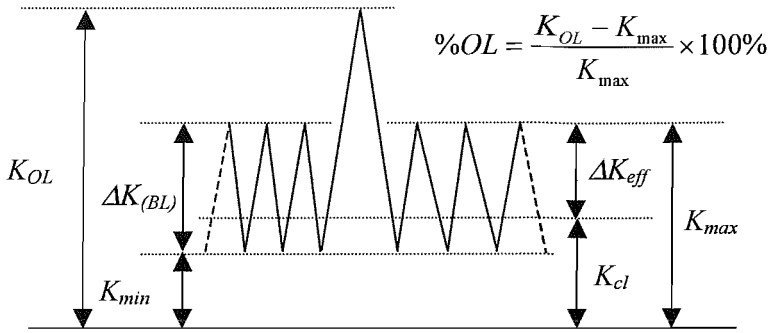

(b)

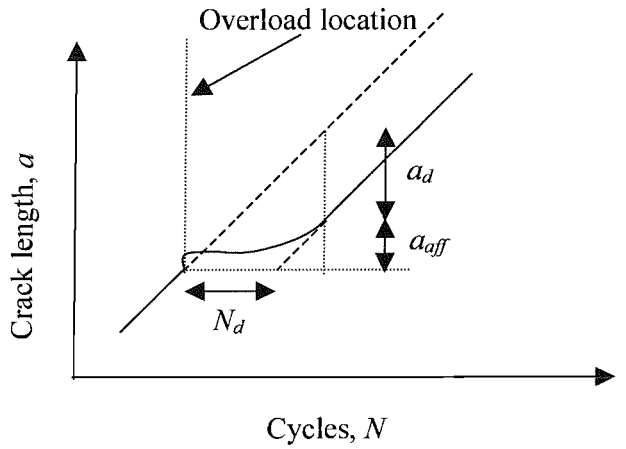

(c)

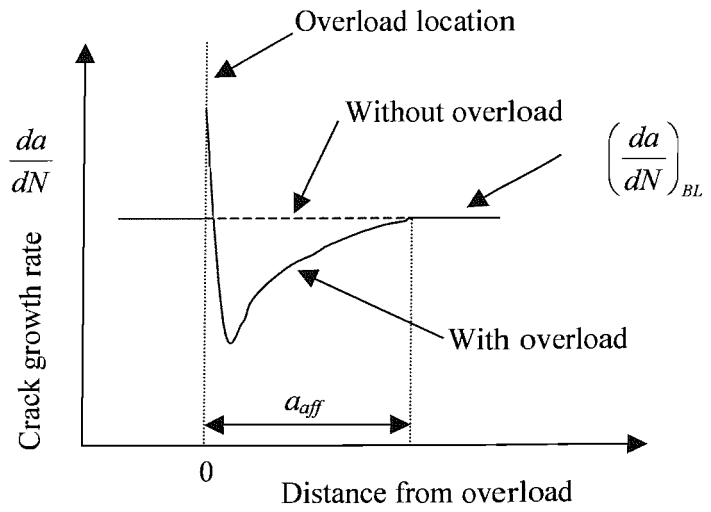

Figure 2.10: Schematic illustration of the effect of a spike (single) tensile overload, showing (a) loading nomenclature, (b) crack length vs number of cycles behaviour, and (c) crack growth rate vs crack length behaviour (after Venkateshwara and Rao, 1988, Ward-Close and Ritchie, 1988).

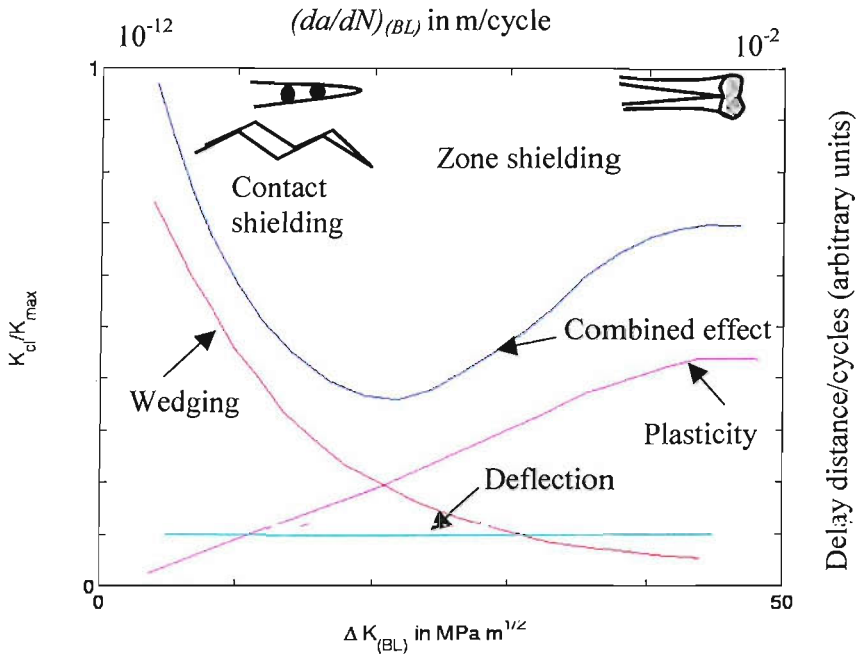

Figure 2.11: Schematic representation of the variation in crack closure with post-overload baseline stress intensity range ($\Delta K_{(BL)}$) [after Venkateshwara Rao and Ritchie, 1988].

Chapter 3

3 Basic modelling configuration and assessment of constant amplitude loading

An investigation of plasticity induced crack closure (PICC) and roughness induced crack closure (RICC) behaviour using FE methods is presented for cracks subjected to constant amplitude loading and small scale yielding (SSY) conditions. Undeflected cracks have been examined under both plane strain and plane stress conditions, whilst plane strain analyses have been particularly considered for deflected cracks. Previous analytical treatment of RICC (Parry, 2000) has been extended to produce continuous closure model behaviour to match the FE findings, and compared to detailed experimental findings.

3.1 Introduction

Numerical crack simulation techniques (e.g. finite element methods (e.g. McClung *et al.,* 1991, Parry, 2000) and finite difference methods (e.g. Llorca and Galvez, 1990, Nowell, 1998)) employed to understand PICC and RICC phenomena have given significant impetus for the last three decades in enhancing the current knowledge of fatigue crack growth processes. Numerous researchers have adopted FE methods to model closure because of its inherent advantages; *viz.* 1) ability to evaluate full field displacements, stresses and strains fields, and 2) treatment of multiple problems via changes in the input conditions. Insights into closure mechanics may then help in both improved physical understanding, and in the development of computationally efficient models for life prediction [McClung, 1999]. Since the first reported FE analyses of PICC (*viz.* Miyamoto *et al.,* [1973, 1974], Ohji *et al.,* [1974], and Newman and Armen [1975]), many efforts have been focussed on analysing both plane stress and plane strain models (e.g. Fleck and Newman, 1988, Anquez and Baudin, 1988, McClung and Sehitoglu, 1989, 1989a, McClung *et al.,* 1991, Parry, 2000, Solanki *et al.*, 2003,2003a, Anderson *et al.*, 2001, 2004, Antunes *et al.,* 2004). Despite this, there are issues regarding basic modelling parameters and results generated; e.g. location of closure under plane strain conditions (near-tip or pre-crack tip closure), anomalous

contact of the first node behind the current crack tip, and the choice of crack propagation scheme (particularly the use of one or more cycles of loading for every discrete increment of crack), that may then influence the closure results. As such it is considered valuable to study the details of micromechanics involved for a reliable prediction of closure. Whilst attempts have been made to study RICC using numerical techniques e.g. Llorca [1992] using finite difference methods, and Parry [2000] adopting the FE method (as discussed in Section 2.3.5.7), to the best of our knowledge, the FE model by Parry was the first to provide an insight into the local plasticity origins of the shear offsets at the asperity points necessary for RICC. As such, it is important that the basic findings of Parry regarding RICC are checked and confirmed.

In this chapter, studies are presented on undeflected and deflected cracks subjected to constant amplitude loading under small scale yielding conditions. Both plane strain and plane stress conditions have been examined for the undeflected cracks, however only plane strain analyses have been conducted for the deflected cracks. Preprocessing has been carried out in MSC/PATRAN [1999]. Elastic-plastic analysis has been performed using the general purpose commercial FE code ABAQUS [1998]. In the first instance the modelling was carried out with several objectives:

1. To confirm basic model results and understanding identified by Parry [2000] via remodelling of equivalent load cases and extension of the range of load cases.
2. To assess certain basic details of model behaviour in relation to the literature, particularly the incidence of 'anomalous' crack contacts.
3. To identify order of magnitude influence of basic model parameters on crack closure behaviour.
4. To ascertain asperity size effects on closure levels for deflected cracks and extend previous simple analytical modelling of RICC processes based on the understanding derived from the FE modelling.
5. Compare RICC modelling predictions to recent detailed experimental findings.

3.2 Problem description

A conventional rectangular center-cracked plate (CCP) subjected to far field tension has been considered for the present FE analyses. The geometry, along with the relevant boundary conditions, is given in Figure 3.1. The geometry is similar to that considered by Parry [2000], with the dimensions being, length, $L' = 250.0$ mm, width, $W' = 75$ mm, thickness, $B = 7.5$ mm, half notch length, $a = 7.5$ mm, notch angle of 30°, notch width, $h_o = 1.0$ mm and half initial crack length, $a_o = 8.0\,\text{mm}$. For RICC studies fatigue surface roughness was idealised with a simple zigzag geometry with deflection angle θ, and length L. To simplify the analyses, cracks are assumed to deflect only in the plane normal to the thickness direction, hence the model is essentially two-dimensional (three dimensional effects are also considered analytically later in this chapter). Crack deflection angles of 30°, 45° and 60°; along with deflection lengths of 18.75 μm, 37.5 μm, 75 μm and 150 μm (see summary in Table 3.1) were considered.

The material properties chosen are typical of damage tolerant aerospace alloys, e.g. 2024-T351 and 2124-T351, corresponding to Young's modulus, E = 74 GPa, Poission's ratio, $\nu = 0.33$, yield stress, σ_y = 370 MPa, hardening modulus (bilinear model), $H = 0.07\,E$ [Ritchie *et al.,* 1978, Parry, 2000]. A kinematic hardening law is chosen unless otherwise stated.

For the undeflected cracks, two baseline loading conditions were considered, *viz.*, $\Delta K = 4.6\,\text{MPa m}^{1/2}$, corresponding to near threshold crack growth [Xu, 2001], and $\Delta K = 12.0\,\text{MPa m}^{1/2}$, corresponding to typical Paris law conditions. Low loading ratios of R = 0.0 and R = 0.1 were considered as most pertinent to crack closure investigation (see Table 3.2). Deflected cracks were studied for ΔK = 8.5, 10.0, 12.0, 15.0 and 17.0 MPa $\text{m}^{1/2}$ and a load ratio of $R = 0.1$ (Table 3.1).

3.3 FE formulation

Due to symmetry, only one half of the panel is modelled in FE for deflected crack conditions (one quarter for undeflected cracks). Figure 3.2 shows a typical mesh. A typical half plate FE mesh consists of ~7000 four-noded quadrilateral isoparametric elements. Selective reduced integration is used to prevent mesh-locking and to provide an accurate solution for incompressible material behaviour [ABAQUS, 1998]. As the accuracy of near-tip zone modelling is governed by the local element size [McClung and Sehitoglu, 1989] no appreciable gain in accuracy is expected with the use of higher order elements, such as eight-noded quadrilaterals. Moreover, the use of higher order elements would be computationally expensive. No special crack-tip elements were employed, as the nature of the near-tip field singularity at the tip of a propagating fatigue crack with closure is not well understood [Ritchie *et al.*, 1987, Fleck and Newman, 1988] (attempts using four-noded isoparametric elements by McClung and Davidson [1991] resulted in a complex near-tip strain distribution, approximated by semi-logarithmic relationships in some region near the tip and power law variation in the region ahead). Whilst singular elements for ductile fracture problems are reported to predict stresses which are too large and strains which are too small [Leibowitch and Moyer, 1989], some researchers [Nakagaki and Atluri, 1979, 1980, Zhang *et al.*, 1992] have attempted to capture near-tip field using special singular elements, however this approach is inappropriate as the closure phenomenon itself changes the form of crack-tip field [McClung, 1999]. The requirement for crack propagation with retention of prior deformation further constrains the choice of crack tip elements in this work. A typical crack tip element size (L_e) along the propagation path was set at 2 μm, which is approximately one ninth of the smaller plane strain plastic zone size investigated (for ΔK = 4.6 MPa m$^{1/2}$ and R = 0.0) as given by Irwin [1960] (Equation A.6), thus satisfying the criterion suggested by McClung and Sehitoglu [1989] for closure modelling of fatigue cracks. A coarser element size of about 9 μm is adopted for ΔK = 12 MPa m$^{1/2}$ ($r_p/L_e \approx 13$ for plane strain conditions) in line with the analyses reported by Parry [2000]. The same meshes have been adopted for plane stress analyses where plastic have dimensions are of course somewhat larger.

3.4 Crack propagation algorithms

The crack propagation algorithms considered here employed the 'spring' type boundary conditions following those of Newman and Armen [1975], McClung and Sehitoglo [1989], Palazotto and Mercer [1990], Parry [2000], Pommier and Bompard [2000], Wang *et al.*, [2002] and Andersson *et al.*, [2004]. Opposite nodes along the planned crack propagation path are initially held by two very short linear spring elements. The first spring has a very high stiffness in tension and no stiffness in compression, whilst second has very high stiffness in compression and no stiffness in tension. The compressive spring stiffness particularly acts normal to the crack face preventing interpenetration without affecting the shear displacement of the crack faces. Spring stiffness values of 7.4×10^{8} Nm^{-1} were previously investigated to be sufficiently high to give consistent reasonable crack behaviour [Parry, 2000]. Cracks were allowed to propagate one element at a time by releasing the tension spring at maximum load. Two types of propagation algorithm were then identified. The first follows the pattern 'loading-debonding-unloading' (LDU), whilst the second follows the pattern, 'loading-debonding-unloading-loading-unloading' (LDULU). It may be seen that there is one additional 'static' load cycle in the LDULU algorithm. Figures 3.3 and 3.4 illustrate schematically the LDU and LDULU algorithms for crack propagation respectively. Following the approach of Parry [2000], each 'debonding' of tensile springs is realised through three steps, to circumvent convergence problem associated with sudden release of the springs. Propagating the crack one element length in each loading cycle is clearly a convenient and simple choice, however it has been postulated by McClung and Sehitoglu [1989] that the sudden release of a node at or near maximum load could lead to artificial residual strains and stresses which would not vanish before the next node release occurred. It was further noted that progressing a crack every cycle is equivalent to 'pushing' the crack tip through the previous near-tip fields distribution at unnaturally high velocities [McClung *et al.*, 1991]. It may be noted that Nicholas *et al.*, [1988], McClung and Sehitoglu [1989], McClung and Davidson [1999], McClung [1999], Pommier and Bompard [2000], Zhao *et al.*, [2004], and Antunes *et al.*, [2004] suggested extending cracks after two cycles of loading for stabilised near-tip stress, strain and displacements loops for equivalent hardening behaviour to that adopted here (i.e. linear kinematic). Zhang *et*

al., [1992] adopted some 10 load cycles for every increment of crack advance for cyclic stabilisation using a mixed hardening law. However in the present study, only two load cycles per growth increment (similar to the work of Sehitoglu and McClung and McClung and Davidson) are considered for the sake of computational time as long as crack propagation distances are considered necessary here (particularly for the overload work described in Chapters 4 and 5). Further rational for using such LDULU algorithms is considered later. A typical run of the ABAQUS program for the current models took about 3-7 days of CPU time given the available computer facilities[1].

3.5 Closure determination

Forces in the compression springs in the crack wake were monitored to assess crack closure behaviour. In addition, specimen compliance (ASTM E647, 2003) has been assessed using normalised applied stress intensity factors (K/K_{max}) and displacements (δ) taken at various locations on the sample; *viz.*, the crack mouth, the back face and near tip of the specimen. The location of the different displacement gauges are shown schematically in Figure 3.5. Three back face displacement gauge points (*viz.*, BF1, BF2 and BF3) were located at 1.2 mm, 2.4 mm and 3.6 mm respectively from the crack line. Near tip gauges, (*viz.*, NTR and NTL) were located at 1 mm from the crack line, 1.5 mm ahead of, or behind, the crack tip. The associated compliance curves have been plotted as an offset from a straight line fit to the upper linear part of the curve to improve sensitivity to the onset of non-linear behaviour [Parry, 2000]. The sensitivity of the compliance method depends further on the fineness of the decrements in the unloading cycle; based on trial runs, decrements of 0.04 (i.e. 25 steps/cycle) of the applied maximum load in the unloading cycle, and increments of 0.10 (i.e. 10 steps/cycle) of the applied maximum load in the loading cycle, have been used for the present analyses. Attempts using finer steps per cycle have been reported by Solanki *et al.*, [2003] (80 steps per cycle), Zhao *et al.*, [2004] (160 steps per cycle) and Antunes *et al.*, [2004] (~5-202 steps per cycle). The results from Antunes *et al.*, indicated that a minimum of 20 cycles ensures a stable closure values, consistent with the present values of 25 steps per cycle.

[1] SGI ORIGIN 2000 with 400 MHz MIPS R12000 processors

3.6 Results and discussion

3.6.1 Undeflected cracks

3.6.1.1 Direct comparison with previous work

To gain initial confidence in the current modelling effort, results were prepared for direct comparison with those reported by Parry [2000]. In Figure 3.6 the response of the spring (compression) elements behind the crack tip is shown for plane strain unloading, at $\Delta K = 4.6$ MPa $m^{1/2}$, $R = 0.0$ using the LDU crack propagation algorithm. The total crack propagation distance was ~ 100 μm, which is approximately six maximum plastic zone sizes (r_p). It can be seen that the first element behind the crack tip goes into compression (i.e. closing the crack tip) at 0.28-0.30 of the maximum applied stress intensity factor K/K_{max}. On further unloading, multiple spring elements at the original pre-crack tip (i.e. far from the current crack tip) are seen to close between K/K_{max} = 0.06-0.08. The results are consistent with an essentially equivalent analyses carried out by Parry [2000] ($\Delta K = 4.63$ MPa $m^{1/2}$, $R = 0.0$) where contact of the first node behind crack tip was reported to occur at K/K_{max} = 0.25, with compression of spring elements at the pre-crack tip being seen at K/K_{max} = 0.07.

Figure 3.7 shows the corresponding offset compliance plot of the data plotted in Figure 3.6, where it is seen that deviation of the compliance from linearity (i.e. the offset displacement becomes non-zero) occurs around K/K_{max} = 0.07, coinciding with the crack face contact at the pre-crack tip A similar agreement of closure values (K_{cl}/K_{max}) obtained by the offset compliance method and the contact of elements at the pre-crack tip has been reported by Parry [2000].

Figures 3.8 and 3.9 show the response of the compression springs and offset compliance curves respectively for unloading in the plane stress case for $\Delta K = 4.6$ MPa $m^{1/2}$, $R = 0.0$, $\Delta a = 100\mu$m, using the LDU crack propagation algorithm. The first node behind the crack tip is found to close at K/K_{max} = 0.56, with more distributed compression of spring elements immediately behind the tip then starting at K/K_{max} = 0.28, i.e. closure occurs at significantly higher values than those observed

for the plane strain loading case, and is seen at many elements running back from the crack tip (Figures 3.8). The distributed contact of nodes behind the crack tip in the plane stress model coincides with the onset of non-linearity in the associated offset compliance curves Similar plane stress analysis with a lower load (ΔK = 2.69 MPa $m^{1/2}$, $R = 0.0$, $\Delta a = 100\mu$ m, LDU crack propagation algorithm) performed by Parry [1999] showed only a gradual build up of the closure at the plane stress crack tip during unloading starting at K/K_{max} = 0.35, i.e. the "anomalous" high initial contact load of the first node behind the tip did not occur.

Observing closure behaviour from Figures 3.6 and 3.7 (plane strain conditions) and Figures 3.8 and 3.9 (plane stress conditions), it is evident in both cases that closure of the first node behind crack tip does not affect the overall specimen compliance and appears to be independent of any more distributed build up of contact with further unloading. Such notionally anomalous contact of the first node behind the crack tip in FE models has been indicated in the studies of Fleck [1986], Fleck and Newman [1988], Biner *et al.*, [1994], Parry [1999], Wei and James [2000] and Parry [2000] for plane strain and McClung and Sehitoglu [1989] and Kibey, *et al.*, [2004] for plane stress conditions. However various studies, e.g. those made by Blom and Holm [1985], Ritchie *et al.* [1987], Lalor and Sehitoglu [1988], Llorca and Sanchez Galvez [1990], do not mention report on such details of crack face contact in their models. The incidence of near-tip node contacts is considered in further detail in Section 3.6.1.2 below.

3.6.1.2 Plane strain crack behaviour

The following section considers both LDU and LDULU crack propagation methods under plane strain loading. A propagated crack length of 1000.8 μm (~60 r_p for ΔK = 4.6 MPa $m^{1/2}$ and R = 0.0) has been used, i.e. significantly larger than above, providing an additional assessment of steady-state crack growth conditions.

- $\Delta K = 4.6$ *MPa* $m^{1/2}$, $R = 0.0$, *plane strain conditions*

Figure 3.10 shows typical complete crack profiles for loading, debonding and unloading using the LDULU crack propagation algorithm (loading and unloading

profiles are monitored in the first and last step respectively for the LDULU algorithm). Two conditions are plotted for unloading:

1. at the onset of crack closure, identified as $K_{cl}/K_{max} = 0.12$ in this case: for the purposes of this and subsequent sections/diagrams, the onset of crack closure, and the symbol, K_{cl}, are specifically identified with the onset of *distributed* contact along the crack wake (i.e. building up continuously over many nodes in the crack wake as unloading progresses), independent of the behaviour of the first node behind the crack tip.
2. at minimum (zero) load

A transient 'lump' in crack opening at the pre-crack tip is clearly seen in Figure 3.10 (inset figure). Contact of the transient lump near the pre-crack tip is the origin of distributed crack contact during the unloading. The region behind the pre-crack tip constitutes the residual stretch free zone (RSFZ), where the material is clearly free from residual plastic deformation due to propagation (and hence elastic behaviour prevails). The region ahead of the pre-crack tip (near the crack surface) has been plastically stretched, identified as the residual stretch zone (RSZ). Figure 3.11 shows the corresponding variation of transverse displacements (U_x), parallel to the crack growth direction, both at maximum load and at closure. Negative values of U_x indicate transverse contraction due to applied loading. It can be seen that the magnitude of U_x decreases (i.e. become less negative) in a fairly uniform manner from loading to unloading, consistent with reduction in transverse contraction due to bulk Poisson's effects. Near the pre-crack tip however a sharp local transient in the U_x variation can be observed which must be attributed to plastic deformation near the pre-crack tip. Near the pre-crack tip in the RSFZ, there is a marked local decrease in the transverse contraction (as seen by the local rise in the U_x), indicating forward relative movement of the material towards the pre-crack tip: thus for distributed crack flank contact to have occurred (as opposed to single near-tip nodal contact) in the plane strain condition, a local in plane movement of material is identifiable, consistent with the requirements of volume conservation in plasticity induced crack closure (see Figure 3.10). This occurrence of closure near the pre-crack tip is consistent with the findings reported by Fleck [1986], Fleck and Newman [1988], Sehitoglu and Sun [1991] and Wei and James [2000] through FE studies. However, McClung *et al.*,

[1991] reported that plane strain crack closing is a continuous zipping up of the crack, beginning at the crack tip. They speculated that the observed discontinuous plane strain closure reported by Fleck [1986] and Fleck and Newman [1988] could be due to 1) the mesh being too coarse, 2) element performance problems in using constant strain triangle elements to capture the severe stress gradients near the tip and 3) possible incompressibility issues near the tip (although Fleck used a 'union jack' configuration near the tip to meet the incompressibility requirements associated with large plastic strains as suggested by Nagtegaal *et al.,* [1974]). They also linked discontinuous crack closure of the type reported by Fleck with Q4 elements which did not incorporate Nagtegaal's recommendations to prevent element locking. Crack profiles at minimum load (R = 0.0) reported by Zhao *et al.*, [2004] using Q8 (with a reduced integration scheme) only showed first node contact behind the tip after cracks had propagated for more than $4r_p$ from the pre-crack tip, however CODs near the pre-crack tip were found to be much smaller then those of the near crack tip region, suggesting the presence of a pre-crack transient lump. The present FE modelling technique using Q4 element (with selective reduced integration technique [ABAQUS, 1998] as mentioned in Section 3.3) has been tested to model accurately incompressible material behaviour [Parry, 2000] and may be considered to circumvent the above speculation of McClung *et al.,* [1991]. Thus it may be concluded that the discontinuous closure is not an artefact of the Q4 element adopted in the present analysis. A further possible source of disagreement on crack face contact build up (near the pre-crack tip in particular) may be associated with the methodology adopted to simulate the changing boundary conditions: i.e. McClung *et al.,* directly imposed the boundary conditions on the crack line, whereas Fleck's and the present models used spring release systems (as discussed in Section 3.4). However, McClung *et al.*, themselves acknowledged only very minor effects of changing from a spring removal propagation algorithm (such as that used here), and the changing boundary condition approach. What is more significant is the fact that the results presented by McClung *et al.* only cover growth through a distance of just over 2 r_p, whilst the present results show the initial transient lump to be of the order of 2.5 r_p (in the growth direction). It may be then be seen that their results may not be fully representative of steady-state crack propagation. It is significant to note that McClung *et al.* relate the presence of the plane strain PICC to strains in the x-direction

(parallel to the crack), consistent with the forward displacements seen near the crack–tip in Figure 3.11. This process of necessity generates tensile residual stresses in the crack wake (see Figure 3.12): such stresses must be absent behind any initial pre-crack tip, whilst their presence at a propagated crack-tip will resist in-plane displacements that are required for plane strain PICC to occur.

It may be noted that although discontinuous closure near the pre-crack tip has been reported by various researchers using FE methods (including the present results), there are very few experimental reports (e.g. Fleck, 1984). Fleck [1984] conducted tests on 3mm thick BS4360 50B steel specimens and reported discontinuous contact near the notch root. However it must be noted that the experiments were conducted by allowing ΔK to decrease exponentially from 51.4 to 25 MPa $m^{1/2}$ at $R = 0.05$, hence the closure may be due to the large residual deformations associated with the early stages of the test resulted in closure at the notch root.

Figure 3.13 shows magnified unloading crack profiles for both LDU and LDULU crack propagation algorithms. Distributed crack closure is specifically seen at the pre-crack tip transients. The transients appear sharp and localised in Figure 3.13, however the proportions of these features are in fact equivalent to those reported previously [Parry, 2000]: the particular appearance of Figure 3.13 is due to the relatively large crack propagation distance that was used and consequently high ratio of x:y axis magnifications (10,000:1) in the figure (small local fluctuations in crack opening profile are also enhanced by the extreme magnification differences).

In comparing LDU and LDULU propagation, it is seen in Figure 3.13 that the LDULU algorithm (with the additional loading cycle for each propagation step) has a higher closure level of ($K_{cl}/K_{\max} = 0.12$), than the LDU algorithm (corresponding to $K_{cl}/K_{\max} = 0.06$), explaining the greater overall crack opening for the LDULU algorithm in Figure 3.13. The critical difference in the two propagation methods (viewed at this scale at least) is the size of the pre-crack transient in the direction of crack opening. Identifying the size of the pre-crack transient in relation to the overall crack opening profile for each case, it is evident that the transient 'lump' is somewhat larger in the LDULU case (~0.015 μm) compared to the LDU case (~0.01 μm).

Given the different pre-crack transients, crack opening behaviour along the remainder of the cracks cannot be strictly compared, as the transients will have influenced subsequent behaviour (particularly reverse plasticity). When unloaded fully, both cracks are however seen to be closed for about 85% of their propagated length, with the differences between LDU and LDULU COD profiles appearing to be negligible.

Near-tip crack profiles are shown in Figure 3.14. Three of the profiles in the figure appear to show interpenetration of the crack face, however this is a consequence of the finite stiffness of the crack wake spring elements and the very high magnification of the diagram in the y-direction. At the onset of distributed crack closure (i.e. at the pre-crack tips in this case) it may be seen that the first node behind the propagated crack tip is in fact closed for the LDU algorithm, as discussed by Fleck and Newman [1988] and Parry [2000], whilst no such contact is observed for the LDULU algorithm. At $K/K_{max} = 0.0$, local contact of the near-tip node is seen in the LDULU model, although it is evident that the compressive load associated with the contact is much reduced in relation to the LDU case (i.e. the interpenetration is less in the LDULU case). The figure highlights the fact that in both LDU and LDULU cases near-tip closure was always limited to the first node behind the tip in the plane strain condition. Given the extended crack propagation in the present models (more than 60 r_p), it would seem reasonable to consider this behaviour is indeed a representative feature of steady-state crack growth is not particularly influenced by pre-crack transient contact/closure (as appears to be the case for McClung *et al.*, [1991]). Fleck and Newman [1988] suggested that the abnormally high closure of the first node is due to the large residual tensile plastic strain (ε_{yy}^{pl}) left in the unloaded crack tip: they found that the abnormally high closure decreased with more cycles with the crack held stationary, consistent with the present finding (i.e. apparent first node interpenetration is reduced with the additional cycling of the LDULU algorithm.

- $\Delta K = 12.0$ *MPa* $m^{1/2}$, $R = 0.0$ *and 0.1, plane strain conditions*

Figure 3.15 and 3.16 shows unloading crack profiles for the higher baseline load case of $\Delta K = 12$ MPa $m^{1/2}$ at R = 0.0. It may be seen that the pre-crack transients are significantly larger than those corresponding to $\Delta K = 4.6$ MPa $m^{1/2}$ (in both crack opening and growth directions). It is difficult to attach an exact size to the transient

features in Figure 3.15, however the increase in scale compared to Figure 3.13 appear to be around an order of magnitude, in keeping with the factor of 7 increase in r_p between the two load cases. The overall COD values shown for the LDULU algorithm are higher than those for the LDU algorithm at closure, with the key feature again being the scale of the pre-crack transient being greater in the LDULU case. It may be seen that closure levels are again quite low, being of the order of K_{cl}/K_{max} = 0.05-0.10 for $\Delta K = 4.6$ and 12.0 MPa $m^{1/2}$ for both LDU and LDULU algorithms. This is particularly distinctive in relation to experimental data, where results for intrinsically plane strain dominated near-threshold conditions are widely reported to be of the order of $K_{cl}/K_{max} > 0.6$ for many aerospace alloys. The difference may be expected of course as the present FE simulates only PICC, whereas in real materials other closure mechanisms such as RICC and oxide induced crack closure (OICC) will add to the closure effect. On the other hand, when only PICC is considered, crack closure level is reported to be proportional to both R and K_{max} [Hudak and Davidson, 1988]. FE studies by McClung and Sehitoglu [1989] based on plane stress models, suggest that PICC increases with decreasing maximum stress and hence ΔK (S_{open}/S_{max} increases as S_{max}/σ_o decreases). However their results pertain to non-SSY conditions, where the constraint necessary for closure to occur is gradually lost. Budiansky and Hutchinson [1978] modelling show PICC effects to be independent of K levels for SSY-type conditions. When unloaded fully both LDU and LDULU algorithms show a similar closed length of ~70 % of the propagated crack. The negligible difference between COD profiles between LDU and LDULU algorithms at minimum load is consistent with that of the lower load case i.e. $\Delta K = 4.6$ MPa $m^{1/2}$, consistent with essentially steady-state growth conditions being established (pre-crack transients having a limited influence over the total crack length). From the near-tip profiles (Figure 3.15), closure of the first node behind the crack tip is again observed with both LDU and LDULU algorithms at zero load. First node contact is also evident at the onset of distributed contact in the LDULU case however, i.e. this was not seen at low ΔK.

Unloading crack profiles for an R-ratio of 0.1 (i.e. more typical of experimental crack growth testing than R = 0.0) are shown in Figure 3.17. It can be seen that with the LDU algorithm, closure was not achieved even after full unloading, however closure

just occurred at the minimum load (K_{cl}/K_{max} = 0.1) when the LDULU algorithm is used. The size of the pre-crack transient along the crack path appears slightly larger than for the previous $\Delta K = 12$ MPa m$^{1/2}$ /R = 0.0 results, consistent with increasing r_p levels. Although the transient is seen to be larger in the crack opening direction when using the LDULU algorithm, the onset of distributed closure occurs at a similar load (K_{cl}/K_{max} = 0.1) as compared to the R = 0.0 case (K_{cl}/K_{max} = 0.08). Again, interpenetration of the first node behind the crack tip is seen with both LDU and LDULU algorithms, but is reduced with the LDULU algorithm (Figure 3.18).

- *Hardening law effects*

1. LDU Algorithm

In Figure 3.19 unloading crack profiles using isotropic hardening and kinematic hardening (for $H = 0.7E$) material behaviour are shown ($\Delta K = 4.63$ MPa m$^{1/2}$, $R = 0.0$, LDU crack propagation algorithm). The hardening rule has an effect on the pre-crack transient lump size, with kinematic hardening producing a smaller transient lump: however the measured closure loads are very similar for the models, even though contact at the pre-crack is again the controlling feature. The larger transient lump for isotropic hardening is consistent with the greater plastic deformation as compared to that of kinematic hardening (as discussed by Antunes *et al.*, 2004). The difference in overall crack opening profiles for the kinematic hardening model and isotropic models are small and are of the order of 0.015 μm, which is closely consistent with results reported by Parry [2000]. Near-tip crack profiles are shown in Figure 3.20. It is seen that the first node behind the tip goes into compression at minimum and closure load for both hardening cases considered (i.e. showing a limited dependence of constitutive law).

2. LDULU Algorithm

Unloading crack profiles for LDULU algorithm for both isotropic and kinematic hardening ($H = 0.7E$) are shown in Figure 3.21 ($\Delta K = 4.63$ MPa m$^{1/2}$, $R = 0.0$). It may be seen that, the hardening rule again has an effect on the pre-crack transient, but

result in similar closure levels. The larger transient lump size may again be related to the larger plastic deformation associated with isotropic hardening behaviour. In keeping with the present results, Parry [2000] also indicated that the use of different hardening laws had a limited effect on crack closure levels using the LDU crack propagation algorithm: the present results show that such consistency between the different hardening laws may in fact involve subtle changes in crack behaviour, although the general form in which closure occurs is clearly consistent.

Near-tip profiles are shown in Figure 3.22. It may be observed that the first node behind the tip goes into compression at minimum load for both hardening cases shown (i.e. showing a limited dependence of constitutive law), with isotropic hardening producing slightly lesser compressive spring forces. It is interesting to note that for isotropic hardening the near-tip node is nearly in contact at $K/K_{max} = 0.12$, but is evidently less close to occurring in the kinematic case. Hence there appears to be some effect of hardening laws on the near-tip contact when LDULU algorithm is used.

- *Effect of debonding step*

It is interesting to note that when the LDULU propagation is stopped before the last load unload cycle (i.e. using a single LDU cycle at the end of LDULU growth), near-tip contact behaviour is simply equivalent to that of the pure 'LDU' crack. Thus the debonding step has some influence on the contact of the first node behind the tip (as suggested by Fleck, 1988) and not the overall cyclic load history/propagation. To investigate the influence of the debonding step, a crack may be closely monitored in terms of the U_y displacement of the first node behind the crack tip, as shown in Figure 3.23 ($\Delta K = 12.0$ MPa m$^{1/2}$, $R = 0.0$, LDULU). It can be seen that the first tip node goes into contact at $K_{cl}/K_{max} = 0.16$ for LDU and at $K_{cl}/K_{max} = 0.0$ for LDULU. Although debonding of the tensile element was done in three equal steps (mentioned in Section 3.4), the displacement of the node in the y-direction is not increased in equal increments, with maximum increase being in the last step. Figure 3.24 shows the U_y variation of LDU propagation where eight tensile spring elements (each of one-eight the stiffness of the spring used in Figure 3.23, i.e. $k_{i=1-8} = k_s/8$, where $i = 1, 2...8$, denoting the spring indices and k_s is the stiffness are used in place of a single

spring (this propagation is termed LD8U). Each of the eight springs are released successively, in three steps each (debonding 1 corresponding to the first spring release and so on) to generate gradual relaxation of crack tip strains. It may be seen that the maximum displacement takes place when the last spring is released with no change in the closure level ($K_{cl}/K_{max} = 0.16$). In order to have relatively uniform increases in U_y, multiple springs (9 springs) of varying stiffness (spring stiffness are varied as per $k_{i=1-9} = (32/2^{i-1})k_f$, where $k_f = k_s/63.875$) were tested (the propagation process termed as LD64VU). The springs are released in decreasing stiffness order with this particular formation being established by a process of the trial and error to produce a uniform crack opening process. Figure 3.25 shows the near-tip result of the LD64U algorithm (debonding 32 indicates the release of highest stiffness spring; $k_1 = 32\ k_f$, and so on). It can be seen that there is indeed a gradual increase in U_y, although the near-tip closure level remains unchanged ($K_{cl}/K_{max} = 0.16$). From Figures 3.25, 3.26 and 3.27 it can be observed that there is indeed little effect of the various debonding steps (LDU, LD8U and LD64VU) on the first node behind the tip contact, although the relaxation of the tip strains is influenced by the choice of debonding steps. It is evident that, contrary to the suggestion of Fleck and Newman [1988], first node contact is not a consequence of 'erroneous' load redistribution during instantaneous crack advance, with the present thesis results therefore adopting the simple single spring release.

3.6.1.3 Plane stress crack behaviour

Figure 3.26 shows typical crack profiles for loading, debonding and unloading using the LDULU algorithm ($\Delta K = 4.6$ MPa $m^{1/2}$, $R = 0.1$). It may be observed that, unlike the plane strain case, there is limited evidence of a pre-crack transient lump. In the first instance this is consistent with the through-thickness contractions now allowed by plane stress conditions dominating the crack wake stretch. Comparing the profiles in the RSFZ and RSZ, the appended residual stretched material in the crack wake is evident as suggested by Budiansky and Hutchinson [1978]. Similar crack profiles have also been reported by Zhang *et al.*, [1992], Zhao *et al.*, [2004], Atunes *et al.*, [2004]. Closure is seen to occur as a continuous build up from the first node behind the crack tip, starting at $K_{cl}/K_{\max} = 0.37$. Figure 3.27 shows the variation of transverse displacement (U_x) for loading and unloading (at closure). It can be observed that variation of U_x for both RSFZ and RSZ is essentially linear (with little

discontinuity at the pre-crack tip location unlike that in the plane strain case [see Figure 3.11]) suggesting that transverse displacement is not significantly altered by the plastic deformation in the crack wake. This is again in agreement with the 'supply' of appended residual stretched material from the out-of-plane direction. Figure 3.28 compares the crack profiles of plane stress and plane strain for equivalent conditions at closure. It can be seen that the plane stress crack is closed at a higher load (K_{cl}/K_{max} = 0.37), starting at the tip, as compared to that of plane strain (K_{cl}/K_{max} = 0.12), where closure starts at the pre-crack tip. The size of the transient lump in the plane strain case is observed to be smaller by more than 1 order as compared to the plane stress residual stretched material. For the LDULU algorithm, closure is seen to occur as a continuous build up from the first node behind the crack tip, starting at $K_{cl}/K_{\max} = 0.36$: for the LDU algorithm however, contact initially occurs at the first node behind crack tip at $K/K_{\max} = 0.5$, with distributed contact building up behind crack tip from $K_{cl}/K_{\max} = 0.30$ which is closely consistent with the second node behaviour of the LDU model (see Figure 3.29 and 3.30). These results confirm the findings of Section 3.6.1 in that near-tip anomalous contact occur under plane stress conditions, but may indeed be removed by additional load cycling after debonding (in keeping with the plane strain models). It may be mentioned that in the analyses performed by McClung and Sehitoglu [1989], using two load cycles per crack growth increment, the first two nodes behind crack tip tended to close at the same load increment but in the present model there appears to be more gradual closure starting with the first node behind the crack tip. In the first instance this may be due to the finer resolution of the load decrement considered for the analysis here (50 decrements) as compared to the previous analyses, and also due to the finer mesh adopted in the present analysis (r_p/L_e ~ 30 which is significantly more refined than r_p/L_e ~ 10 suggested by McClung and Sehitoglu).

Figures 3.31 and 3.32 show the unloading crack profiles and near-tip crack profiles for both the LDU and LDULU algorithms at $\Delta K = 4.6$ MPa $m^{1/2}$, $R = 0.1$. Behaviour is essentially very similar to the previous section, with initial closure in the LDU case taking place at the first node behind the crack tip at $K/K_{\max} = 0.41$; further contact behind the crack tip then builds up from $K_{cl}/K_{\max} = 0.31$. For the LDULU

algorithm, a progressive build up of contact is observed from the first node behind crack tip, with the closure value of the first node behind the tip corresponding to $K_{cl}/K_{\max} = 0.37$. Comparing results for the onset of distributed closure for each propagation algorithm with those for $R = 0.0$, there would appear to be a limited influence of R-ratio on closure levels. Given the plane stress loading conditions, it is reasonable to compare this behaviour with the analytical results of Hutchinson and Budiansky [1978], as shown in Figure 3.33 (K_{cont} in Figure 3.33 being equivalent to K_{cl} in this work). Whilst closure levels reported by Hutchinson and Budiansky are generally higher than those obtain here by FE modelling, the limited influence on K_{cl} (K_{cont}) of varying R between 0.0 and 0.1 is quantitatively consistent with the present plane stress results, with very similar results being here obtained for $\Delta K = 12.0$ MPa $m^{1/2}$, $R = 0.1$, which is again as predicted from the Budiansky and Hutchinson results (PICC is independent of ΔK level).

- *Overall FE model performance*

From the present analyses it is seen that 'bulk' (or progressive) PICC in plane strain particularly builds-up from the pre-crack root towards the crack tip during unloading consistent with Sehitoglu and Sun, 1991, Fleck, 1986, Fleck and Newman, 1988 and Parry, 2000. The pre-crack transient size is then critical in determining initial closure levels. As the pre-crack was ideally sharp in the present models, the plane strain transient is not simply attributable to a lack of constraint from an initial notch of finite width/angle. It is clear that the stress-strain history of the material behind the crack is then important, with steady-state crack growth representing an 'equilibrium' between residual stress-strain fields of previous crack growth, and the current active deformation. It is clear from the present results that starting from a non-deformed crack-tip, initial loading can effectively draw material forward from the crack wake in the manner suggested by Sehitoglu and Sun [1991] but is unnecessary in plane stress conditions. Considering the apparent volumes of material movements ahead of and behind the crack-tip (seen in the crack profiles, such as Figure 3.10), it is evident that closure at this pre-crack tip is predominantly a function of the mechanism suggested by Sehitoglu and Sun, and not that suggested by Riemelmoser and Pippan [1998] (i.e. material moves along the crack wake towards the tip to generate the necessary stretch in the plastic wake for plane strain PICC). This is consistent with the apparent wake

dependence of PICC in plane strain (i.e. it only really arises at the pre-crack tip), in that material; displacement behind the crack-tip will be susceptible to the build up of a deformed wake, whilst the mechanism of Riemelmoser and Pippan would be occurring in 'virgin' material as crack propagation occurs. It is also observed that the plane strain pre-crack transient is hardening law and propagation algorithm sensitive, so exact crack closure results associated with any one modelling set-up must be examined with caution. In this respect in particular, the present results must be considered in relation to variable amplitude/overload studies, as the present models may in fact be considered a logical extrapolation of low-high block loading where the initial low load levels become vanishingly small. Whilst modelling strategies can of course be increasingly refined (e.g. in the use of more elaborate and notionally accurate hardening laws [Zhang *et al.*, 1992]), the purpose of the present work is to use FE modelling to provide micromechanistic understanding of behaviour, rather than exact quantitative results (the micromechanistic understanding is then to be used in analytical model formulation). Indeed, it may be argued that given the complexity of real crack deformation, behaviour in the near-tip region will be influenced by micromechanical phenomena that are beyond even the most refined FE modelling strategies currently available, such as heterogeneous work softening by precipitate shear, environmental contributions to near-tip deformation from adsorbed and/or absorbed hydrogen, grain boundary sliding, and the development of different dislocation cell/substructures as a function of specific strain paths surrounding the crack tip (particularly for planar slip materials such as underaged Al-alloys), the pursuit of second order model parameter effects is at present irrational. Within this context, it may be said that the present models behave in a reasonably consistent manner, whilst clarifying potential uncertainties in the approach for future reference.

As published in the literature, the contact of the first node behind the tip is seen when a LDU-type algorithm is used. Given the near-tip nodal contact in the plane strain models was: (a) isolated to the region of greatest uncertainty for the present models (i.e. at the crack tip), and (b) was not a part of a more general "zipping-up" of the crack that may be anticipated for simple constant amplitude loading, there are therefore limited grounds for considering this to be a "real" closure event. The present results for different propagation algorithms support the assertion that first

node contact is indeed due to unrepresentative residual strains/stresses when the crack tip moves by a large discrete step in relation to the tip stress/strain fields (McClung *et al.*, 1991), rather than any artefact of the spring release process. As noted by Parry [2001], McClung *et al.*, [1991], have however linked anomalous contact behind the crack tip to element 'locking' problems in modelling stress gradients in plane strain. Since a selective reduced-integration technique was used in the present analysis, possible element locking is circumvented [Parry, 2000]. Overall, the present analyses corroborate the view taken by Fleck [1986], Fleck and Newman [1988] and Parry [2000] that contact of first node behind the crack tip in plane strain FE models of PICC is essentially anomalous and an artefact of a stepwise crack propagation scheme.

3.6.2 Deflected cracks

The previous sections have addressed a number of issues in FE model formulation, in particular artefacts that can arise in plane strain models, and variability in exact closure levels associated with underlying modelling parameters. Given the particular interest in plane strain behaviour, where PICC effects are expected to be minimal and the intrinsic prevalence of plane strain conditions at low ΔK levels where crack roughness levels are typically greatest, the following work on deflected cracks on plane strain conditions, neglecting near-tip nodal contact and pre-crack tip transients effects.

3.6.2.1 Comparision with previous work

Figure 3.34 shows a typical deformed mesh for a periodically deflected crack (L = 150.0 μm, $\theta = 45^{\circ}$, ΔK = 12.0 MPa $m^{1/2}$, R = 0.1) when it is unloaded fully ($K < K_{cl}$). Closure can be observed at discrete points near the asperity tips, with major portions of the crack remaining open, as seen experimentally by Walker and Beevers [1979]. Changes in the sense (i.e. direction) of relative shear displacements of the upper and lower fracture surfaces at each asperity are observed. An identical closure pattern has been observed by Parry [2000]. In this respect it should be noted that, to the best of our knowledge, Parry was the first to provide such a unique insight, suggesting that observed closure is due to the *residual* shear offsets at the asperities and not due to the

'global' displacements of the upper and lower crack faces resulting from the mode mixity behaviour at the active crack tip.

The effect of deflection angle on closure levels is shown in Figure 3.35. The closure levels are strongly influenced by deflection angle, with higher closure levels for steeper deflection angles. Quasi-stabilised closure levels are reached when the crack has propagated through the first few deflections (after the 3rd deflection in the Figure 3.35). The closure levels are seen to vary cyclically, having maximum values just after each deflection, and dropping off gradually as the crack moves away from the point of deflection. Similar cyclical closure processes and influence of angle on closure for deflected cracks are also reported by Parry [2000].

3.6.2.2 Asperity size effects

In order to examine relative asperity size effects on closure, analyses were performed with varying ΔK and L (see Table 3.1), for $\theta = 45^{\circ}$ keeping $R = 0.1$. The results are plotted in Figure 3.36. The asperity length L is normalised by r_p, as suggested by Parry [2000] although this was based on a limited set of load cases. Variation of maximum (corresponding to maximum values in the cyclic closure process (see Figure 3.36) and mean (weighted mean of the closure values along a deflected length) closure levels are considered. It is evident that at small L/r_p values, the maximum closure levels appear to fall, with little difference between maximum and mean values. A plateau in maximum closure levels is seen when the deflection lengths approximately equal to, or greater than, the plastic zone size (i.e. $L/r_p \cong 1.0$). Similar behaviour has been observed by Parry for lower R, L and ΔK values ($R = 0.0$, $L = 5$-100 μm, $\Delta K = 3.6$-5.7 MPa $m^{1/2}$). The present results (Figure 3.36 for $\Delta K = 8.5$, 10.0, 12.0, 15.0, 17.0 MPa $m^{1/2}$ and $R = 0.1$) show reasonable accord with those of Parry for this R-ratio regime, however closure values are slightly raised for the present work. This difference is however attributable to crack propagation algorithm adopted with all of the present deflected crack models, i.e. using the LDULU algorithm, as opposed to LDU in Parry's work (see Section 3.6.1.3). The normalisation of asperity sizes in the form L/r_p is a novel outcome from Parry's work providing a simple apparent scaling of roughness effects against both loading conditions (ΔK) and material aspects (yield stress and microstructural scales). As a further specific test of the consistency

of the L/r_p normalisation, variation of closure levels with ΔK for a fixed L/r_p are plotted in Figure 3.37. It is significant to note that the range of ΔK considered in these results is critical for much of the growth regime necessary of conventional airframe life calculations. It is seen that L/r_p control of closure levels is indeed closely maintained, highlighting a consistent role of L/r_p normalisation in defining RICC conditions. The present finding is contrary to the mechanism proposed by Pippan *et al.,* [1994], where RICC is caused when the plastic zone size is the same order of magnitude or larger than the characteristic size of fracture features (i.e. hills or valleys as shown in Figure 2.6) implying low closure to occur when $L/r_p > 1$. It may be seen that the present work exhibits a straight-forward and intuitively reasonable effect of surface asperity size on RICC, in that closure levels primarily diminish as $L \rightarrow 0.0$, rather that exhibiting increasing and decreasing trends with varying L.

3.6.2.3 Analytical modelling

- *2D analytical model:*

Based on the micromechanical insight of the deflected crack FE models, Parry formulated an analytical model considering growth of the fatigue crack at some distance from the turning points where the residual strain at the asperity tips has passed fully into the crack wake (simple elastic expressions for the crack opening are used). On loading a deflected crack, a degree of shear deformation occurs at an asperity tip, which on unloading, the elastic constraint of the enveloping material causes a limited degree of reverse plastic deformation. If the crack then changes direction (i.e. the point in question becomes an asperity tip) this net forward shear leads to premature contact in the crack wake when the crack has propagated. This process is lustrated schematically in Figure 3.38, and may be seen to give rise to the alternating shear offsets of the FE models (Figure 3.34). The residual shear deformation may be considered to produce an effective displacement of the asperity tip h (see Figure 3.39). In the first instance h is assumed to scale with residual crack tip shear displacement ($CTSD_{res}$) at the asperity turning point. Combining $CTSD$ expressions (using Dugdale type strip yield model [Rice, 1967]) with elastic crack opening and deflected crack tip stress intensities [Bilby *et al.,* 1977] gives:

$$CTSD_{res} = h = \frac{\sqrt{3}K_{Imax}^2(1-\nu^2)(1/2+R-1/2R^2)(\sin\theta/2+\sin 3\theta/2)^2}{16E\sigma_y} \quad (3.1)$$

Some variation in the analytical expressions of *CTSD* are available in the literature [e.g. Rice, 1967, Li, 1990]. As such the value of h in Equation 3.1 may be replaced by $\beta_{II}h$, where β_{II} is a scaling parameter which may vary from 1 to 4 based on the various CTSD approximations. As such β_{II} may be used as a fitting parameter, allowing for inaccuracies in the various assumptions made (e.g. microstructural factors influencing slip character which might be expected to influence the accuracy of Dugdale estimate of CTSD are not treated in this model).

It can be seen from Figure 3.39 that crack closure will take place when COD (δ) = h $sin(2\theta)$. Combining the expression for $CTSD_{res}$ (Equation 3.1) with the elastic crack opening expression and rearranging, the closure level can be determined as,

$$\frac{K_{cl}}{K_{max}} = \frac{\beta\sqrt{3\pi}K_{max}(1-\nu^2)(1/2+R-1/2R^2)(\sin\theta/2+\sin 3\theta/2)^2\sin 2\theta}{16\sigma_o\sqrt{a^*}(3\cos\theta/2+\cos 3\theta/2)} \quad (3.2)$$

a^* is the distance of the crack tip from the last asperity peak. Results for a crack moving past three asperity tips using Equation 3.2, are shown in Figure 3.40 for a L = 20.0 μm, θ = 45°, ΔK = 4.6 MPa $m^{1/2}$, R = 0.0. Each section of the plot (passing one asperity at a time) is obtained by implementing Equation 3.2 in relation to each crack turning point (i.e. $0 < a^* < L$). The model results in a set of asymptotic curves from each crack turning point, i.e. when a^* tends to zero. Although the simple model predicts unrealistic closure levels near the asperity points, it is possible to find reasonable accord with the FE models once the crack moves away from the immediate crack turning region. In Parry's work, the distance from which the analytical model was seen to fit with FE results was seen to scale approximately with plastic zone size, and a parameter λ was identified as a scaling factor defining near the turning point region where the analytical model does not hold. A linear closure approximation was then adopted between the end of each deflected crack section out to a distance of λr_p from the next asperity tip. This interpolation was used to produce continuous crack closure prediction result, where it may be seen that the resultant blue line in Figure 3.40 is a reasonable approximation of the cyclic crack closure results seen in the FE models in Figure 3.35. However, when $L < \lambda r_p$ the interpolation may

be seen to become fundamentally irrational, as this would always result in increasing mean closure levels as deflection size decreases. If L became smaller than λr_p, the linear interpolation would in fact become entirely irrational, as there would be no end points where the underlying physical model was believed to be reasonable. At this point it is worthwhile to consider that when evaluating crack closure immediately following a deflection, it may be rational to assume that the crack must propagate some distance into the deformed material at the asperity turning point for that material to effectively move into the crack wake to induce closer, i.e. shielding due to residual strains at the asperity turning points cannot become effective immediately at the crack tip as Parry's analytical formulation suggests. This may be identified as analogous to the incidence of delayed crack retardation following a tensile overload: overload induced closure effects on crack growth do not act immediately at the point of overload, but only once overload deformed material has moved into the crack wake. Thus the current RICC model may be modified by considering that closure is only generated as residual deformation passes into the crack wake: the key modification is the notion that h must effectively tend to 0 as $a^* \rightarrow 0$ (see Figure 3.39). The distance over which the crack then needs to propagate in order for the asperity tip deformation to act fully in the closure process may be assumed to be some multiple (or fraction) of the plastic zone size, λr_p, as crack tip deformation length dimensions will scale with $(K/\sigma_y)^2$. Hence the analytical model given by Equation 3.1 is again considered to be invalid for $a^* < \lambda r_p$. In the present modification, the transition in shielding in the region $0 \leq a^* \leq \lambda r_p$ is identified in terms of h' to represent the effective fraction of h as function of a^* (normalised by λr_p) that acts to generate closure in the crack wake, thus the following relationship is suggested to approximate h:

$$h' = h'(a) = h\left(\frac{a^*}{\lambda r_p}\right)^{\alpha} \qquad \text{for } a^* < \lambda r_p \tag{3.3a}$$

$$h' = h'(a) = h \qquad \text{for } a^* \geq \lambda r_p \tag{3.3b}$$

where α is an empirical factor that may be determined experimentally or by FE modelling and h is given by Equation 3.1. In the first instance, α is taken to be 1, i.e. h is assumed to be a simple linear function of a^* (normalised by λr_p) for $a^* < \lambda r_p$ to

represent the effective influence of asperity deformation at small a^* values. A simple geometrical representation of this model may be seen as the presence of near-tip asperity offset, as shown in Figure 3.41, where the crack tip progress along the downward flank of the asperity along the curved dashed line. As a^* increases, a greater fraction of h is effectively seen in the crack wake. When $\alpha = 1$ the curved part of the asperity deformation is simplified to a straight line. This new model formulation results in a continuous closure model behaviour (i.e. without singularities) as illustrated in Figure 3.42, which appears to fit well with equivalent FE results for $\beta_{II} = 1.0$, $\lambda = 0.5$. Figure 3.43 shows a comparison of closure levels predicted by FE model and analytical model for varying deflection angles. The analytical plots are made for $\beta_{II} = 1.0$ and λ=0.5: although analytical results are on the low side, it may be noted that a slightly higher value of $\beta_{II,}$ may be used to bring fit the FE and analytical results. Here the key focus is the fact that present analytical model is able to demonstrate functionally equivalent the closure behaviour to the FE model, implying that the mechanistic understanding of the FE results is indeed reasonable. It can be seen that the increase of closure levels with increasing deflection angle is well predicted (in agreement with the RICC prediction of Suresh and Ritchie [1982] for example).

Figure 3.44 compares the current analytical modelling and FE results for both $R = 0.0$ (corresponding to Parry's [2000] work) and $R = 0.1$ (corresponds to the present work) as function of relative asperity size for a fixed deflection angle. Analytical results are plotted for $\beta_{II} = 1.0$ and $\lambda = 0.5$ in the first instance. It is seen that results from both FE and analytical analyses are reasonably consistent. It may be seen in particular that the present analytical representation of RICC captures well the apparent L/r_p control of closure levels (including the initial rise and then plateau in closure effect associated with increasing L/r_p). It may be noted that the analytical treatment of closure levels when a^* (or indeed L) is less than λr_p is somewhat simplified (e.g. in the treatment of near-tip elastic-plastic tip opening and residual compressive stress effects). It is also possible to give better correlation between the FE and analytical models by adjusting the values of β_{II} and λ, however the key here however is not achieving exact correlation of FE and analytical predictions, but seeking to capture of the basic trends predicted by the assertion that RICC's is indeed primarily a function of residual

plastic shear deformation in the crack wake and how this may be treated in a simple analytical manner as L/r_p varies. As such an efficient, simple RICC modelling framework may be achieved for realistic engineering application.

- *3D analytical model:*

Recent direct 3D imaging of crack closure processes using high resolution synchrotron tomography has suggested the importance of contact of parallel ridges to crack growth direction, indicative of possible mode III effects [Toda *et al.*, 2003, Khor, 2004]. As such, any complete description of crack micro-mechanics should entail the 3D nature of real cracks. This is computationally expensive in terms of FE modelling, and, bearing in mind the long model run times already involved in the 2D FE models, it is valuable to consider the potential to extend the physical understanding that is captured in the present 2D analytical modelling. In this respect it may be noted that if a crack is twisted about the crack growth direction (i.e. inclinations orthogonal to those considered so far), then the dominant shear effect will be mode III in character. In the first instance it may supposed that as forward and reverse deformations at the crack tip must again be asymmetric (loading deformation is much less than the unloading deformation), the residual mode III shear offsets may be expected to act in such a crack, analogous to that illustrated in Figure 3.38 for in-plane crack zigzags. There are of course a number of ways in which a 3D crack may be imagined to deflect about the crack growth direction (whilst simultaneously zagging in plane). Three simple cases are shown in Figure 3.45. In the simple configuration in Figure 3.45a if mode III shear is considered to act on both the incline planes, it would lead to 'pressing against' each other at the peak of the mode III twists. A saw-tooth (Figure 3.45b) crack plane would generate immediate crack contact for any mode III shear on the inclined face (in the absence of shear on the vertical face). Figure 3.45c shows a trapezoidal crack profile, where it may be seen that mode III offset arising from the tilt sections of the crack may be simply linked to a reduction of crack opening along the edge of the flat sections and hence premature closure. Whilst real crack profiles will of course be more complex and irregular, Figure 3.45c is identified as a suitable, tractable model geometry that may give some estimate of mode III deformation influences on crack face contact. If an irreversible shear is considered to act on the incline face (Figure 3.45c), it would result in a shear

offset, h_{III}, analogous to the h_{II} deformation in the zigzag crack path of Figure 3.41. In the first instance, superimposing the trapezoidal and zigzag configuration may be seen to generate a 3D crack surface profile as shown in Figure 3.46. If this idealised profile is assumed, we can readily simply sum mode II and mode III residual offset effects to indicate a maximum potential interaction/contribution to closure due to tilt and twist.

Analogous to the mode II, residual CTSD due to local mode III loading ($CTSD_{IIIres}$) may be obtained as:

$$CTSD_{IIIres} = \frac{\sqrt{3}K_{II\,\mathrm{Im}ax}^2(1+\nu)\left(\frac{1}{2}+R-\frac{1}{2}R^2\right)}{E\sigma_y} \tag{3.4}$$

It may be noted that for the case of mode II offset in a zigzag crack, there is a β_{II} (the scaling parameter) in the expression of $CTSD_{IIres}$. A similar scaling parameter could be present in the expression for $CTSD_{IIIres}$ (Equation 3.4). Whilst it is possible to identify two 'β' parameters (for both mode II and III deformations), a common β is chosen in the present work in the interest of simplicity.

Based on the elastic estimates of pupative, local stress intensity conditions, residual mode III displacement based on the $CTSD_{IIIres}$, may then be obtained as;

$$h_{III} = \frac{\sqrt{3}K_{\mathrm{Im}ax}^2(1+\nu)\left(\frac{1}{2}+R-\frac{1}{2}R^2\right)\cos^8\left(\theta/2\right)\left[\sin\phi\cos\phi\left(\cos^2\left(\theta/2\right)-2\nu\right)\right]}{E\sigma_y} \tag{3.5}$$

Combining with Equation 3.5 with expressions for elastic crack opening [Tada *et al*, 2000] and residual mode II displacement (h_{II}) [Parry, 2000] gives;

$$\frac{K_{cl}}{K_{\max}} = \frac{\sqrt{3\pi}K_{\mathrm{Im}ax}\left(\frac{1}{2}+R-\frac{1}{2}R^2\right)}{16\sigma_o\sqrt{a^*}\left(3\cos\theta/2+\cos 3\theta/2\right)}\left[\left(\sin\theta/2+\sin 3\theta/2\right)^2\sin 2\theta + \frac{16(1+\nu)}{(1-\nu^2)}\cos^8\theta/2\sin\theta\sin^3\phi\cos^3\phi\left[\cos^2\theta/2-2\nu\right]\right] \tag{3.6}$$

It may be noted that there are several ways to approximate the local mode II and III stress intensity factors, k_2 and k_3 at a kinked and twisted crack tip (e.g. see Faber and

Evans, 1983): basically both kink and twist angle can be made to influence k_2 and k_3, or they can be thought to act independently. However, it is that the differences prove to be quite small for the crack shapes of real interest (for moderate kink and twist angles up to 45°).

Before examining general behaviour of the kinked and twisted crack model, it should be noted that the result given by Equation 3.6 above neglect the effect of previous deformation of the active crack tip. In the previous 2D model, the remotely applied R is considered in determining the residual CTSDs, however it may be noted that it may be unrealistic to use the applied R for a propagating crack, as there will be an effectively increased R at the crack tip due to closure at previous asperities. If the increased effective R (R_{eff}) is used ($R_{eff} = K_{cl}/K_{max}$), it leads to an 'iterative' R model (Figure 3.47), as such the R_{eff} at the start of any deflection turns out to be the minimum K_{cl}/K_{max} for the previous deflection, as this will be the R-ratio determining forward and reverse deformation at the tip of the new asperity Figure 3.48 shows the variation of closure levels with crack length that may arise using the iterative R model ($\Delta K_{(BL)}$ = 4.6 MPa m$^{1/2}$, R = 0.1, L = 20 μm, $\theta = \phi = 30°$, β = 2.0, λ = 0.5). It can be seen that there is an appreciable increase in closure levels that then stabilises after about 3 or 4 deflections, consistent with previous FE results.

Basic parametric studies of the model behaviour (represented in the iterative form of Equation 3.6) are shown in Figure 3.49 and 3.50. Figure 3.49 shows the typical effect of ϕ (twist angle) on closure levels for varying the tilt angle (θ) for fixed ΔK, L, and R (ΔK = 6.3 MPa m$^{1/2}$, R = 0.1, σ_y = 370 MPa, L = 50 μm, $\beta_{II} = \beta_{III}$ = 2, λ = 0.5). Results shows the increase in closure levels with increasing ϕ is lesser compared to that with increasing θ, suggesting that the kink angle, θ is the main fracture surface parameter. Figure 3.50 shows variations of closure levels with ΔK for varying L from 2-256 μm (ΔK = 6.3 MPa m$^{1/2}$, R = 0.1, σ_y = 370 MPa, $\theta = \phi = 25°$, $\beta_{II} = \beta_{III}$ = 2, λ = 0.5), spanning a wide range of what are critical grain dimensions in a variety of Al-alloys products. It can be seen that between L = 2-128 μm in particular, significant changes in closure levels can be observed. The behaviour at L of 2 μm may be seen as consistent with the reportedly low closure/high growth rate behaviour of powder metallurgy materials, whilst the larger dimensions are characteristics of conventional

wrought alloys where closure levels are significant (e.g. see Venkateshwara Rao and Ritchie [1992]).

- *Experimental comparison*

Having made a number of modifications and extensions of the analytical model to represent a simplified 3D crack surface and associated tilt and twist effects on crack closure, it is clearly valuable to obtain some confirmation of the models accuracy. Having identified that 3D FE models were not of reasonable, comparison with actual experimental results is clearly a more practical, but potential complex procedures.

A. Qualititative comparision

Xu's [2001] detailed experimental results on fatigue crack growth and plane strain closure levels in commercial aluminium 2024-T351 plate and an advanced variant 2024A-T351 form have shown consistent agreement in closure levels at near threshold K_{cl} values when L/r_p values become large for both materials and both materials exhibit fully faceted crack growth. However at higher ΔK values, closure levels drop less rapidly for 2024A (see Figure 3.52). Fractographic observations show that the smaller grained 2024 displayed consistently smaller fracture asperities than the large grained 2024A. And as such, the present closure modelling results (see Figure 3.44) are seen to be broadly consistent with experimental observations, particularly in the convergence of closure levels in the two alloys in the near threshold regime, where L/r_p would be large for both alloys (>1), but the larger fracture surface asperity size of the 2024A would indeed be predicted to have little benefit over the 2024.

B. Quantitative comparision

In the literature few reports pertaining to fracture surface geometry measurements (*viz.*, L, θ and ϕ parameter) are available (e.g. Xu, 2001 and Khor, 2004). Table 3.3 shows the fracture surface measurements in some of the advanced Zn containing variant of commercial aluminium 2024 plate *viz.*, 2024A [Xu, 2001], 2027-ReX(8), 2027-ReX(55), and 2027-ReX(100), where 'ReX' number shown here indicates the recrystalisation fraction of specific batches tested [Khor, 2004] at ΔK = 6.0 and 9.0 MPa $m^{1/2}$ (R = 0.1) using a high resolution optical profilometry technique (Taicaan

profilometry). Typical 3D fracture surface reconstruction using Taicaan measurements for 2024A and 2027-ReX(8) are shown in Figure 3.51a and 3.51b for $\Delta K \sim 6.0$ MPa $m^{1/2}$ and $R = 0.1$ [Khor, 2004]. It may be noted that the fracture surface measurements are not straight-forward and involves the following steps:

1. digitising fracture surface to 12.27 μm steps (model indicates L smaller than this will have little closure effect for r_p dimensions of interest),
2. searching 2 mm along crack surface profiles running back from the crack tip for the highest predicted K_{cl}/K_{max} on that line on the basis of L, θ and ϕ values measured at every asperity tip (defined by every point where the sign of the crack deflection angle θ changes),
3. searching multiple profiles at 12.27 μm spacings for every load and material of interest, eventually covering some 2 x 4 mm^2 area of fractrure surface for each condition, and
4. averaging of all the L, θ and ϕ values for all the closure 'high-points' found in Steps 2 and 3 to give some indication of the crack geometry that may be controlling closure over the small percentage of fracture surface that tomographic imaging indicates to control RICC processes in these materials [Toda *et al.*, 2003].

Two important points should be raised at this point:

1. the measurements described were carried out as part of a complimentary alloy development project [Khor, 2004] and are quoted here particularly for comparison with this modelling effort, and
2. the tabulated values of L, θ and ϕ are recognised as a considerable simplification of how cracks will close in reality, where a distributed build-up of contact points may of course be expected due to local surface variability of the local geometry of high points that may be controlling closure in the various material, with a view to assessing in predicted closure levels are at least of the correct order.

Using the experimental values of L, θ and ϕ in Table 3.3, and Equation 3.6 closure levels are predicted ($\beta_{II} = \beta_{III} = 2.0$, $\lambda = 0.5$) for ΔK (or ΔK_{app}) = 6.0 and 9.0 MPa $m^{1/2}$ ($R = 0.1$) which are then compared with the measured experimental closure levels

in Figure 3.52. Error bars based on repeat measurements on different fracture surfaces are also superimposed on the analytical results to give an idea of the dependence of different surface locations on the closure levels. In the first instance Figure 3.52 may be seen to provide a remarkable endorsement of the present RICC modelling approach given the simplifications involved. It is seen that:

1. predicted closure levels from the fracture surface measurements are indeed of the correct order,
2. closure level predictions are seen to rise with decreasing ΔK_{app} levels, and
3. the 2024A closure predictions are consistently the highest of the 4 alloys considered, consistent with the experimental data.

It must be recognised that 2 main fitting parameters exist within the modelling. In this instance $\beta = 2.0$ has been identified as a good fit with the experimental data, and is within physically reasonable bounds. λ was not particularly adjusted for Figure 3.52, being left at a values settles from the comparison of the analytical 2D model with the relevant FE models. The determination of L, θ and ϕ also be seen to involve important assumptions that may be expected to influence the predictions. However, as a novel idealised model of complex 3D crack behaviour, it may be seen that the present analytical approach can be supported by experimental results from materials of practical interests. The author is unaware of any alternative quantitative model of RICC that deals with 3D crack shapes and is found on a consistent fracture mechanics description of how crack deflections generate the physical offsets necessary for RICC to occur

3.7 Conclusions

1. Where direct comparisons have been made, the present models show close accord with the previous work of Parry.
2. Anomalous near-tip closure in FE models has been identified to occur under both plane stress and plane strain conditions and is seen to vary with baseline load levels and crack propagation algorithm.
3. Anomalous near tip closure is favoured by: (i) use of the LDU crack propagation algorithm, (ii) plane strain loading, and (iii) isotropic work hardening. When using LDULU crack propagation, it is the additional

loading and unloading of the current cycle that particularly alleviates near-tip closure, consistent with this being an artefact of step-wise crack propagation.

4. The use of LDU or LDULU propagation algorithms is also seen to influence closure at the pre-crack in the plane strain models.
5. In general terms it may be said that *none* of the plane strain models showed crack closure that could be related to ongoing/steady state crack growth: - crack closure in all cases was dominated by pre-crack contact, and/or anomalous near-tip contact, even for the relatively long crack propagation used in the low ΔK models. As such, the concept that an absence of through-thickness contraction in plane strain can inhibit PICC is confirmed in this work. The suggestion in the literature that material transport parallel to the crack can generate closure is confirmed for initial growth from deformation free defects, however the steady-state deformation conditions of a propagating crack do not show any significant influence of such mechanisms.
6. Plane stress models are found to exhibit 'rational' distributed crack closure: R-ratio and baseline load level trends are found to be consistent with predictions of Hutchinson and Budiansky (for the values relevant to this work at least), although overall closure levels are lower than the analytical predictions, as also seen by Parry.
7. FE assessment of closure levels in regularly deflecting crack profiles confirms and significantly extends the regime over which normalized asperity size (expressed as L/r_p) is seen to control RICC.
8. Within the present modelling framework, an understanding has been obtained of how crack closure may vary quantitatively with exact model formulation: - whilst differences in behaviour were identified with changes in the model details, it is believed that sound *mechanistic* insight into closure behaviour is obtained via the FE methods.
9. Previous simple analytical treatment of RICC [Parry, 2000] considering fatigue crack growth at some distance from the turning points where the residual strain at the asperity tips has passed fully into the crack wake using elastic approximations for crack opening has been modified by assuming that closure is generated as residual deformation passes into the wake in an

effectively linear manner. This modification results in a continuous closure model behaviour, which appears to fit well the available FE results.

10. The 2D analytical model has been extended to represent a simplified 3D crack surface and associated tilt (θ) and twist (ϕ) effects on closure and found to support the experimental findings from Xu [2001] and Khor [2004].

θ	ΔK in Mpa $m^{1/2}$								
	8.5		10.0	12.0			15.0	17.0	
	L in μm								
	37.5	150.0	150.0	18.75	37.5	75.0	150.0	150.0	150.0
30°							♣		
45°	♣	♣	♣	♣	♣	♣	♣	♣	♣
60°							♣		

♣ analyses performed

Table 3.1: FE analysis matrix for deflected cracks subjected to constant amplitude loading ($R = 0.1$).

Analysis	Crack propagation algorithm	ΔK in MPa $m^{1/2}$			
		4.6		12.0	
		R			
		0.0	0.1	0.0	1.0
Plane strain	LDU	♣		♣	♣
	LDULU	♣		♣	♣
Plane stress	LDU	♣	♣	♣	♣
	LDULU	♣	♣	♣	♣

♣ analyses performed

Table 3.2: FE analysis matrix for undeflected cracks subjected to constant amplitude loading.

Alloy: (σ_y in MPa)	2024A (345.0)		2027-ReX(8) (394.0)		2027-ReX(55) (385.0)		2027-ReX(100) (368.0)	
ΔK (MPa $m^{1/2}$)	6.0	9.0	6.0	9.0	6.0	9.0	6.0	9.0
L (μm)	25.30	22.33	26.81	25.27	32.12	24.78	28.81	22.52
θ (degrees)	39.24	38.55	34.77	29.24	33.05	31.93	30.69	31.33
ϕ (degrees)	31.35	28.54	28.09	16.07	22.36	13.57	23.53	18.19

Table 3.3: Taicaan measurements of surface features of 2024A (after Xu, 2001), 2027-ReX(8), 2027-ReX(55) and 2027-ReX(100) (after Khor 2004).

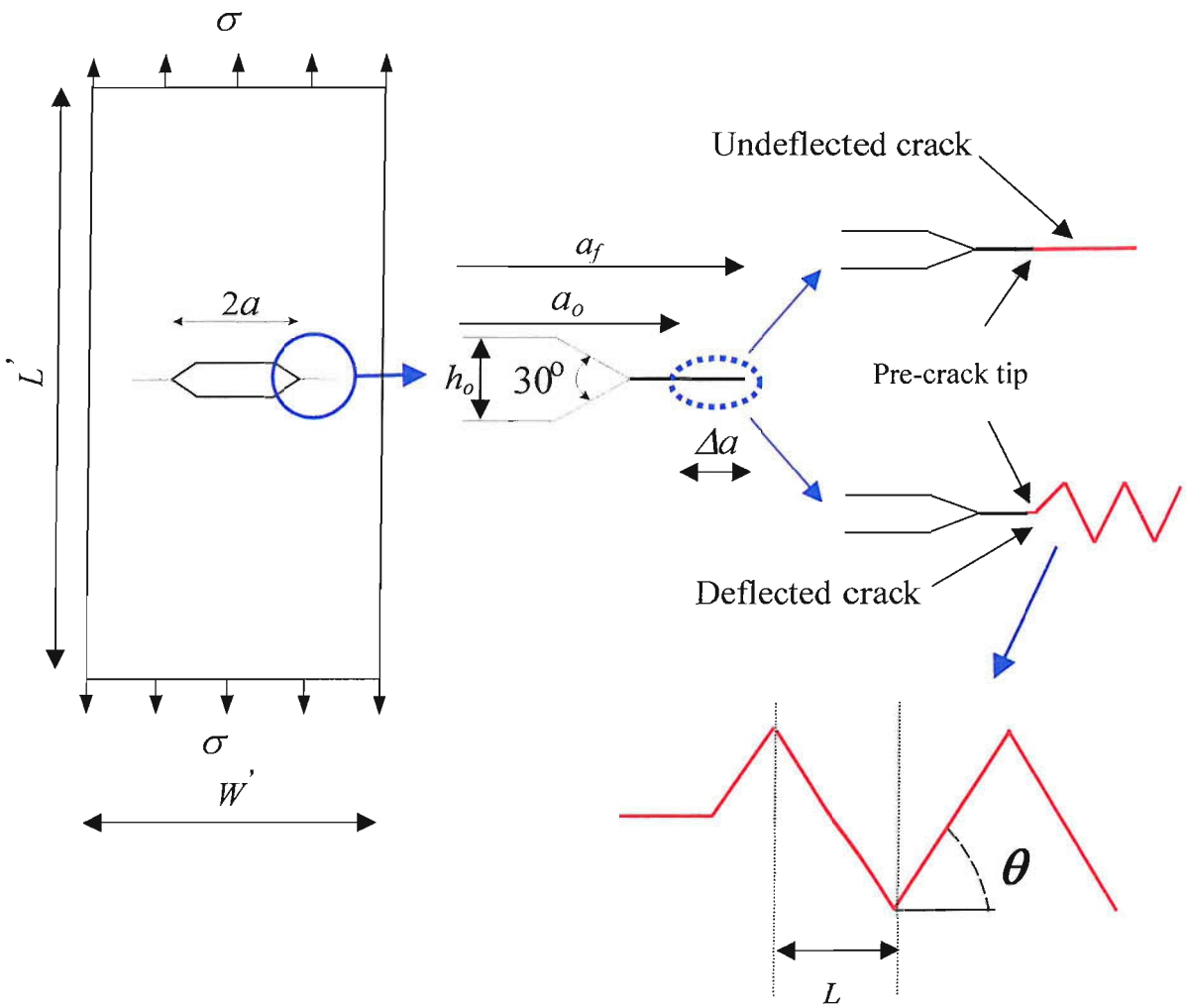

Figure 3.1: Schematic diagram of the geometry and loading of the center cracked panel (CCP) specimen.

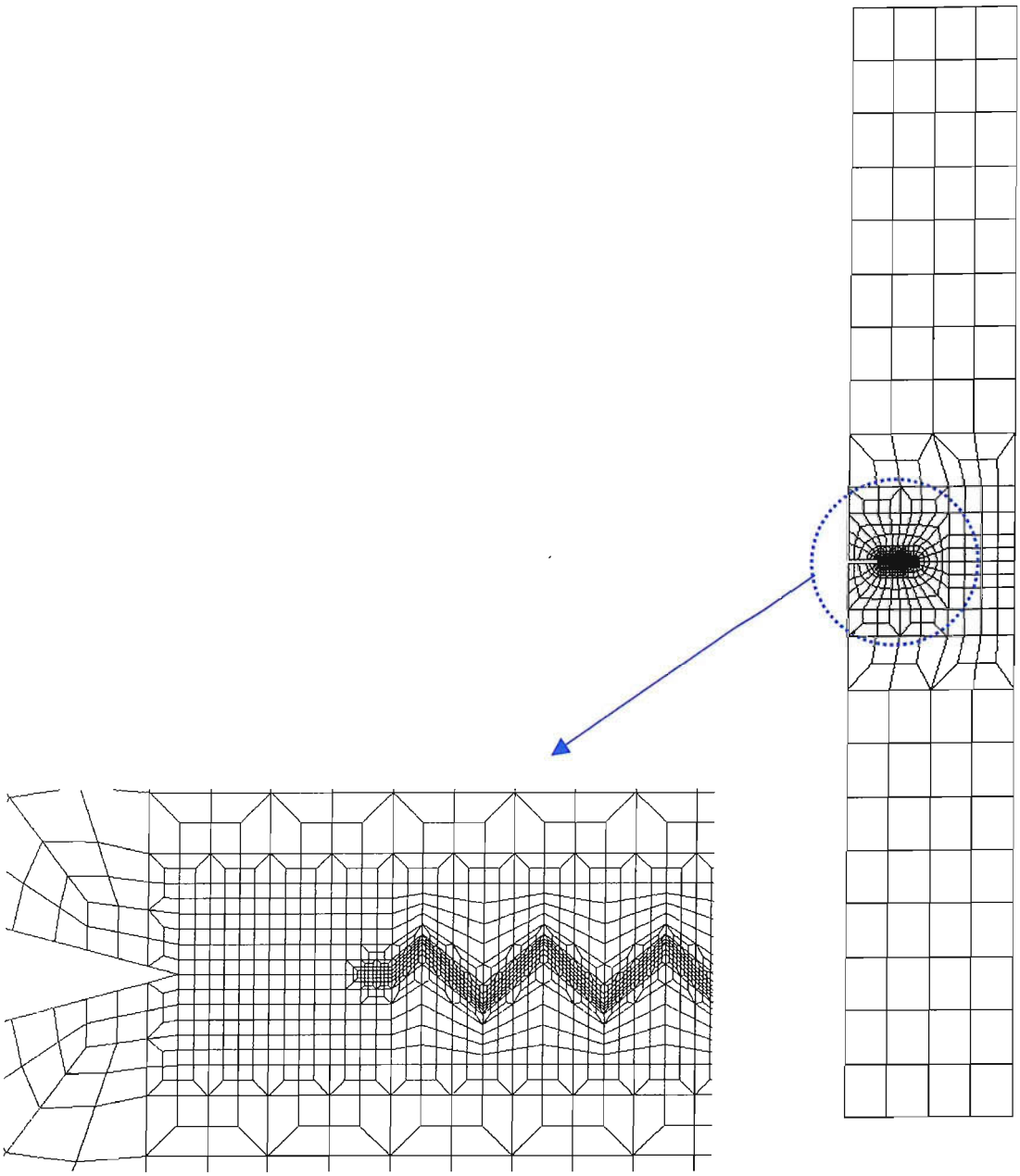

Figure 3.2: Typical finite element mesh of one half of the CCP specimen used for the analysis. Shown here is a deflected crack model for $L = 150$ μm and $\theta = 45^{\circ}$ (6888 four noded isoparametric quadrilateral elements and 7458 nodes).

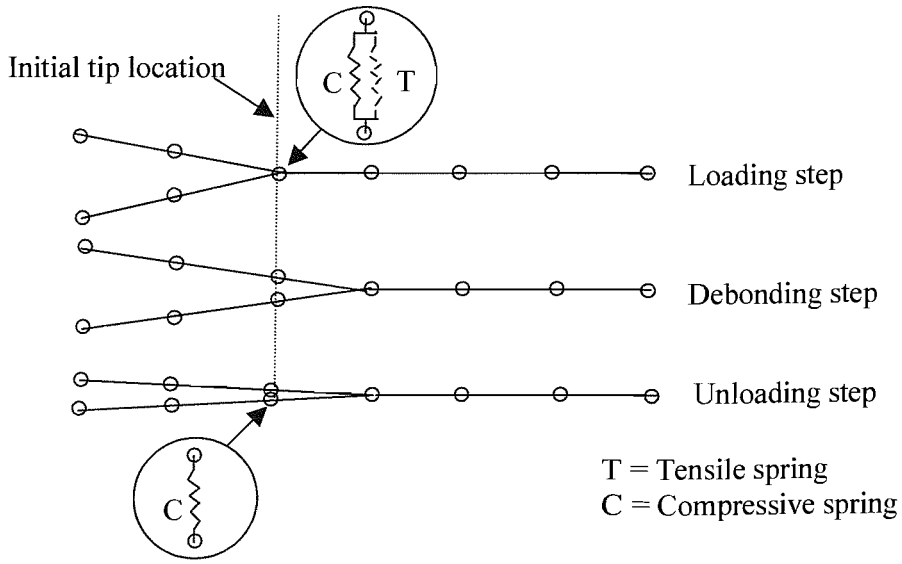

Figure 3.3: Schematic illustration of the LDU crack advance scheme [Parry, 2000].

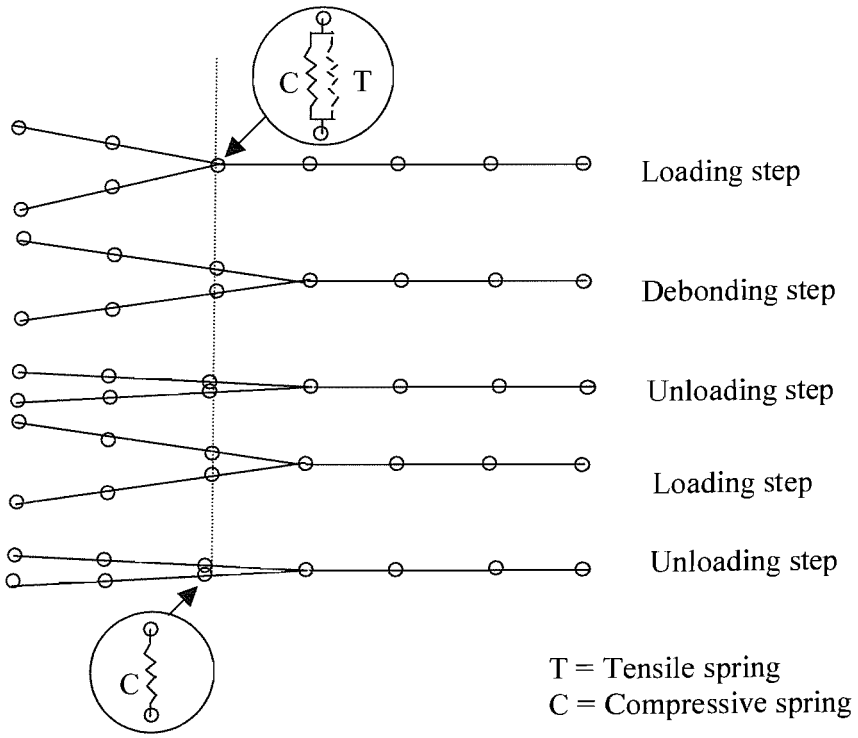

Figure 3.4: Schematic illustration of the LDULU crack advance scheme.

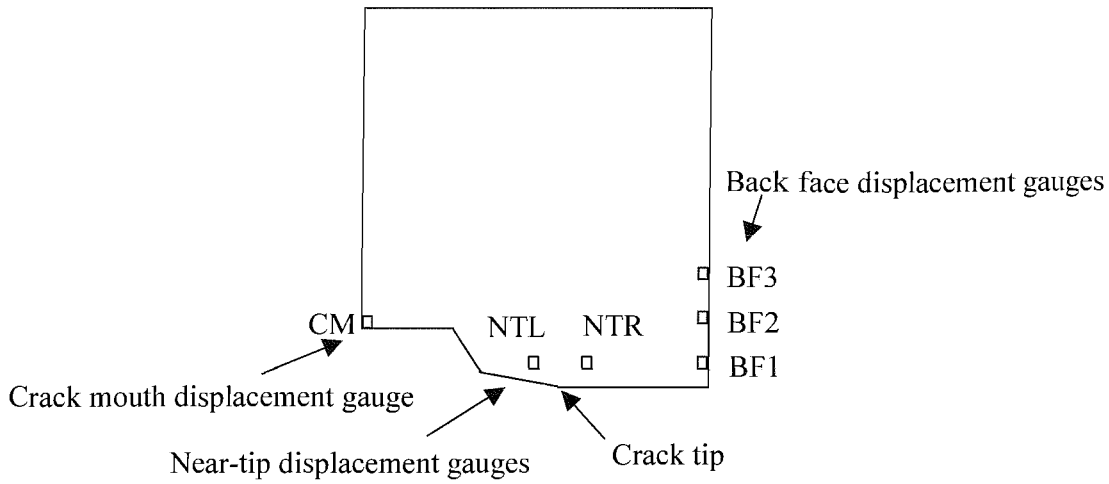

Figure 3.5: Location of displacement gauges in CCP specimen models.

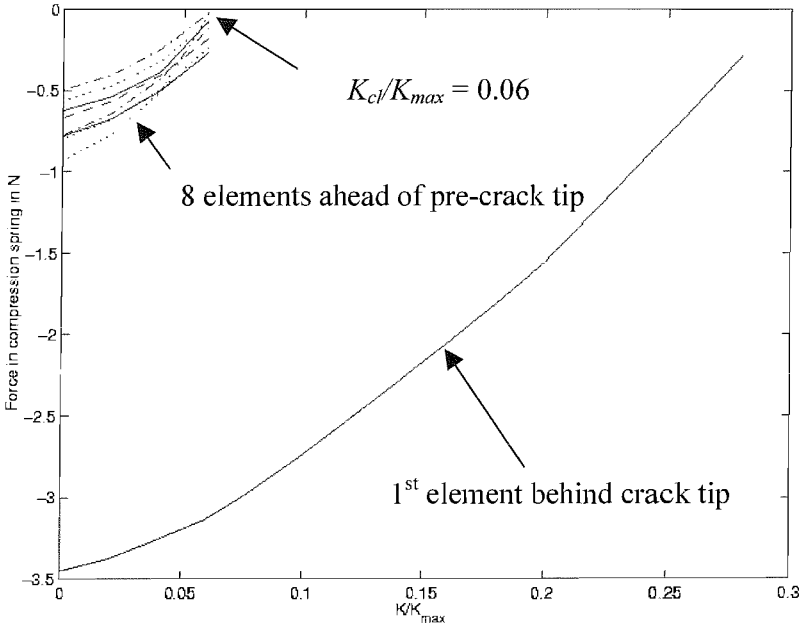

Figure 3.6: Response of compression elements behind the crack tip in plane strain, $\Delta K = 4.6$ MPa m$^{1/2}$, $R = 0.0$, $\Delta a = 100\mu$ m, LDU algorithm.

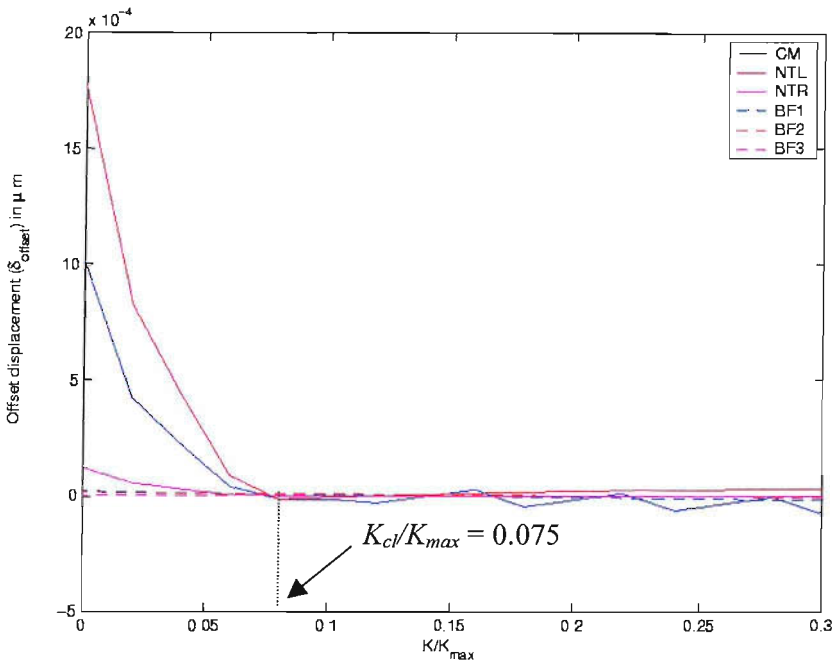

Figure 3.7: Offset compliance plot for plane strain case, $\Delta K = 4.6$ MPa $m^{1/2}$, $R = 0.0$, $\Delta a = 100\mu$ m, LDU algorithm. See Figure 3.5 for legend of measurement locations.

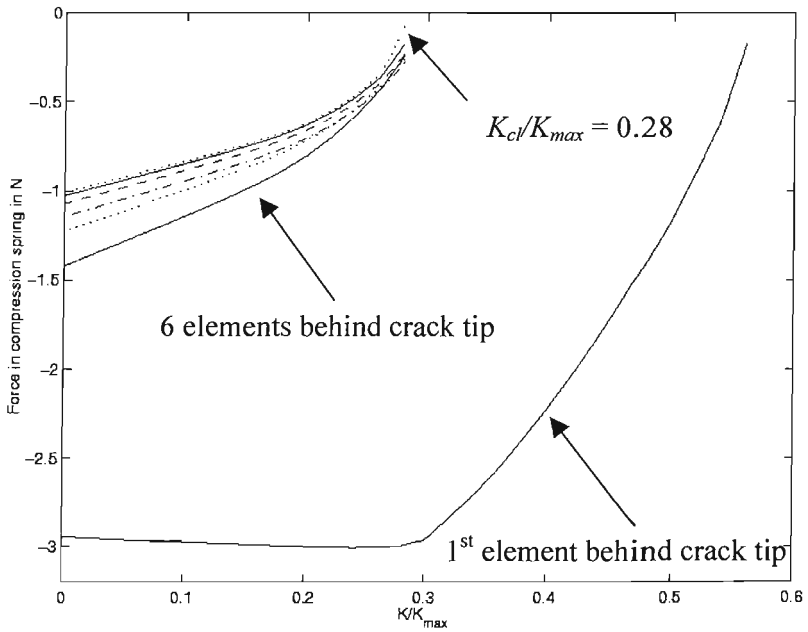

Figure 3.8: Response of compression elements behind the crack tip in plane stress, $\Delta K = 4.6$ Mpa $m^{1/2}$, $R = 0.0$, $\Delta a = 100\mu$ m, LDU algorithm.

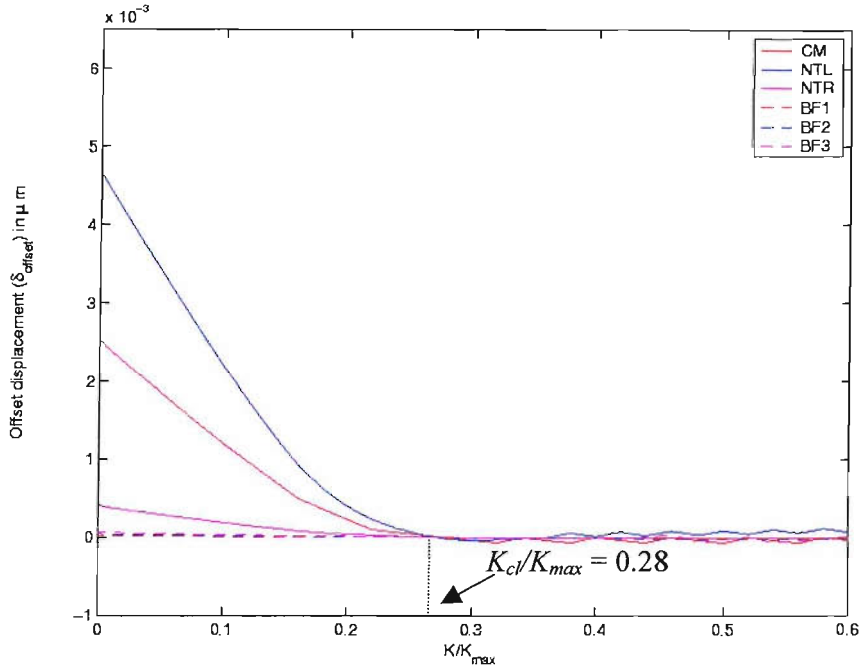

Figure 3.9: Offset compliance plot for plane stress case, $\Delta K = 4.6$ MPa m$^{1/2}$, $R = 0.0$, $\Delta a = 100\mu$ m, LDU algorithm.

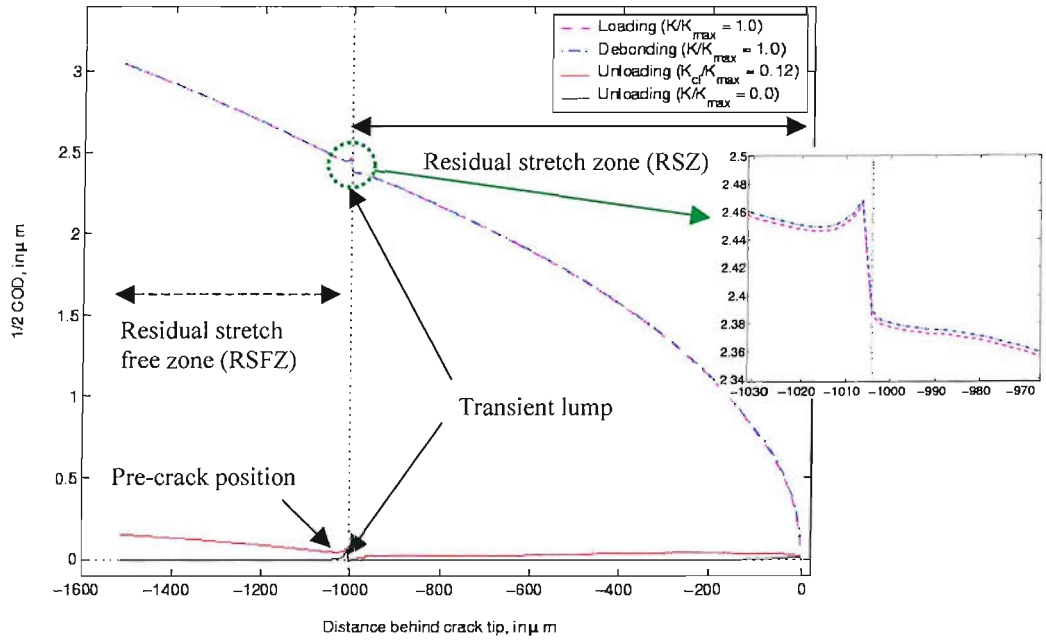

Figure 3.10: Crack profiles, $\Delta a = 1000.8\mu$ m, $\Delta K = 4.60$ MPa m$^{1/2}$, $R = 0.0$, LDULU algorithm, plane strain.

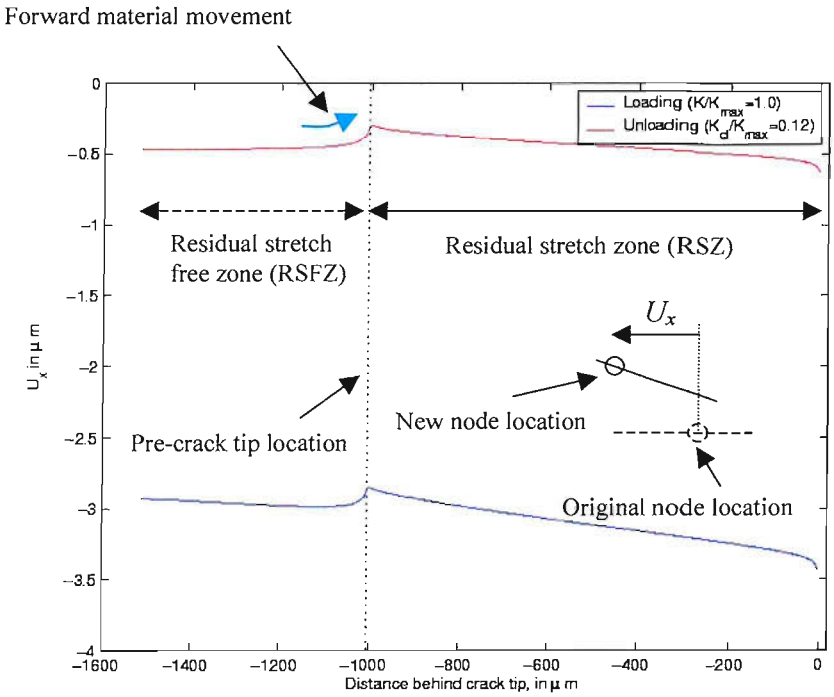

Figure 3.11: Variation of transverse displacements, $\Delta a = 1000.8\mu$m, $\Delta K = 4.60$ MPa m$^{1/2}$, $R = 0.0$, LDULU algorithm, plane strain.

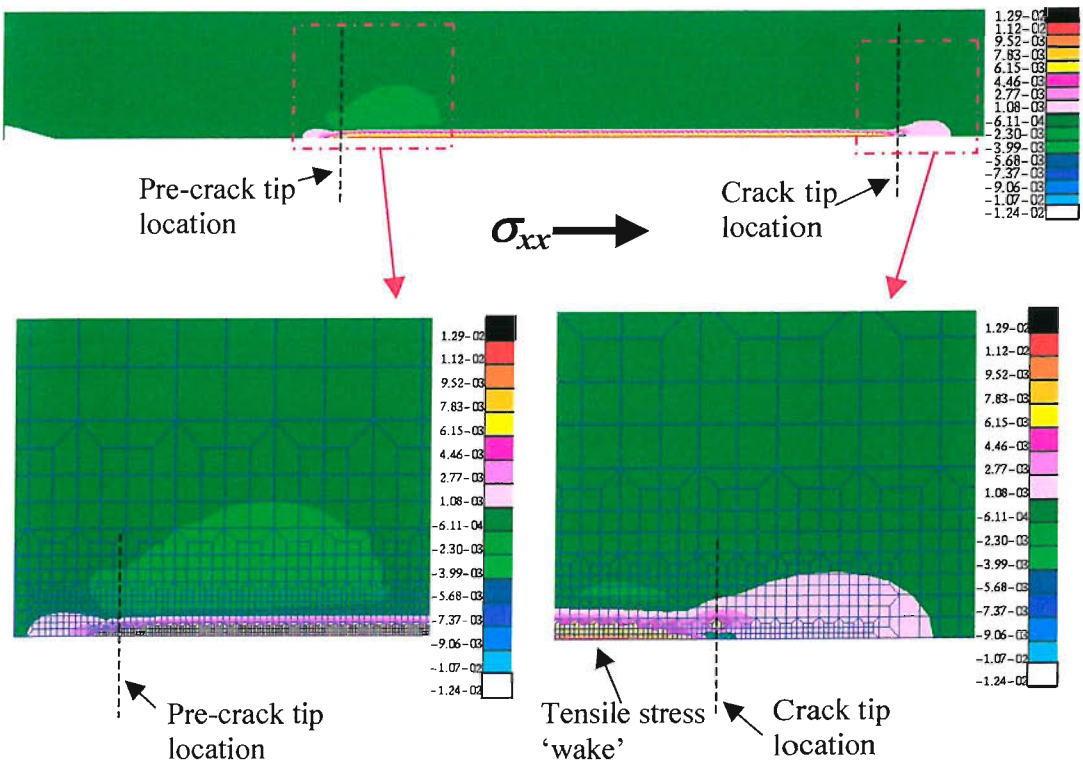

Figure 3.12: σ_{xx} (in N/(mesh unit)^2; 1 mesh unit = 6 μm) variation at minimum load ($\Delta a = 1000.8\mu$m, $\Delta K = 4.60$ MPa m$^{1/2}$, $R = 0.0$, LDULU algorithm, plane strain), highlighting tensile residual stress wake at propagating crack tip.

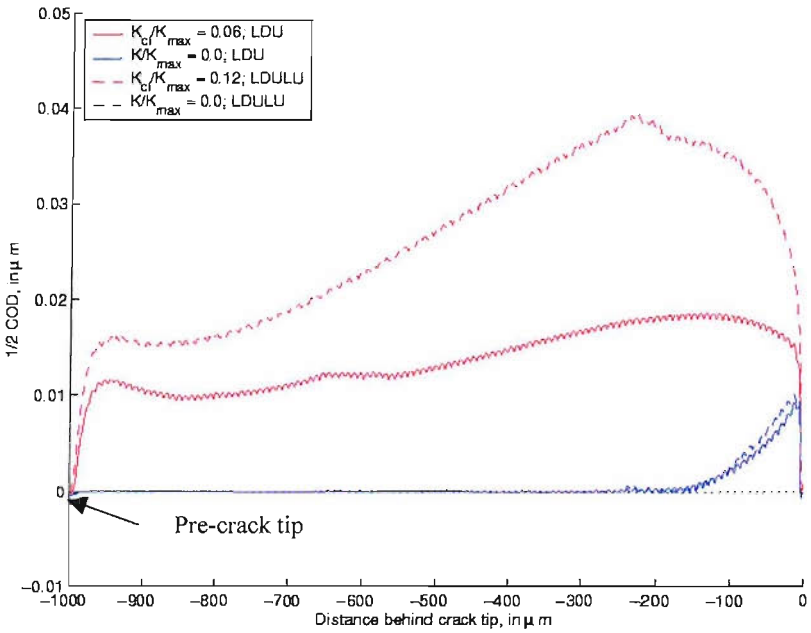

Figure 3.13: Crack profiles due to LDU and LDULU crack propagation algorithms, $\Delta a = 1000.8\mu$m, $\Delta K = 4.60$ MPa m$^{1/2}$, $R = 0.0$, plane strain. Profiles shown for onset of distributed contact/closure and at minimum loading.

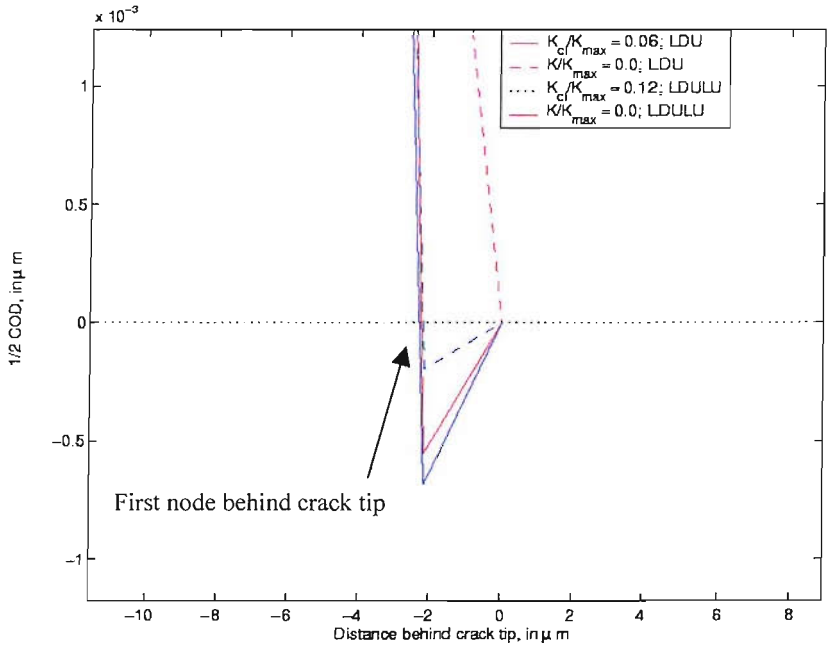

Figure 3.14: Near-tip crack profiles due to LDU and LDULU crack propagation algorithms, $\Delta a = 1000.8\mu$m, $\Delta K = 4.60$ MPa m$^{1/2}$, $R = 0.0$, plane strain. Profiles for conditions shown in Figure 3.13.

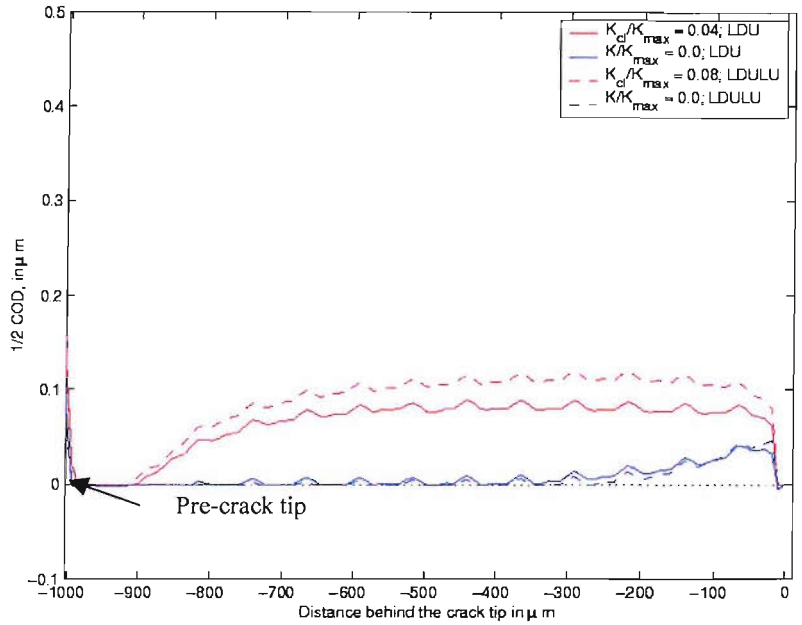

Figure 3.15: Crack profiles due to LDU and LDULU crack propagation algorithms, $\Delta a = 1000.8\mu$m, $\Delta K = 12.0$ MPa m$^{1/2}$, $R = 0.0$, plane strain. Profiles shown for onset of distributed contact/closure and at minimum load.

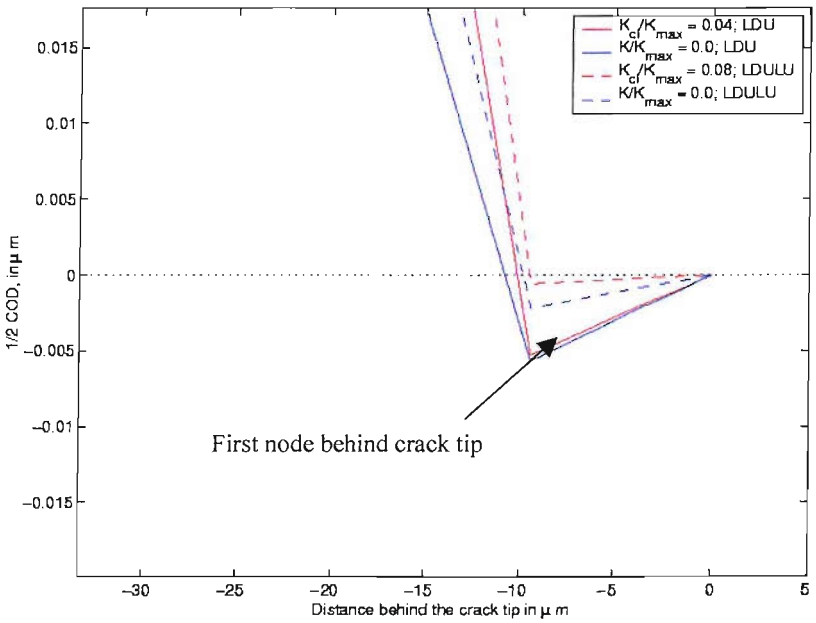

Figure 3.16: Near-tip crack tip profiles due to LDU and LDULU crack propagation algorithms, $\Delta a = 1000.8\mu$m, $\Delta K = 12.0$ MPa m$^{1/2}$, $R = 0.0$, plane strain. Profiles shown for conditions in Figure 3.15.

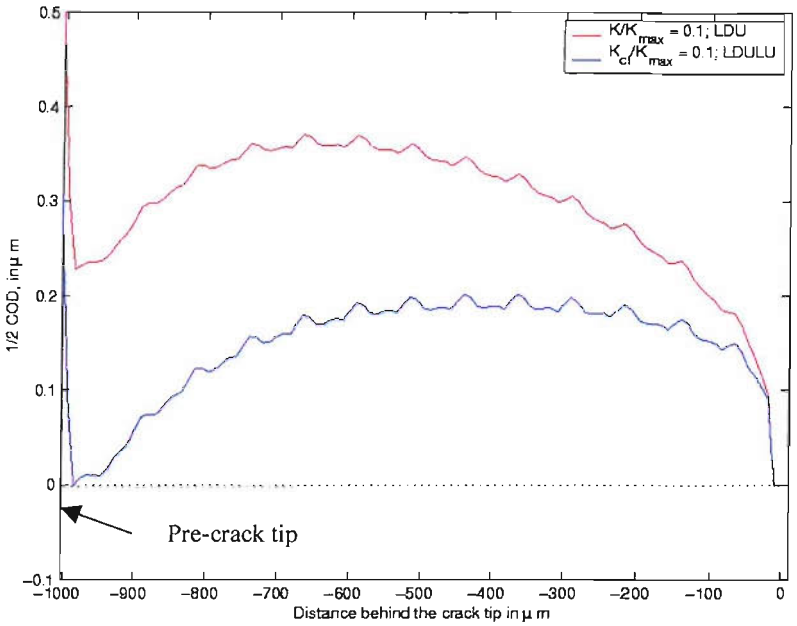

Figure 3.17: Crack profiles due to LDU and LDULU crack propagation algorithms, $\Delta a = 1000.8\mu$m, $\Delta K = 12.0$ MPa m$^{1/2}$, $R = 0.1$, plane strain. Profiles shown for onset of distributed contact/closure and at minimum load.

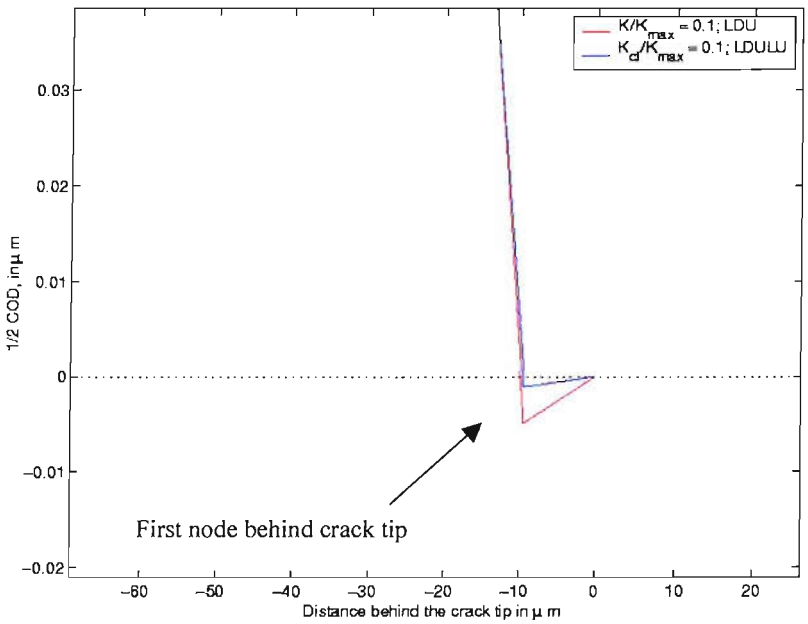

Figure 3.18: Near-tip crack tip profiles due to LDU and LDULU crack propagation algorithms, $\Delta a = 1000.8\mu$m, $\Delta K = 12.0$ MPa m$^{1/2}$, $R = 0.1$, plane strain. Profiles shown for conditions in Figure 3.17.

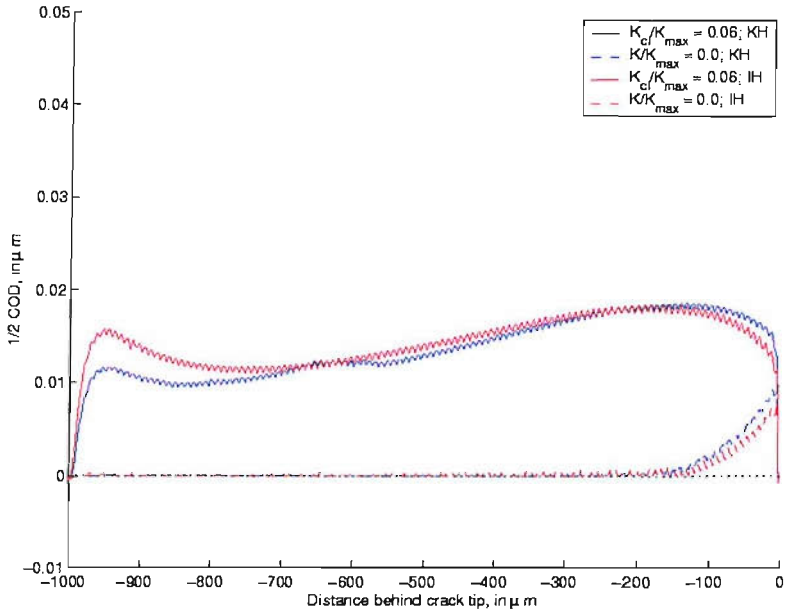

Figure 3.19: Crack profiles for isotropic hardening (IH) and kinematic hardening (KH), $\Delta a = 1000.8\mu$m, $\Delta K = 4.6$ MPa m$^{1/2}$, $R = 0.0$, LDU algorithm, plane strain. Profiles shown for onset of distributed contact/closure and at minimum load.

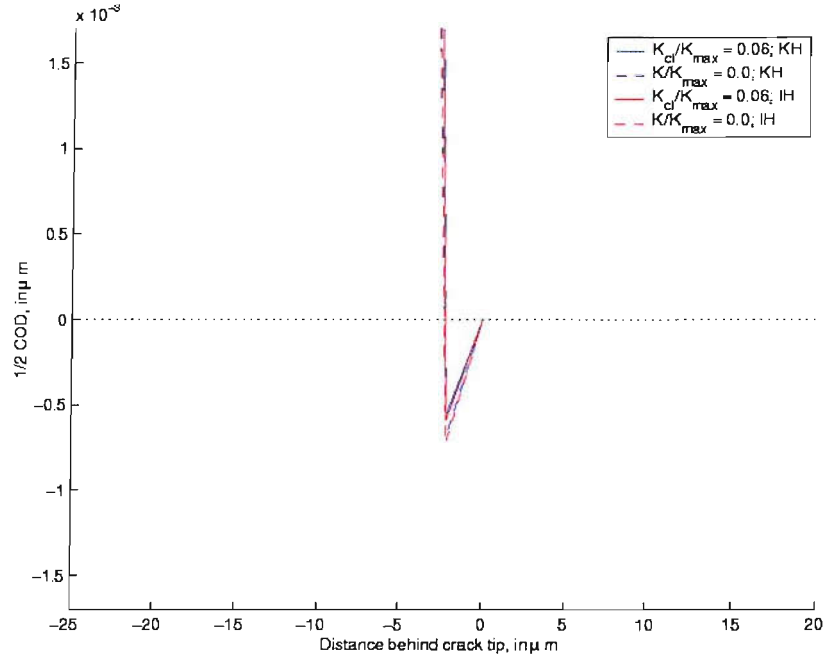

Figure 3.20: Near-tip crack profiles for isotropic hardening (IH) and kinematic hardening (KH), $\Delta a = 1000.8\mu$m, $\Delta K = 4.6$ MPa m$^{1/2}$, $R = 0.0$, LDU algorithm, plane strain. Profiles shown for conditions in Figure 3.19.

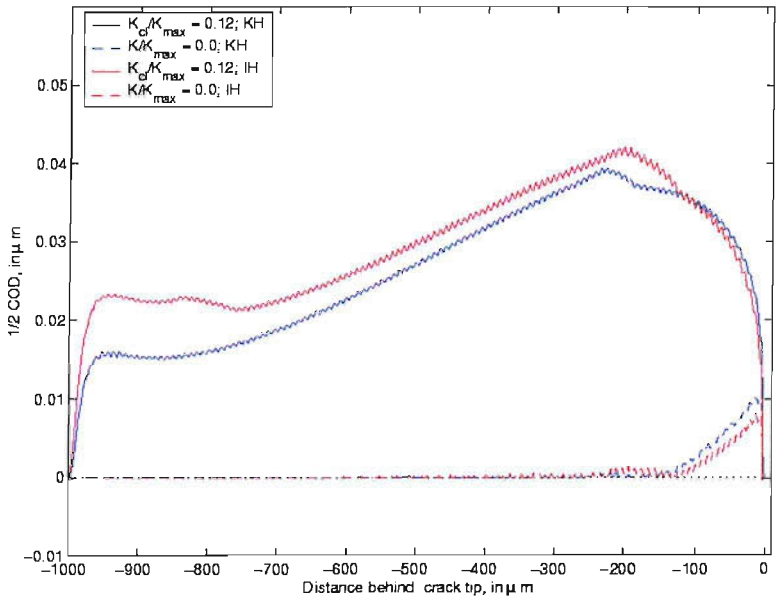

Figure 3.21: Crack profiles for isotropic hardening (IH) and kinematic hardening (KH), $\Delta a = 1000.8\mu$m, $\Delta K = 4.6$ MPa m$^{1/2}$, $R = 0.0$, LDULU algorithm, plane strain. Profiles shown for onset of distributed contact/closure and at minimum load.

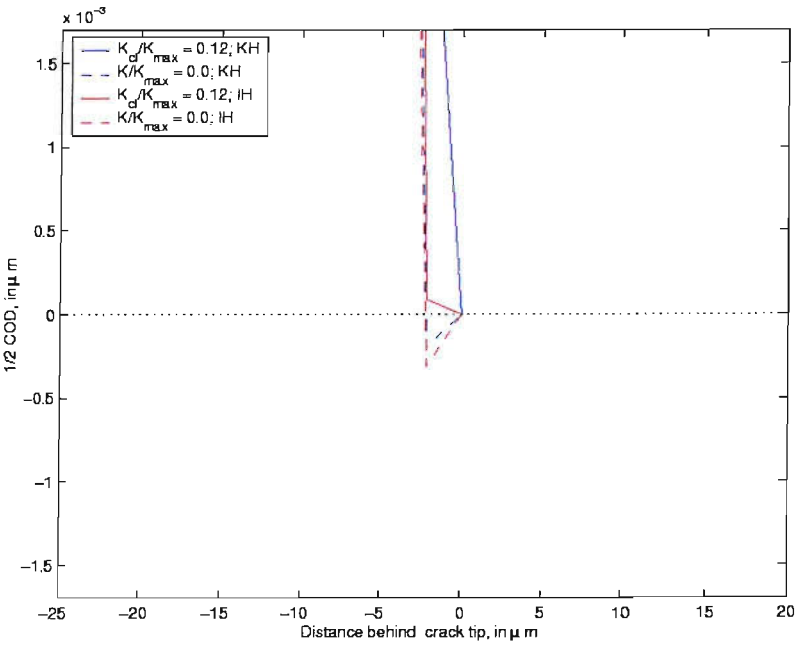

Figure 3.22: Near-tip profiles for isotropic hardening (IH) and kinematic hardening (KH), $\Delta a = 1000.8\mu$m, $\Delta K = 4.6$ MPa m$^{1/2}$, $R = 0.0$, LDULU algorithm, plane strain. Profiles shown for conditions in Figure 3.21.

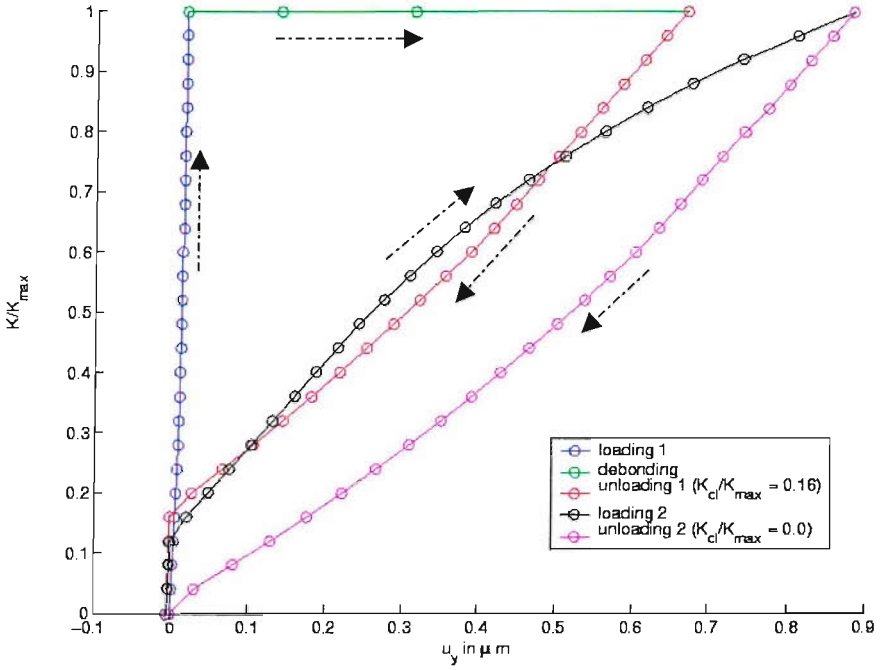

Figure 3.23: U_y variation of pre-crack tip node, $\Delta a = L_e$, $\Delta K = 12.0\,\text{MPa m}^{1/2}$, $R = 0.0$, LDULU algorithm, plane strain. Single tensile spring used to connect crack face nodes.

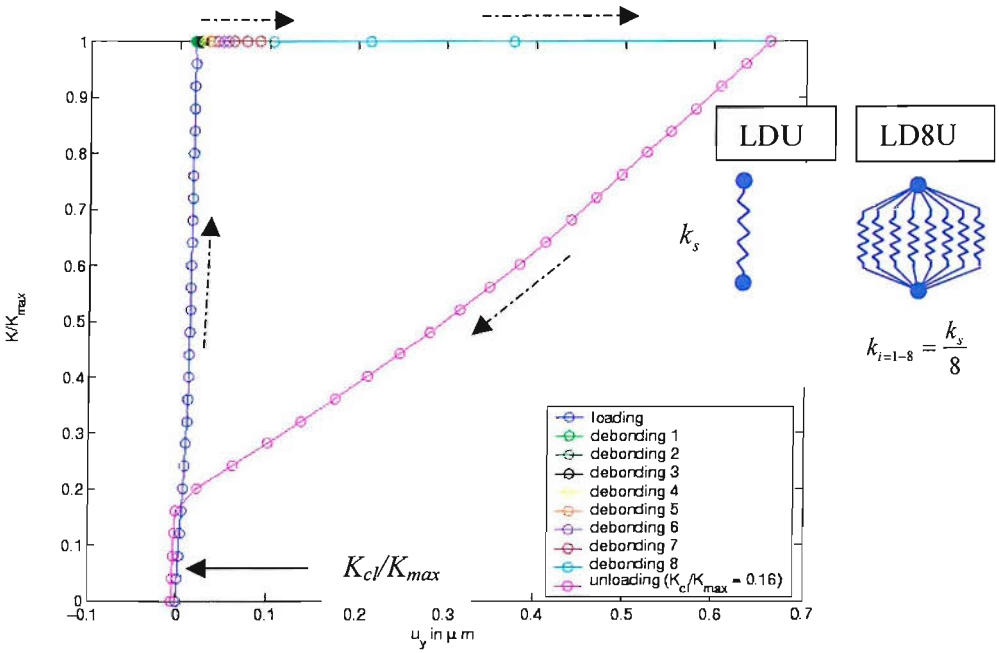

Figure 3.24: U_y variation of pre-crack tip node, $\Delta a = L_e$, $\Delta K = 12.0\,\text{MPa m}^{1/2}$, $R = 0.0$, LDULU algorithm, plane strain. Multiple tensile springs of equal stiffness used to connect crack face nodes for LD8U algorithm.

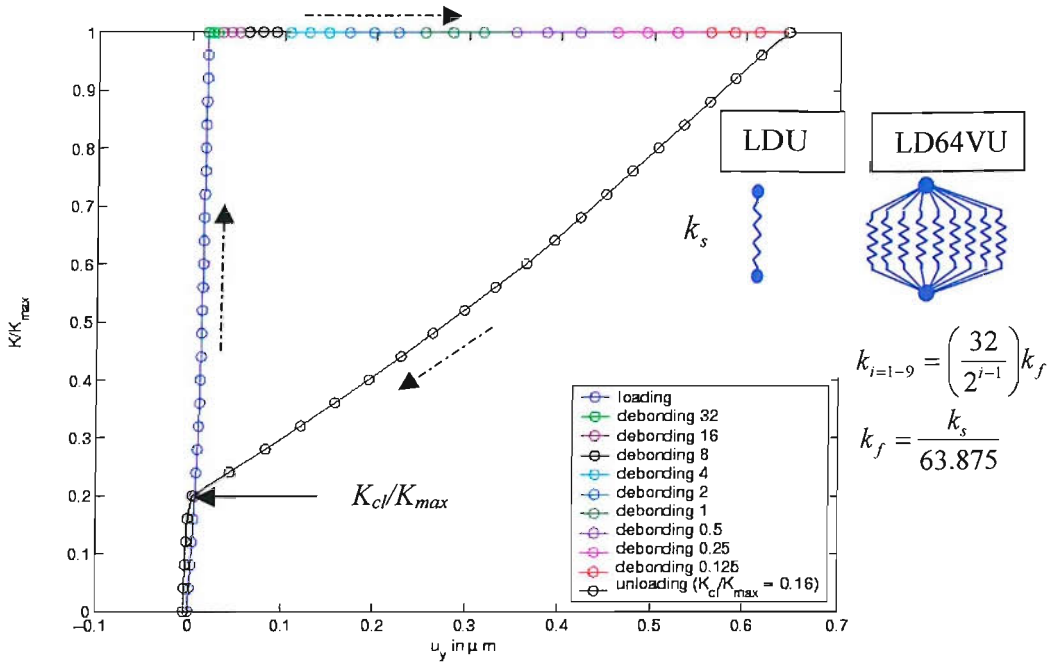

Figure 3.25: U_y variation of pre-crack tip node, $\Delta a = L_e$, $\Delta K = 12.0\,\text{MPa m}^{1/2}$, $R = 0.0$, LDULU algorithm, plane strain. Multiple tensile springs of varying stiffness used to connect crack face nodes for LD64VU algorithm.

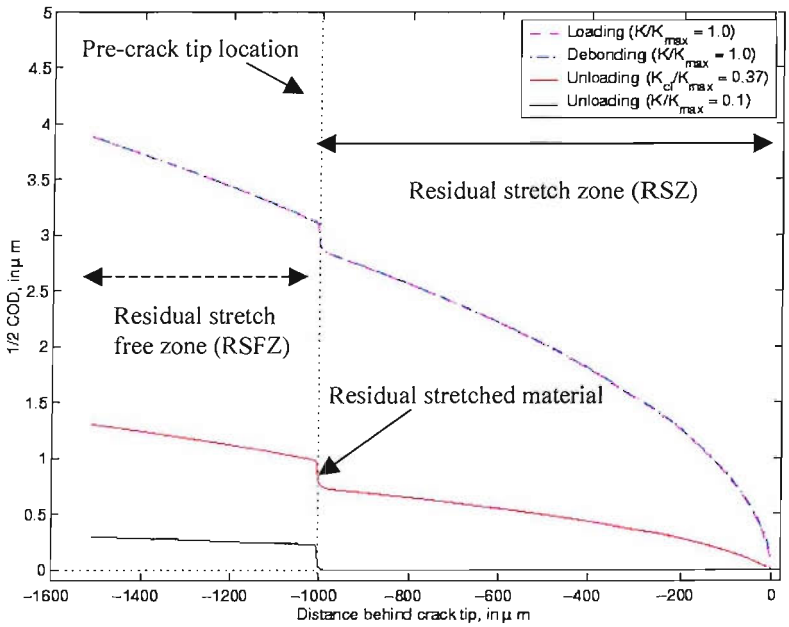

Figure 3.26: Crack profiles, $\Delta a = 1000.8\mu\,\text{m}, \Delta K = 4.60\,\text{MPa m}^{1/2}$, $R = 0.1$, LDULU algorithm, plane stress.

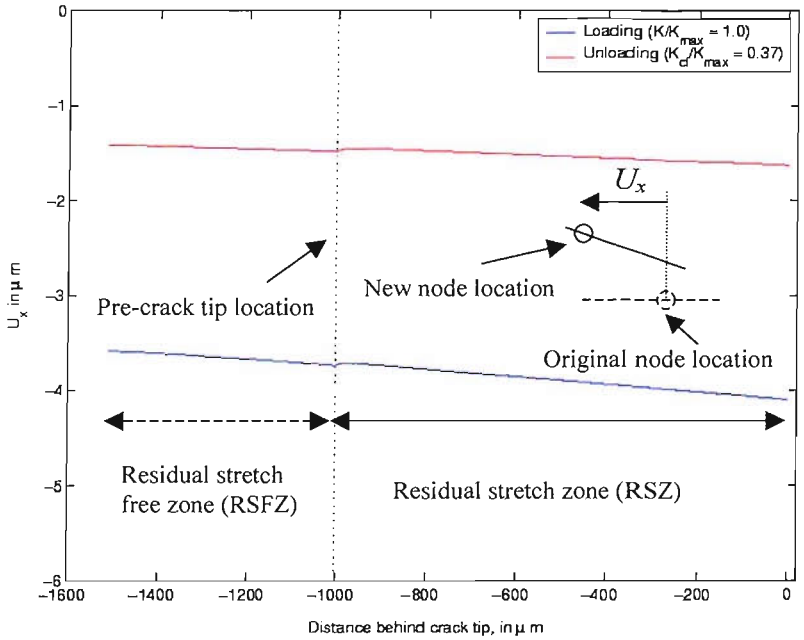

Figure 3.27: Variation of transverse displacement, $\Delta a = 1000.8\mu\text{m}, \Delta K = 4.60\,\text{MPa m}^{1/2}$, $R = 0.1$, LDULU algorithm, plane stress.

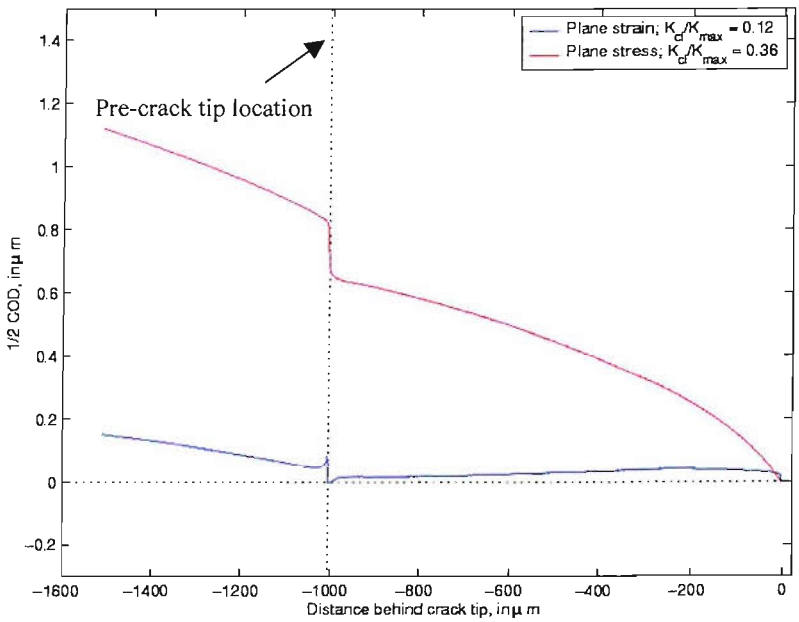

Figure 3.28: Crack profiles due plane stress and plane strain conditions, $\Delta a = 1000.8\mu\text{m}, \Delta K = 4.60\,\text{MPa m}^{1/2}$, $R = 0.0$, LDULU algorithm.

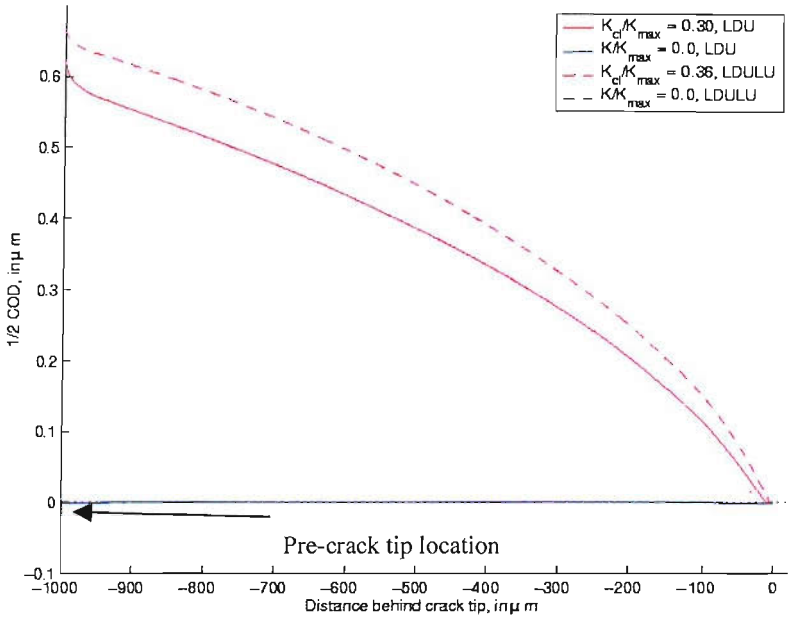

Figure 3.29: Crack tip profiles due to LDU and LDULU crack propagation algorithms, $\Delta a = 1000.8\mu$m, $\Delta K = 4.6$ MPa m$^{1/2}$, $R = 0.0$, plane stress. Profiles shown for onset of distributed contact/closure and at minimum load.

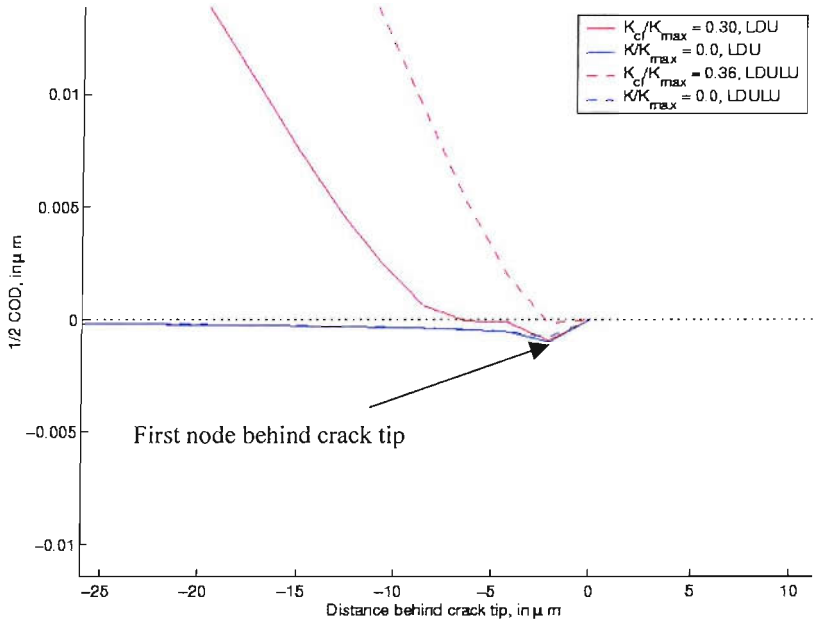

Figure 3.30: Near-tip profiles due to LDU and LDULU crack propagation algorithms, $\Delta a = 1000.8\mu$m, $\Delta K = 4.6$ MPa m$^{1/2}$, $R = 0.0$, plane stress. Profiles shown for conditions in Figure 3.29.

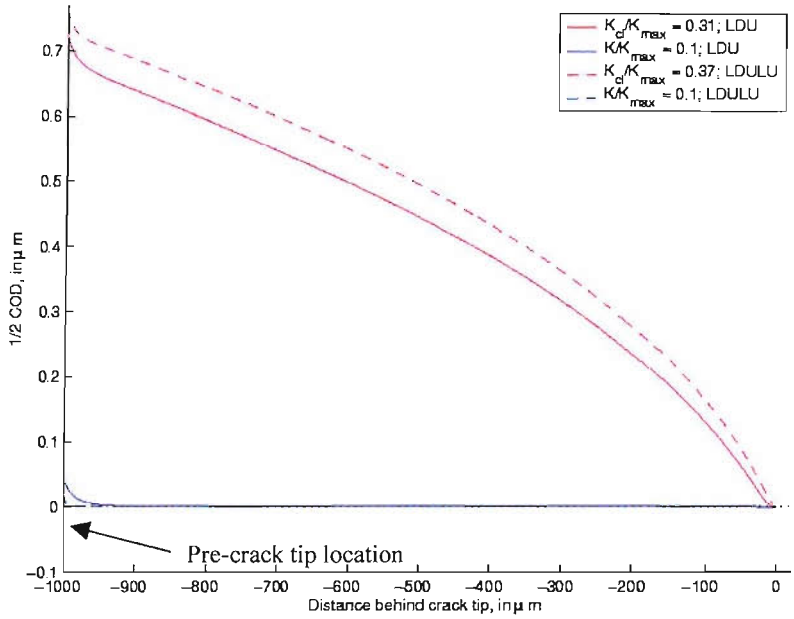

Figure 3.31: Crack profiles due to LDU and LDULU crack propagation algorithms, $\Delta a = 1000.8\mu$m, $\Delta K = 4.6$ MPa m$^{1/2}$, $R = 0.1$, plane stress. Profiles shown for onset of distributed contact/closure and at minimum load.

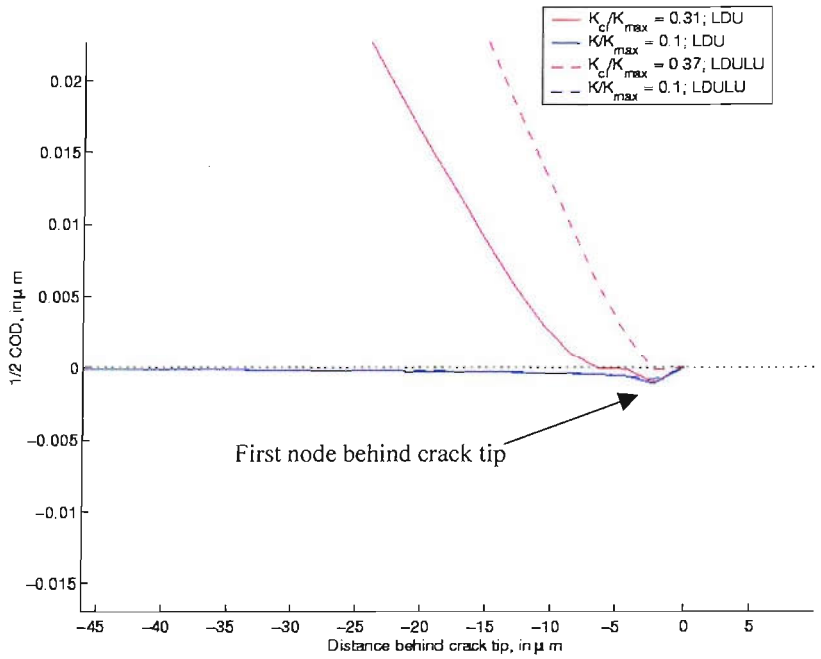

Figure 3.32: Near-tip profiles due to LDU and LDULU crack propagation algorithms, $\Delta a = 1000.8\mu$m, $\Delta K = 4.6$ MPa m$^{1/2}$, $R = 0.1$, plane stress. Profiles shown for conditions in Figure 3.31.

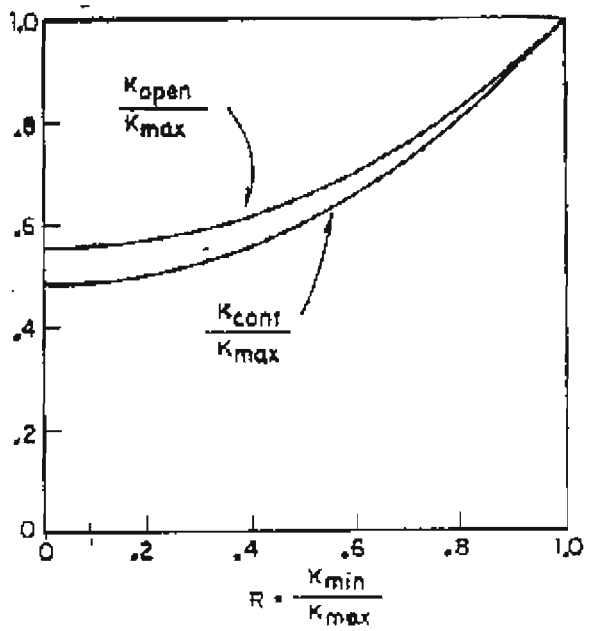

Figure 3.33: Variation of opening and contact load ratios versus K_{min}/K_{max} for plane stress [Budiansky and Hutchinson, 1978].

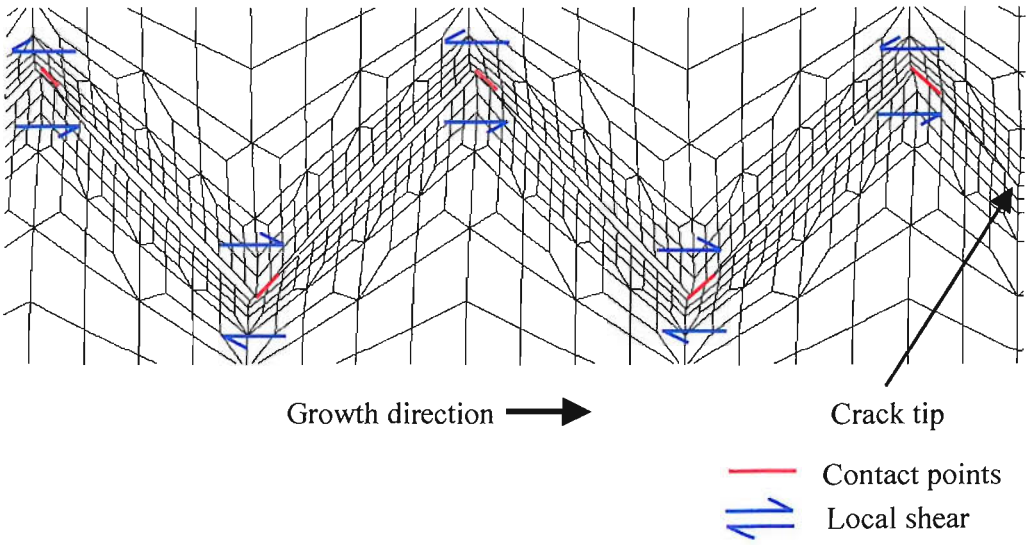

Figure 3.34: Deformed mesh showing contact at the turning points when unloaded fully, L = 150.0 μm, θ = 45°, ΔK = 12.0 MPa $m^{1/2}$, R = 0.1. Displacement magnification x5.

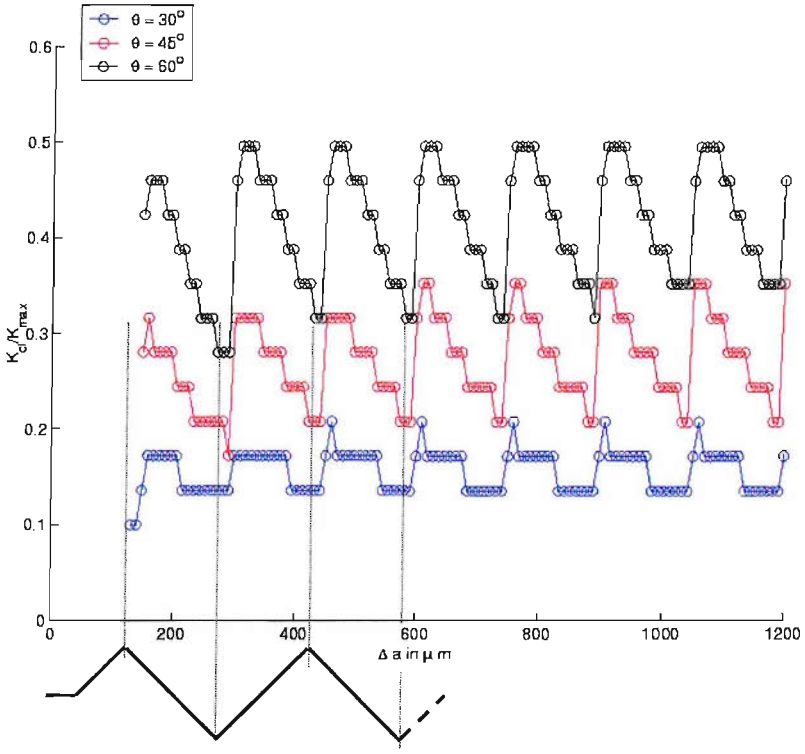

Figure 3.35: Variation of normalised closure SIF with crack length for different deflection angles, $L = 150.0$ μm, $\theta = 45°$, $\Delta K = 12.0$ MPa m$^{1/2}$, $R = 0.1$.

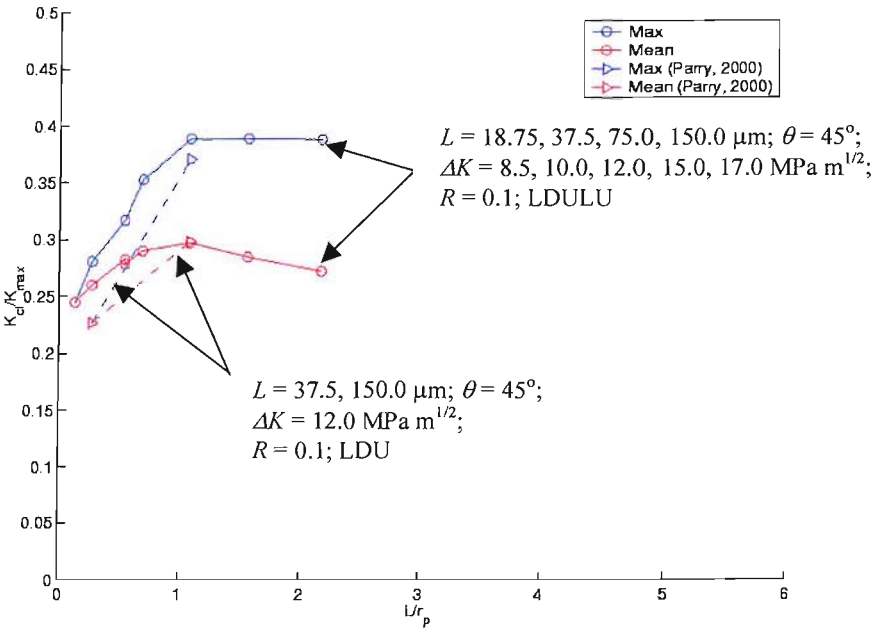

Figure 3.36: Asperity size effect on normalised closure SIF.

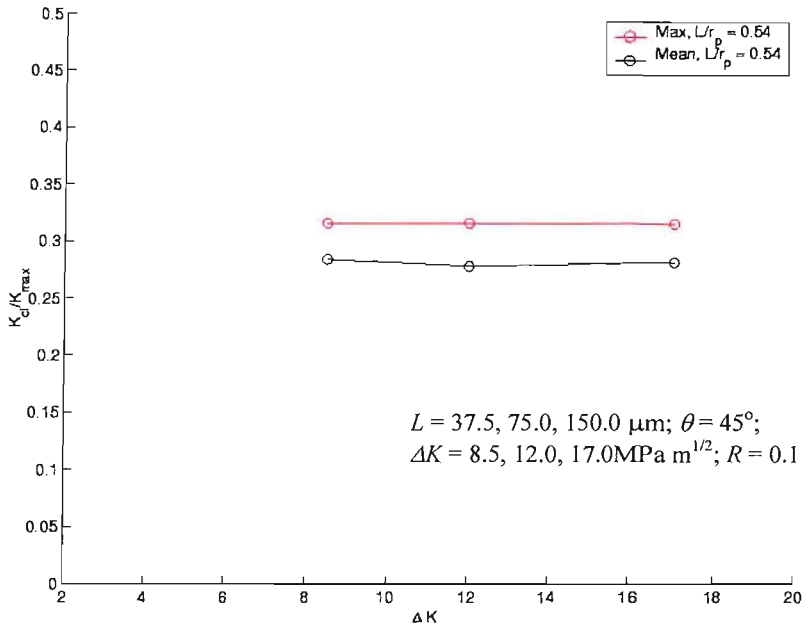

Figure 3.37: Variation of normalised closure SIF with ΔK for a fixed L/r_p ratio.

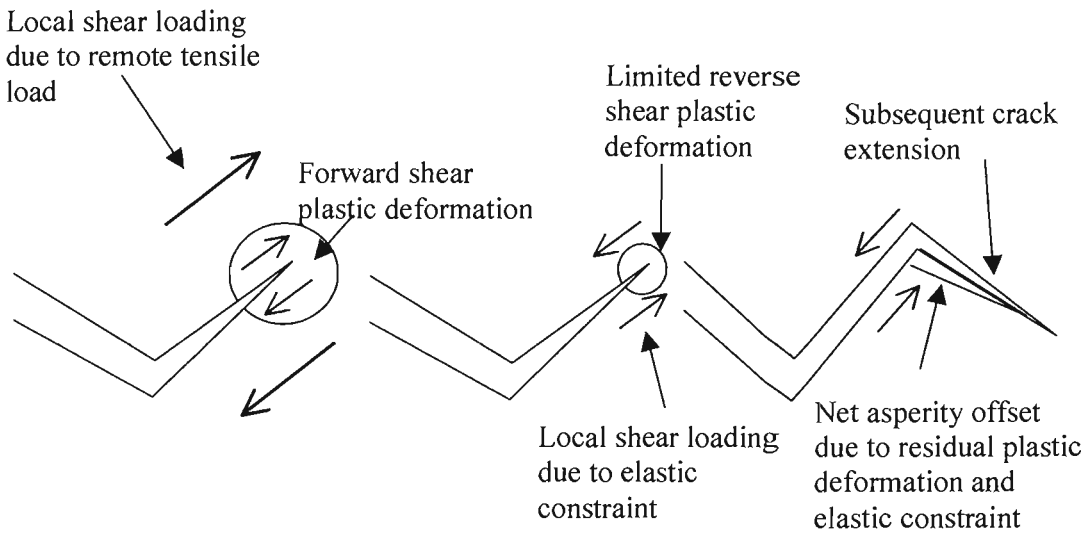

Figure 3.38: Crack closure mechanism due to residual shear deformations in the crack wake [Parry, 2000].

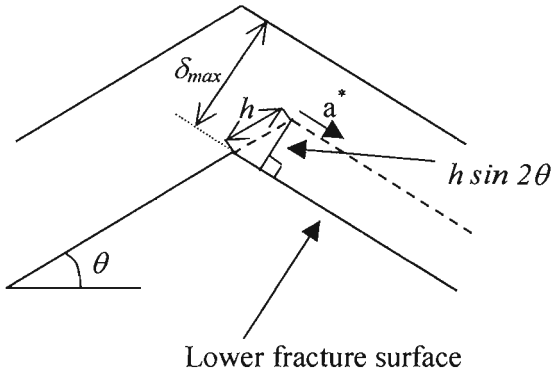

Figure 3.39: Schematic diagram of the geometry of the analytical crack deflection model [Parry, 2000].

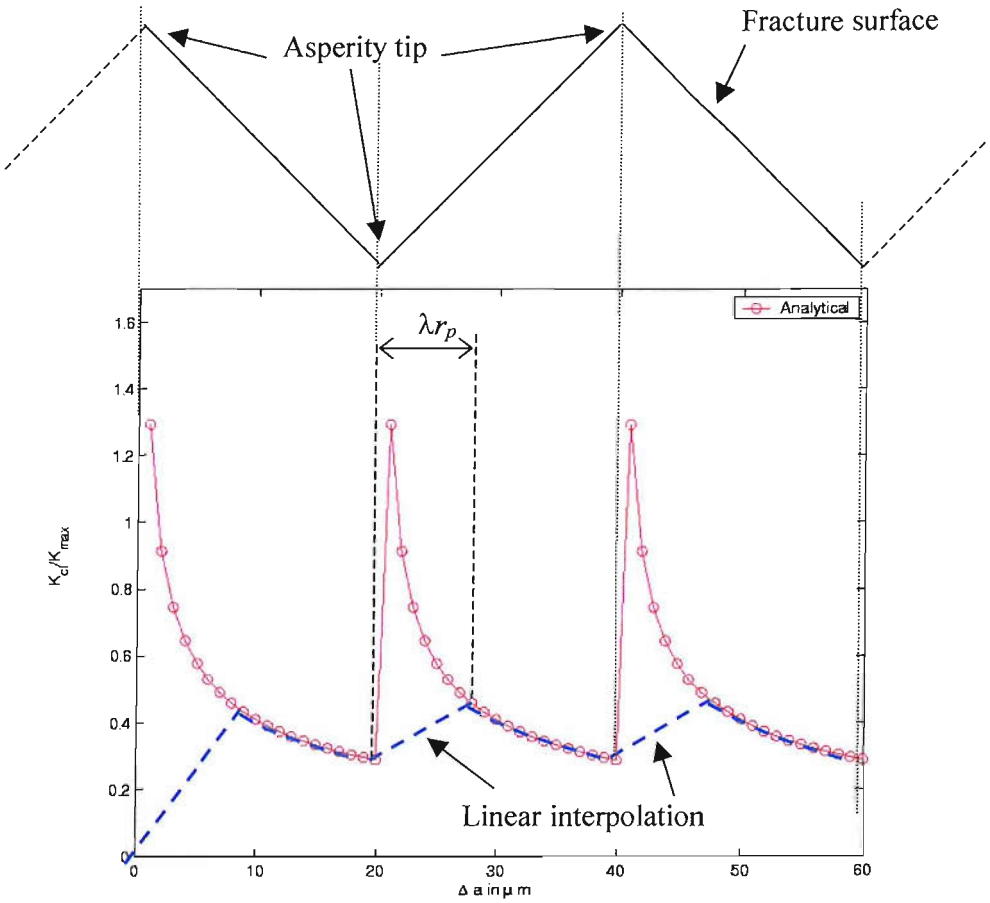

Figure 3.40: Results from the analytical RICC model, $L = 20.0$ μm, $\theta = 45°$, $\Delta K = 4.6$ MPa $m^{1/2}$, $R = 0.0$ (after Parry, 2000).

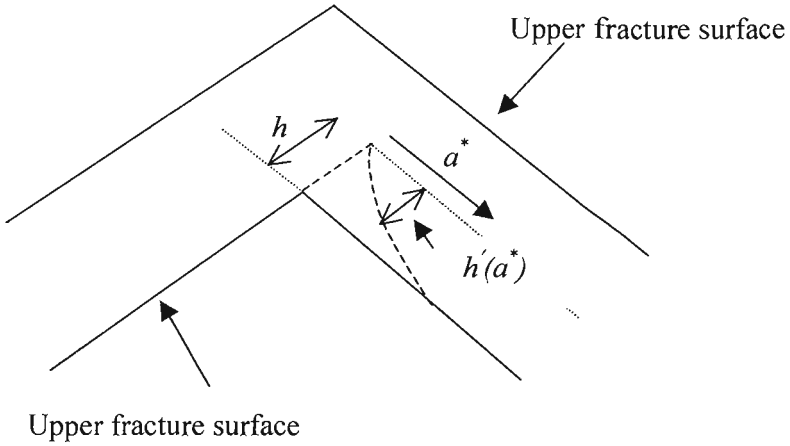

Figure 3.41: Continuous analytical model description of near-tip asperity deformation.

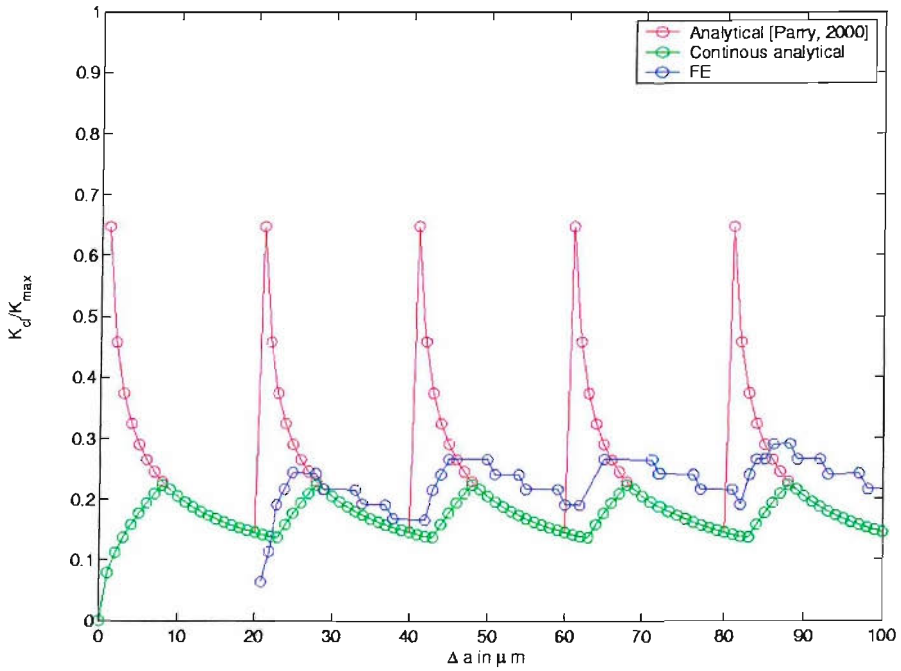

Figure 3.42: Results from continuous closure model, $L = 20.0$ μm, $\theta = 45^{\circ}$, $\Delta K = 4.6$ MPa $m^{1/2}$, $R = 0.0$, $\beta_{II} = 1.0$, $\lambda = 0.5$.

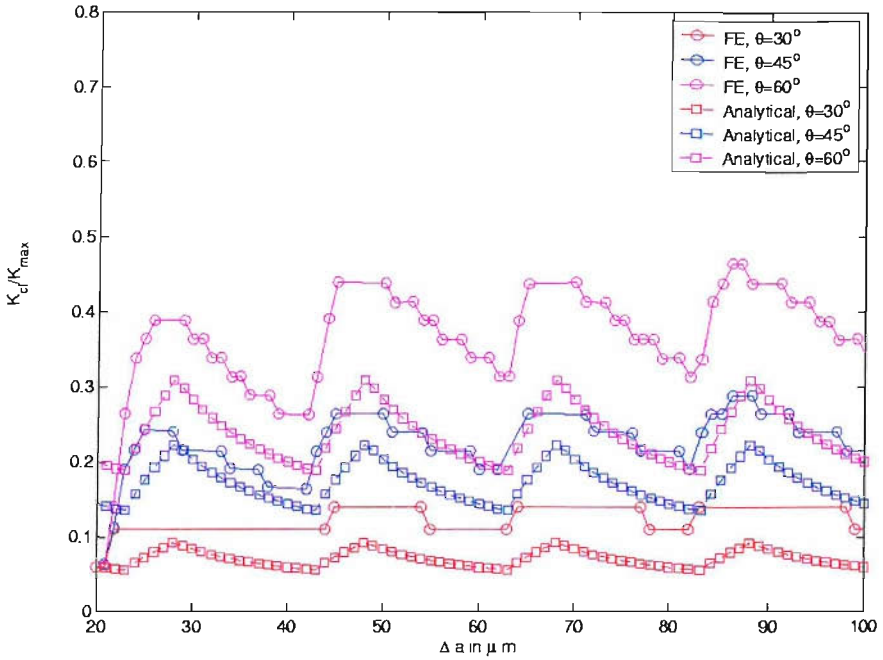

Figure 3.43: FE and analytical model closure level comparison, L = 20.0 μm, ΔK = 4.6 MPa m$^{1/2}$, R = 0.0, β_{II} = 1, λ = 0.5 [Kamp *et al.*, 2004].

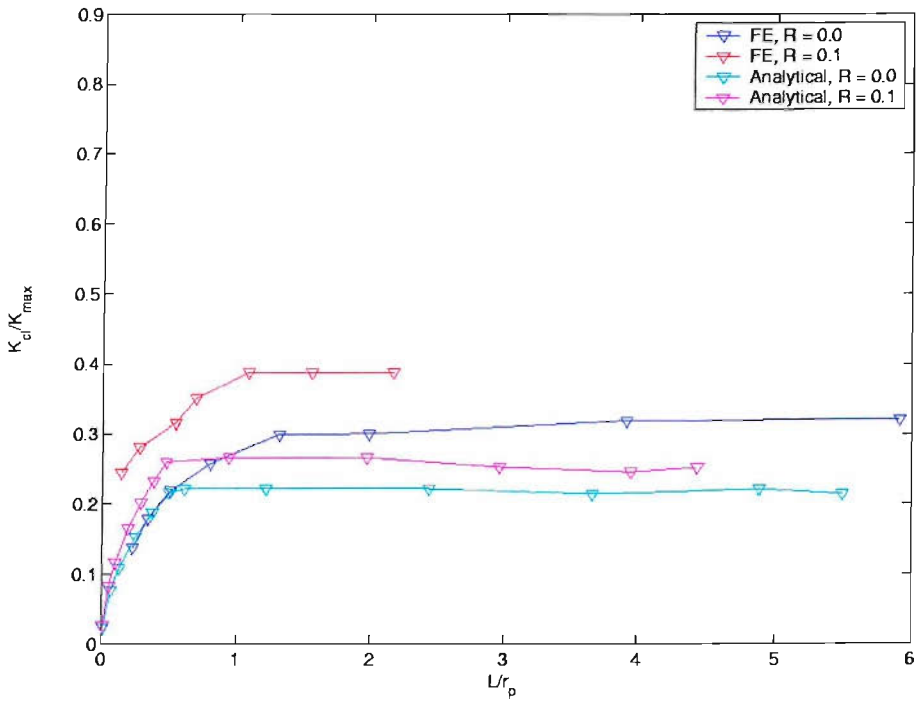

Figure 3.44: Comparison of FE (R = 0.0 corresponds to Parry's [2000] work and R = 0.1 corresponds to the present work) and analytical results (maximum closure levels), β_{II} = 1.0 and λ = 0.5. Plastic zone sizes approximated using Irwin's formula.

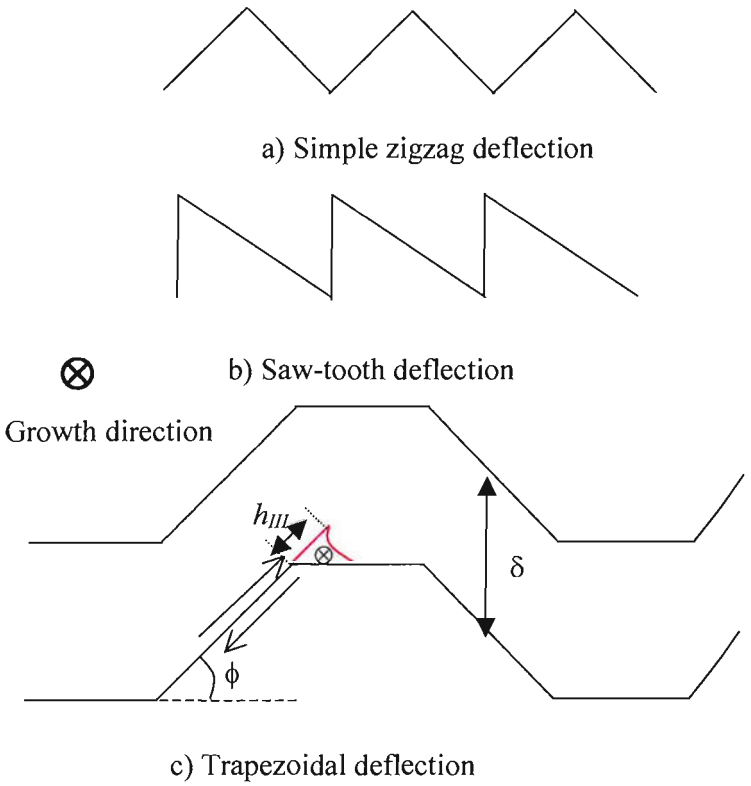

Figure 3.45: Schematic diagram showing various possible crack deflection geometries: a) simple zigzag deflection, b) saw-tooth deflection and c) trapezoidal deflection.

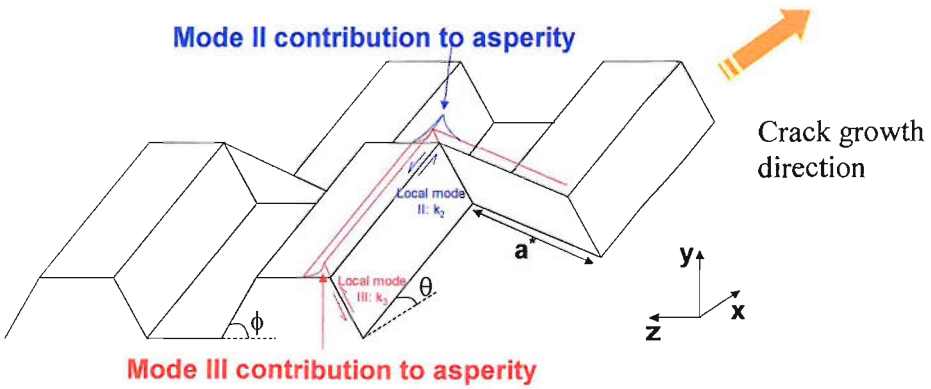

Figure 3.46: Schematic diagram showing 3D crack deflection geometry.

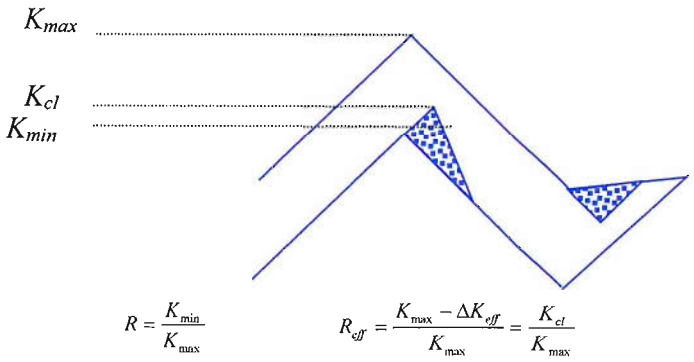

Figure 3.47: Schematic diagram showing K_{max}, K_{cl}, and K_{min} levels for a multiple deflecting crack.

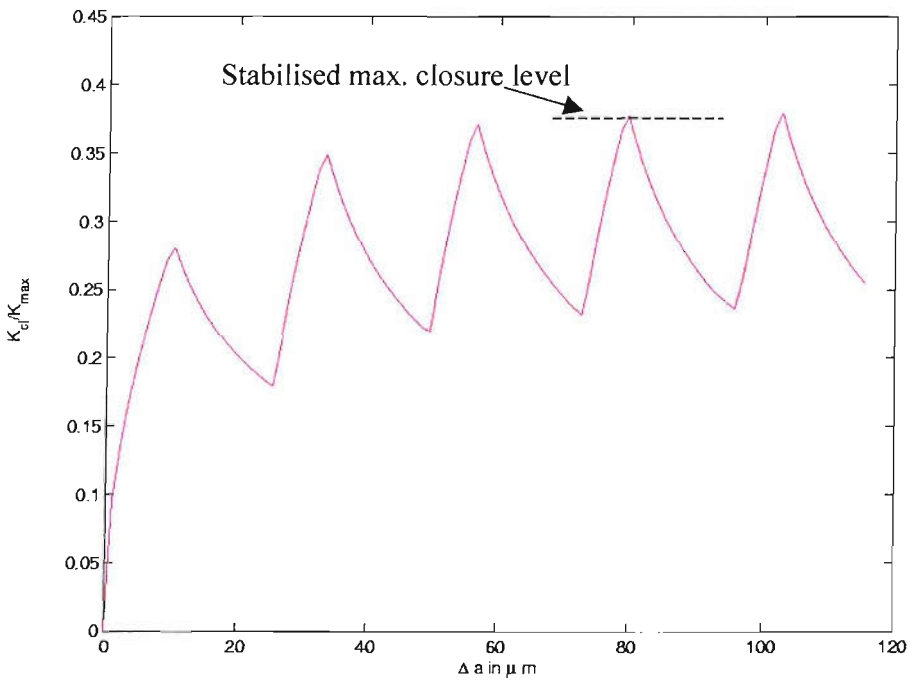

Figure 3.48: Variation of closure levels in the 'iterative' R model with crack length ($\Delta K_{(BL)}$ = 4.6 MPa m$^{1/2}$, R = 0.1, L = 20 μm, $\theta = \phi = 30^{o}$, β = 2.0, λ = 0.5) undergoing multiple deflections.

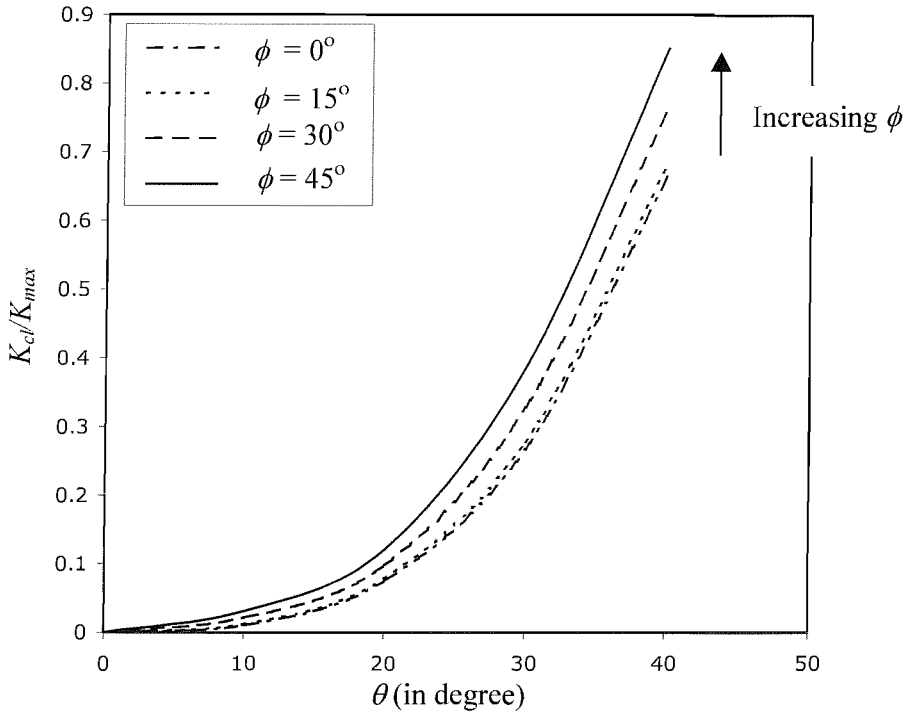

Figure 3.49: Predicted variation of K_{cl}/K_{max} with kink angle (θ) for varying twist angle (ϕ) (ΔK = 6.3 MPa m$^{1/2}$, R = 0.1, σ_y = 370 MPa, L = 50 μm, β = 2, λ = 0.5).

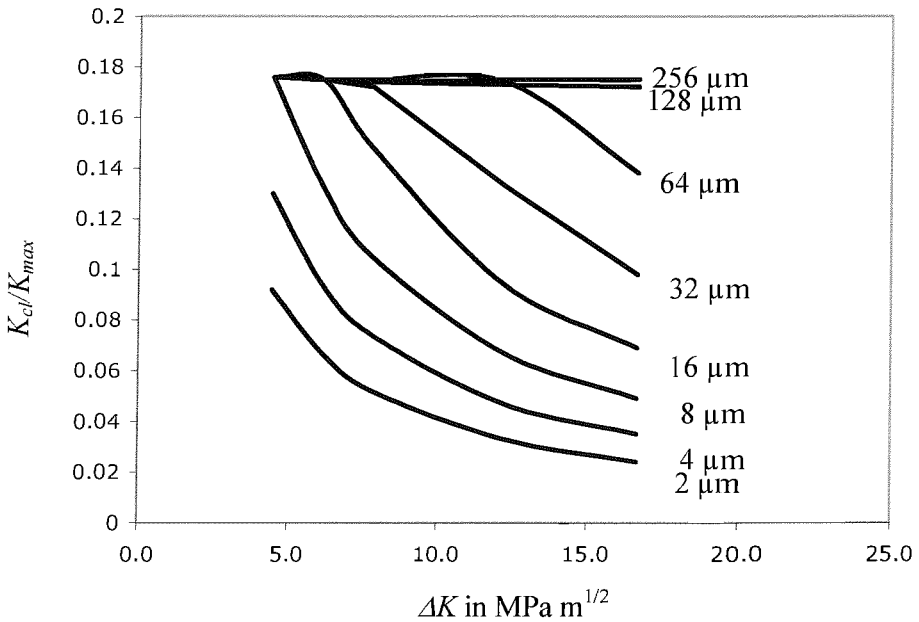

Figure 3.50: Predicted variation of K_{cl}/K_{max} with ΔK for varying L (ΔK = 6.3 MPa m$^{1/2}$, R = 0.1, σ_y = 370 MPa, $\theta = \phi = 25^o$, β = 2, λ = 0.5).

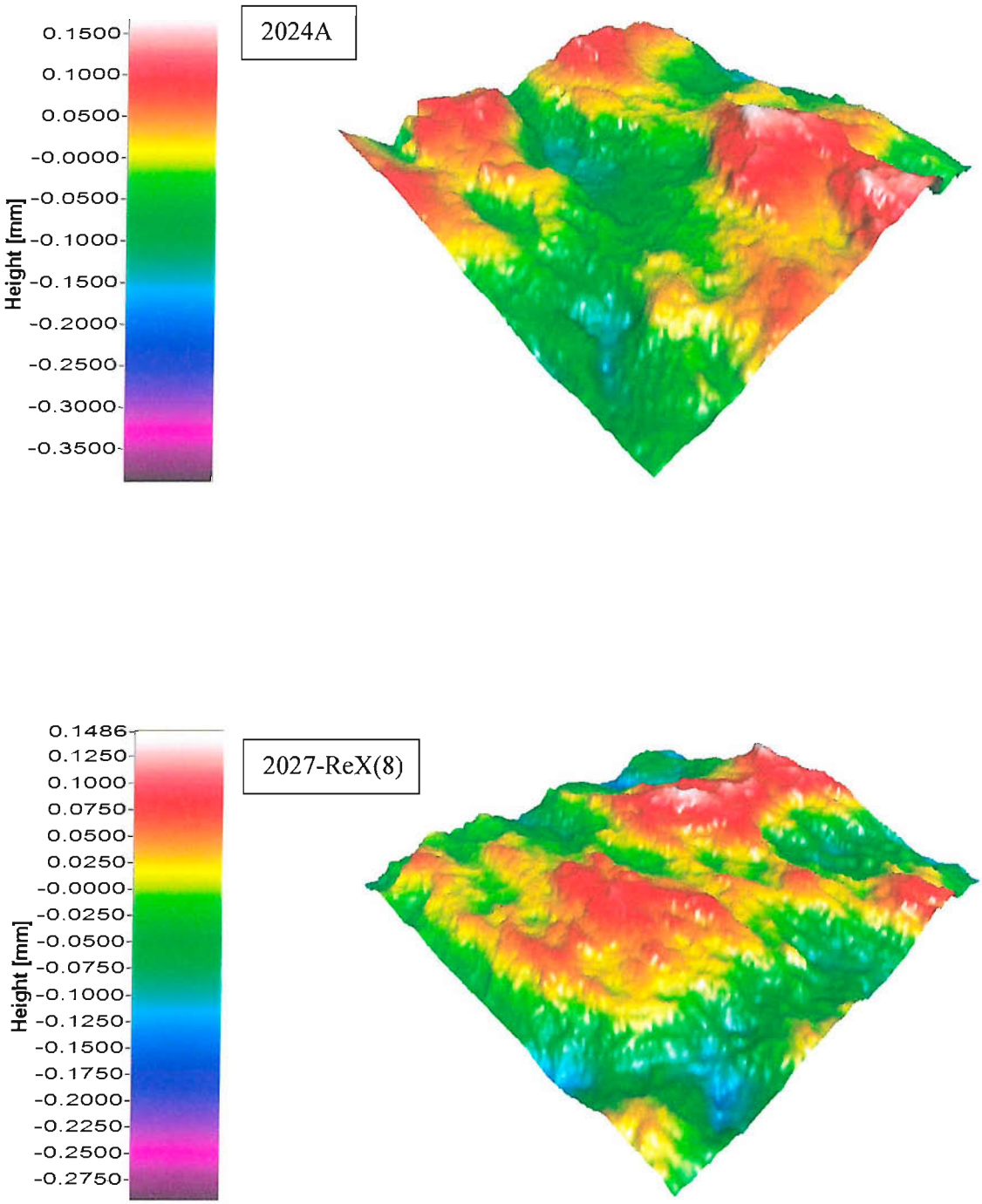

Figure 3.51: 3D fracture surface reconstruction using Taicaan optical profilometry measurements for 2027-ReX(8) for $\Delta K \sim 6.0$ MPa $m^{1/2}$ and $R = 0.1$; 2mm X 2mm surface area: a) 2024A and b) 2027-ReX(8) [Khor, 2004].

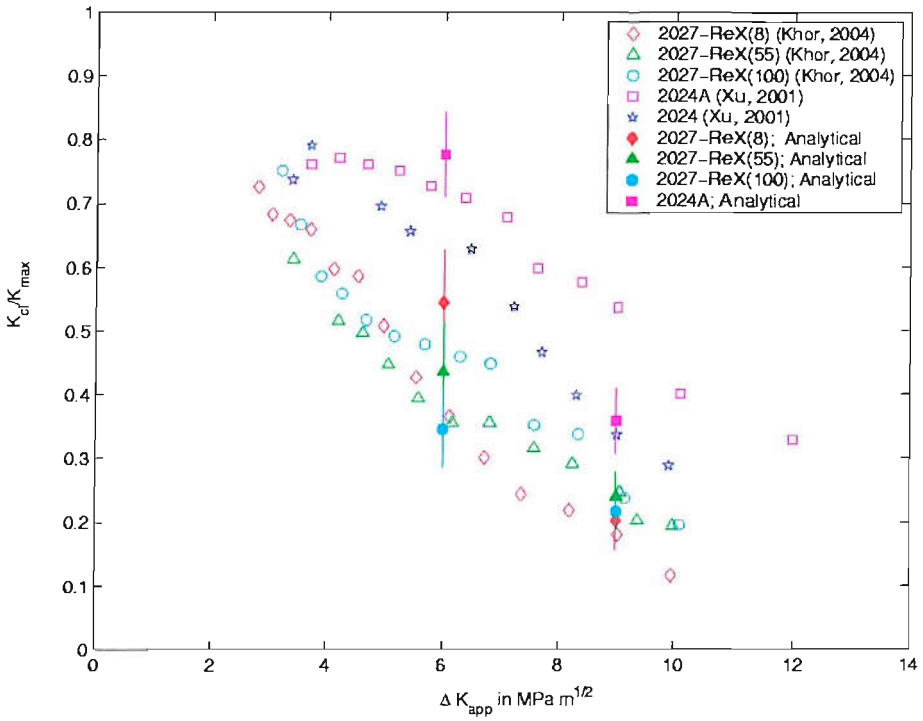

Figure 3.52: Comparison of predicted and experimental variation of K_{cl}/K_{max} with ΔK_{app} ($\beta = 2$, $\lambda = 0.5$).

Chapter 4

4 Modelling of RICC and PICC under single overloads

In the previous chapter, FE and analytical investigations of both PICC and RICC for cracks subjected to CA conditions have been shown. In this chapter, results from FE modelling of PICC and RICC for cracks subjected to single overloads are presented. A single overload analytical model of PICC proposed by Parry has been modified following similar arguments to the RICC model discussed in the previous chapter. An analytical RICC model presented in the previous chapter has further been modified to address single overload effects. Competitive influences of PICC and RICC effects during single overloads are identified in both the FE and simplified analytical models. A modified 'strip yield' analytical model of the 'FASTRAN'-type (Xu, 2001) has also been used to simulate PICC effects during single overloads. Comparisons of models and experimental closure and growth rate studies are presented.

4.1 Introduction

For many fatigue critical structural components, fatigue crack propagation under real service conditions involves variable amplitude loading, rather than constant amplitude conditions. As noted in Chapter 2 irregularities in fatigue loading are well known to result in transient effects in crack growth [e.g. Kumar, 1992, Skorupa, 1998, Ellyin and Wu, 1999, Kermanidis and Pantelakis, 2001]. An understanding of fatigue behaviour under VA load histories may of course help in the design and safe operation of damage tolerant structural components. Whilst various attempts have been made to understand fatigue behaviour under simple single overload transients [e.g. Geary, 1992, Bao and McEvily, 1995, Brown, 1978, Alzos *et al.*, 1976, Ellyin and Wu, 1999, Ward-Close *et al.*, 1989, Venkateshwara Rao and Ritchie, 1988], to the best of our knowledge, Parry [2000] is the first to apply FE methods to investigate potential interaction between crack deflection and simple single load transients. In the present work, the study of Parry is further extended by considering wider ranges of crack geometry, $\Delta K_{(BL)}$ (baseline stress intensity factor range), and overload ratios

(see Table 4.1a and 4.1b). A modified Dugdale-type 'strip yield' analytical model of similar formulation Newman's (1981) '*FASTRAN*' model [Xu, 2001] has also been used to study PICC effects during single overloads. In previous work by Xu [2001] it was reported that strip yield modelling showed better correlation of closure levels under plane stress as compared to plane strain conditions (consistent with the essentially plane stress nature of the strip yield approach), with plane strain apparently demonstrating a more complex synthesis of PICC and RICC effects. Hence in this work, efforts will be directed towards analysing plane strain conditions for both PICC and RICC effects.

- *FE formulation*

Essentially equivalent procedures of FE modelling that have been discussed in Chapter 3 are followed for modelling fatigue crack growth under VA loading conditions. Table 4.1a and 4.1b show the matrix of key model parameters *viz.*, $\Delta K_{(BL)}$ and *%OL* considered for undeflected and deflected crack analyses respectively. $\Delta K_{(BL)}$ values between 4.6 and 17.0 MPa $m^{1/2}$, and L values between 18.75 and 225 μm were used to observe the various effects of L and $\Delta K_{(BL)}$ on the overload transient behaviour of deflected cracks (Table 4.1b). It may be noted that in Parry's [2000] work, only two deflected lengths (*viz.*, L = 37.5 and 150.0 μm) were considered. To identify the effects of RICC on overloads, corresponding undeflected crack models were also studied (i.e. representative of no possible RICC influence). In all the deflected cracks analyses, a common deflection angle of 45° was adopted in the first instance. A load ratio (R) of 0.1 was adopted for both undeflected and deflected analyses. *%OL* levels between 25 and 150 were considered. Overloads were applied at the turning points in deflected crack paths as the relative location of the overload has been seen to have little effect on the crack closure response [Parry, 2000]. A kinematic hardening model with yield strength of 370 MPa, elastic modulus of 70GPa and hardening modulus, $H = 0.07E$ is again chosen for the analyses: Parry [2000] reports only a slight increase in closure levels with decreasing hardening modulus (from $0.07E$ to $0.035E$) consistent with the observed lower crack opening associated with lower hardening modulus. Only plain strain analyses are considered at present as RICC effects are again expected to exert a more important relative influence due to the constraint of

PICC effect. Results from FE analyses are shown first, with comparison then being made with the proposed simple analytical and strip yield models.

4.2. FE modelling of undeflected cracks

4.2.1 Crack profiles

Figure 4.1a, 4.1b and 4.1c shows a typical deformed mesh for an undeflected crack with an overload in its wake ($\Delta K_{(BL)}$ = 12.0 MPa m$^{1/2}$, R = 0.1, $\%OL$ = 100.0) at the onset of closure (K_{cl}/K_{max} = 0.244). Contacts are observed over an area immediately following the OL location, with a wedge (or hump) of residual deformation being observed in the crack profile, see Figure 4.1b, with a wider COD being seen immediately behind the wedge. In the first instance, the wider COD behind the wedge is clearly consistent with crack tip blunting at the OL location due to local increase in K_{max} (on overload application). The presence of a wedge immediately following the overload location is consistent with the findings of Parry [2000] via FE modelling, and those of Fleck [1988], Shin and Hsu [1993] and Brahma *et al.*, [1989] via experimental observations.

4.2.1.1 Effect of overload conditions

Figure 4.2 shows typical FE results for COD profiles associated with overload loading in a crack wake, plotted at the onset of closure, with corresponding COD profiles for CA baseline loading at equivalent load levels ($\Delta K_{(BL)}$ = 12.0 MPa m$^{1/2}$, R = 0.1). The overload was applied when the crack had propagated for about 3.1 $r_{p(BL)}$. The COD profiles were shown after the crack has propagated approximately 31 $r_{p(BL)}$ (or ~5 $r_{p(OL)}$ for 150% OL; where $r_{p(OL)} = \frac{1}{3\pi}\left(\frac{K_{OL}}{\sigma_y}\right)^2$ is the overload plastic zone size based on Irwin's analysis), so that the residual wedge of overload deformation is far enough from the final crack tip to be clearly distinguishable from the steady state growth profiles.

From Figure 4.3 it is convenient to define residual wedge size (h_{rw}) in the overload crack wakes by measuring the wedge height at closure from the wedge-free crack

surfaces, perpendicular to the crack growth direction (shown schematically as the inset diagram of Figure 4.3). As observed in Figure 4.2, there is a clear increase in the size of residual wedge with increasing *%OL*.

From Figure 4.2 it may be seen that the crack closure point appears to be quite straight-forwardly defined by the 'adding' of a wedge of material to the approximate COD profile of the baseline crack. Figure 4.4 shows the variation of normalised residual wedge size, $h_{rw}/r_{p(OL)}$: the normalisation with $r_{p(OL)}$ is made to compare with known experimental results which are conducted at different load levels. It may be seen that the modelled wedge profile extends to a distance of about 2 $r_{p(OL)}$ beyond the OL location. Experimental results from Fleck [1988] ($\Delta K_{(BL)}$ = 25.0 MPa $m^{1/2}$, R = 0.05, σ_y = 352 MPa, sample thickness = 24 mm, BS4360 50B steel) and Shin and Hsu [1993] ($\Delta K_{(BL)}$ = 22.0 MPa $m^{1/2}$, R = 0.1, σ_y=340 MPa, sample thickness = 2mm, AISI 304 steel) are also plotted for comparison. It may be seen that whilst $K_{(BL)}$ conditions are somewhat higher than those associated with Figure 4.3, the yield stresses considered by Fleck and Shih are comparable to that used here. The size of the residual wedge from Fleck's data appears some 40% smaller than the equivalent model data. Shin and Hsu's results shows a wedge size marginally larger than the relevant model prediction, although it should be noted that this experimental result is likely to be close to plane stress conditions, as opposed to the present plane strain conditions. Whilst there is a discrepancy with the present models and the most direct experimental comparison (Fleck's data), it may be seen that the scale of the predicted residual wedge is of the correct order.

As noted in Chapter 3, the incidence of PICC under plane strain conditions is fundamentally contentious, particularly in terms of volume conservation of crack wake material. Crack contact behaviour shown in Figure 4.2 can only arise from plastic deformation, hence it is valuable to consider the deformation patterns involved. Figure 4.5a shows the undeformed mesh near an OL location whilst Figure 4.5b shows the deformed mesh at closure (K_{cl}/K_{max} = 0.388) near the OL location. The meshes are drawn with the overload locations exactly aligned to highlight the mesh deformation about this point. In particular it can be seen that, analogous to the pre-crack closure transients seen in plane strain in Chapter 3, material has moved forward

from behind the overload location, achieving the volume conservation necessary for PICC to occur in plane strain. In the first instance, it is evident that there is both forward and backward material movement in the crack growth plane with respect to the OL location, consistent with the observations of Sehitoglu and Sun [1991] and Riemelmoser and Pippan [1998a] for CA plane strain conditions (discussed in Section 2.3.3.1), although inspection of the crack blunting deformation and residual wedge size suggest that forward deformation is the more significant, consistent with the less constrained nature of the crack wake.

4.2.1.2 Effect of baseline loading level

The effect of varying baseline stress intensity factor range on the COD profiles is shown in Figure 4.6, for $\Delta K_{(BL)}$ = 12, 15 and 17 MPa $m^{1/2}$, R = 0.1 and $\%OL$ = 100. It can be seen that there is an increase in the residual wedge size with increasing $\Delta K_{(BL)}$, consistent with increasing overload plastic zone size. The profiles of the residual wedge sizes are plotted in Figure 4.7, showing an increase in h_{rw} with increasing $\Delta K_{(BL)}$. It may again be seen that wedge essentially extends to a distance of about 2 $r_{p(OL)}$.

4.2.2 Crack Closure

The closure behaviour of FE models of an undeflected crack loaded with 0% and 100% OL ($\Delta K_{(BL)}$ = 12.0 MPa $m^{1/2}$, R = 0.1) is shown in Figure 4.8. The plot shows the variation of U (= $\Delta K_{eff}/\Delta K_{app}$) versus normalised post-overload extension ($\Delta a/r_{p(BL)}$). Results from Parry's work [Parry, 2000] using a LDU crack propagation algorithm are also plotted for comparison. Pre-crack tip closure levels (actually very low, with U ≅ 1) are obtained after the crack has propagated for about 7 $r_{p(BL)}$ for the CA (i.e. 0% OL) loading condition. It may be noted that in Parry's work, baseline closure did not occur for a similar problem, probably due to the lower closure effect associated with LDU algorithm used for crack propagation (discussed in Chapter 3).

It is observed that for the present undeflected cracks under single overloads, contact of the crack faces invariably occurs at the location of the residual wedge that arises at the overload location. This discontinuous closure (due to the overload residual wedge)

enhances the closure such that the baseline closure level is not reached even after the crack has propagated for about 7 $r_{p(OL)}$. Thus for undeflected cracks, post overload closure is essentially dominated by the residual wedge (or 'Wedge Controlled Zone', WCZ). The WCZ starts from the location shortly after the OL location (it may be noted that closure does not take place immediately after the OL is applied: it requires the crack to grow a small distance away from the OL location for the residual wedge to become 'effective'). There is a slight change in the post-overload closure levels evident with changing growth algorithm in Figure 4.8, in line with the effects of LDULU vis-à-vis LDU as discussed in Chapter 3, but overall behaviour seems to agree well using either propagation algorithm. It can be noted that undeflected crack FE models are 'artificial' (c.f. experimental data, as shown in Chapter 3) in exhibiting little baseline closure, (e.g. Xu, 2001). Hence, it is likely that post-overload closure levels would attain the baseline levels sooner than suggested in Figure 4.8.

It can be seen that immediately following the application of an overload, for a distance ~ 0.19 $r_{p(BL)}$ (or ~0.04 $r_{p(OL)}$) no closure was observed; then U drops sharply and attains a minimum value (U_{min}) of 0.40 (for the conditions shown) at a post-overload distance ($a_{umin,}$ is then defined as the distance from the overload location to the U_{min} location, see Figure 4.8) of about ~0.6 $r_{p(BL),}$ or ~0.15 $r_{p(OL)}$. Crack shielding then begins to decrease, with U rising to 0.5 U_{ret} (where $U_{ret} = \frac{U_{BL} - U_{\min}}{2} + U_{\min}$, U_{BL} is the value of U at baseline loading) once the crack has grown through approximately 9 $r_{p(BL),}$ or 2.5 $r_{p(OL)}$ (termed as $a_{uhalf,}$ see Figure 4.8). The behaviour of delayed reduction of U to a minimum value, and then gradual return to a stable value is of course consistent with those identified experimentally in the literature [e.g. Arkema and Schijve, 1976, Geary, 1992, Skorupa, 1999, Fleck, 1988, Shin and Hsu, 1993, Xu, 2001, Borrego *et al.*, 2003, Khor, 2004]. Several mechanisms have been proposed to explain this behaviour (see Chapter 2). Considering crack closure effects, growth must occur into the overload plastic zone (which is about four times the baseline plastic zone, for 100% OL) before the increased residual deformation (resulting from overload application) is able to promote crack surface contact, reducing the effective stress intensity range (ΔK_{eff}).

Fleck [1988], and Sin and Hsu [1993] concluded from their experiments that the primary cause of crack growth retardation in overloads is PICC, specifically the effects of the 'wedges' seen in Figure 4.5. It is noted that crack-tip blunting and residual compressive stress may not play a predominant role but become significant only when PICC is inhibited from occurring (e.g. for R values of 0.65 and above, [Shin and Hsu, 1993]). Studies at high R (e.g. 0.8) by Lang and Marci [1999] found no evidence for crack closure although crack retardation was observed, thereby the authors concluded that post-overload behaviour can be governed by residual compressive stresses in front of the crack tip. McEvily and Yang [1990], Bao and McEvily [1995] and McEvily and Ishihara [2001, 2002] note that the relaxation of residual compressive stresses as the crack moves into the overload plastic zone actually gives rise to the enhanced crack closure levels, leading to the crack growth retardation, hinting that both the processes are closely linked. In some sense it must be noted that PICC and residual stress effects are closely 'equivalent', arising from the same mechanical origin: enhanced residual stresses in the crack tip region immediately ahead of the crack are due to increased tensile residual strains in the plastic zone being constrained by surrounding elastic material. The wedge of deformed material seen in a crack wake when propagation has occurred into the overload plastic zone is simply the relaxation of this constraint by the presence of a free surface (i.e. the propagated crack flanks).

To support the retarding role played by the residual wedge, Shin and Hsu [1993] infiltrated an epoxy resin (which was allowed to harden) into a crack after a constant amplitude crack had stabilised: the intention of the epoxy resin lump being to simulate an overload induced residual wedge. On allowing the crack to continue growing with the attached resin lump, a similar retardation transient in crack growth was observed (as that of an overload induced transient) suggesting the primary role played by the overload induced residual wedge on the retardation behaviour. In another test to assess the underlying role played by the overload induced residual wedge, Trebules *et al,* [1973] made a saw-cut in the crack flank after an overloaded fatigue crack has grown into the overload affected region. It was seen that on resumption of testing the crack growth rate jumped back discontinuously to the pre overload value indicating the key role of the crack wake associated with the overload, consistent with the effect of a residual wedge.

Fleck [1988] further argued the key role of PICC due to discontinuous contact (via an overload induced wedge in the crack wake) in post-overload retardation, noting that: fracture surface damage (in terms of abrasion and oxidation) found immediately ahead of the overload location is much greater than that shown under constant amplitude loading at the same growth rates. Allison [1979] measured the post-overload compressive residual stresses across the crack flanks soon after the crack tip passes into the overload plastic zone. It was observed that residual stress reached a maximum of about two-thirds the compressive yield stress just ahead of the overload point, whereas only a maximum one-third of the compressive yield stress was determined prior to the application of overload (i.e. corresponding to the baseline loading), implying that fracture damage in the crack surface near the overload location might result from the presence of a residual wedge and corresponding compressive stress fields. Similar findings have also been reported by Taira and Tanaka [1979].

The present results certainly indicate that enhanced crack closure can arise from PICC effects in plane strain, where transverse local displacement at the overload point generate a residual wedge in the crack wake. Delayed crack retardation and subsequent re-establishment of baseline growth conditions over distances significantly larger than the overload plastic zone are then explicable in terms of crack contact at the residual wedge.

4.2.2.1 Effect of overload ratio

The effect of overload ratio on crack closure behaviour is shown in Figure 4.9 for OL ratios of 25%, 50%, 75%, 100% and 150% (ΔK = 12.0 MPa $m^{1/2}$, R = 0.1) by plotting U versus normalised crack length ($\Delta a/r_{p(BL)}$). An increase in the U_{min} effect is clearly observed for increasing $\%OL$. The variation of maximum closure levels (or U_{min}) with normalised overload plastic zone size ($r_{p(OL)}/r_{p(BL)}$) is shown in Figure 4.10, where it can be seen that $[K_{cl}/K_{max}]_{max}$ increases with $\%OL$s in a non-linear manner.

Figure 4.11 shows the variation of normalised a_{umin} with normalised overload plastic zone size ($r_{p(OL)}/r_{p(BL)}$). It must be noted that U_{min} occurs over a range of crack lengths

beyond the overload location due to stepwise nature of the FE closure determination, hence an average distance is considered for a_{umin} measurement. Observed $[K_{cl}/K_{max}]_{max}$ values occur within a range of 0.20-0.6 $r_{p(OL)}$ of the overload location, with most of the results for overload conditions of practical interest (50%-150%) falling close to $0.25r_{p(OL)}$. A comparatively high value of a_{umin} (~0.6 $r_{p(OL)}$) for 25% overload may in fact be an artefact of the FE load decrement that could not pick up the fine changes in closure levels (due to relatively smaller residual wedge), see the rather 'flat' transient peak for 25% OL in Figure 4.9.

In Figure 4.9, U approaches to the baseline value at about 5.5 $r_{p(BL)}$ (~ 3.5 $r_{p(OL)}$) for 25% *OL*, however for higher *%OL*s, it appears that even after the crack has propagated for about 8 $r_{p(OL)}$, baseline closure level (U_{BL} = 1, see Figure 4.8) is not reached. In terms of a_{uhalf} it can be observed that there is an approximately linear increase of $a_{uhalf}/r_{p(OL)}$ with $r_{p(OL)}/r_{p(BL)}$, i.e. overload affected distance scales with plastic zone size, see Figure 4.12.

4.2.2.2 Effect of baseline loading level

The effect of varying baseline stress intensity factor range on closure response is shown in Figure 4.13, for 100% OL, and $\Delta K_{(BL)}$ = 12.0, 15.0 and 17 MPa $m^{1/2}$ (R = 0.1). The variation of U is again plotted against normalised crack length ($\Delta a/r_{p(OL)}$). It can be seen that there is a slight increase in the post-overload closure levels with increasing $\Delta K_{(BL)}$. This agrees well with that of Parry's analyses with $\Delta K_{(BL)}$ = 4.0, 8.0 and 12.0 MPa $m^{1/2}$. Figure 4.14 shows the variation of maximum closure levels $[K_{cl}/K_{max}]_{max}$ with $r_{p(OL)}$ for increasing $\Delta K_{(BL)}$. It can be observed that there is limited change in the magnitude of maximum closure levels for the problem considered, although an increase in residual wedge size is seen with increasing in $\Delta K_{(BL)}$ (see Figure 4.6 and 4.7). This may of course be linked to the fact that even though the residual wedge size (due to overload) is increased with increasing $\Delta K_{(BL)}$, post-overload closure level is influenced by the increased crack opening with increased $\Delta K_{(BL)}$. Figure 4.15 shows the variation of normalised a_{umin} ($a_{umin}/r_{p(OL)}$) with $r_{p(OL)}$. It can be observed that the values of $a_{umin}/r_{p(OL)}$ lie within ~0.2-0.35 consistent with most of the results in Figure 4.11.

4.3 Simple analytical modelling of OL effects on undeflected cracks

4.3.1 Model formulation

Given the previous observations of a residual wedge in the crack wake following an overload, the potential for a relatively simple geometrical description on the crack wake contact may be identified, where basic fracture mechanics may provide a first order description of the processes involved. It may be mentioned that this follows from previous analytical models proposed by Parry [2000], with a number of important refinements being developed here. The basic model geometry is described in Figure 4.16. The COD at overload is identified with wedge size due to an overload as the most direct indication of the scale of plastic deformation processes close to the crack tip. Flank displacements for a CA plane strain, through-thickness fatigue crack away from the tip are in the first instance, approximated using an elastic displacement field (after Tada *et al.*, 2000), as given below;

$$u_l = \frac{2K_I\left(1-\nu^2\right)}{E\sqrt{\pi a}}\sqrt{2al-l^2}\,\frac{V}{F} \tag{4.1}$$

where, V and F are the geometry and displacement geometry correction factors, l, the distance behind the crack tip, and a is the half crack width of a center-cracked plate, E is the Young's modulus, ν is the Poission's ratio, and K_I is the mode I stress intensity factor. Here, the difference in the crack flank displacements between an elastic crack and a fatigue crack, which could arise through crack tip plastic blunting and/or through the presence of previously plastically stretched material in the crack wake is neglected. This elastic crack opening is then used as a baseline crack shape to which the overload wedge is 'appended'. The $h_{rw(max)}$ due to the tensile overload is approximated in the first instance as the *residual CTOD* due to the *overload* at the point where the overload is applied;

$$h_{rw(\max)} = \beta_l \frac{1}{2}\left(CTOD_{res(OL)} - CTOD_{res(BL)}\right) \tag{4.2a}$$

where $CTOD_{res(BL)}$ and $CTOD_{res(OL)}$ are the residual crack tip opening displacements for the baseline and overload cycles and are related as;

$$CTOD_{res} = CTOD_{\max} - \Delta CTOD \tag{4.2b}$$

where $CTOD_{max}$ and $\Delta CTOD$ are the maximum and cyclic crack tip opening displacements for the relevant cycle conditions, Equation 4.2a then becomes;

$$= \beta_I \frac{K^2_{\max(BL)}}{8\sigma_y E}\left(\xi^2 + 2R\xi - 2R - 1\right) \tag{4.2c}$$

where $\xi = K_{max(OL)}/K_{max(BL)}$, $R = K_{min}/K_{max(BL)}$ and β_I is a scaling parameter reflecting the approximations in $CTOD$ estimation. In the first instance β_I may be viewed as the mode I scaling parameter arising from $CTOD$ opening (to distinguish from scaling parameter β_{II} which arise from the mode II opening displacement i.e. CTSD, discussed in Section 3.6.2.2). By obtaining the residual wedge size from Equation 4.2a it may then be seen that some compensation is made for baseline plastic deformation, even though the crack opening expression (Equation 4.1) is purely elastic. Closure is said then to occur when;

$$h_{rw(\max)} = u_I \tag{4.3}$$

Thus equating Equation 4.1 and 4.2c, and rearranging, the expression for closure can be written as;

$$\frac{K_{cl}}{K_{\max}} = \beta_I \frac{K_{\max(BL)}\sqrt{\pi a}}{16\sigma_y\left(1-\nu^2\right)\sqrt{2al - l^2}} \frac{F}{V}\left(\xi^2 + 2R\xi - 2R - 1\right) \tag{4.4}$$

From Figure 4.4, maximum height of the residual wedge ($h_{rw(max)}$) was obtained for various OLs (for fixed $\Delta K_{(BL)}$ at 12 MPa $m^{1/2}$). Magnitudes of $h_{rw(max)}/r_{p(OL)}$ from both analytical (using Equation 4.2c) and FE results are compared in Figure 4.17. A reasonably good agreement can be seen between analytical and FE results (β_I is assumed to be 1.0 in the first instance). Variation of $h_{rw(max)}/r_{p(OL)}$ with $\Delta K_{(BL)}$ for 100% OL is shown for both FE (from Figure 4.8) and analytical models in Figure 4.18. It can be seen that the variation of analytical $h_{rw(max)}/r_{p(OL)}$ is independent of $\Delta K_{(BL)}$ for a particular $\%OL$, however there is a variation rise of ~ 20% in the FE results for $h_{rw(max)}/r_{p(OL)}$ for the available $\Delta K_{(BL)}$ conditions.

As it is described above, $h_{rw(max)}$ is allowed to act in the crack wake in terms of closure as soon as the crack tip passes across the OL location, which results in a closure singularity near the OL location, much like the near-asperity tip behaviour that in the CA-RICC model presented in Chapter 3. In order to deal with this unrealistic situation

near the OL location, a residual wedge profile has been identified in the first instance (Figure 4.19). Here, the residual wedge height h'_{rw} effectively acting behind the crack tip is assumed to be a function of a^* (distance from the OL location) normalised by $\lambda r_{p(OL)}$ for $a^* < \lambda r_{p(OL)}$. The expression of h'_{rw} takes the form,

$$h'_{rw} = h'_{rw}(a^*) = h_{rw(\max)}\left(\frac{a^*}{\lambda r_{p(OL)}}\right)^{\beta'} \qquad \text{for } a^* < \lambda r_{p(OL)} \tag{4.5a}$$

$$h'_{rw} = h_{rw(\max)} \qquad \text{for } a^* \geq \lambda r_{p(OL)} \tag{4.5b}$$

where β' is an empirical factor that may be determined by FE or experimentally. In the first instance β' is arbitrarily considered to be 1, i.e. a simple linear interpolation is adopted to represent the effective residual wedge influence at small a^* values, in a manner directly equivalent to that described for the CA-RICC analytical model.

4.3.2 Results

Figure 4.20 shows a typical comparison of FE and analytical closure results for ($\Delta K_{(BL)}$ = 12.0 MPa m$^{1/2}$, R = 0.1, $\%OL$ = 100 and λ = 0.5: - see below for consideration of λ values). It can be observed that the analytical model predicts reasonably well the peak closure level of the FE model although it may be seen that the length of overload transient effect is under-predicted to some extent (by about 30% in terms of a_{uhalf}). With the modification in residual wedge profile (Equation 4.5), the singularity in closure levels observed in the original model [Parry, 2000] near the OL location is avoided giving a more 'realistic' representation of closure behaviour.

The variation of predicted analytical closure levels are compared with FE predictions in Figure 4.21 for $\%OL$ = 25, 50, 75, 100 and 150, using a λ of 0.5. It can be seen that peak closure levels are in close accord with the FE results. For $\Delta a/r_{p(OL)} > 0.5$, the rising trend of U is well predicted for all the OLs considered, although a slightly shorter analytical transient is generally evident. The sensitivity of peak closure level predictions to λ in the analytical model is presented in Figure 4.22 for λ = 0.2, 0.5 and

0.7. It can be observed that for a λ of 0.2, the models under-predicts FE results, whilst a λ of 0.7 over-predicts the FE results, with $\lambda = 0.5$ giving a good general agreement with the FE values.

In Figure 4.23 the analytical predictions are compared with FE results for 100% OL for a baseline stress intensity range of 12, 15 and 17 MPa $m^{1/2}$. It can be seen that there is a mild dependence of analytical post peak closure ($\lambda = 0.5$) levels on $\Delta K_{(BL)}$ in the FE results, whilst the analytical model showed no dependence of peak closure levels on $\Delta K_{(BL)}$. The sensitivity of λ in predicting peak closure levels is again checked for values of 0.2, 0.5, and 0.7 in Figure 4.24: it is observed that there is again good agreement between FE and analytical results for $\lambda = 0.5$. Although the dependence of closure transient length on $\Delta K_{(BL)}$ for the FE models is not predicted by the analytical method, peak post OL closure is reasonably well captured by $\lambda = 0.5$.

Figure 4.25 compares FE and analytical predictions of $a_{umin}/r_{p(OL)}$ with $r_{p(OL)}/r_{p(BL)}$ for varying *%OL* ($\Delta K_{(BL)}$ = 12.0 MPa $m^{1/2}$, $R = 0.1$) for λ values of 0.2, 0.5, and 0.7. It can be seen that for λ values of 0.2, analytical results are closest to the FE results. It may be seen that whilst there is evidently some conflict in λ values required to 'capture' closure transient length and magnitude (see Figure 4.22 and 4.24), the present model provides a remarkably good approximation of the FE model behaviour given the simplicity of the wedge model (see Figure 4.21).

Having identified closure behaviour with a notional wedge shape and size, it is of course interesting to compare the effective OL wedge shape 'required' by the analytical model to achieve comparable closure levels to the FE models (i.e. $\lambda \cong 0.5$), and the wedge shape indicated by the FE models. Such a comparison is shown for a 100% OL in Figure 4.26. If post overload closure levels are assumed to be controlled by the effective height of wedge material acting behind the current crack tip (i.e. as in the analytical model), it may be seen that actual crack closure level predictions in the FE models rise more rapidly than expected (i.e. the FE OL wedge drops off more gently than that of the analytical model). This may particularly be seen out to a normalised crack extension distance of $\sim 0.2 r_{p(OL)}$, corresponding to the location of maximum overload closure effect in the FE models, with the FE wedge shapes

actually being quite flat out to this location, with little effective wedge height then being passed into the crack wake to cause premature flank contact. At such proximity to the overload location (well within one $r_{p(OL)}$) residual stress effects may be expected to act in the FE models, effectively lowering the R-ratio experienced at the crack tip. It may be then seen that by using the notional wedge shape for the analytical model as shown in Figure 4.26, the analytical model is effectively approximating both residual stress and residual wedge effects on closure behaviour by having a more rapid increase in effective wedge height passed into the post-overload crack wake than indicated in the FE results. The fact that good approximations of maximum post-OL crack closure effect are given by the analytical model is then attributable to the previous assertion of the underlying link between the wedge size and residual stresses: i.e. they come from the same tensile stretch of the OL plastic zone material. The fact that very near-OL-tip effects (such as peak closure location) are less accurately predicted by the analytical models should not then be taken as an undue deficiency in the analytical model, as the influence of the main mechanisms (residual stress and wedge contact) is biased towards residual stress close to the OL point, which is not explicitly reflected in the analytical model, even though the physical driving force for shielding (the plastic stretch of material in the OL plastic zone and the elastic constraint of the surrounding material) is essentially the same. In the first instance it may be seen that, as a starting point for a simple and efficient description of post-overoad crack shielding, the present analytical model behaves well in relation to the various FE models, provided a λ value of 0.5 is used, and the exact location of the post-overload closure minimum is not critical.

4.4 Strip-yield modelling of undeflected cracks

4.4.1 Model formulation

Within the literature several attempts have been reported to model PICC effects by modifying the established Dugdale strip yield model [1960] to leave plastically deformed material in a propagating crack wake (e.g. Dill and Staff, 1979, Budiansky and Hutchinson, 1978, Fuhring and Seeger, 1979). Such models are essentially applicable to plane stress analyses, without considering three-dimensional constraint

on closure behaviour. An attempt was made by Newman [1981] to study both plane stress and plane strain closure behaviour using a similar modified Dugdale model, by introducing a 'constraint factor' (essentially a fitting parameter) on tensile yielding to account for such three-dimensional effects (also discussed in Section 2.3.4), incorporated in the *FASTRAN* code. Newman's *FASTRAN* calculations been implemented by Xu [2001]: to differentiate Xu's code from Newman's original model, Xu's code will be referred to as a strip yield model. This strip yield approach is briefly described below.

The model considers a CCP specimen subjected to uniform applied stress (Figure 4.27a). It is assumed that all plastic deformation is contained within a thin strip along the crack line. Thus the specimen is composed of three regions:

1. a linear elastic region containing a fictitious crack of length $2(a_o + r_p)$. This is Region A,
2. Region B is a plastic region of length r_p ahead of the crack tip, and
3. a residual plastic deformation region (Region C) of length a_o.

The material within the Region B and C is represented by a series of finite-width rigid-perfectly plastic bar elements with flow stress σ_o. On applying a stress, these bar elements are either intact (in the plastic zone i.e. Region B) or broken (in the residual plastic deformation region, i.e. Region C). Elements in Region B can carry both tensile and compressive stresses, while the crack wake elements (in Region C) in contact can only carry compressive stresses and yield at $-\sigma_o$. The plastic zone size and crack surface displacements are computed by superposition of two elastic problems *viz.*, a crack in a finite-width pate subjected to either:

1. remote uniform stress (σ) or
2. uniform stress applied over a segment of the crack surface (see Figure 4.27b).

The crack opening stress (σ_{op}) may be calculated either from:

1. displacement analysis: by defining the applied stress required to fully open the crack surfaces to be σ_{op} [Newman, 1999]) or
2. contact stress analysis: the applied stress intensity factor at σ_{op} is equated to the stress intensity factor caused by the contact stresses at the minimum stress, $\sigma_{min.}$ (e.g. Fuehring and Seeger, 1979, Newman, 1981, 1992, 1997).

Region B and C are modelled using a fixed number of elastic-perfectly plastic elements (100 is chosen), as shown schematically in Figure 4.27a. 60 elements are used for Region C and 40 elements for Region B, the element widths being varied with their relative positions, with finer elements concentrated around the physical crack tip and behind the fictitious crack tip. Fixing the number of elements is expected to result in a more reliable and consistent crack opening behaviour, than the common practice of lumping elements (e.g. Newman, 1981) far away from the crack tip into a single element. Although computing time may be reduced in the lumping procedure, sharp changes in the crack opening loads at certain distance are sometimes reported [Newman, 1999]. The initial length of the 40 bar elements in Region B is based on the opening displacements of the fictitious crack surfaces at the peak load of the first cycle, while the length of the 60 bar elements in Region C is initially set to zero and continually updated with crack growth.

4.4.2 Governing equations:

Symmetry allows only one quarter of the CCT specimen to be modelled. Figure 4.27c shows schematically the loading, basic nomenclature of the bar element, and coordinate system used in the model. The rigid perfectly-plastic bar element of width, $2w_j$ is connected to the point j located on the elastic-plastic boundary, and is subjected to a compressive stress σ_j. The element is in contact when the crack surface displacement (V_j) is less than the element length (L_j). The stress σ_j is applied to make $L_j = V_j$. The residual stresses and plastic deformations of the bar elements are computed by requiring that compatibility be met between the elastic plate and the entire bar elements in Region B and C. The displacement at point i is given by:

$$V_i = \sigma f(x_i) - \sum_{j=1}^{100} \sigma_i g(x_i, x_j) \qquad \text{for } i = 1-100 \tag{4.6a}$$

where $f(x_i)$ and $g(x_i, x_j)$ are influence functions given by:

$$f(x_i) = \frac{2(1-\eta^2)}{E}\sqrt{(d^2 - x_i^2)\sec\frac{\pi d}{W}} \tag{4.6b}$$

$$g(x_i, x_j) = G(x_i, x_j) + G(-x_i, x_j) \tag{4.6c}$$

$$G(x_i, x_j) = \frac{2(1-\eta^2)}{E}\left\{(b_2 - x_i)\cosh^{-1}\left(\frac{d^2 - b_2 x_i}{d|b_2 - x_i|}\right)\right.$$
$$-(b_1 - x_i)\cosh^{-1}\left(\frac{d^2 - b_1 x_i}{d|b_1 - x_i|}\right)$$
$$\left.+\sqrt{d^2 - x_i^2}\left[\sin^{-1}\left(\frac{b_2}{d}\right) - \sin^{-1}\left(\frac{b_1}{d}\right)\right]\right\}$$
$$\left[\frac{\sin^{-1} B_2 - \sin^{-1} B_1}{\sin^{-1}\left(\frac{b_2}{d}\right) - \sin^{-1}\left(\frac{b_1}{d}\right)}\right]\sqrt{\sec\left(\frac{\pi d}{W}\right)} \qquad (4.6d)$$

where

$$B_j = \frac{\sin\left(\frac{\pi b_k}{W}\right)}{\sin\left(\frac{\pi d}{W}\right)} \qquad \text{for } j = 1 \text{ or } 2 \qquad (4.6e)$$

η is a material constant, $\eta = 0$ for plane stress and $\eta = \nu$ for planes strain, $d = a_o + r_p$, $b_1 = x_j - w_j/2$ and $b_2 = x_j + w_j/2$.

The Gauss-Seidel iterative method [Carnahan *et al.*, 1969] is used to solve the linear system of equations (i.e. Equation 4.6a), to obtain the crack surface stresses used for the calculation of the crack opening point. Boundary conditions are applied in Equation 4.6a and are of two types caused by: 1) tensile or compressive yielding of the bar elements in Region B, and 2) separation of elements in Region C. The Region B boundary conditions are:

$$\text{If } V_i^{(k)} \geq L_i^{(k-1)}\left(1 + \alpha\frac{\sigma_o}{E}\right) \Rightarrow \begin{cases} & L_i^{(k)} = V_i^{(k)}\left(1 - \alpha\dfrac{\sigma_o}{E}\right) \\ \text{if} & \sigma_i^{(k)} \geq \alpha\sigma_o \Rightarrow \sigma_i^{(k)} = \alpha\sigma_o \end{cases} \qquad (4.6f)$$

$$\text{If } V_i^{(k)} < L_i^{(k-1)}\left(1 + \alpha\frac{\sigma_o}{E}\right) \Rightarrow \begin{cases} & L_i^{(k)} = V_i^{(k)}\left(1 + \alpha\dfrac{\sigma_o}{E}\right) \\ \text{if} & \sigma_i^{(k)} \leq -\alpha\sigma_o \Rightarrow \sigma_i^{(k)} = -\alpha\sigma_o \end{cases} \qquad (4.6g)$$

$$\text{Or else} \begin{cases} L_i^{(k)} = V_i^{(k)} \\ \sigma_i^{(k)} = \sigma_i^{(k-1)} \end{cases} \tag{4.6h}$$

The boundary conditions in Region C are:

$$\text{If } V_i^{(k)} \geq L_i^{(k-1)} \Rightarrow \begin{cases} L_i^{(k)} = L_i^{(k-1)} \\ if \quad \sigma_i^{(k)} \geq 0 \Rightarrow \sigma_i^{(k)} = 0 \end{cases} \tag{4.6i}$$

$$\text{If } V_i^{(k)} < L_i^{(k-1)}\left(1+\frac{\sigma_o}{E}\right) \Rightarrow \begin{cases} L_i^{(k)} = V_i^{(k)}\left(1+\frac{\sigma_o}{E}\right) \\ if \quad \sigma_i^{(k)} \leq -\sigma_o \Rightarrow \sigma_i^{(k)} = -\sigma_o \end{cases} \tag{4.6j}$$

$$\text{Or else} \begin{cases} L_i^{(k)} = V_i^{(k)} \\ \sigma_i^{(k)} = \sigma_i^{(k-1)} \end{cases} \tag{4.6k}$$

The superscripts on σ_i, L_i and V_i indicate the iteration number of the iterative solution procedure in solving the linear system of Equation 4.6a. Equation 4.6a can then be recast to solve for σ_i as:

$$\sigma_i^{(k)} = \left[\sigma f(x_i) - V_i - \sum_{j=1}^{i-1}\sigma_i^{(k)} g(x_i, x_j) - \sum_{j=i+1}^{100}\sigma_i^{(k-1)} g(x_i, x_j)\right] \Big/ g(x_i, x_i) \tag{4.6l}$$

Initial guesses for σ_i are taken as zeros and substituted into the right-hand side of Equation 4.6l. The stresses ($\sigma_i^{(k)}$) are checked against the boundary conditions (Equation 4.6f-k), and are updated if necessary. The newly calculated values of $\sigma_i^{(k)}$ are inserted in the Equation 4.6l as soon as they are obtained. This process is repeated until the changes in σ_i are less than $0.01\sigma_o$. The crack opening stress (σ_{op}) is computed based on the following criteria: 1) the applied stress increment (σ_{op}-σ_{min}) that is used to effectively separate the crack face contact (<$0.01\delta_{tmax}$, where δ_{tmax} is the maximum CTOD of the physical crack tip) in Region C, and 2) the applied stress increment is used to effectively remove all the contact stresses (< $0.01\sigma_o$) in Region B.

4.4.3 Plastic-zone size approximations:

Using the finiteness condition of Dugdale, the plastic-zone size (r_p) for a finite-width crack specimen can be determined. This condition demands that the stress intensity factor at the tip of the fictitious crack be zero and is given by:

$$K_\sigma + \sum_{i=1}^{40} K_{\sigma_i} = 0 \tag{4.6m}$$

where

$$K_\sigma = \sigma\sqrt{\pi(a_o + r_p)\sec\left(\frac{\pi(a_o + r_p)}{W}\right)} \tag{4.6n}$$

and

$$K_{\sigma_i} = \frac{2\sigma_i}{\pi}\sqrt{\pi(a_o + r_p)\left[\frac{\sin^{-1}B_2 - \sin^{-1}B_1}{\sin^{-1}\left(\frac{b_2}{(a_o + r_p)}\right) - \sin^{-1}\left(\frac{b_1}{(a_o + r_p)}\right)}\right]\sqrt{\sec\frac{\pi d}{W}}} \tag{4.6o}$$

where

$$B_k = \frac{\sin\left(\frac{\pi b_k}{W}\right)}{\sin\left(\frac{\pi(a_a + r_p)}{W}\right)} \tag{4.6p}$$

Here b_1 and b_2 are the distances from the mid point of the crack and the two ends of the stressed segment in the specimen as indicated in Figure 4.27b. Equation 4.6m is solved numerically to give r_p.

4.4.4 Results

Figure 4.28 shows an example comparison of closure variation between strip yield results and FE results for $\Delta K_{(BL)}$ = 12.0 MPa $m^{1/2}$, R = 0.1, $\%OL$ = 100. Strip yield results are plotted for different values of α (= 1.9, 2.5 and 3.0). It can be seen that there is an increase in closure levels both in pre-overload (i.e. constant amplitude conditions) and post-overload transient, with increasing α. An α value of 2.5 predicts a peak-overload transient close to the FE value, although a shorter transient is obtained (i.e. it returns to the baseline closure levels more rapidly).

The response to the $\%OL$ variation for both strip yield and FE models is shown in Figure 4.29 ($\Delta K_{(BL)}$ = 12.0 MPa $m^{1/2}$, R = 0.1, α = 2.5). It can be observed that both the models can predict close agreement of the peak-closure transients for 100% OL, however the FE modelling is seen to be rather more sensitive to overload level, particularly in terms of the lowest $\%OL$ shown in Figure 4.29. Figure 4.30 shows the effect of varying baseline stress intensity factor on closure response for 100% OL, and $\Delta K_{(BL)}$ = 8.0 and 12.0 MPa $m^{1/2}$ (R = 0.1, α = 2.5), where it can be seen that the peak-closure transient and baseline closure levels are not noticeably changed, although the length of the transient is slightly increased with increasing baseline load. It may be seen that by manipulation of the α parameter some control over the qualitative agreement of the models is achieved, although it is evident that the details of the post overload transient shape cannot be 'resolved': e.g. equivalent transient peak levels may be achieved for one α value, whilst a more comparable transient length may require higher α. Overall it should be noted that both modelling methods are of course only approximations of the processes that may occur in reality, particularly for the strip yield approach, where the formulation is fundamentally for plane stress deformation conditions. Inspection of Figure 4.29 and 4.21 shows that the wedge overload model described earlier is capable of a more consistent approximation of plane strain overloads investigated by FE, despite the model's simplicity. Further consideration of the validity and choice of modelling approach, and associated fitting parameters (such as α), is considered in relation to experimental crack closure data in Section 4.7.

4.5 FE modelling of deflected cracks

Figure 4.31a, 4.31b and 4.31c show the deformed mesh for a deflected crack (L = 150.0 μm, θ = 45°, ΔK = 12.0 MPa m$^{1/2}$, R = 0.1, $\%OL$ = 100.0) when unloaded fully, with an overload having been applied at point 'A' in Figure 4.31a, and the current tip now lying at point 'B'. Contacts are observed at deflected crack sections immediately following the OL, and behind the current crack tip. A wedge (or hump) of residual deformation is observed immediately following the OL location (identified with wider crack opening displacement behind the wedge), consistent with Parry's [2000] observation using the LDU crack propagation algorithm.

Figure 4.32 shows the comparison of LDU based closure results [Parry, 2000], with current LDULU results under a single OL loading for a periodically deflected crack (L = 150.0 μm, θ = 45°, $\Delta K_{(BL)}$ = 12.0 MPa m$^{1/2}$, R = 0.1, $\%OL$ = 100.0). The plot shows the variation of U versus normalised post-overload extension $\Delta a/r_{p(BL)}$. The overload was applied at the turning point located at the end of the third deflection when the crack had propagated approximately 3.1 $r_{p(BL)}$ (similar to the undeflected case as discussed in Section 4.2). It can be seen that both LDU and LDULU crack propagation algorithms predict similar behaviour, with LDULU giving slightly enhanced closure levels.

Figure 4.33 shows a comparison of deflected (L = 150.0 μm, θ = 45°, $\Delta K_{(BL)}$ = 12.0 MPa m$^{1/2}$, R = 0.1) and undeflected ($\Delta K_{(BL)}$ = 12.0 MPa m$^{1/2}$, R = 0.1) cracks for both CA and OL ($\%OL$ = 100.0) cases. A comparison of CA behaviour shows enhanced closure levels for deflected cracks as discussed in Chapter 3. The post-overload behaviour (for $\Delta a/r_{p(BL)}$ upto ≅ 9 $r_{p(BL)}$ or 2.2 $r_{p(OL)}$) of the deflected crack appears very similar to that of the undeflected crack, with crack closure within this zone appearing to be controlled solely by plastic deformation at the OL location (i.e. no effect of crack roughness). Following this wedge controlled zone (or 'WCZ'), a zone is seen in which closure is controlled by both the contacts at the asperity turning points (identified by the cyclic variation of U, as discussed in the previous Chapter 3, and also shown in Figure 4.33 for constant amplitude growth of the deflected crack) and contacts due to the overload deformation, which may be termed the WTPZ, for 'Wedge and Turning Point controlled closure Zone'. The evidence of wedge controlled closure in the WTPZ is seen in the truncated cyclic variation of U, where

during some portion of loading, first unloading contact occurs near the overload location wedge. For the problem considered, the WTPZ extends for about ~19 $r_{p(BL)}$ or 5 $r_{p(BL)}$ (approximately twice the WCZ). Beyond the WTPZ, closure is controlled by contact at the near-tip crack turning points (termed the Turning Point controlled Zone, TPZ), equivalent to the CA case. As noted earlier in the case of undeflected cracks, baseline closure levels are not reached for the post-overload propagation lengths considered (~ 31 $r_{p(BL)}$ or 7.5 $r_{p(OL)}$).

It can be seen from Figure 4.33 that the maximum closure level (i.e. U_{min}) occurs after the crack has propagated for about one fifth of the OL plastic zone size (i.e. a_{umin} $\cong$ 0.2 $r_{p(OL)}$) with crack face contact seen to occur slightly behind the crack tip, close to the OL point propping open the deflected crack tip. Given the early similarity of the straight crack and deflected crack overload behaviour, and the manner in which the overload and near-tip baseline contact processes appear to interact in the WTPZ region, it is evident that the overall rough crack overload process may be closely described as competition between a PICC dominated overload event, and underlying baseline RICC potential, where the crack closure level that is seen at any point in the propagation process is simply the highest due to either mechanism when considered independently.

4.5.1 Effect of overload ratio

The effects of overload ratio on crack closure in both deflected and undeflected cracks are shown in Figure 4.34 for various OL ratios of 0.0%, 50%, 100% and 150% (L = 150.0 μm, θ = 45°, ΔK = 12.0 MPa $m^{1/2}$, R = 0.1). The effect of crack deflection on the variation of U for the 100% and 150% OL analyses in the WCZ is limited for the problem considered suggesting that transient closure behaviour is essentially PICC dominant in both these cases: however, at the lower OL ratio considered (i.e. 50%), there seems to be an increase in closure levels when compared to the undeflected crack case.

4.5.2 Effect of asperity length

Figure 4.35 shows the effect of varying the projected length of asperity in the rough crack models from L = 18.75, 37.5, 75.0 and 150 μm for θ = 45°, ΔK = 12.0 MPa $m^{1/2}$, R = 0.1, $\%OL$ = 100.0. Thus the $L/r_{p(BL)}$ ratios were 0.11, 0.22, 0.44, 0.88 i.e. in the ratio 1:2:4:8. The size of the elements along the propagation length was kept at 1/9.06, 1/18.13, 1/36.26 and 1/72.52 $r_{p(BL)}$ for L = 150, 75, 37.5 and 18.75 μm respectively, so that a minimum of eight elements was provided along each deflected length (a more limited extent of crack propagation was necessary for L = 37.5 and 18.75 μm models due to the large computational requirements). There is no appreciable change in the post-overload peak closure behaviour for the asperities considered in these cases suggesting that peak closure is again governed by overload PICC effect. Some 'noise' may be seen in the post-overload behaviour, but this may be expected as the comparisons are made for different mesh discretisation. Contrary to the work of Parry [2000] results for L = 37.5 and 150 μm in particular, the present results showing limited dependence of post-overload behaviour on L; an issue that has since been found to be attributable to an input error in a specific file in the earlier work [Parry, 2003]. The implication of these results and RICC effects on crack closure behaviour is considered below.

4.6 Normalised asperity size analysis

4.6.1 FE modelling

In Section 3.6.2 the apparent L/r_p control of closure levels under CA loading, particularly the initial rise and plateauing effect of increasing L/r_p was discussed. It is then significant to extend this asperity size normalisation to OL conditions where we may consider both baseline and overload plasticity effects to be relevant (in terms of $r_{p(BL)}$ and $r_{p(OL)}$) to possible RICC-OL effects. Table 4.1b shows an overview matrix of various parameters (*viz.*, $\%OL$, $\Delta K_{(BL)}$ and L), which have been considered for the FE analyses, with $L/r_{p(BL)}$ ranging from 0.136-11.11 and $L/r_{p(OL)}$ ranging from 0.034-4.94. As noted earlier, various undeflected models were also run to provide 'normalisation' for potential RICC/OL interaction.

To fully quantify the 'magnitude' of an overload, various parameters, such as retardation distance and retardation cycles, can be considered, as noted earlier (e.g. Venkateshwara Rao and Ritchie, 1988, Mills and Hertzberg, 1976, Skorupa, 1998). In the first instance peak (maximum) closure effect ($[K_{cl}/K_{max}]_{max}$) of a given transient (see Figure 4.36) may be identified as a clear measure of its severity, as peak severity and duration of the overload interactions are seen to scale quite consistently in the FE results obtained here (see Figure 4.9). The interaction between RICC and PICC due to single overload loading may then be studied through the 'Normalised Transient Effect' (*NTE*) which we defined here as:

$$NTE = \frac{(K_{cl}/K_{\max})_{\max-RICC}}{(K_{cl}/K_{\max})_{\max-PICC}} \tag{4.7}$$

where the maximum peak closure level of the deflected crack transient model is normalised by that of an equivalent un-deflected crack model. As such, a separation of RICC and PICC effects on overload is achieved. For *NTE* values of 1, closure effects of deflected and undeflected crack models are equivalent and no RICC contribution to overload may be considered to act, whilst *NTE* > 1 suggests OL transient closure is being enhanced by crack roughness effects.

Following the understanding of L/r_p normalisation (see Figure 3.36 and 3.44) for CA loading conditions, normalisation of L with both $r_{p(BL)}$ and $r_{p(OL)}$ is considered valuable. In Chapter 3, the assessment of RICC effects in terms of asperity size and scale of plasticity was straight forward, with the L/r_p parameter being utilised. Under transient loading, two parameters are evident by analogy: $L/r_{p(BL)}$ and $L/r_{p(OL)}$. As such, results need to be presented in terms of both parameters, with Figure 4.37 showing a representative map of the regime of interest. Figure 4.37 shows schematically $L/r_{p(BL)}$ and $L/r_{p(OL)}$ axes for values of realistic interest in the present work (for aerospace applications). Lines corresponding to 0%, 50%, 100%, 150% and 900% OLs are shown. Moving along a *%OL* line, towards increasing $L/r_{p(OL)}$ values may be equated to increasing L (for fixed $\Delta K_{(BL)}$), whilst decreasing $L/r_{p(OL)}$ values may be equated to decreasing $\Delta K_{(BL)}$ (for fixed L). Noting the results from Figure 4.37 and 4.38, the unity line on $L/r_{p(BL)}$ indicates the onset of the plateau region in the CA-RICC effect. Figure 4.38 shows the location of data points that have been considered for the present FE modelling. The variation of *NTE* for all the available models is

shown in Figure 4.39. Looking at the results for 100% overload first, it is seen that most of the data is in fact very close to 1 (i.e. no RICC effect on overload behaviour): however results for the two highest L/r_p conditions do show a distinct rise, achieving values of ~ 1.2. The results for 50% overload show a more distinct rise at high L/r_p values, with evidence of a plateauing effect, similar to the CA-RICC results considered in Chapter 3. Whilst there are some fluctuations in *NTE*'s value seen for the 150% OL results, no consistent rise is seen, with the results falling within the discretisation errors intrinsic to the FE modelling. Whilst these variations in *NTE* are clearly not a simple function of $L/r_{p(OL)}$ values, it is evident that the increases in *NTE* are associated with $L/r_{p(OL)}$ values approaching or exceeding 1. It is certainly evident that *NTE* values of 1 are consistently obtained for $L/r_{p(OL)} < 0.4$. Considering these relationships between *NTE* and $L/r_{p(OL)}$ values, it may , in the first instance, be suggested that RICC influences on OL occur in a mechanistically similar way to RICC effects constant amplitude failure. This hypothesis is therefore investigated in the following section.

4.6.2 Analytical modelling

In the first instance the analytical modelling of deflected cracks subjected to overload loading is treated in a similar fashion as the CA-RICC model, except that shear displacement at the deflection point is defined by OL conditions (Figure 4.40). Crack opening displacements beyond the deflection point are then assumed to be governed by baseline loading, and treated elastically, as before. It is again assumed that the overload is applied at the turning point and causes an increase in reverse shear displacement. As noted earlier Parry [2000] reports that relative location of the overload along the deflected the FE models face has a limited effect on the closure response. X-ray microtomography results (Khor *et al.*, 2004) indicate that crack closure due to roughness is controlled by fracture surface high points making up only a small fraction of an overall fracture surface. The fact that some points along a crack front will always be close to asperity peaks suggests that modelling OL deformation at the asperity peaks is reasonable in the first instance.

- *Crack profile*

A deflected crack section with multiple deflections is again approximated to an undeflected crack with a single pupative kink (i.e $a^* << b$) at the end as shown in Figure 4.40. The elastic crack opening displacements (CODs), δ under plane strain (after Tada *et al.*, 2000), are again given by

$$\delta = 2u_y = \frac{4k_1(1-\nu^2)\sqrt{a^{*2}-x^2}}{E\sqrt{\pi a^*}} \tag{4.8}$$

where u_y is the elastic displacement of the crack flank in the y-direction at a distance x from the asperity point (see Figure 4.40), and k_I is the local mode I stress intensity factor at the tip pupative kink. In the event $a^* << b$, k_I is given by [Bilby *et al.*, 1977];

$$k_1 = \frac{1}{4}\left(3\cos\frac{\theta}{2} + \cos\frac{3\theta}{2}\right)K_I \tag{4.9}$$

Hence, Equation 4.8 becomes,

$$\delta = 2u_y = \frac{\left(3\cos\theta/2 + \cos 3\theta/2\right)K_I(1-\nu^2)\sqrt{a^{*2}-x^2}}{E\sqrt{\pi a^*}} \tag{4.10}$$

- *Residual deformation of the asperity due to overload*

On the premise that the forward plastic deformations associated with fatigue crack tip displacements due to overload are larger than those occurring in reverse during unloading, residual shear deformations due to the application of overload at the asperity tip may be considered to generate an effective residual shear displacement, $h_{rw(OL)}$, near the overload location that is left in the crack wake when the crack turns (see Figure 4.41), leading to crack face contact at the asperity. In the first instance, $h_{rw(OL)}$ is then equated to the $CTSD_{res(OL)}$ (residual crack tip displacement due to the OL) associated with the asperity tip.

Considering a Dugdale-type strip yield model, $CTSD_{(OL)}$ under far field mode II loading plane strain conditions is expressed as (in line with Rice's [1967] formulation),

$$CTSD_{(OL)} = \frac{\sqrt{3}K_{II(OL)}^2\left(1-\nu^2\right)}{E\sigma_y} \tag{4.11}$$

where $K_{II(OL)}$ is the maximum mode II stress intensity factor due to overload. During unloading, a degree of reverse sliding will occur. The $\Delta CTSD_{(OL)}$ is then expressed as a function of $\Delta K_{II(OL)}$ [Rice, 1967];

$$\Delta CTSD_{(OL)} = \frac{\sqrt{3}\Delta K_{II(OL)}^2 (1-\nu^2)}{E(2\sigma_y)} \tag{4.12}$$

Thus, $CTSD_{res(OL)}$ is then given by,

$$CTSD_{res(OL)} = CTSD_{\max(OL)} - \Delta CTSD_{(OL)} \tag{4.13a}$$

$$= \frac{\sqrt{3(1-\nu^2)}}{E(2\sigma_y)} \left(2K_{II(OL)}^2 - \Delta K_{II(OL)}^2\right) \tag{4.13b}$$

The residual CTSD of a crack under far field mode II loading can be related to the kinked crack case by replacing K_{II} by k_2, the local mode II stress intensity factor at the kinked crack. k_2 at the tip of a pupative kink can be expressed in terms of global K_I (following similar argument for k_1 as in Equation 4.9) as:

$$k_2 = \frac{1}{4}\left(\sin\frac{\theta}{2} + \sin\frac{3\theta}{2}\right) K_I \tag{4.14}$$

Combining Equation 4.11b and 4.12, and equating $h_{rw(OL)}$ to $CTSD_{res(OL)}$, $h_{rw(OL)}$ can be expressed as,

$$h_{rw(OL)} = \frac{\sqrt{3}(1-\nu^2)\left(\frac{1}{4}\left(\sin\theta/2 + \sin 3\theta/2\right)\right)^2 K_{\mathrm{Imax}(BL)}^2}{E\sigma_y} \left(\xi^2 + R - \frac{1}{2}R^2 - \frac{1}{2}\right) \tag{4.15}$$

Following the arguments in Section 3.6.2.2 regarding the shape of the residual deformation profile and scaling of CTSD, the expression of $h_{rw(OL)}$ is further modified as;

$$h'_{rw(OL)} = h'_{rw(OL)}(a^*) = \beta_{II} h_{rw(OL)} \left(\frac{a^*}{\lambda r_{p(OL)}}\right)^{\eta} \quad \text{for } a^* < \lambda r_{p(OL)} \tag{4.16a}$$

$$h'_{rw(OL)} = \beta_{II} h_{rw(OL)} \quad \text{for } a^* \geq \lambda r_{p(OL)} \tag{4.16b}$$

where η is an empirical factor that may be determined experimentally or by FE modelling and β_{II} is the CTSD scaling factor. In the first instance the exponent, η is again taken to be 1, i.e. $h_{rw(OL)}$ is assumed to be a simple linear function of a^*

(normalised by $\lambda r_{p(OL)}$) for $a^* < \lambda r_{p(OL)}$ to represent the effective influence of asperity deformation at small a^* values.

- *Crack closure estimation*

It can be seen from Figure 4.41 that crack closure will take place when $\delta = h_{rw(OL)} sin2\theta$. Combining Equation 4.10 and 4.15 and rearranging the closure level can be expressed as:

$$\frac{K_{cl}}{K_{\max}} = \beta_{II} \frac{K_{\max}\sqrt{3\pi}\left(\frac{1}{4}\left(\sin\frac{\theta}{2}+\sin\frac{3\theta}{2}\right)\right)^2}{\sigma_y\left(3\cos\frac{\theta}{2}+\cos\frac{3\theta}{2}\right)\sqrt{a^*}} \xi^2\left[\frac{1}{2}-\frac{R^2}{2}+R\right] \left(\frac{a^*}{\lambda r_{p(OL)}}\right) \tag{4.17}$$

Figure 4.42a shows a comparison of FE and analytical *NTE* results for $\beta_I = \beta_{II} = 1$ and $\lambda = 0.5$. In the analytical modelling, *NTE* is based on simple competition between the straight crack and deflected crack OL models. As such, predictions of closure levels for a given deflected crack geometry (and load levels) are obtained first via the deflected crack model identified above, and secondly by using an equivalent straight crack overload model as outlined in Section 4.3. The higher of the two closure predictions is then used, i.e. it is implied that the closure mechanisms are effectively competitive, where we note that the sense of the deformations giving rise to crack face contact are effectively orthogonal. Thus the following conditions are thus enforced;

$$\frac{(K_{cl}/K_{\max})_{\max-RICC}}{(K_{cl}/K_{\max})_{\max-PICC}} \leq 1; = 1 \quad > 1; value \tag{4.18}$$

It can be seen in Figure 4.42a that the appearance of a plateau pattern in *NTE* values is well captured by the analytical model for 50% OL, however for 100% and 150% OL the analytical model (with $\beta_I = \beta_{II} = 1.0$) shows no influence of RICC i.e. $NTE = 1$. In Figure 4.42b, $\beta_I = 1.0$, and β_{II} has been increased to 2.0. It may be seen from Figure 4.42b that the appearance of the plateau pattern in NTE values is again depicted by the analytical models, and is now evident in all three OL levels tested. It may be noted

that by further tuning of the fitting parameters λ and β's (i.e. β_I and β_{II}), the FE and analytical models can be made to agree more closely. However, enforcing an exact fit between the modelling methods is not the main objective at present what is more significant however is that the simple analytical model is able to reproduce functional trends in *NTE* predicted by FE modelling, with the implication of:

1. an effective competition existing between straight and deflected crack influences on OL magnitude, and
2. the efficacy of crack deflection in enhancing post-overload closure levels has a similar relationship to the ratio of plastic zone size and deflection length identified for CA-RICC conditions, implying that enhanced OL retardation due to fracture surface roughness will be most effective at low stress intensity levels levels, much like in CA-RICC.

As noted earlier (see Figure 3.44), RICC effects are predicted to decrease dramatically when the asperity size falls below the active plastic zone size. With overload plastic zone sizes of necessity being larger than the associated baseline loading (plastic zone size scales with the square of the stress intensity), an important prediction of this work is that that relatively large asperity sizes are needed for effective RICC contributions to overload transients. In the case of an overloaded crack, two conditions of closure effect may then be considered to arise:

1. when crack asperity sizes are small relative to overload plastic zone size, tensile displacements associated with the load transient are most effective in generating closure and the overload transient is essentially a PICC controlled event and microstructural effects are limited, and
2. when crack asperity sizes are large relative to overload plastic zone size, shear displacements associated with the load transient are more effective in generating closure and the overload transient is enhanced by RICC effects.

The present models predict that for typical Paris regime growth conditions (ΔK of the order of 10MPa$\sqrt{m}$, R = 0.1 for example), in a moderate strength airframe alloy (of the order of 400MPa), crack path asperity dimensions (i.e. L) of 500 μm are required for a strong RICC contribution to a 100% overload transient, i.e. a relatively large scale compared to fracture surface features seen in conventional airframe alloys. This is consistent with experimental plane strain overload results

from Xu [2001] (see Figure 4.43), showing essentially similar overload transient effects in 2024 and 2024A-T351 (12 mm thick, side-grooved CCT) specimens, even though increased baseline crack growth resistance of the 2024A was clearly linked to increased fracture surface roughness and RICC effects [Xu, 2001] (See Figure 4.43). The results of Vankateswara Rao and Ritchie [1988] are then of some interest in providing a direct comparison of the Al-Li alloy 2090-T8E41 (σ_y = 552 MPa, 13 mm thick) with a 2124-T351 alloy. Large crystallographic facets are particularly evident on fracture surfaces of the 2090-T8E41 (σ_y = 360 MPa, 25 mm thick) material, with individual major crack deflections being seen to occur for distances of the order of hundreds of micrometers. Figure 4.44 shows a comparison of plane strain overload transient responses for the 2124 and 2090 material, with the 2090 results clearly showing the stronger overload transient. The stronger peak-overload transient of 2090 may then be related to the apparent large value of $L/r_{p(OL)}$ (> 1) potentially achieved in this material. Whilst this provides some indication of experimental support for the present modelling work, it is clear that detailed comparison with results obtained under systematically varied conditions would be extremely valuable. For direct quantitative comparisons, it is clear the provenance of the data is important, with results obtained recently by Xu [2001] and Khor [2004] being of particular interest. As noted previously these results were obtained in a CCP specimen format, using thick, side grooved samples to maintain a uniform plane strain stress state. This is expected to be extremely important as overloads are distinctly sensitive to stress states (Xu, 2001): the following section therefore provides a detailed comparison of the present modelling approaches and this body of test data.

4.7 Comparison with experimental data

4.7.1 Crack closure levels

- *FE modelling results*

Figure 4.43 shows a basic comparison of FE and experimental closure levels ($\Delta K_{(BL)}$ = 12.0 MPa $m^{1/2}$, R = 0.1, $\%OL$ =100). The experimental results (Xu, 2001 and Khor, 2004) are for Al 2024, 2024A, 2027-Rex(8) and 2027-Rex(100). The unique quality

of these experiments should be re-emphasised, being conducted on 12 mm thick side grooved specimens to maintain plane strain conditions for the applied loading with multiple near-tip strain gauges and a non-subjective curve fitting method being used to analyse specimen compliance. The FE result corresponds to 2024 material parameters: additional models show that there is a marginal variation in the predicted closure levels for the yield stress levels (σ_y) of interest, and hence current comparisons with experimental results are all made with '2024' prediction curves. It can be observed that alloys of different baseline closure levels (e.g. $U_{(BL)}$ for 2024 and 2024A are approximately 0.90 and 0.75 (see Figure 4.45)) do not show strong differences in transient conditions, i.e. the observed differences in the transient results that are apparent may be attributed to experimental limitations in closure measurement [Khor, 2004]. We can see that the baseline closure levels are not well predicted by the straight crack FE model ($U_{(BL)}$ = 1.0 for the FE model), although reasonable agreement in the transient form is predicted but generally understimated. It should be emphasised that a distance range of material conditions is captured by the experimental data in Figure 4.46, with grain sizes varying by a factor > 2, along with varying disperspoid type and volume fraction. There is a distance variation in fracture surface morphologies which is consistent with the variation in baseline closure levels of the materials (as illustrated at the end of Chapter 3). Whilst constant amplitude closure results for the materials showed a correlation with fracture surface morphology, even the minor variations in post-overload closure transients for the different alloys show no simple correlation with fracture surface roughness, implying a limited RICC influence on the overloads tested.

Figure 4.45 shows experimental closure variations of the 2024 and 2024A materials (represented in terms of U) with ΔK at R = 0.1 under constant amplitude loading [Xu, 2001]. It can be observed that there are significant differences in closure levels depending on the material and ΔK conditions. High closure levels are seen at low ΔK values (~ 5 MPa $m^{1/2}$), with the two alloys tending to converge as the threshold ΔK condition is approached. In this respect it may be noted that in variable amplitude closure modelling approaches in the literature, both baseline and overload transient behaviour are not usually considered explicitly at the same time. It may be noted that Newman's *FASTRAN* model (which is of course used for variable amplitude closure

predictions) is shown to achieve reasonable correlation with the experimental crack growth rate predictions by letting α vary empirically with ΔK_{eff} [Newman, 1997, 1997a, 1998, 1998a, 1998b, 1999, 1999a] for CA growth conditions. In particular a decrease of α towards threshold is employed, however this is fundamentally at odds to its use as a measure of constraint for PICC modelling is concerned as threshold crack growth will of necessity be overwhelmingly a plane strain controlled condition as plastic zone sizes become vanishingly small in relation to sample thickness. However, Newman reasoned that lowering α may be necessary to take into account for increases in shielding effects with roughness and oxide induced closure effect becoming more relevant in the threshold regime.

In the deflected crack FE models in Figure 4.46, various fracture facet sizes upto 150 μm at nominal angle of 45° are shown; we can observe an increase in maximum baseline closure levels with increasing asperity length (L) consistent with the increase of baseline closure levels in the materials exhibiting rougher fracture surfaces. Although the rough crack FE overload models produce transients that are consistently lower than the experimental results, the absence of roughness effect on closure transient is obviously consistent with the experimental data. From the *NTE* plot in Figure 4.42, it can be predicted that surface asperities of at least 250 μm ($\sim L/r_{p(OL)}$ = 0.45) are need to generate RICC overload influence ($NTE > 1$), whilst 500 μm ($\sim L/r_{p(OL)} = 1.0$) features would produce a full RICC effect. Thus the lack of RICC-OL influence in the experimental results may be interpreted in terms of fracture surface asperity sizes falling well those required to generate RICC-OL effects as indicated by the experimental measurements of 'L' for these materials shown in Table 3.3. Further qualitative experimental support for the present interpretation of potential RICC effects of overloads is seen in Figure 4.47: these SEM micrographs of the immediate post-overload region of the fracture surfaces in 2024A and 2027ReX(8) ($\Delta K_{(BL)} = 12.0$ MPa $m^{1/2}$, $R = 0.1$, $\%OL = 100$) show the presence of oxide debris (confirmed by EDX, energy dispersive x-ray analysis) in the post-overload region, consistent with locally enhanced closure effects in both cases [Khor, 2004]. In the rough surfaced 2024A case however, oxide is distinctly localised to surface asperities, whilst a uniform oxide coverage is evident in the 2027 material. Whilst not definitive support for the present modelling, it may be seen that such apparent changes in microscopic

contact processes did not significantly affect closure levels is supported by the FE models showing equivalent transient closure effects for ideally straight and deflected cracks when $r_{p(OL)}$ is large.

- *Analytical and strip yield modelling results*

Figure 4.48 shows a comparison of PICC analytical modelling (discussed in Section 4.3) with the experimental results from Xu [2001] and Khor [2004] ($\Delta K_{(BL)}$ = 12.0 MPa $m^{1/2}$, R = 0.1, $\%OL$ =100). Analytical results corresponding to 2024 alloy are plotted for β_I = 1, 1.3 and 1.4. In Figure 4.22 it has been shown that a β_I value of 1.0 predicted comparable closure levels to the FE result. By increasing the value of β_I to 1.3 (i.e. using as a fitting parameter, but within physically reasonable bounds), it can be seen that quite reasonable agreement with the experimental data is obtained. A higher value of β_I (= 1.4) slightly over predicts the peak closure levels. In the first instance a β_I value of 1.3 is investigated here for comparisons with experimental results.

Comparison of strip yield and experimental closure levels are shown Figure 4.49 ($\Delta K_{(BL)}$ = 12.0 MPa $m^{1/2}$, R = 0.1, $\%OL$ =100). With an α value of 1.9, it can be seen that experimental peak overload closure levels are well predicted by the strip yield model. Discussion regarding variation of α has been noted in Section 4.4 and 4.7: for subsequent comparison with experimental results, an α value of 1.9 has been adopted in the strip yield model.

4.7.2 Growth rate comparisons (*da/dN*)

Having identified the possibility of modelling overload transients purely in PICC terms, it is clearly valuable to consider the accuracy of the predictions against a range of loading conditions. In this respect the results of Xu [2001] are again of interest in providing post-overload crack growth rates for $\Delta K_{(BL)}$ of 8.0 and 12.0 MPa $m^{1/2}$, and $\%OL$ of 50 and 100: crack closure data for the lower $\Delta K_{(BL)}$ and $\%OL$ values were considered unreliable by Xu however, as even near-tip compliance changes become hard to detect at lower load levels. Crack growth rates for these alternative load

conditions are however available, and may of course be considered the more important parameter to predict than crack closure levels in themselves.

In the following sections, predicted growth rates from FE, analytical and strip yield models will be shown. Growth rates (*da/dN*) are obtained from experimental *da/dN* vs ΔK_{eff} curves as shown in Figure 4.50, obtained under constant amplitude loading conditions [Xu, 2001, and Khor, 2004]. Growth rates corresponding to each material are approximated by fitting piecewise polynomial curves, as shown in Figure 4.50 (two polynomial curves are used for each material). Using the polynomial curves, predicted *da/dN* is obtained using the overload model ΔK_{eff} predictions.

4.7.2.1 Comparison with Parry's result

Figure 4.51 shows a comparison of transient normalised growth rate predictions ($da/dN/(da/dN)_{(BL)}$) using methods reported by Parry [2000] and the curve fitting approach described above for $\Delta K_{(BL)}$ = 12.0 MPa $m^{1/2}$, R = 0.1 and $\%OL$ = 100, plotted against the normalised crack growth distance ($\Delta a/r_{p(OL)}$). In Parry's method a significant simplification in growth rate behaviour was applied by assuming a constant value of Paris exponent m across the range of operating ΔK. Then the normalised crack growth rate takes the form,

$$\frac{\left(\frac{da}{dN}\right)}{\left(\frac{da}{dN}\right)_{(BL)}} = \frac{C\left(U_{(OL)}\Delta K\right)^m}{C\left(U_{(BL)}\Delta K\right)^m} = \left(\frac{U_{(OL)}}{U_{(BL)}}\right)^m \tag{4.19}$$

where $U_{(OL)}$ is the U value corresponding to OL test. From the FE results, $U_{(BL)}$ = 1.0 and hence, Equation 4.19 is reduced to,

$$\frac{\left(\frac{da}{dN}\right)}{\left(\frac{da}{dN}\right)_{(BL)}} = \left(U_{(OL)}\right)^m \tag{4.20}$$

It is then observed that the slope of constant amplitude *log da/dN* vs *log* ΔK curve for 2124-T351 could vary from ~ 2.5 for ΔK = 4-6.5 MPa $m^{1/2}$, to ~ 5 for ΔK = 6.5-8 MPa $m^{1/2}$, for R = 0.1 [Venkateshwara Rao and Ritchie, 1988]. Although, m may vary depending on the material, (e.g. results presented by Xu [2001] found the slopes in the

corresponding ranges to be 2 and 4), a fixed value of 2.5 was adopted by Parry. It can be seen from Figure 4.51 that normalised transient growth rates behaviour is similar for Parry's method and the present method with more detailed use of measured *da/dN* vs ΔK_{eff} curves, except that Parry's growth rate results are consistently lower. In using 'real' intrinsic growth rate curves for the various materials in question, it is believed the present work gives a more rigorous test of the underlying assumptions.

4.7.2.2 Comparison with Xu's experimental results

- $\Delta K_{(BL)} = 12.0$ MPa $m^{1/2}$, $R = 0.1$, $\%OL = 100$

Figure 4.52 shows a comparison of FE, analytical and strip yield normalised growth rate predictions with experimental results from Xu [2001] for $\Delta K_{(BL)} = 12.0$ MPa $m^{1/2}$, $R = 0.1$, $\%OL = 100$. Analytical, strip yield and experimental results are plotted for both 2024 and 2024A alloys, while FE results are plotted for 2024 only. Strip yield modelling yields $U_{(BL)} = 0.57$ based on an α value of 1.9, where α has been selected to obtain the best fit to the maximum post overload closure level.

For the purposes of the present comparison, we will note that L values measured from fracture surfaces for 2024-type materials (see Chapter 3) are indeed too low to significantly affect overload transient conditions (c.f. pure PICC overload behaviour), at least for the results highlighted in Figure 4.52. For $\Delta K_{(BL)} = 12.0$ MPa $m^{1/2}$ and 100% OL we have previously noted that L would need to be of the order of 100's of micrometers to affect overload transients via RICC (see Section 4.6.2) as opposed to L values of the order of 10's of micrometers that have been measured. In Figure 4.52 and subsequent graphs, analytical closure estimates of overload behaviour are therefore based on PICC-OL model, whilst baseline closure conditions are estimated from experimental data on the presumption that such constant amplitude closure conditions for constant amplitude crack growth can be reasonably well estimated by the analytical RICC model of Chapter 3 when L, θ, or ϕ values are known. Obtaining exactly correct baseline closure levels at a specific applied $\Delta K_{(BL)}$ level is of course important, however we would note that, most significantly, the present RICC-CA model tracts the changes in baseline closure levels with varying ΔK levels, as opposed

to the strip yield method, where baseline closure levels (expressed as K_{cl}/K_{max}) are set by the choice of α and are independent of ΔK.

It can be seen in Figure 4.52 that FE over-predicts the post-overload minimum growth rates (~20% of baseline growth) as compared to the experimental results (~5% and 4% of baseline growth rates for 2024 and 2024A respectively). This is consistent with the previous under-prediction of closure levels (see Figure 4.43) and is in fact seen for all comparisons of experimental and FE predicted transients. With FE modelling the minimum growth rate occurs around 0.15 $r_{p(OL)}$, which is slightly less than the experimental values of ~ 0.4 $r_{p(OL)}$ and 0.5 $r_{p(OL)}$ for 2024 and 2024A respectively. The strip yield models predict minimum growth rates of about 6% and 4% of the baseline growth rates for 2024 and 2024A respectively, which are clearly of the same order as the experimental values. The affected distance is about 50% of the experimental results however, consistent with the relatively short closure transients associated with strip yield models as discussed previously. Such an underestimate of plane strain overload transient distances has been identified previously [Xu, 2001], with strip yield modelling being shown to give rather more accurate descriptions of plane stress overload transient distances, consistent with the plane stress formulation. Transient normalised growth rates predicted by the present analytical methods agree well with those of the experimental results, in terms of transient magnitude and length

Whilst normalised growth rate plots (as in Figure 4.52) are clearly able to compare overload growth rates in relation to the baseline rates, it is possible that they may 'hide' differences in the actual growth rate. Figure 4.53 shows the predicted growth rates of the FE, analytical and strip yield models with experimental results from Xu [2001]. It can be seen that baseline growth rates predicted by strip yield models are slightly lower than the experimental results: overall however, for the conditions shown, overload growth predicted by strip yield and analytical models appears to be of the correct order. At this point it is valuable to recognise again the degree of fitting involved in the analytical and strip yield methods. The choice of α in the Figure 4.52 and 4.53 in the strip yield model is giving an acceptable approximation of baseline *da/dN* and peak overload transient effects for experiments that are designed (via sample side grooving in particular) to be plane strain dominated. The analytical

modelling involves the fitting parameter β_I being set to 1.3 and the presumption that PICC effects will dominate overload behaviour, whilst baseline growth conditions are simply re-established when PICC overload closure effects diminished below those of RICC affected CA growth, where Chapter 3 has established that a value of 2.0 for the associated β_{II} fitting parameter yields reasonably accurate CA closure conditions for a range of ΔK levels. It is of course valuable to assess how the models perform for different loading conditions where plane strain loading is similarly maintained, and hence the underlying fitting parameter values should remain appropriate.

- $\Delta K_{(BL)} = 8.0$ MPa $m^{1/2}$, $R = 0.1$, $\%OL = 100$

Figure 4.54 shows a comparison of normalised growth rates from strip yield and analytical models with that of experimental results (Xu, 2001) for a lower baseline load, $\Delta K_{(BL)} = 8.0$ MPa $m^{1/2}$, ($R = 0.1$, $\%OL = 100$). The experimental results are again for 2024 and 2024A with $U_{(BL)} \cong 0.6$ and 0.5 respectively (see Figure 4.45). Experimental baseline closure levels are adopted for analytical models as discussed previously. $U_{(BL)}$ from strip yield models are approximately 0.57 for both the alloys, as fixed by the α value. Shorter growth rate transients are again produced by strip yield modelling as compared to experimental results, with the analytical models predicting a close agreement with experimental results. Figure 4.54 is re-plotted in Figure 4.55 without normalisation by baseline growth rates. Again it can be seen that analytical models predict a closer crack growth in good agreement with the experimental results as compared to strip yield model results, with the strip yield method showing an increasing discrepancy in baseline growth predictions (c.f. Figure 4.55). This is particularly in terms of the baseline closure conditions of the two alloys, which is not differentiated by the strip yield approach.

- $\Delta K_{(BL)} = 12.0$ MPa $m^{1/2}$, $R = 0.1$, $\%OL = 50$

To assess the effect of lowering overload ratio to 50%, a comparison of normalised growth rates is shown in Figure 4.56. It can be seen that experimental minimum growth rates for both alloys are approximately 50% of the baseline growth compared to the 100% OL case, consistent with the reduction in overload level. Predicted normalised minimum growth rates from both strip yield and analytical models appear to agree well the experimental results, although the strip yield model shows shorter

transients once more. Predicted and experimental growth rates are again plotted without normalisation in Figure 4.57, where it can see that analytical appears to perform better as compared to the strip yield models.

- $\Delta K_{(BL)} = 8.0$ MPa $m^{1/2}$, $R = 0.1$, $\%OL = 50$

Figure 4.58 shows a comparison of normalised experimental (Xu, 2001) and predicted growth rates for $\Delta K_{(BL)} = 8.0$ MPa $m^{1/2}$, $R = 0.1$, and $\%OL = 50$. It can be seen that experimental minimum growth rates are approximately 40% of the baseline growth rates and are well predicted by strip yield models. However, no transient is predicted by the analytical methods, because the baseline closure levels are found to be higher than those predicted post-overload. Comparison of experimental and predicted growth rates without normalisation are shown in Figure 4.59. At this point it is valuable to reconsider the PICC-only presumption of the analytical modelling. The data plotted in Figure 4.60 are representative of the lowest for $\Delta K_{(BL)}$ and $\%OL$ levels provided by Xu [2001], hence the implications for PICC dominance of overload behaviour should be considered. The maximum overload plastic zone size for Figure 4.59 is one sixth of that for Figure 4.52, corresponding to ~ 130 μm. The analytical and FE results presented in Figure 4.42b show that RICC enhancement of overload effects may rise for L value greater that 0.2 $r_{p(OL)}$, i.e. ~ 26 μm. This is in fact of the order of L values measured in these materials, and as such the assumption of pure PICC overload effects in the analytical results in Figure 4.58 and 4.59 may indeed be expected to break down. Selecting an $L \geq 68.15$ μm (i.e. $\geq 0.5\ r_{p(OL)}$) and a crack deflection angle of 40° for the RICC overload model described in Section 4.6, post overload closure behaviour for $\Delta K_{(BL)} = 8.0$ MPa $m^{1/2}$, $R = 0.1$, $\%OL = 50$ is plotted in Figure 4.60 using $\beta_{II} = 2$. It may be seen that a small transient is now predicted from the closure figures (overload closure levels now falls below the baseline closure levels), consistent with the current description of how RICC and PICC influences on transient behaviour may interact. The exact magnitude of the RICC overload interaction may in fact be modified by extending the model to 3D, as outlined in Chapter 3 for the CA RICC modelling. For the purposes of the present thesis however, the key point to note is that in the regime where RICC effects would appear to be necessary to fit with the experimental observations, the understanding of $L/r_{p(OL)}$ influence of the transition to RICC controlled overloads us at least of the correct order. Further assessment of the

model performance against experimental data (accounting for stress state influence such as in the work of Xu [2001] and Khor[2004]) would clearly of value in this respect. However, the results suggest that the mechanistic understanding of the present work can generate a simple but reasonably complete description of baseline and simple OL transient behaviour.

4.8 Conclusions

1. FE models of undeflected and deflected cracks during single overloads have been studied for a wide range of overload and asperity size regimes.
2. Effects of L/r_p ratios on deflected cracks during overloads are seen to be functionally similar to RICC under constant amplitude loading (particularly in the 'saturation' of RICC influence for $L/r_{p(OL)} \geq 1$).
3. A simple model for competitive influences of RICC and PICC effects during overloads has been developed and seen to be functionally comparable to FE results and consistent with a range of experimental data.
4. The present work is seen to map out regimes of loading where RICC and PICC effects may be expected to operate. In conjunction with CA closure understating of Chapter 3, a particularly complete description of overload behavior is produced, with quantitative improvement in overload transient and baseline growth rate predictions over the popular strip yield approach. Whilst the present modeling may be seen as an additional complication over the strip yield (being based on knowledge of fracture surface parameters and involving two fitting parameter in β_I and β_{II}), it is asserted that this represents a more physically correct and therefore a fundamentally more powerful approach.
5. Detailed comparison of OL transient predictions has been made for FE, Strip yield type and simple analytical closure models:
   - For test conditions of interest, simple analytical model found to provide a reasonable description of single OL behaviour, particularly when baseline closure effects are considered
   - The strip yield type approach is seen to be fundamentally limited by choice of α and corresponding ability to treat baseline closure effects

- PICC can be used to explain much of the OL transient behaviour investigated experimentally

A

%OL	$\Delta K_{(BL)}$ in MPa $m^{1/2}$					
	4.6	8.5	10.0	12.0	15.0	17.0
0.0 (CA)				♣♦		
25.0				♣		
50.0	♣	♣	♣	♣	♣	♣
75.0				♣		
100.0	♣	♣	♣	♣♦	♣	♣
150.0	♣	♣	♣	♣♦	♣	♣

B

%OL	$\Delta K_{(BL)}$ in MPa $m^{1/2}$									
	4.6	8.5		10.0	12.0				15.0	17.0
	L in μm									
	225.0	37.5	150.0	150.0	18.75	37.5	75.0	150.0	150.0	150.0
50.0	♣		♣				♣	♣		
100.0	♣	♣	♣♦	♣	♣	♣♦	♣	♣♦	♣	♣♦
150.0	♣		♣				♣	♣♦		

♣ Analyses performed
♦ Results compared directly with Parry (Parry, 2000)

Table 4.1. Analysis matrix for (a) undeflected and (b) deflected cracks subjected to variable amplitude (single overload) loading ($R = 0.1$).

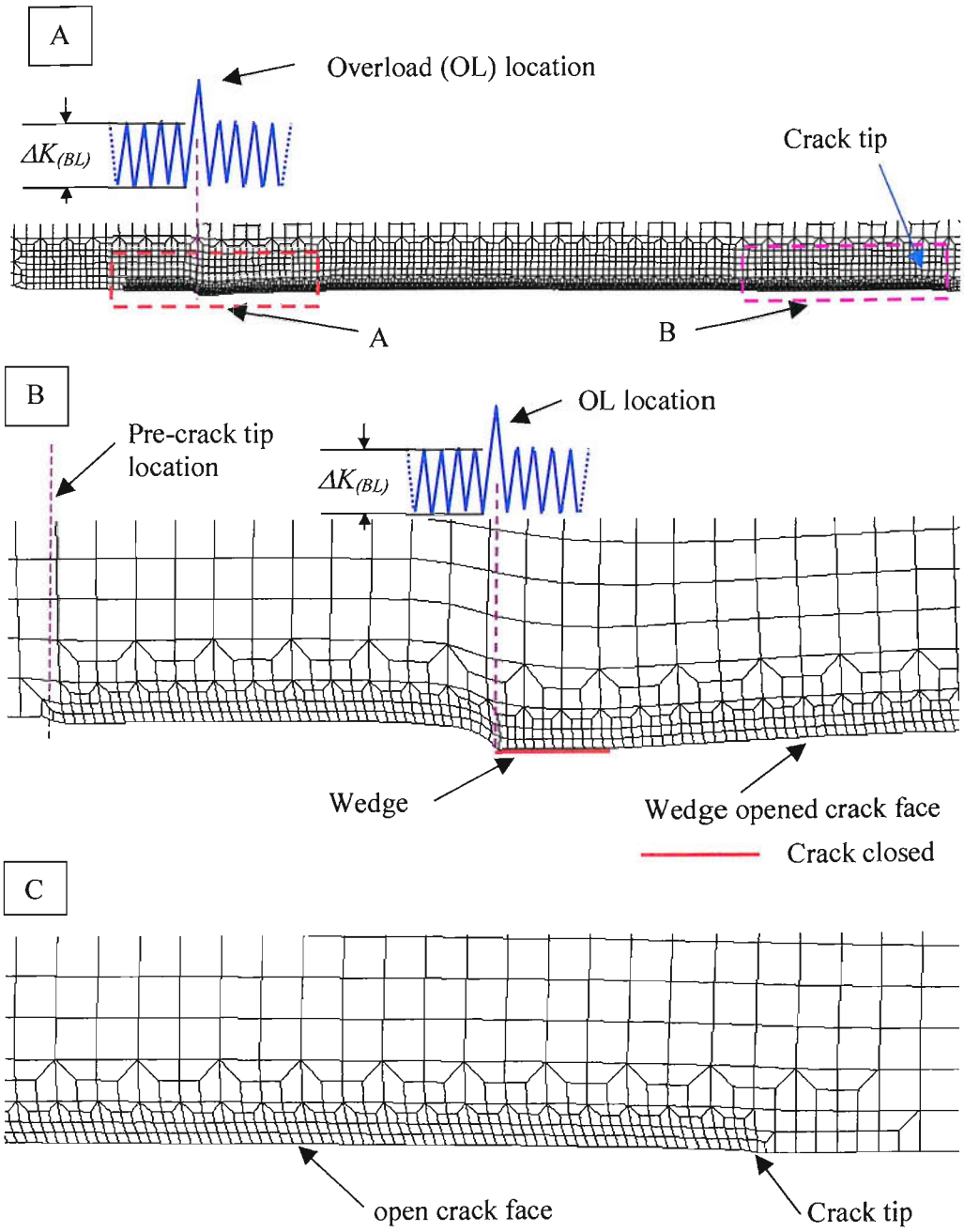

Figure 4.1: Deformed mesh (a) for an undeflected crack, showing the location of a single overload, $\Delta K_{(BL)}$ = 12.0 MPa $m^{1/2}$, R = 0.1, $\%OL$ = 100.0., (b) at closure onset (K_{cl}/K_{max} = 0.244) showing contact near the overload location (region A of Figure 4.1a) and (c) at closure showing opening of near tip region (region B of Figure 4.1a). Displacement magnification x10.

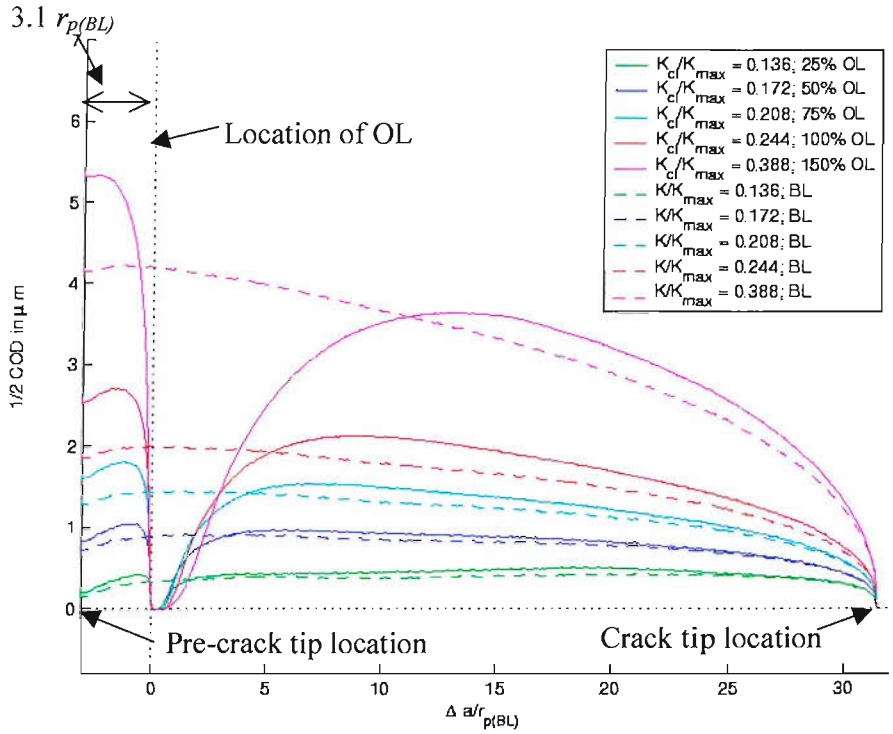

Figure 4.2: COD profiles, $\Delta K_{(BL)}$ = 12.0 MPa m$^{1/2}$, R = 0.1, of undeflected cracks having undergone various overload conditions. Overload applied at $\Delta a/r_{p(BL)} = 0$.

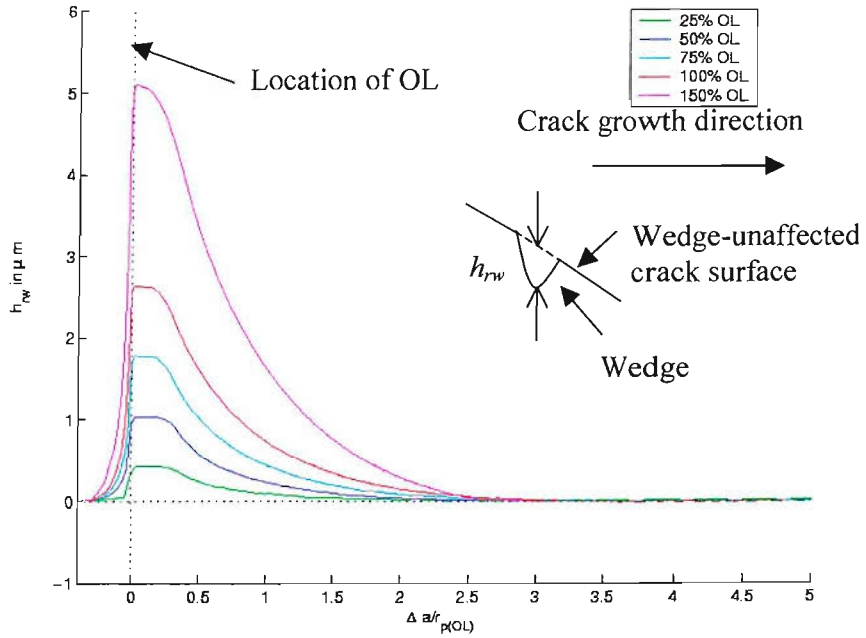

Figure 4.3: Variation of residual wedge size (h_w) with overload level, $K_{(BL)}$ = 12.0 MPa m$^{1/2}$, R = 0.1. Overload applied at $\Delta a/r_{p(OL)} = 0$.

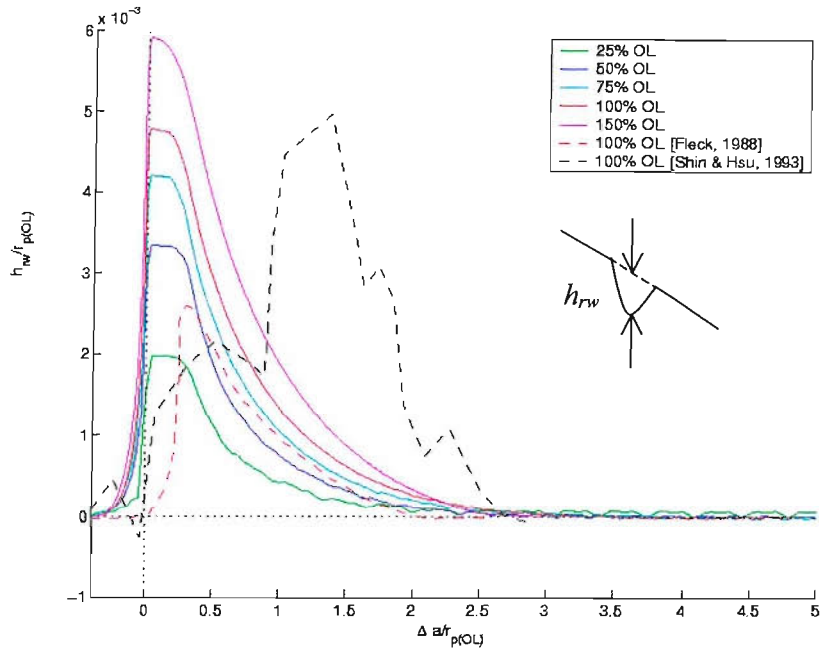

Figure 4.4: Variation of normalised residual wedge size ($h_{rw}/r_{p(OL)}$) with overload level, $\Delta K_{(BL)}$ = 12.0 MPa m$^{1/2}$, R = 0.1, σ_y=370 MPa for present study; $\Delta K_{(BL)}$ = 25.0 MPa m$^{1/2}$, R = 0.05, σ_y=352 MPa, for Fleck [1988], $\Delta K_{(BL)}$ = 22.0 MPa m$^{1/2}$, R = 0.1, σ_y=340 MPa, for Shin and Hsu [1993]. Overload applied at $\Delta a/r_{p(OL)}$ = 0.

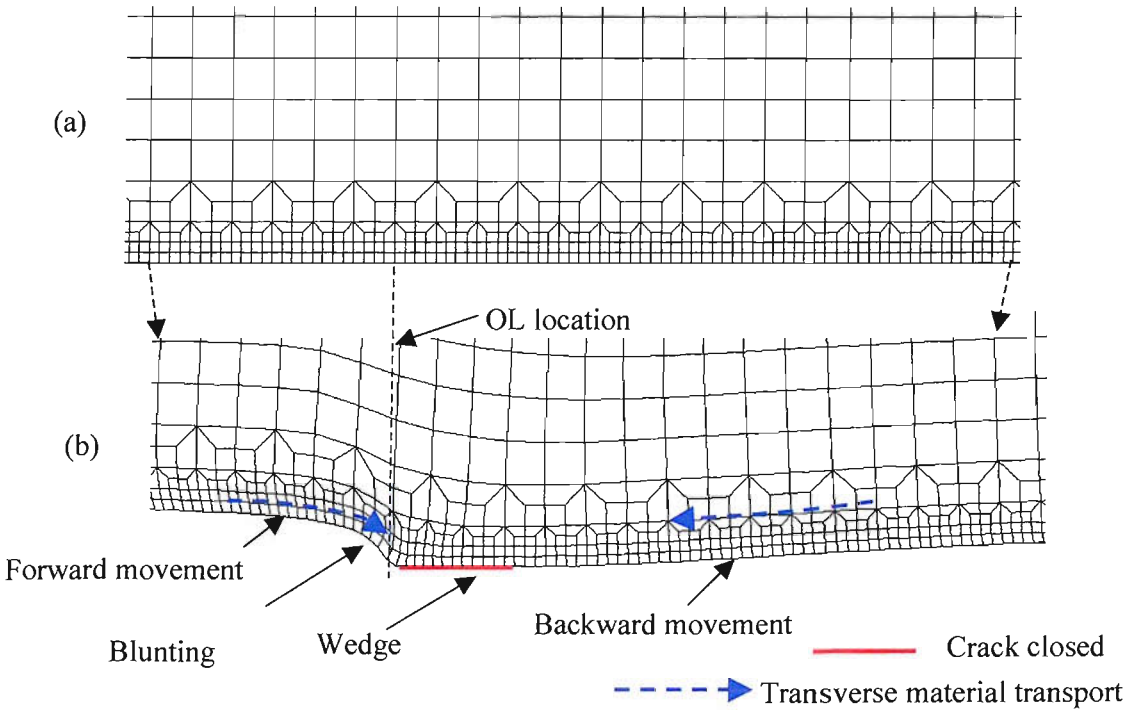

Figure 4.5: a) Undeformed mesh and b) deformed mesh at closure (K_{cl}/K_{max} = 0.388), near the OL location showing direction of the transverse material transport which results in the residual wedge formation, $\Delta K_{(BL)}$ = 12.0 MPa m$^{1/2}$, R = 0.1, $\%OL$ = 150. Displacement magnification x10.

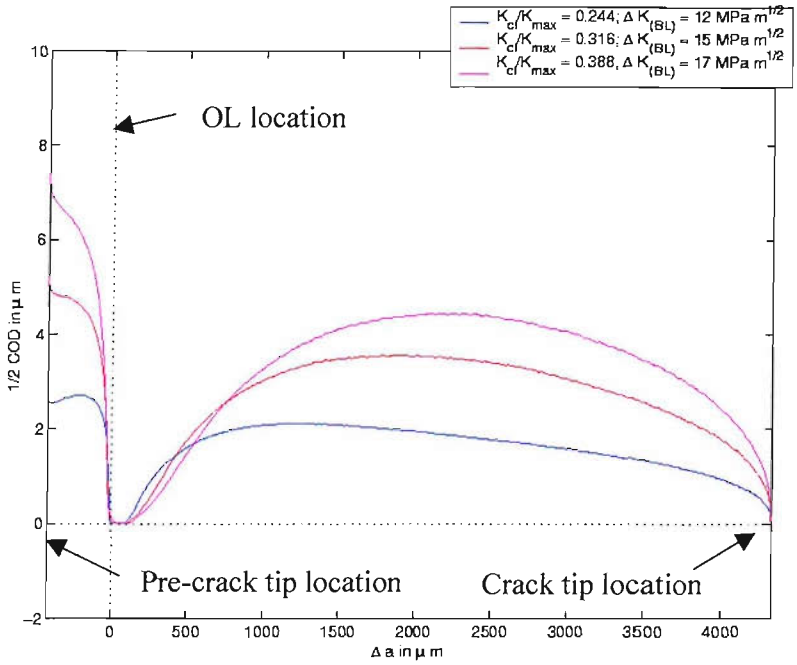

Figure 4.6: COD profiles of undeflected cracks having undergone various baseline conditions, $R = 0.1$, $\%OL = 100$. Overload applied at $\Delta a = 0$.

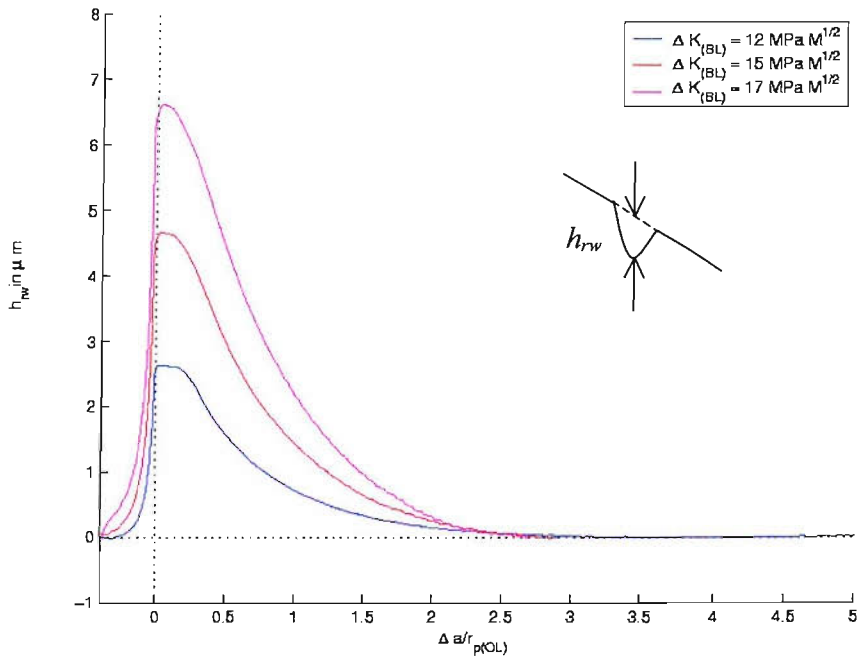

Figure 4.7: Variation of residual wedge size (h_{rw}) with baseline load, $R = 0.1$, $\%OL = 100$. Overload applied at $\Delta a/r_{p(OL)} = 0$.

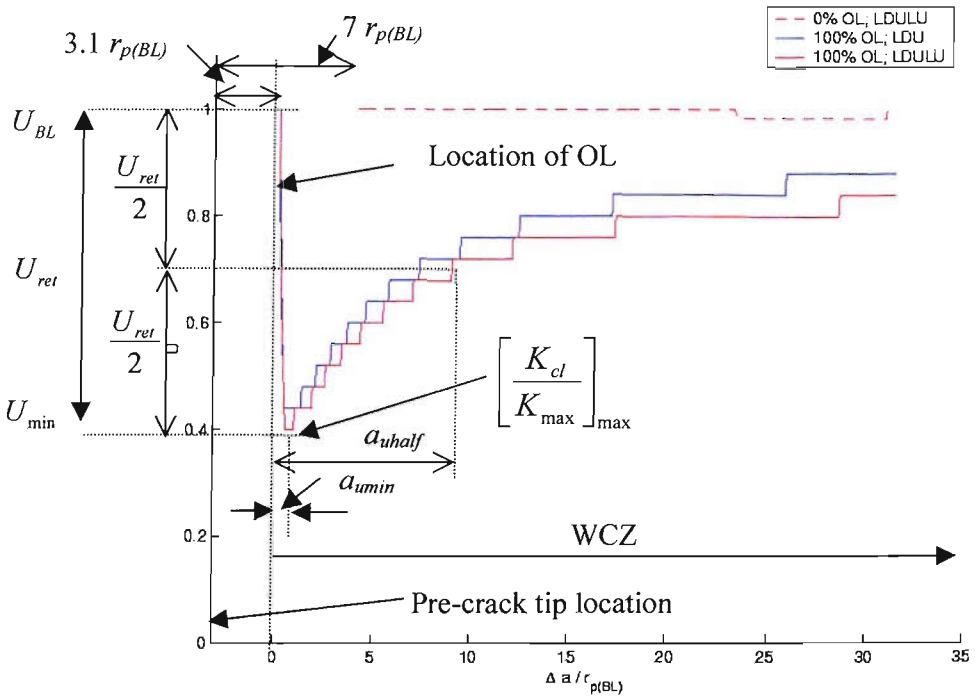

Figure 4.8: Comparison of the FE models using LDU [Parry, 2000] and LDULU (present study) methods for closure level determination of an undeflected crack, $\Delta K_{(BL)}$ = 12.0 MPa m$^{1/2}$, R = 0.1, $\%OL$ = 100. Overload applied at $\Delta a/r_{p(BL)}$ = 0.

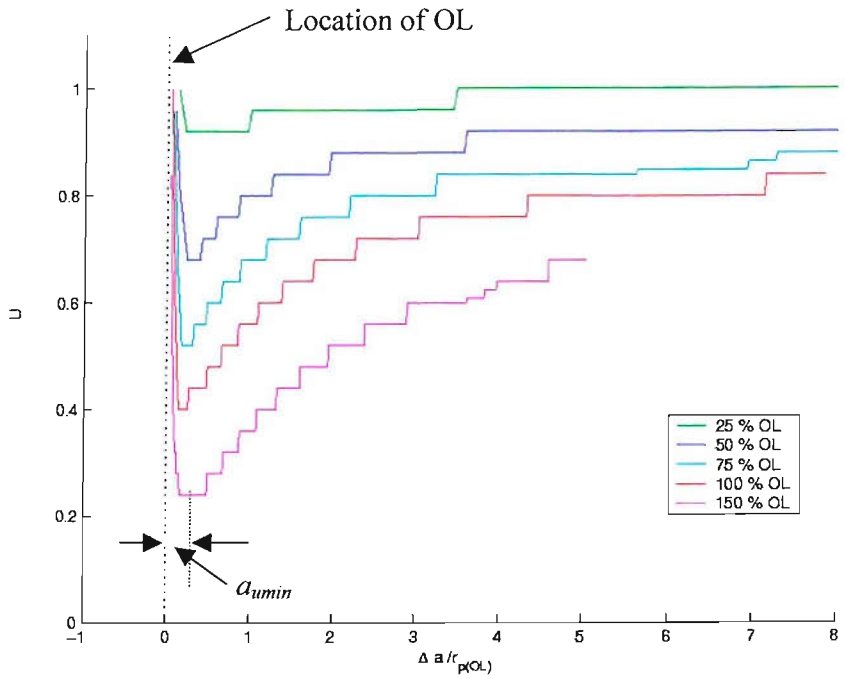

Figure 4.9: Effect of overload ratio on the crack closure behaviour for an undeflected crack, $\Delta K_{(BL)}$ = 12.0 MPa m$^{1/2}$, R = 0.1. Overload applied at $\Delta a/r_{p(BL)}$ = 0.

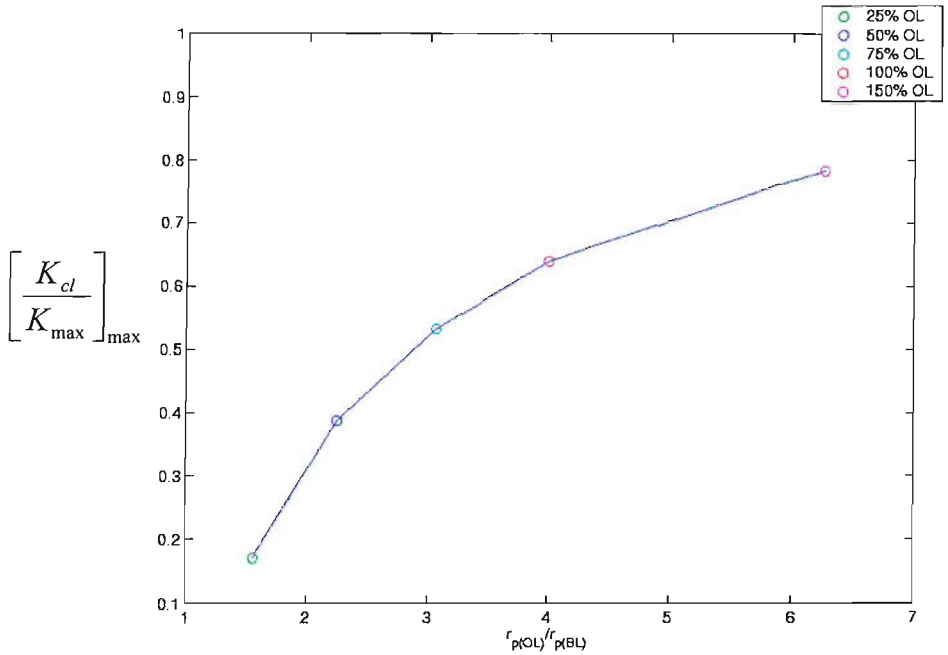

Figure 4.10: Variation of maximum closure levels ($[K_{cl}/K_{max}]_{max}$), $\Delta K_{(BL)}$ = 12.0 MPa $m^{1/2}$, R = 0.1.

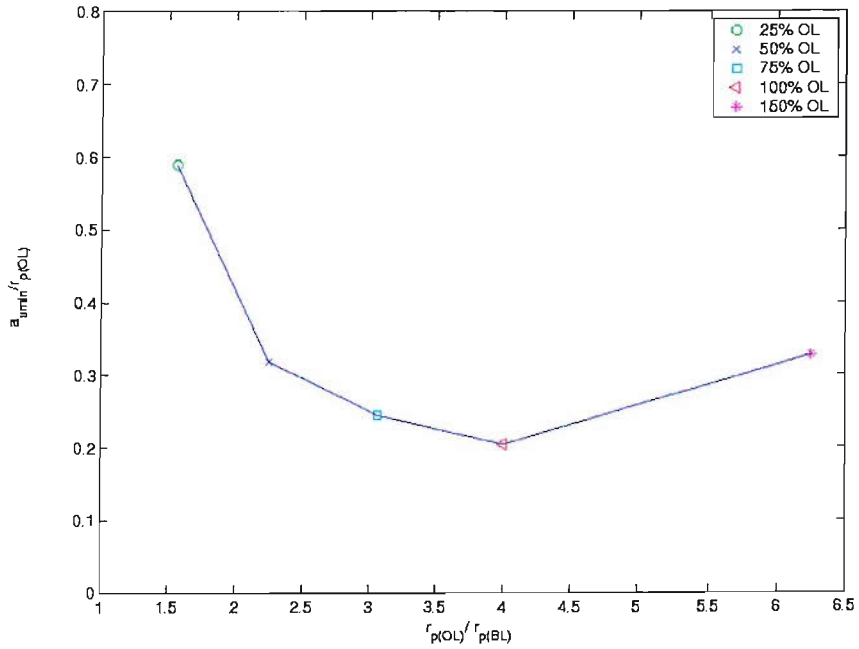

Figure 4.11: Variation of normalised a_{umin} ($a_{umin}/r_{p(OL)}$), $\Delta K_{(BL)}$ = 12.0 MPa $m^{1/2}$, R = 0.1.

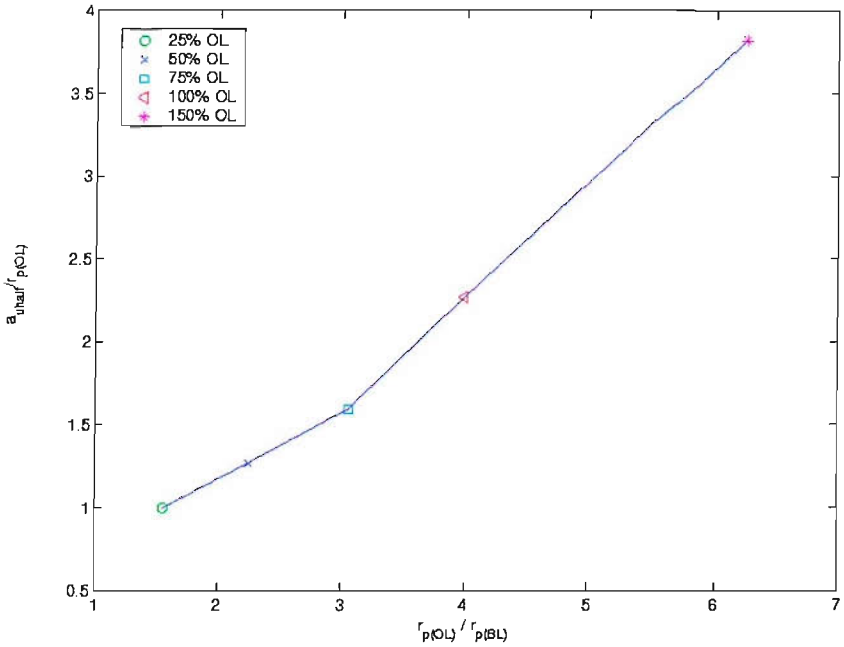

Figure 4.12: Variation of normalised a_{uhalf} ($a_{uhalf}/r_{p(OL)}$), $\Delta K_{(BL)}$ = 12.0 MPa m$^{1/2}$, R = 0.1.

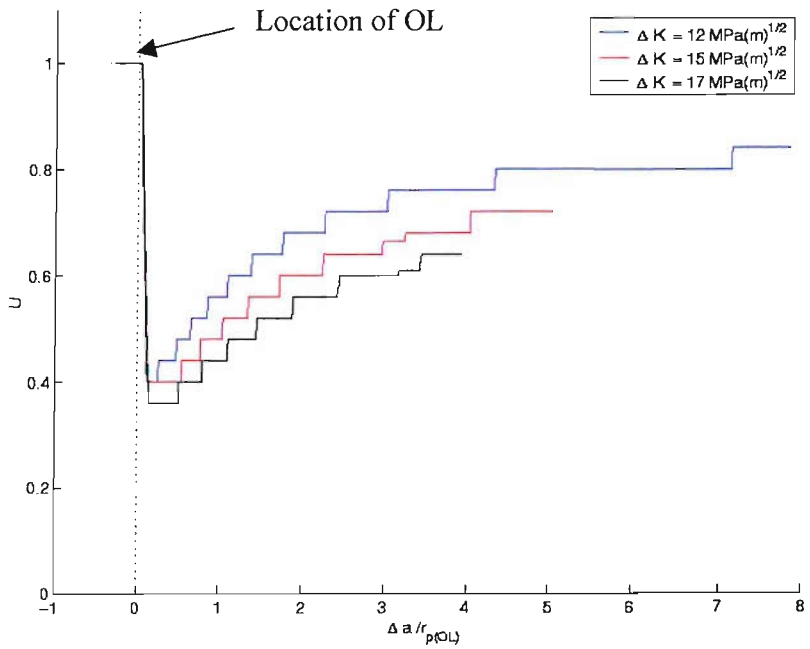

Figure 4.13: Variation of closure levels for different $\Delta K_{(BL)}$ for an undeflected crack, $\%OL$ = 100, R = 0.1. Overload applied at $\Delta a/r_{p(BL)}$ = 0.

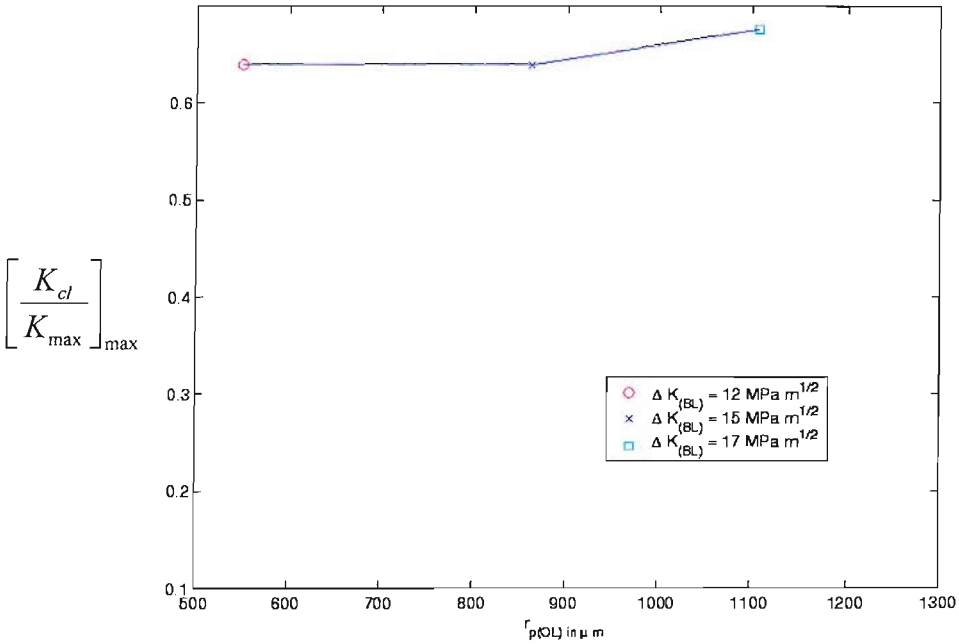

Figure 4.14: Variation of maximum closure levels ($[K_{cl}/K_{max}]_{max}$) with $r_{p(OL)}$, $\%OL$ = *100*, $R = 0.1$.

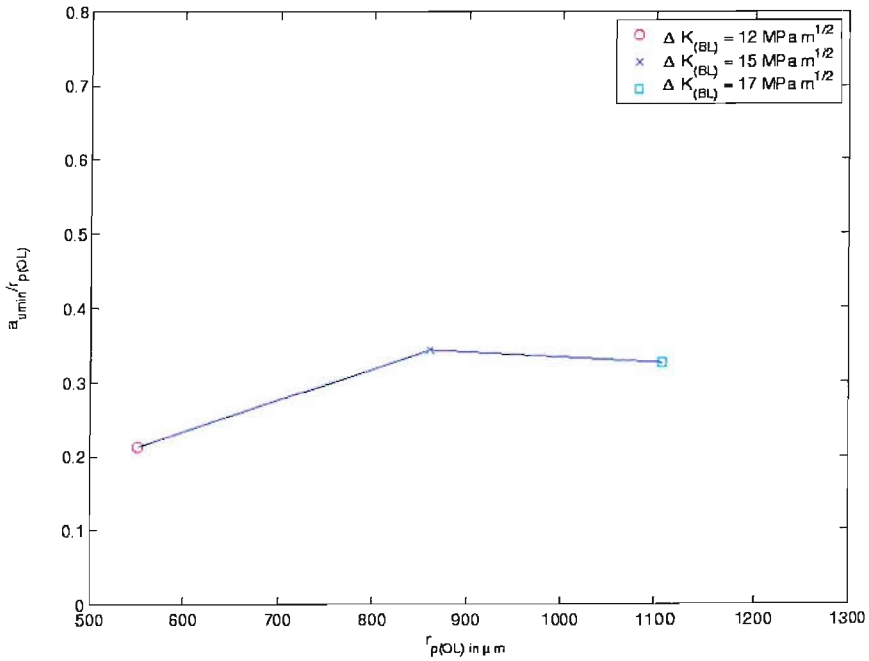

Figure 4.15: Variation of normalised a_{umin} ($a_{umin}/r_{p(OL)}$) with $r_{p(OL)}$, $\%OL$ = 100, R = 0.1.

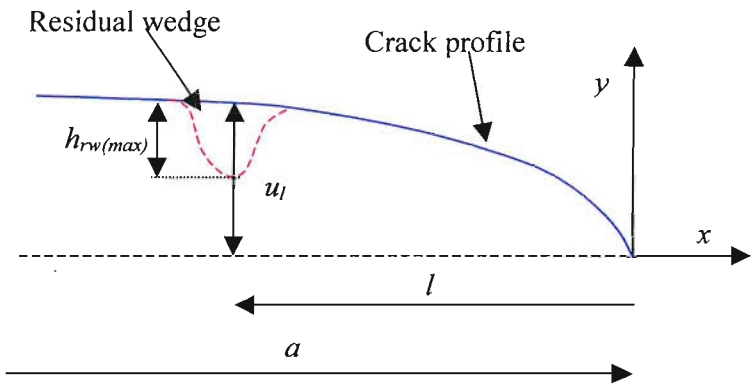

Figure 4.16: Schematic diagram showing residual wedge due to a tensile overload in a straight crack wake.

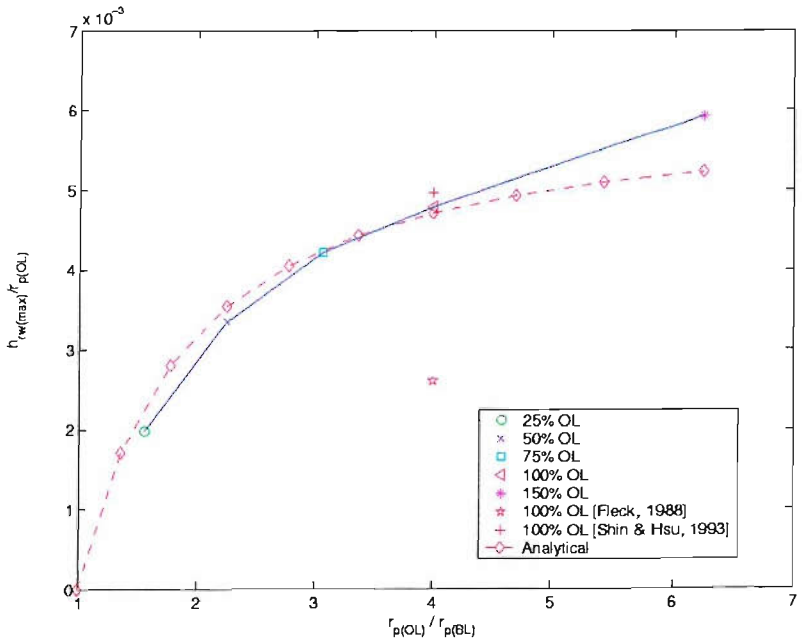

Figure 4.17: Normalised $h_{rw(max)}$ variation for $\Delta K_{(BL)}$ = 12.0 MPa m$^{1/2}$, R = 0.1 (β_l = 1.0).

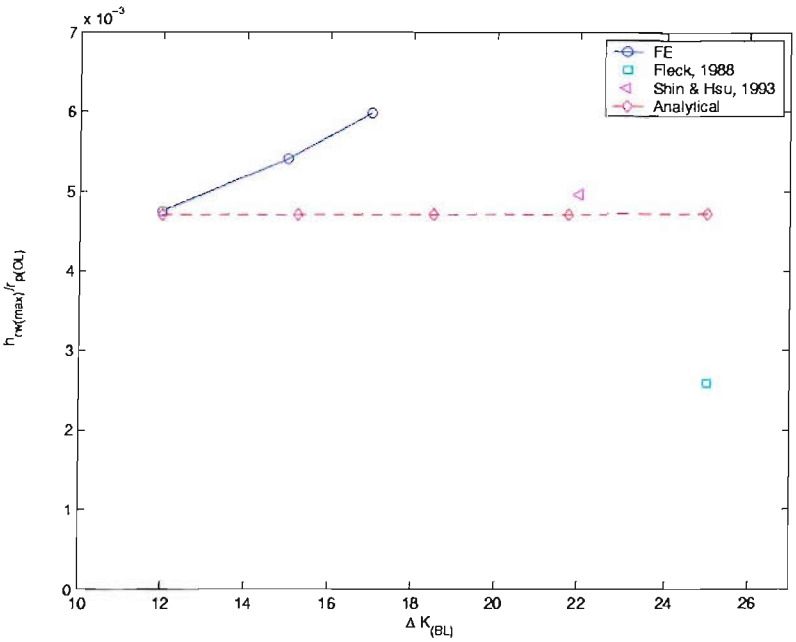

Figure 4.18: Normalised $h_{rw(max)}$ variation for $\%OL$ = 100, $R = 0.1(\beta_1 = 1.0)$.

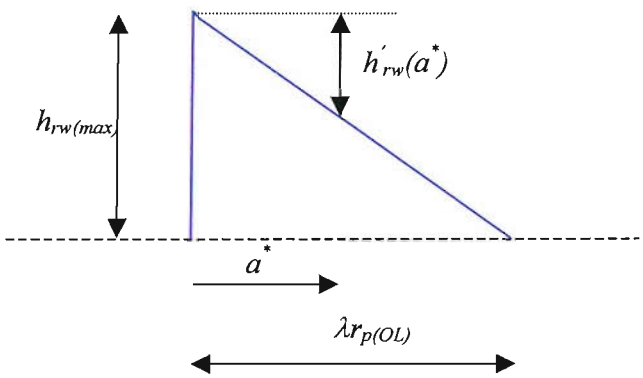

Figure 4.19: Approximation of OL residual wedge variation h_{rw} (undeflected crack).

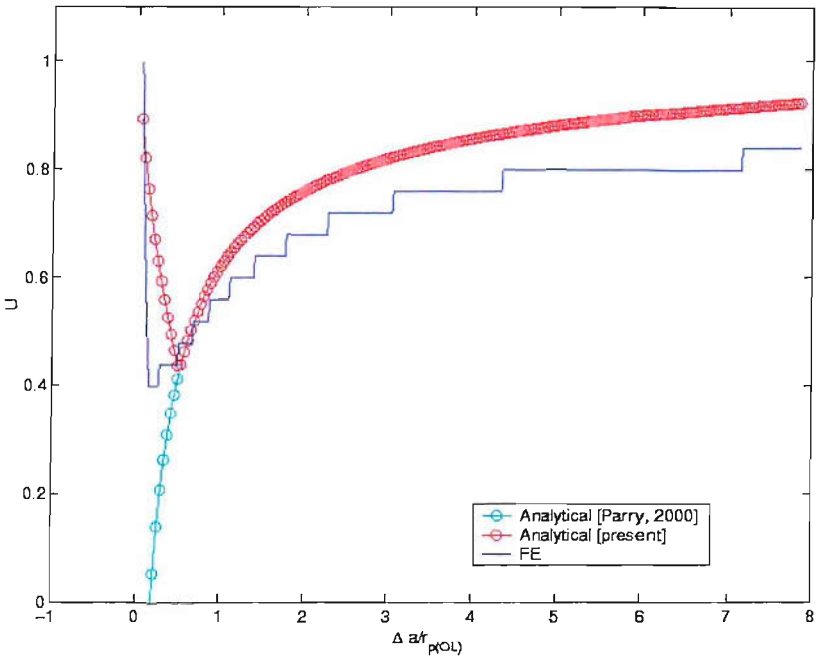

Figure 4.20: Comparison of FE and analytical results for single overloads in terms of closure effect; $\Delta K_{(BL)}$ = 12.0 MPa m$^{1/2}$, R = 0.1, $\%OL$ = 100, λ = 0.5, β_I = 1.0.

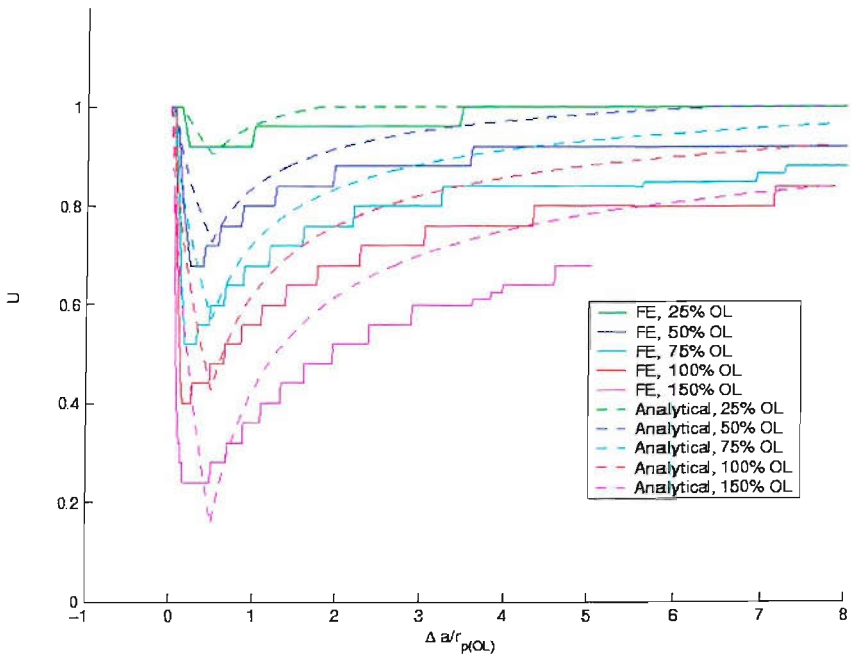

Figure 4.21: Comparison of FE and analytical closure level variation for $\Delta K_{(BL)}$ = 12.0 MPa m$^{1/2}$, R = 0.1, λ = 0.5, β_I = 1.0.

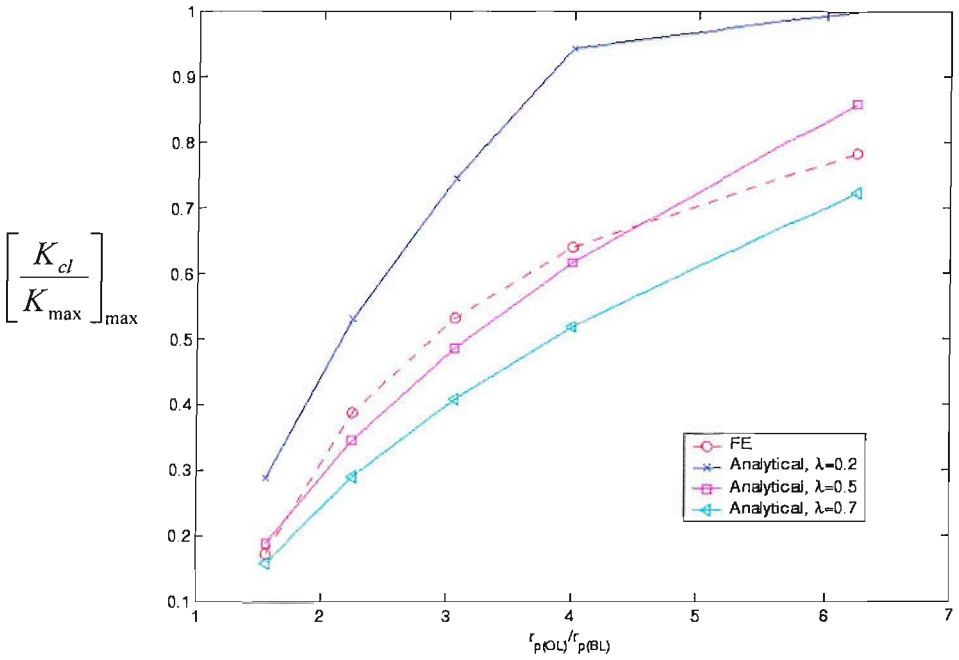

Figure 4.22: Comparison of FE and analytical maximum closure levels ($[K_{cl}/K_{max}]_{max}$) for different values of α; $\Delta K_{(BL)}$ = 12.0 MPa m$^{1/2}$, R = 0.1, β_1 = 1.0.

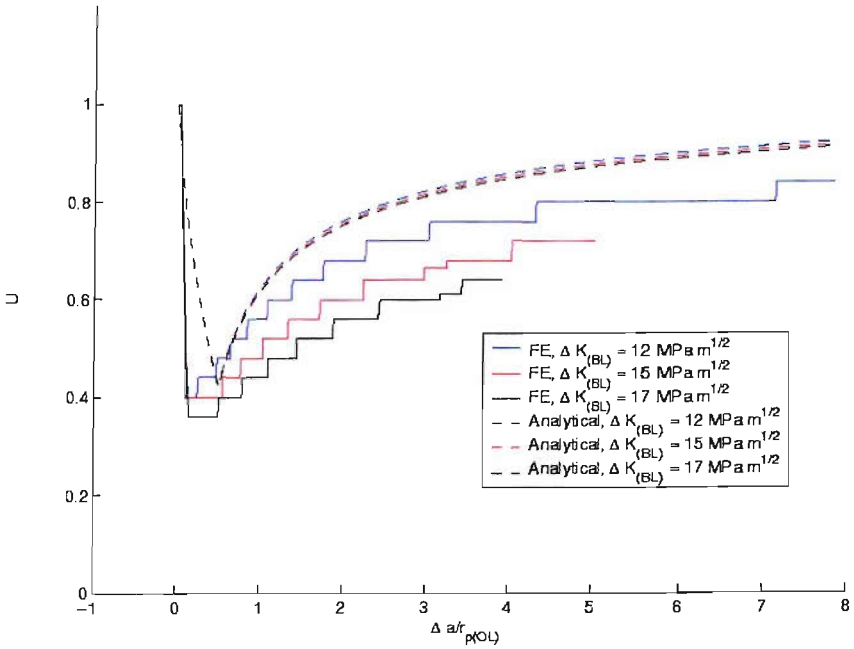

Figure 4.23: Comparison of FE and analytical closure level variation for R = 0.1, $\%OL$ = 100, λ = 0.5, β_1 = 1.0.

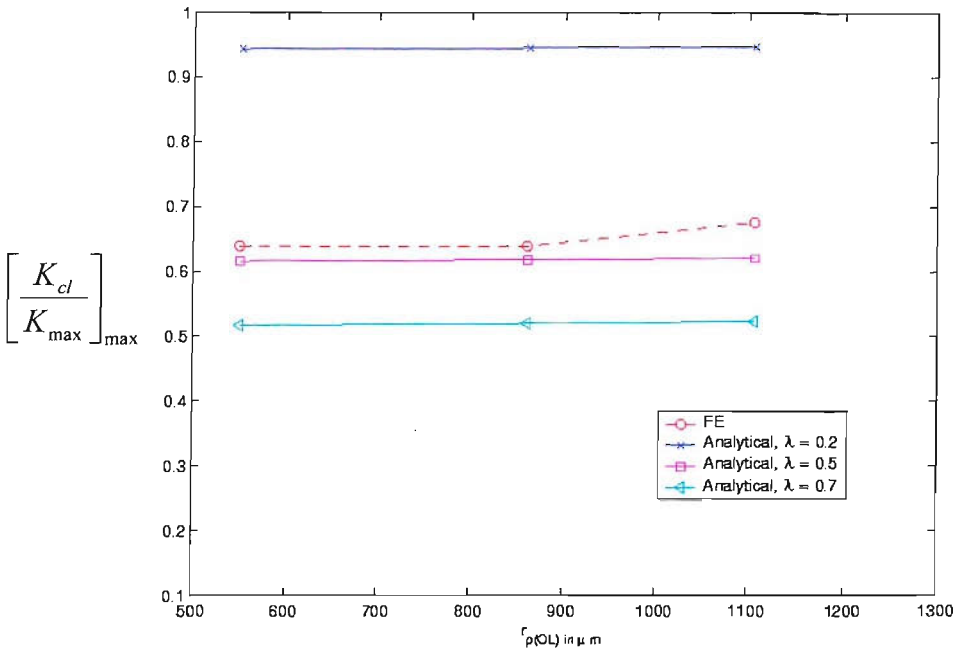

Figure 4.24: Comparison of FE and analytical maximum closure level ($[K_{cl}/K_{max}]_{max}$) for different value of α; $R = 0.1$, $\%OL = 100$, $\lambda = 0.5$, $\beta_l = 1.0$.

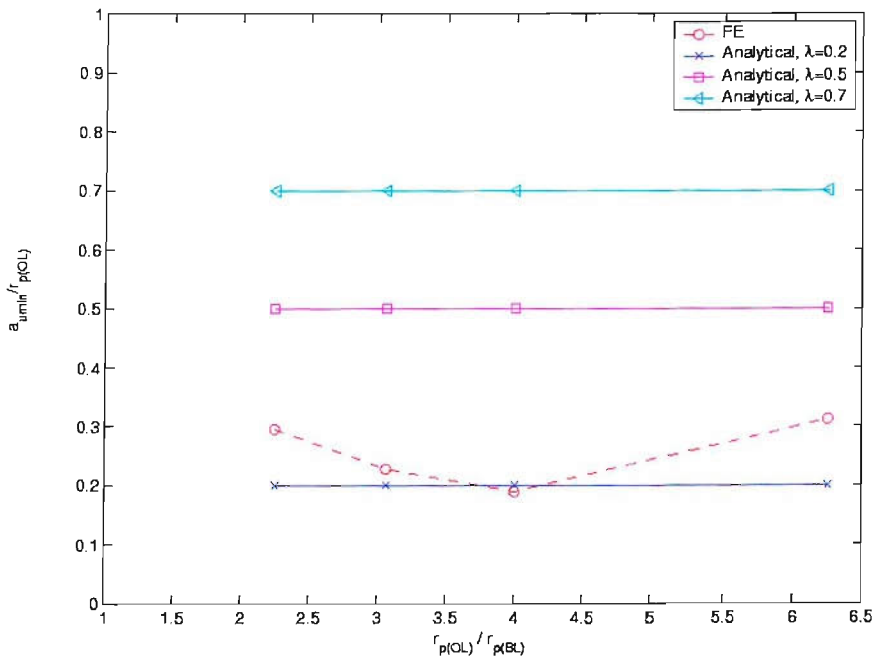

Figure 4.25: Comparison of normalised a_{umin} ($a_{umin}/r_{p(OL)}$) for $\Delta K_{(BL)} = 12.0$ MPa $m^{1/2}$, $R = 0.1$, $\lambda = 0.5$, $\beta_l = 1.0$ for $\%OL = 25$, 50, 100 and 150.

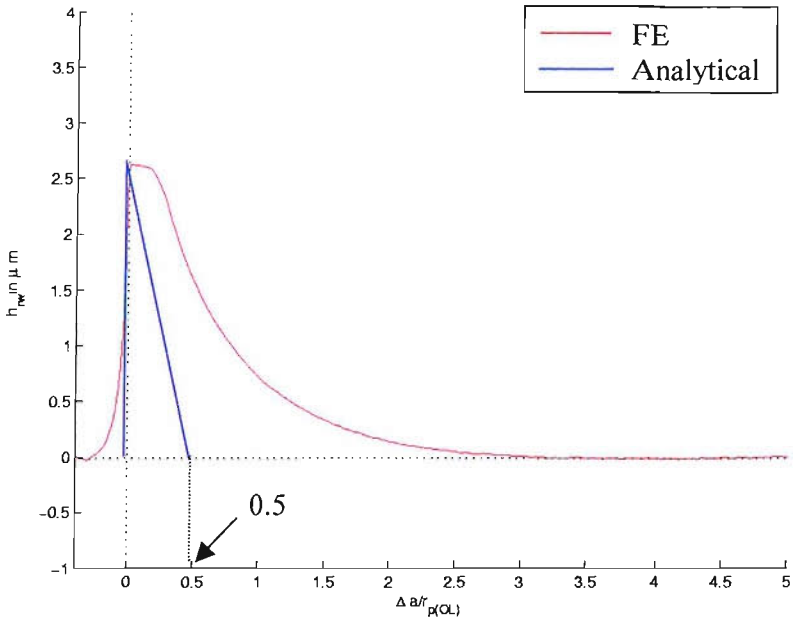

Figure 4.26: FE and analytical residual wedge profiles, $\Delta K_{(BL)}$ = 12.0 MPa m$^{1/2}$, R = 0.1, $\%OL$ =100.

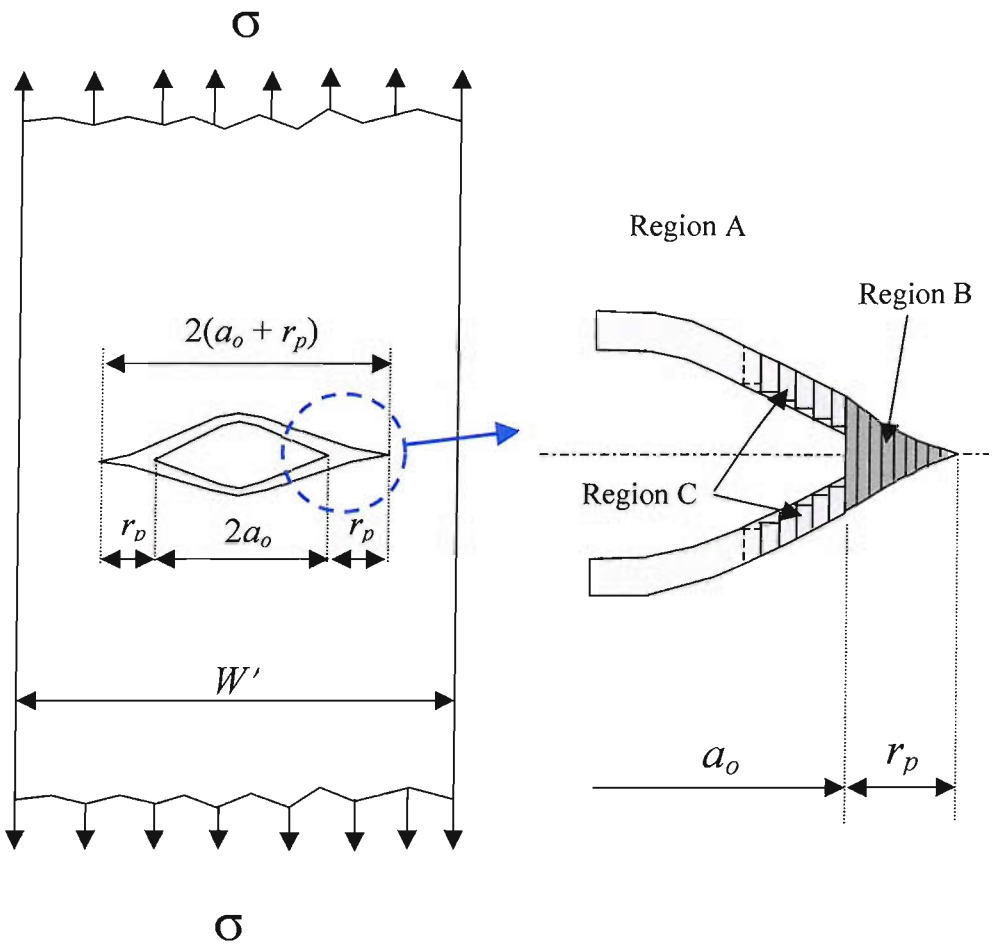

Figure 4:27a. Schematic diagram of the CCT specimen showing Dugdale type residual plastic deformations, identifying linear elastic region (Region A), plastic region ahead of the crack tip (Region B) and residual plastic deformation region along the crack surfaces (Region C) (after Newman, 1981 and Xu, 2001).

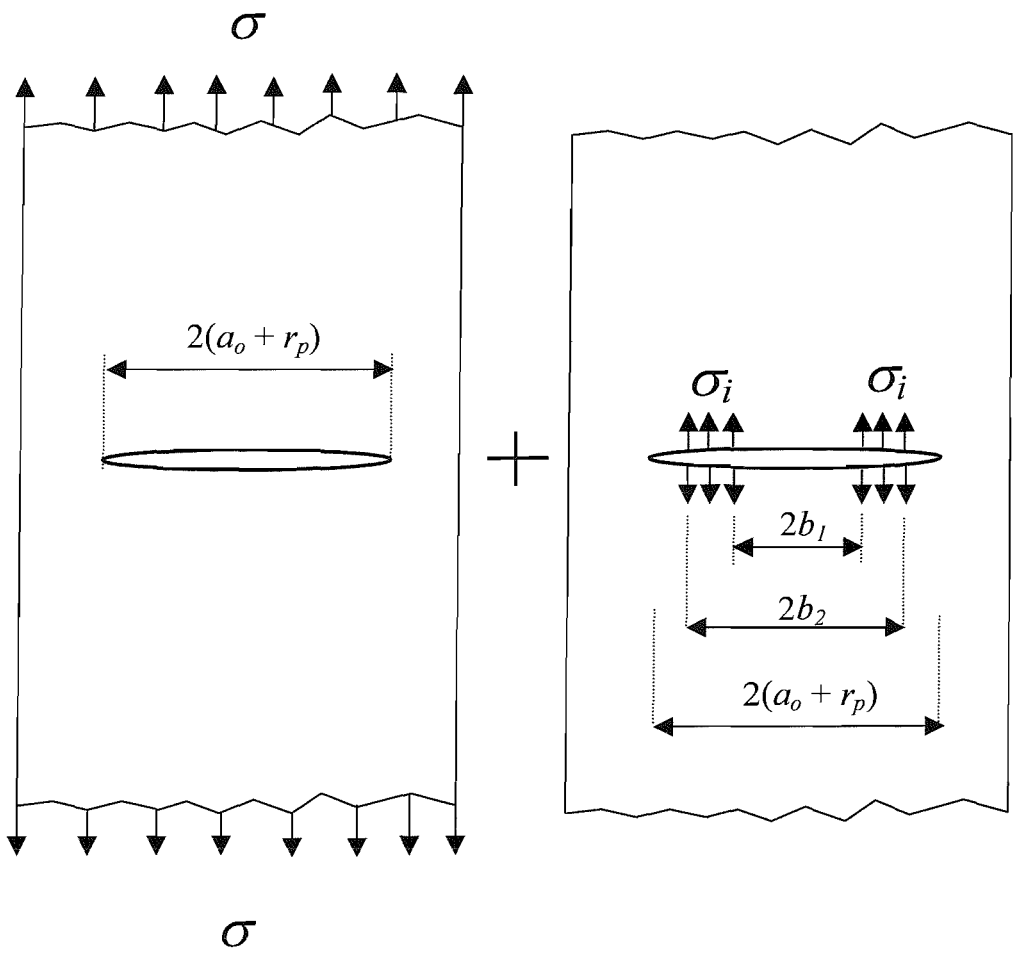

a) Remotely loaded crack

b) Partially loaded crack segment

Figure 4.27b: Schematic diagram showing superposition of two elastic problems of a CCT specimen subjected to a) remote uniform tensile stress (σ) and b) uniform stress (σ_i) over a segment of the crack surface (after Newman, 1981 and Xu, 2001).

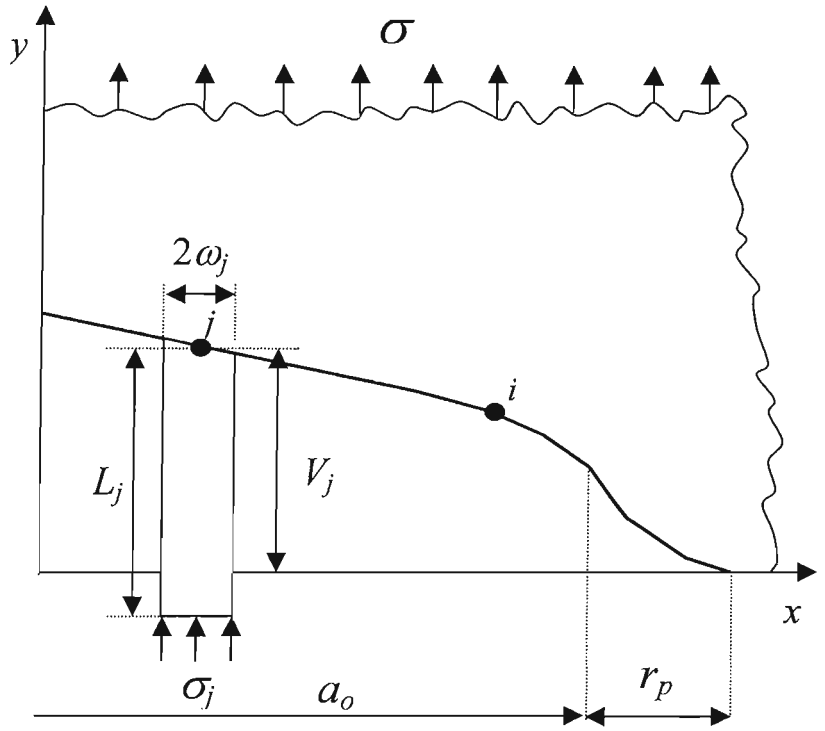

Figure 4.27c: Schematic diagram showing loading and coordinate system used in the analytical closure model (after Newman, 1981 and Xu, 2001).

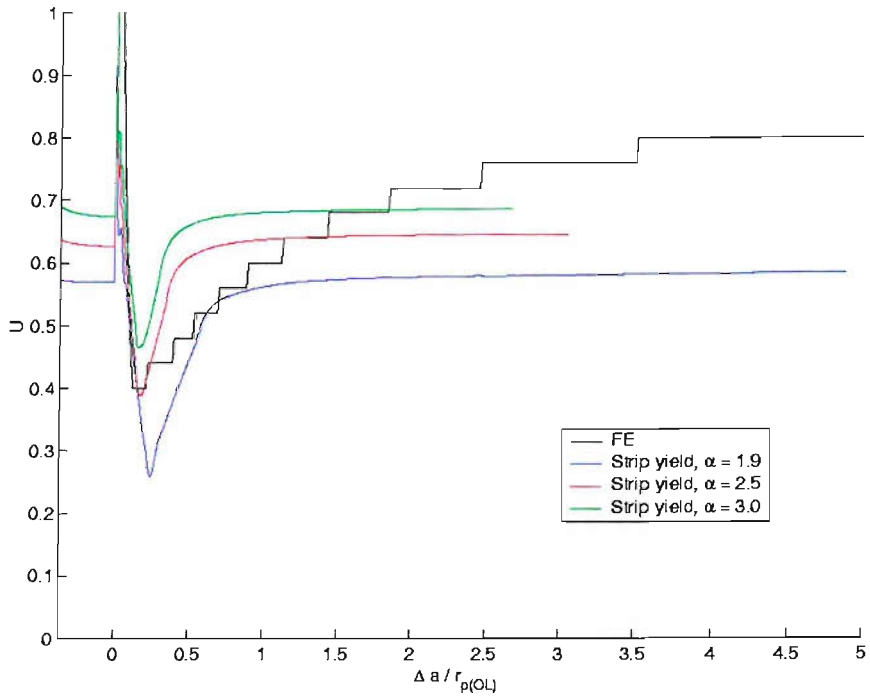

Figure 4.28: Comparison of FE and strip yield results for single overloads in terms of closure effects, $\Delta K_{(BL)}$ = 12.0 MPa m$^{1/2}$, R = 0.1, $\%OL$ = 100.

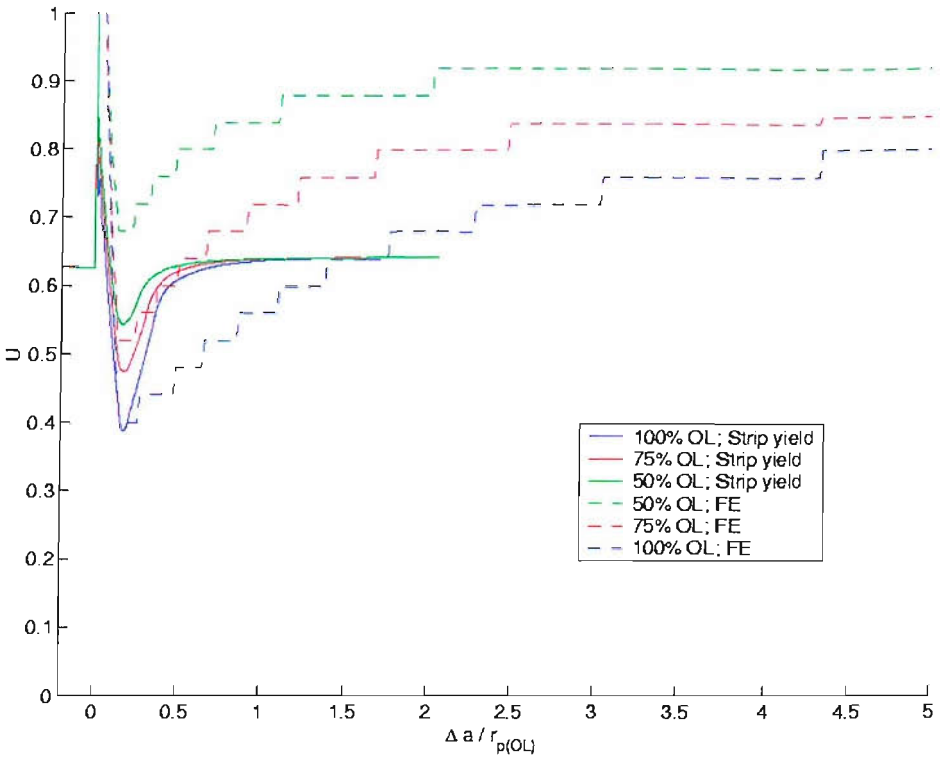

Figure 4.29: Comparison of FE and strip yield closure level variation, $\Delta K_{(BL)}$ = 12.0 MPa m$^{1/2}$, R = 0.1, α =2.5.

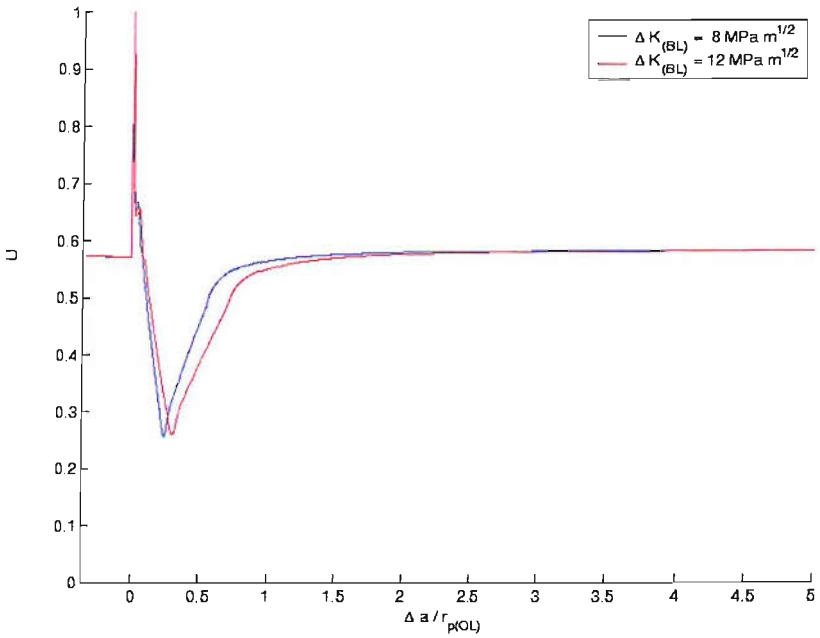

Figure 4.30: Variation of strip yield closure levels for different $\Delta K_{(BL)}$, $\%OL$ = 100, R = 0.1, α =2.5.

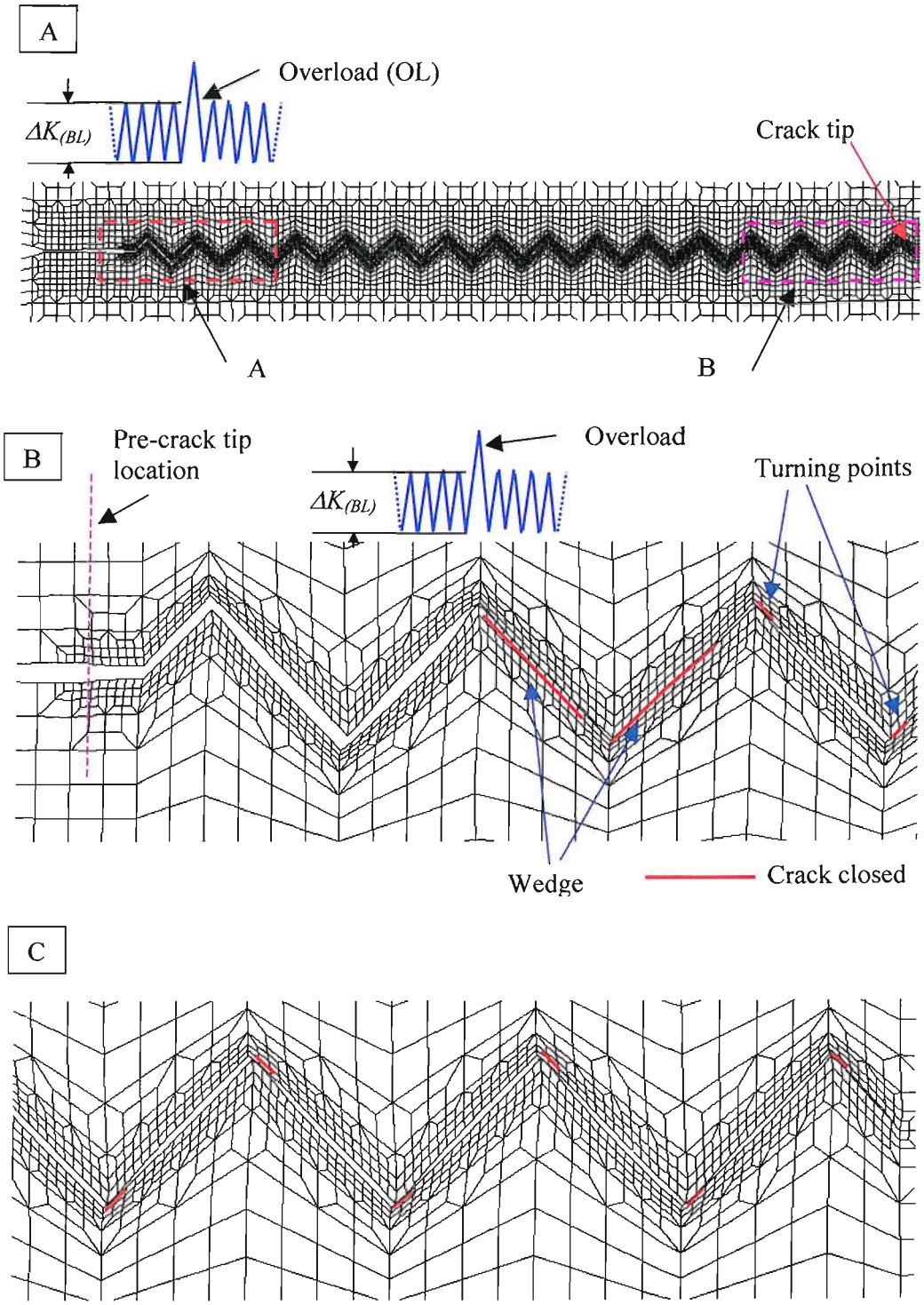

Figure 4.31: Deformed mesh for a deflected crack showing: (a) the location of a single overload, (b) contact at the turning points when unloaded fully (region A in Figure 4.31a) and (c) contact at the turning points when unloaded fully (region B in Figure 4.31a) for L = 150.0 μm, θ = 45°, $\Delta K_{(BL)}$ = 12.0 MPa m$^{1/2}$, R = 0.1, $\%OL$ = 100.0.. Displacement magnification x5.

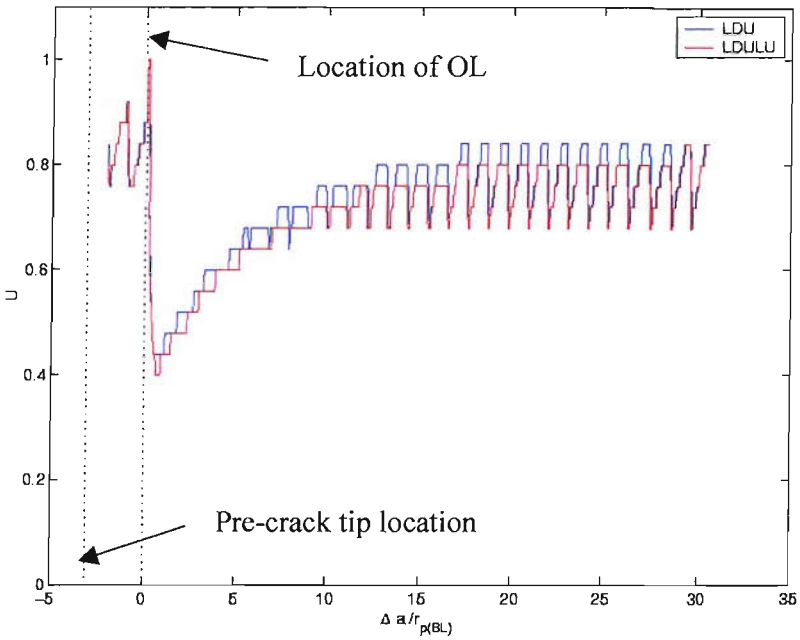

Figure 4.32: Comparison of LDU (Parry, 2000) and LDULU results under single overload, L = 150.0 μm, θ = 45°, $\Delta K_{(BL)}$ = 12.0 MPa m$^{1/2}$, R = 0.1, $\%OL$ = 100.0. Overload applied at $\Delta a/r_{p(BL)}$ = 0.0.

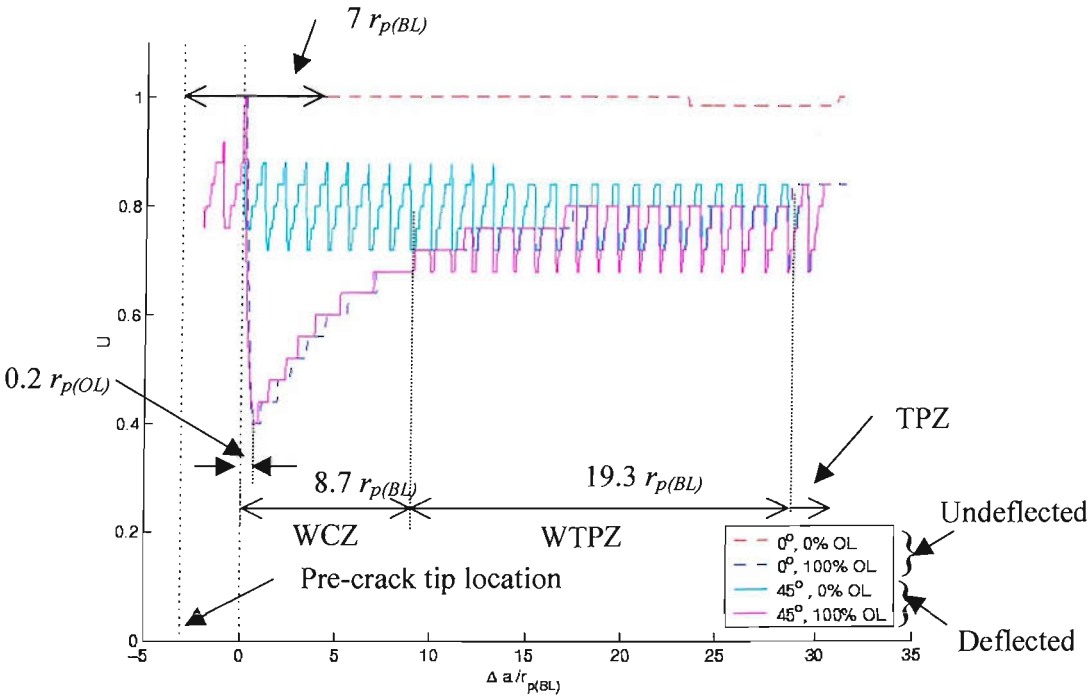

Figure 4.33 Identification of wedge controlled crack closure zone (WCZ), wedge and turning point controlled crack closure zone (WTPZ), and turning point controlled crack closure zone (TPZ) associated with the post-overload transient of a periodically deflected crack, L = 150.0 μm, θ = 45°, $\Delta K_{(BL)}$ = 12.0 MPa m$^{1/2}$, R = 0.1, $\%OL$ = 100.0. Overload applied at $\Delta a/r_{p(BL)}$ = 0.0.

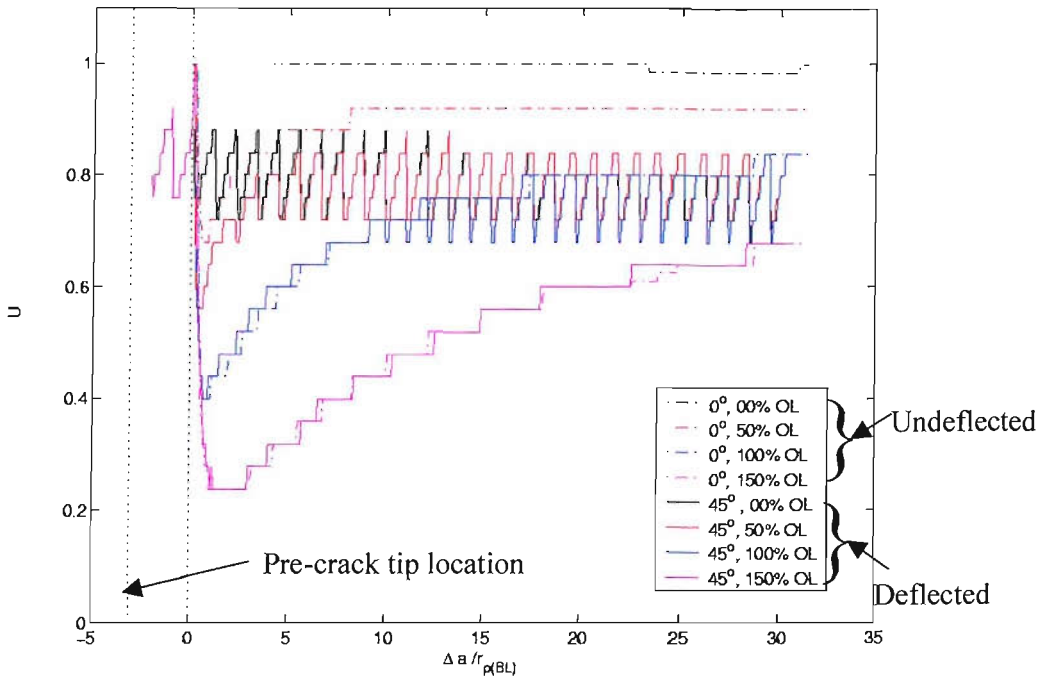

Figure 4.34: Effect of overload ratio on crack closure behaviour of undeflected and deflected cracks, L = 150.0 μm, θ = 45°, $\Delta K_{(BL)}$ = 12.0 MPa m$^{1/2}$, R = 0.1, $\%OL$= 0.0%, 50.0 %, 100.0 % and 150 %. Overload applied at $\Delta a/r_{p(BL)}$ = 0.0.

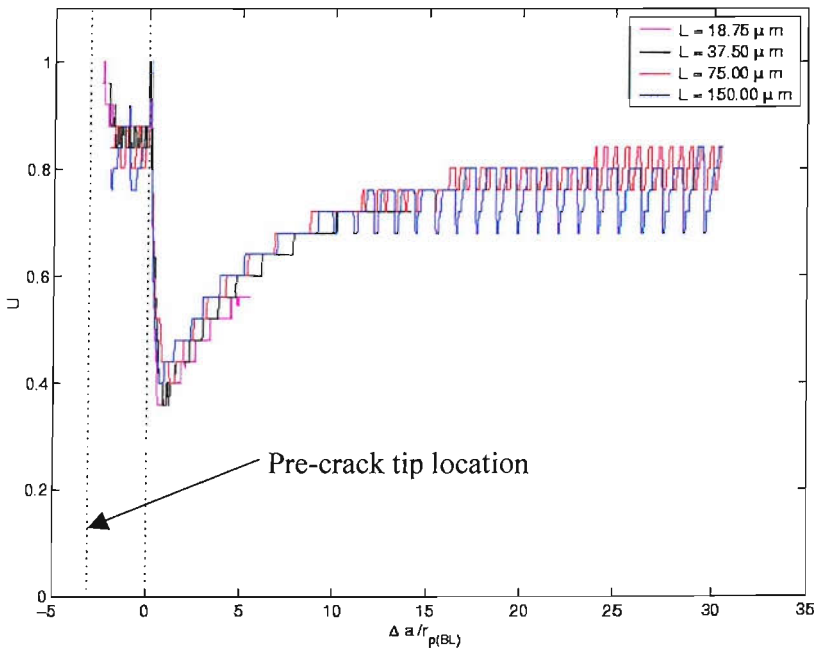

Figure 4.35: Effect of asperity size on crack closure behaviour for a deflected crack, θ = 45°, $\Delta K_{(BL)}$ = 12.0 MPa m$^{1/2}$, R = 0.1, $\%OL$ = 100.0. Overload applied at $\Delta a/r_{p(BL)}$ = 0.0.

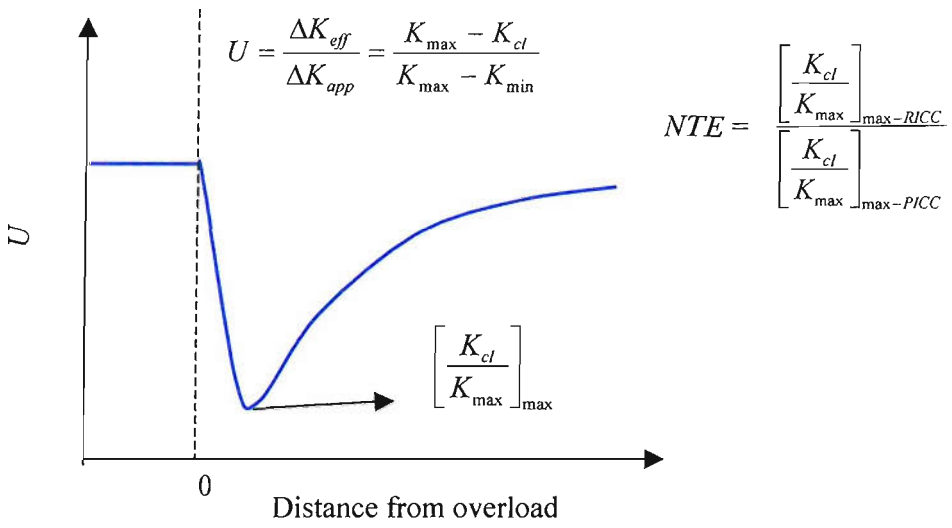

Figure 4.36: Schematic diagram showing identification of *NTE* (Normalised Transient Effect).

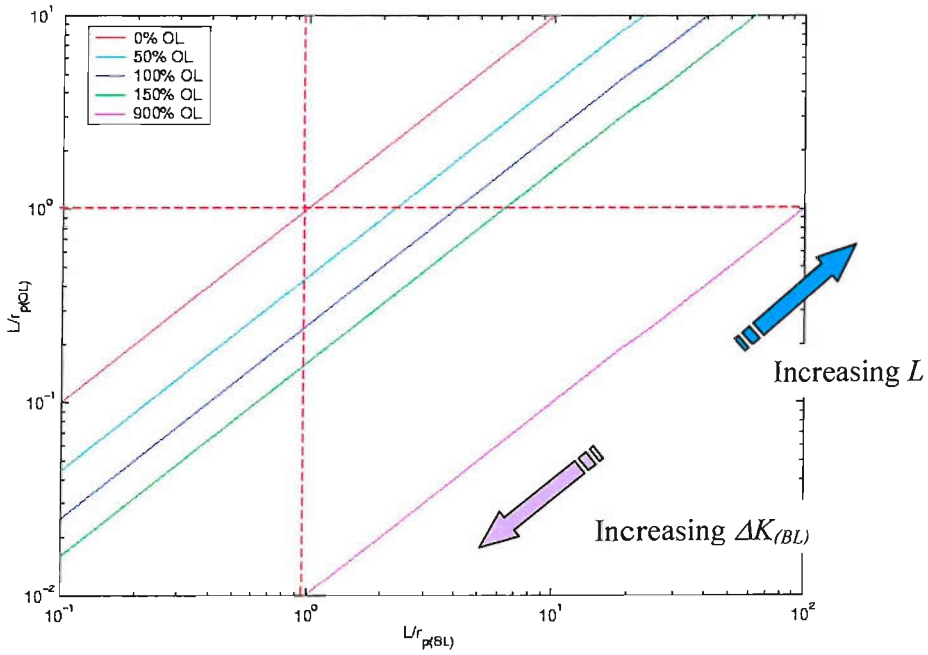

Figure 4.37: Schematic representation of OL lines on $L/r_{p(BL)}$ and $L/r_{p(OL)}$ axes.

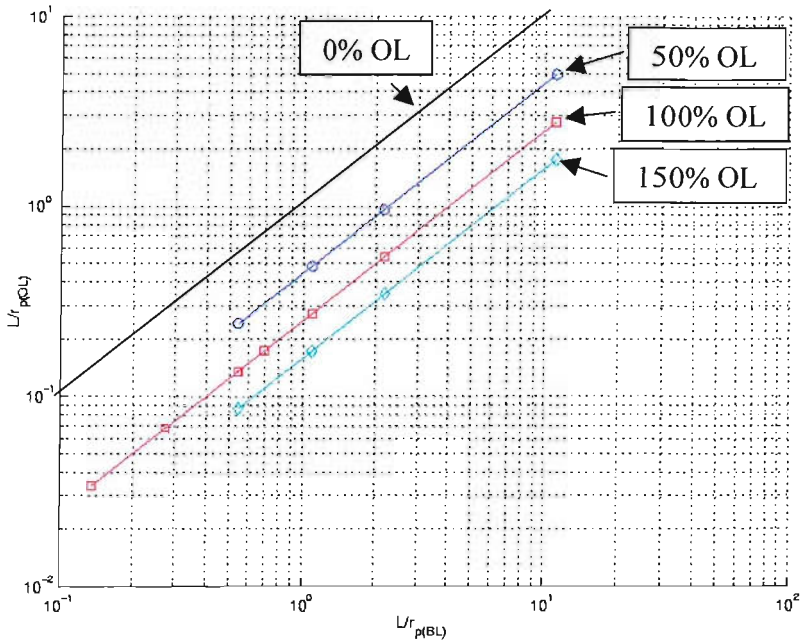

Figure 4.38: Location of FE modelled data points on $L/r_{p(BL)}$ and $L/r_{p(OL)}$ axes.

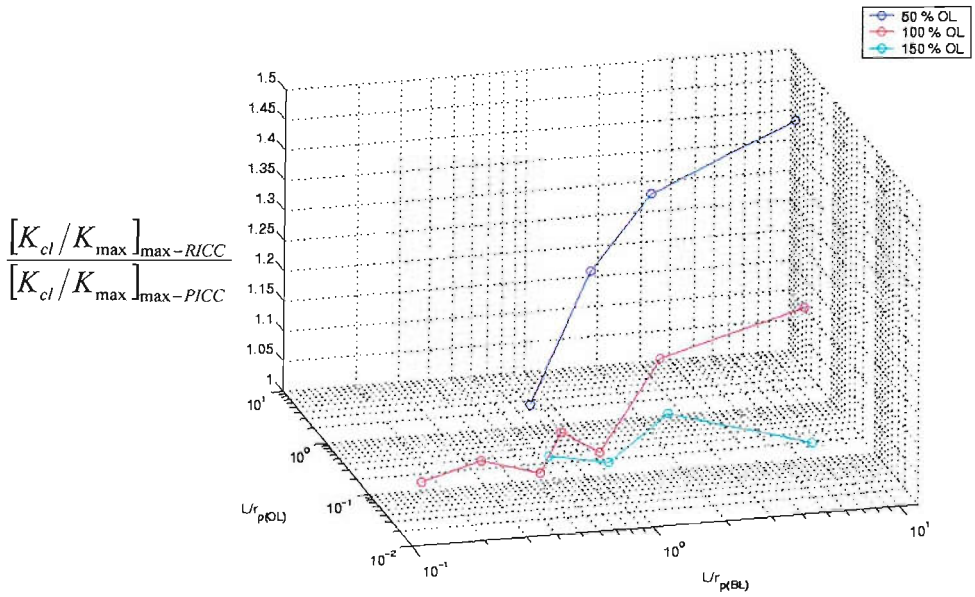

Figure 4.39: Variation of *NTE* with $L/r_{p(OL)}$ and $L/r_{p(BL)}$ predicted by models.

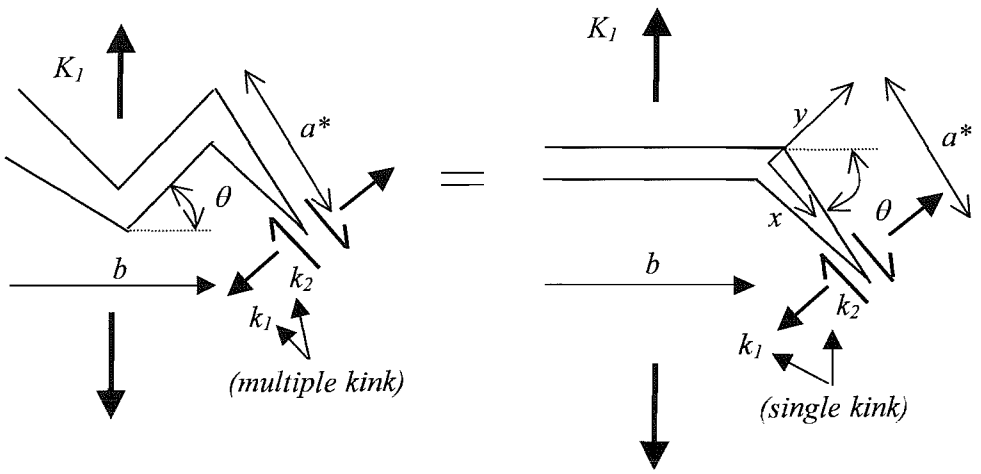

$$k_{1,2(multiple\ kink)} = k_{1,2(single\ kink)}$$

Figure 4.40: Approximation of multiple deflected cracks into an undeflected crack with single pupative kink (i.e. $a^* << b$) [After Parry, 2000].

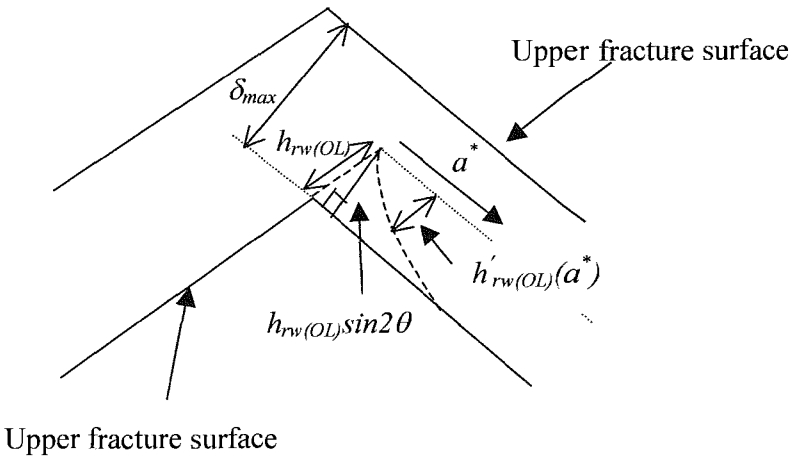

Figure 4.41: Approximation of residual wedge variation ($h_{rw(OL)}$) (deflected crack).

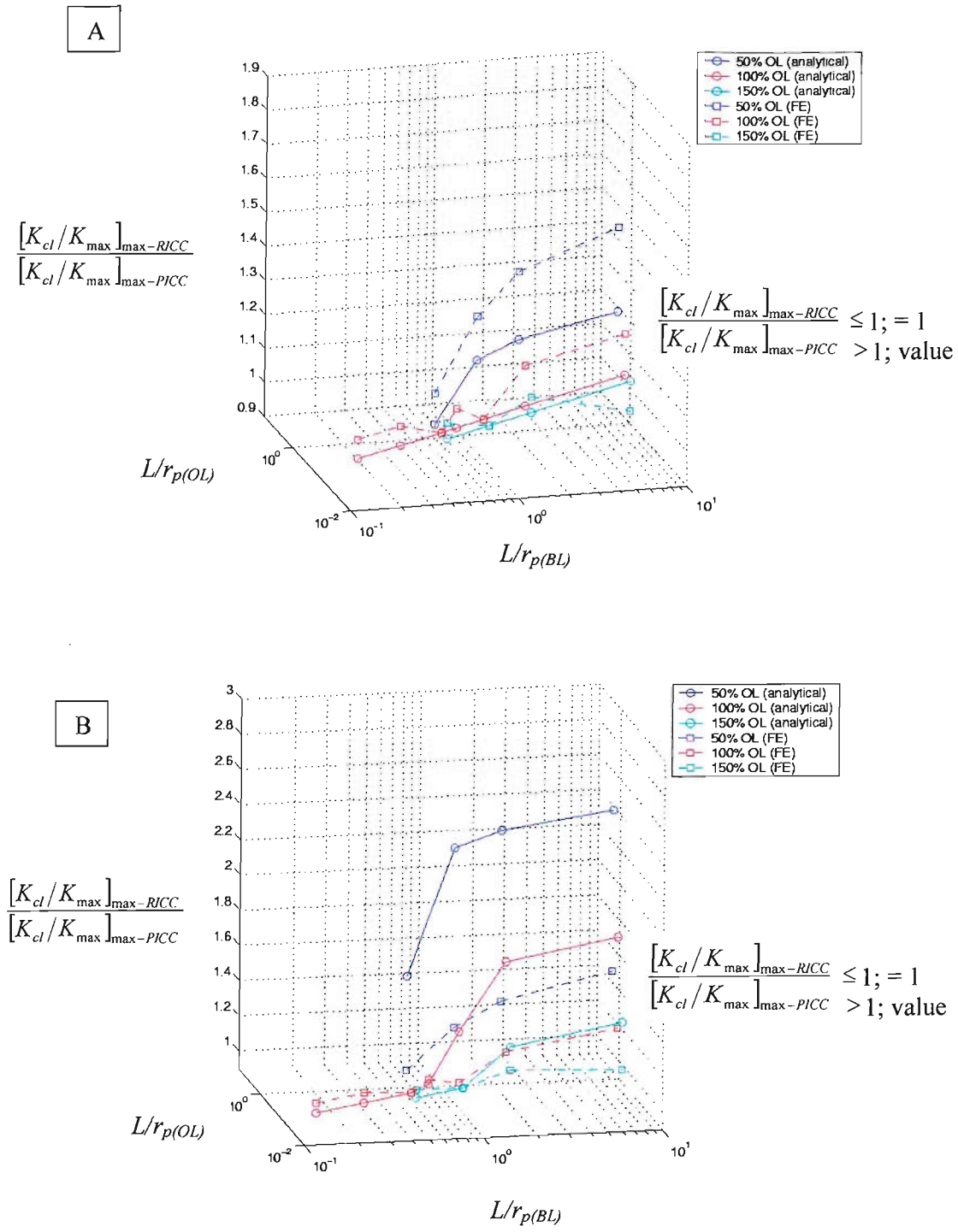

Figure 4.42: 3D Comparison of FE and analytical *NTE* results: (a) β_{II} = 1and (b) β_{II} = 2 (β_I = 1 and λ = 0.5).

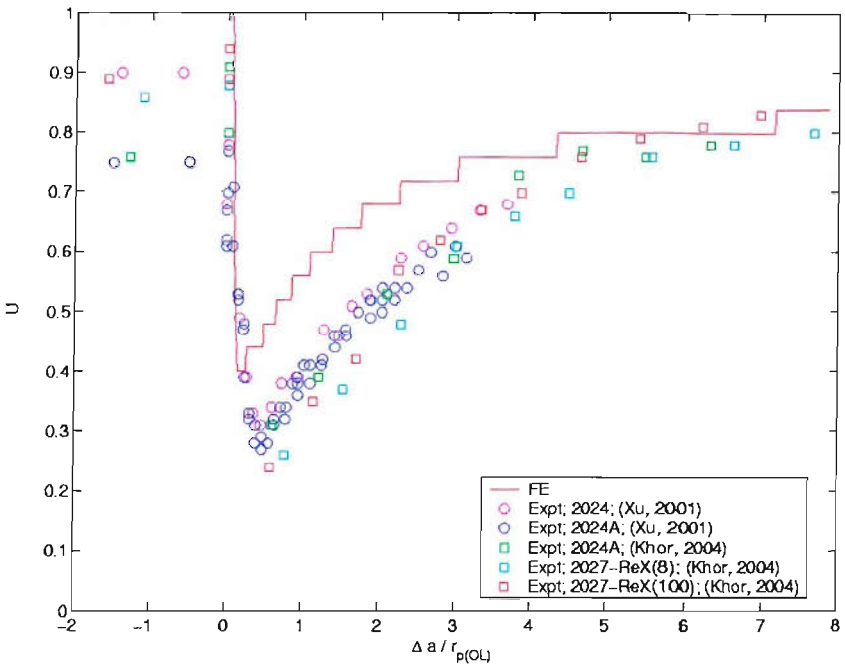

Figure 4.43: Comparison of FE and experimental results, $\Delta K_{(BL)}$ = 12.0 MPa m$^{1/2}$, R = 0.1, $\%OL$ =100.

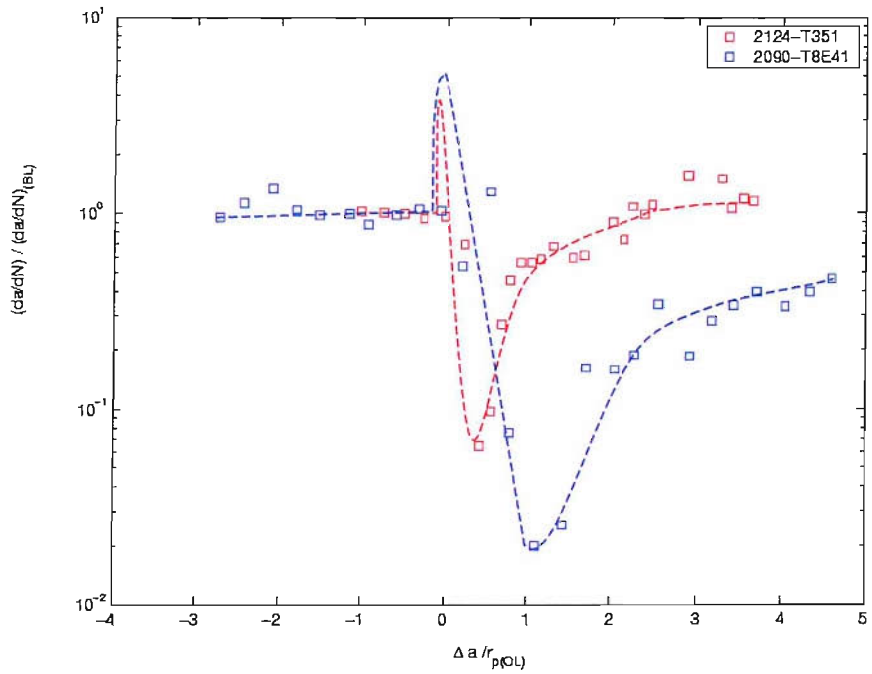

Figure 4.44: Normalised crack growth transients following a single 150% OL, $\Delta K_{(BL)}$ = 8.0 MPa m$^{1/2}$, R = 0.1 (Venkateshwara Rao and Ritchie, 1988).

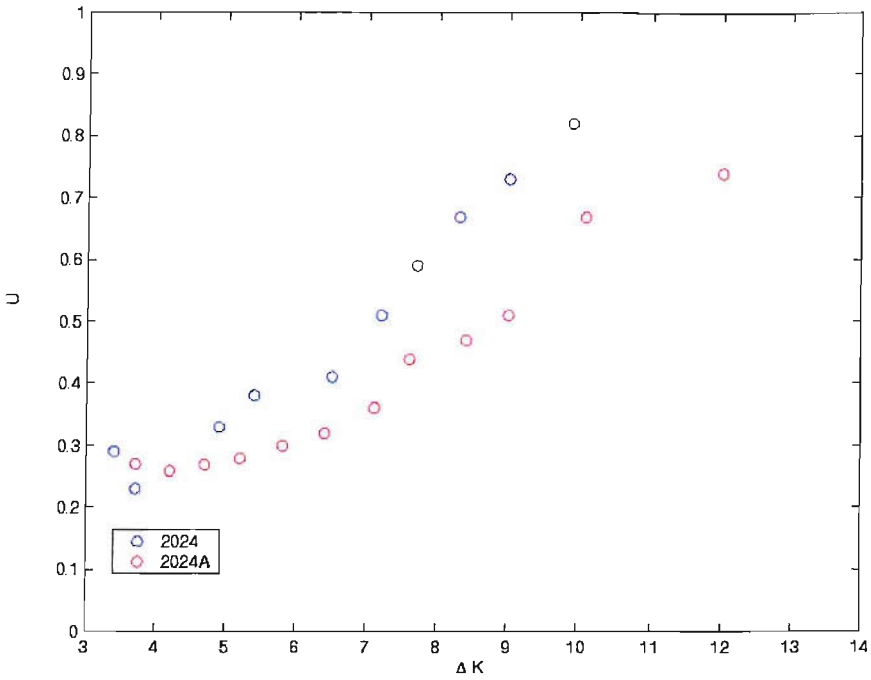

Figure 4.45: Experimental closure variation of 2024 and 2024A, $R = 0.1$ (Xu, 2001).

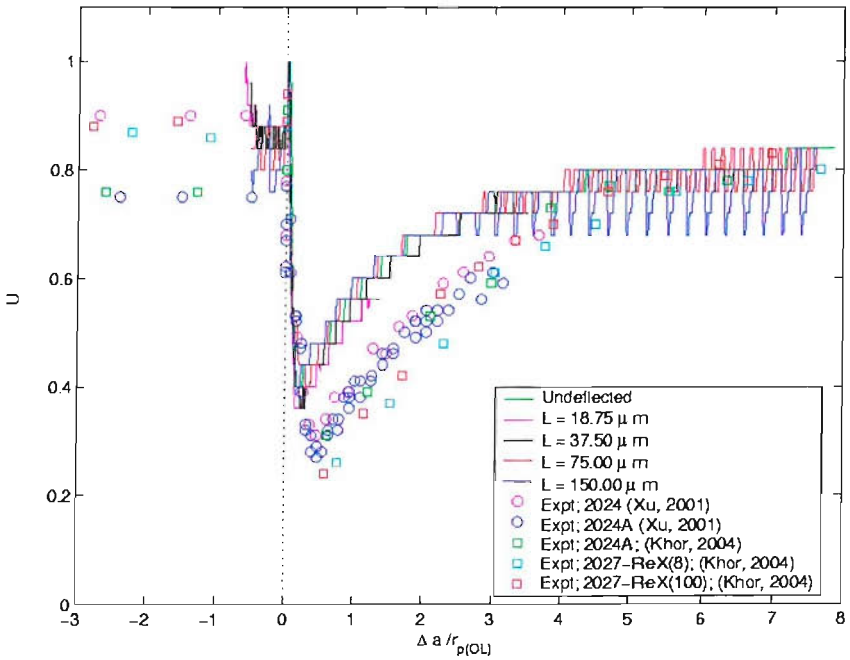

Figure 4.46: Comparison of FE (PICC and RICC models) and experimental closure results, $\Delta K_{(BL)} = 12.0$ MPa m$^{1/2}$, $R = 0.1$, $\%OL = 100$.

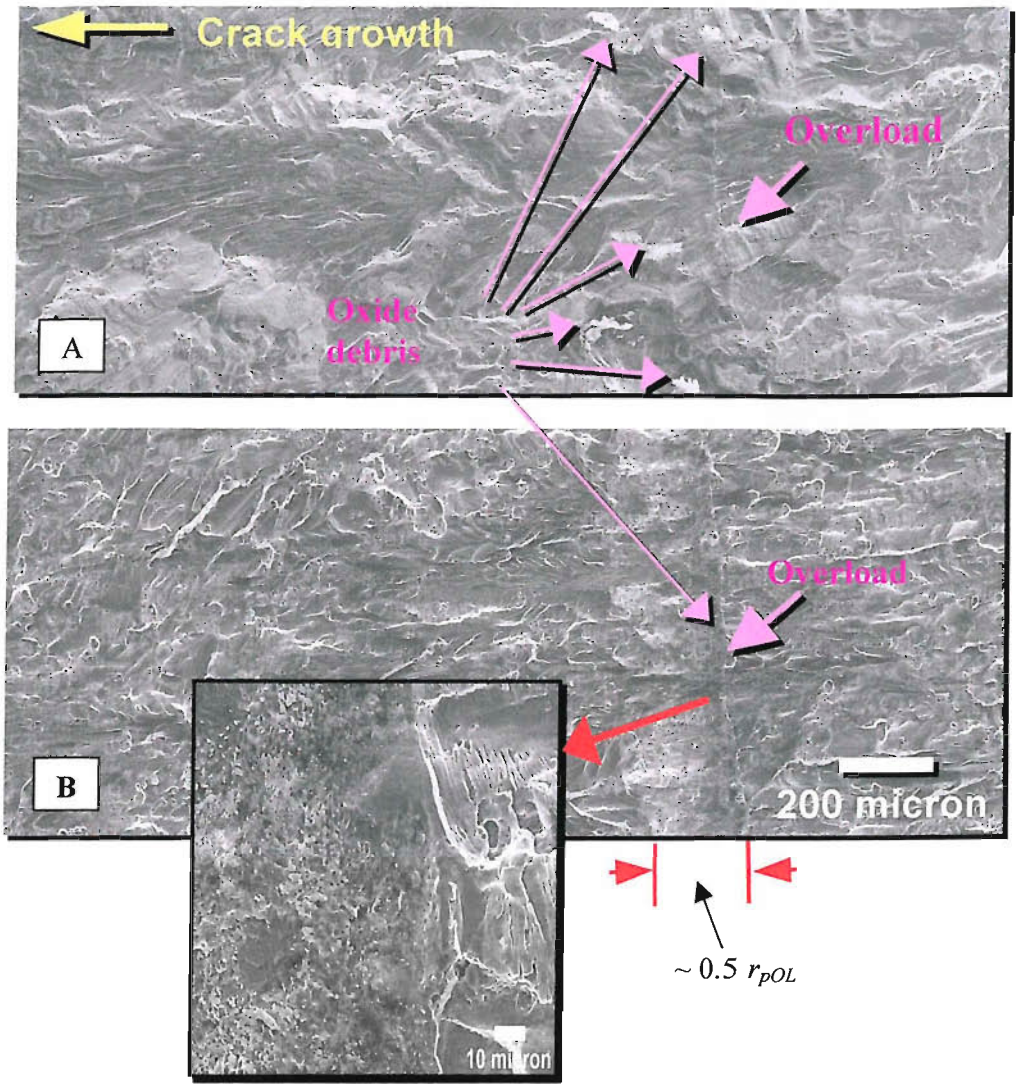

Figure 4.47: Scanning electron microscope images of post OL regions, $\Delta K_{(BL)}$ = 12.0 MPa $m^{1/2}$, R = 0.1, $\%OL$ =100, in (a) 2024A and (b) 2027Rex(8). Areas of surface oxide immediately following the overload are highlighted, with oxide patches seen in the 2024A, and a more continuous oxide layer in the 2027 (after Khor, 2004).

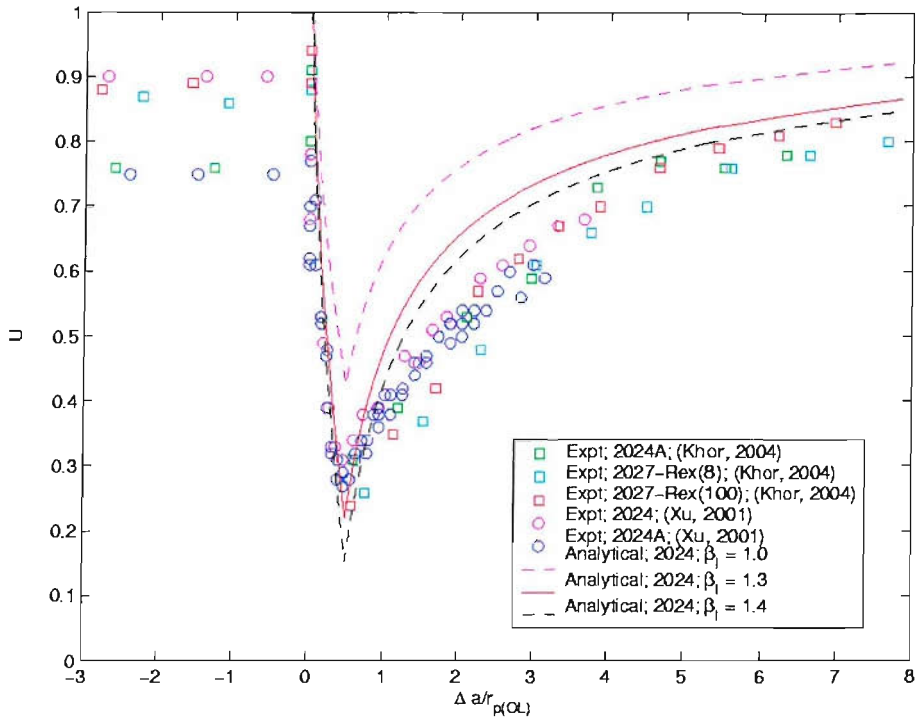

Figure 4.48: Comparison of analytical (PICC and RICC models) and experimental closure results, $\Delta K_{(BL)}$ = 12.0 MPa m$^{1/2}$, R = 0.1, $\%OL$ =100.

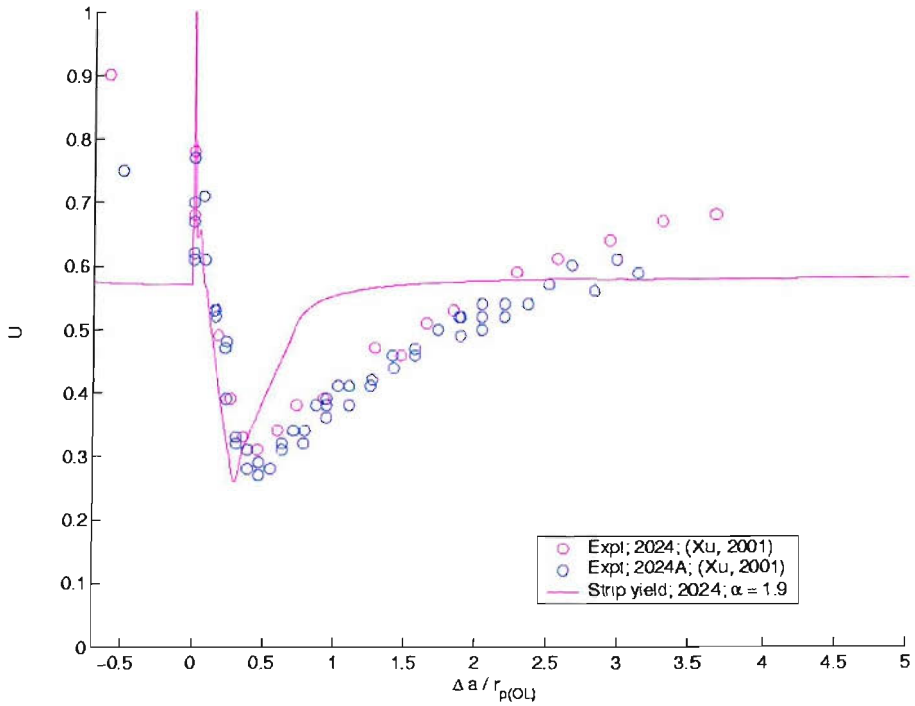

Figure 4.49: Comparison of strip yield and experimental closure results, $\Delta K_{(BL)}$ = 12.0 MPa m$^{1/2}$, R = 0.1, $\%OL$ =100.

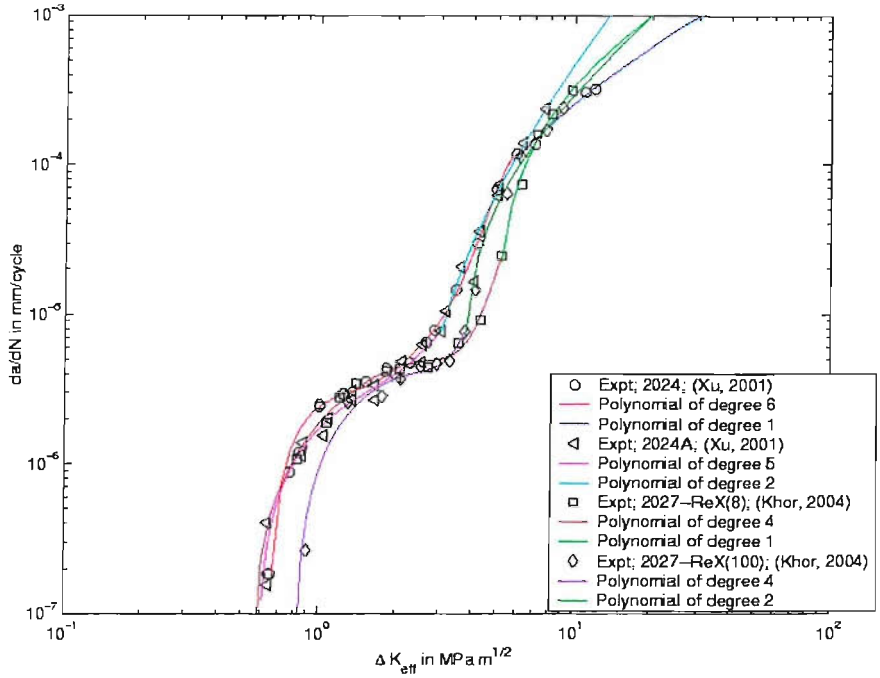

Figure 4.50: Intrinsic crack growth behaviour and their approximations through curve fitting, $R = 0.1$.

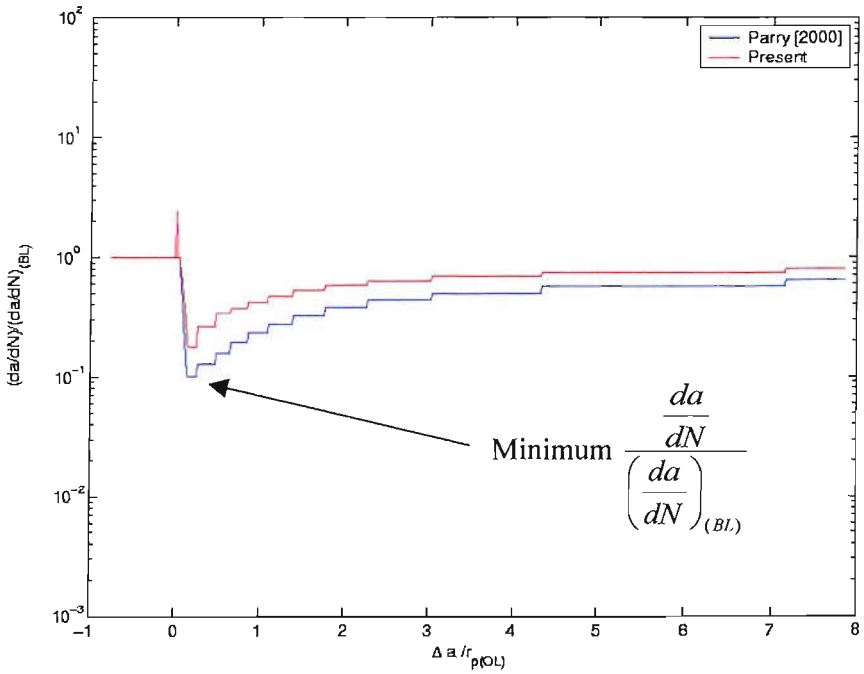

Figure 4.51: Comparison of growth rate predictions using Parry's method and the present curve fitting approach, $\Delta K_{(BL)} = 12.0$ MPa m$^{1/2}$, $R = 0.1$, $\%OL = 100$.

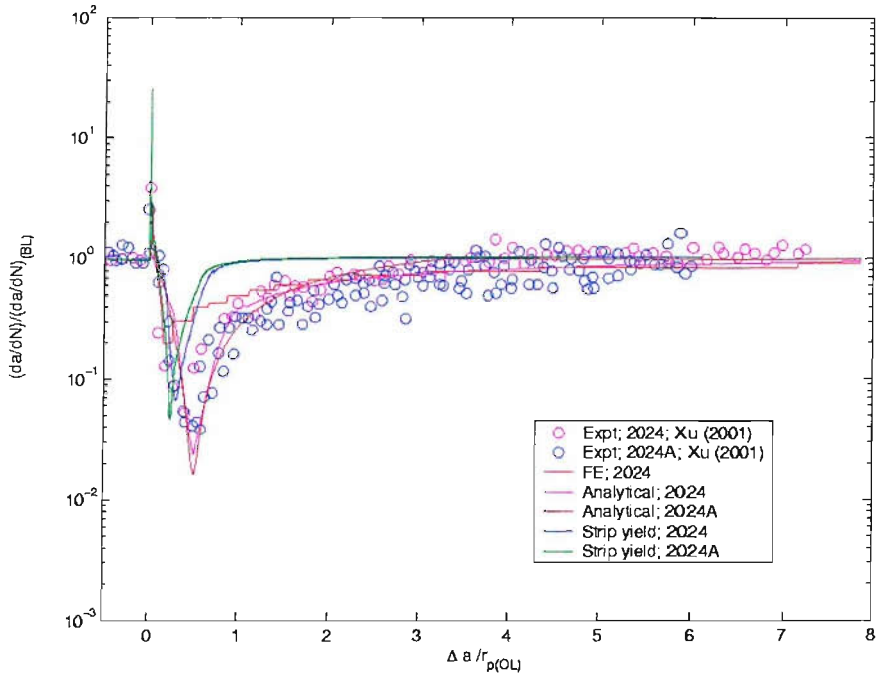

Figure 4.52: Comparison of normalised experimental (Xu, 2001) and predicted growth rates ($(da/dN)/(da/dN)_{(BL)}$), $\Delta K_{(BL)}$ = 12.0 MPa $m^{1/2}$, R = 0.1, $\%OL$ = 100.

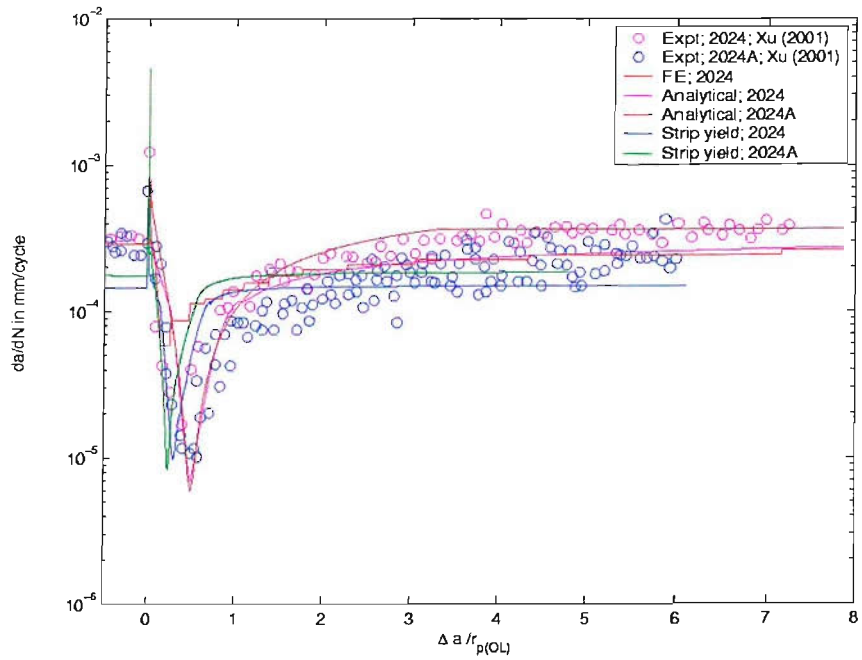

Figure 4.53: Comparison of experimental (Xu, 2001) and predicted growth rates (da/dN), $\Delta K_{(BL)}$ = 12.0 MPa $m^{1/2}$, R = 0.1, $\%OL$ = 100.

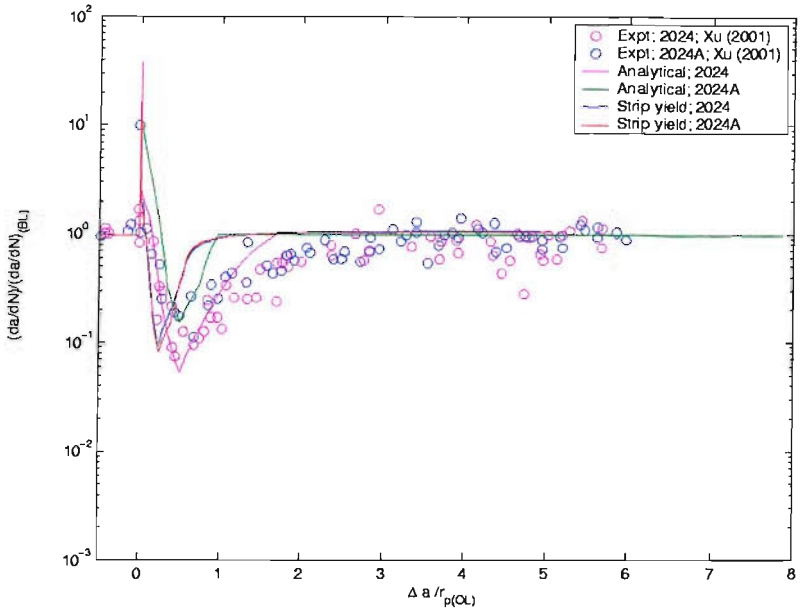

Figure 4.54: Comparison of normalised experimental Xu, 2004) and predicted growth rates ($(da/dN)/(da/dN)_{(BL)}$), $\Delta K_{(BL)}$ = 8.0 MPa m$^{1/2}$, R = 0.1, $\%OL$ = 100.

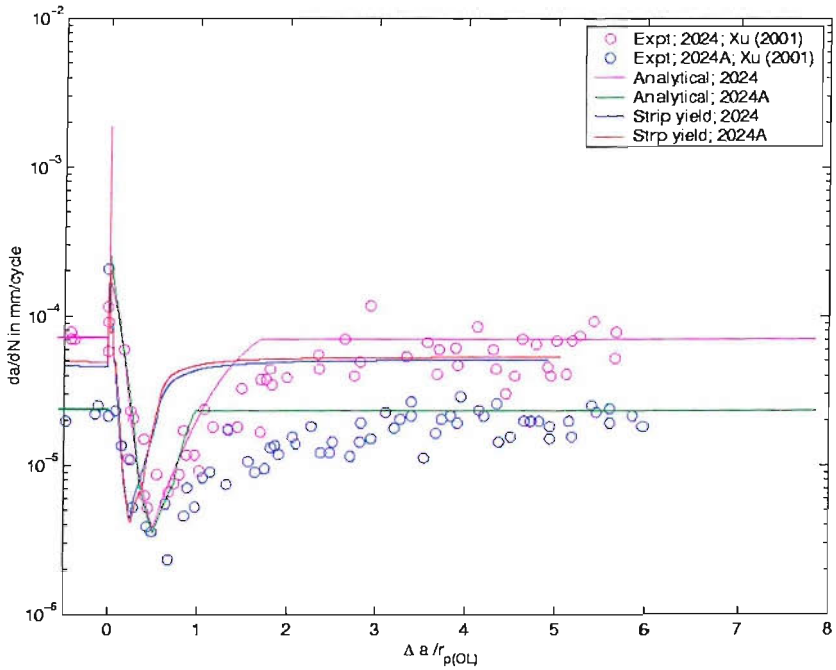

Figure 4.55: Comparison of experimental (Xu, 2001) and predicted growth rates (da/dN), $\Delta K_{(BL)}$ = 8.0 MPa m$^{1/2}$, R = 0.1, $\%OL$ = 100.

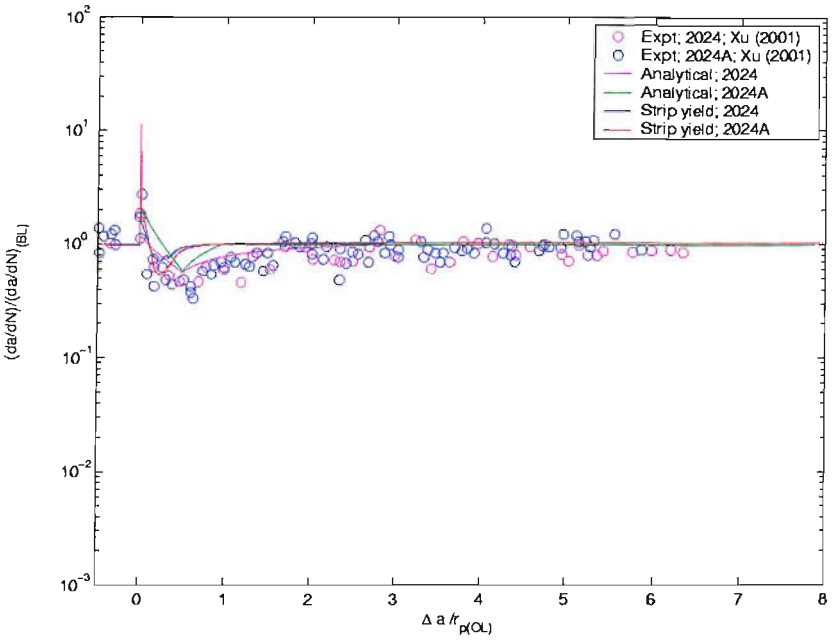

Figure 4.56: Comparison of normalised experimental (Xu, 2001) and predicted growth rates ($(da/dN)/(da/dN)_{(BL)}$), $\Delta K_{(BL)}$ = 12.0 MPa m$^{1/2}$, R = 0.1, $\%OL$ = 50.

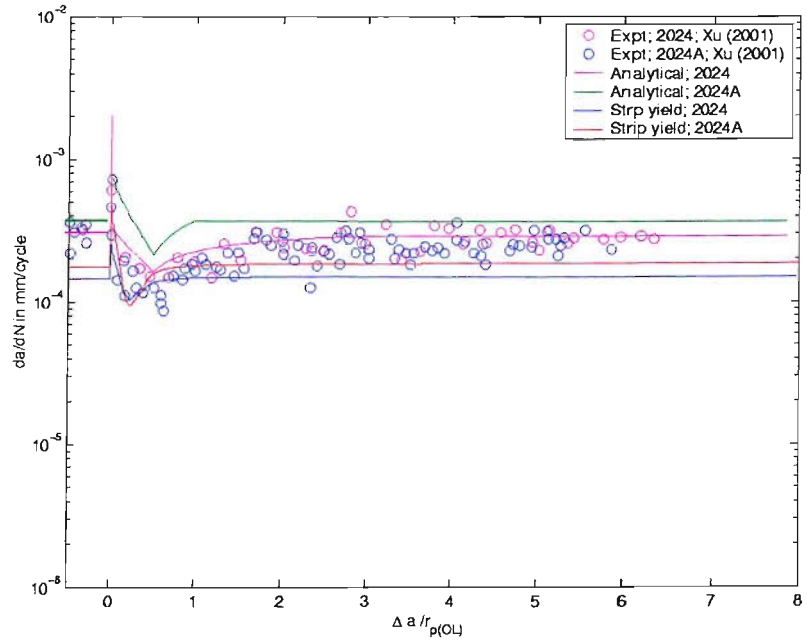

Figure 4.57: Comparison of experimental (Xu, 2001) and predicted growth rates (da/dN), $\Delta K_{(BL)}$ = 12.0 MPa m$^{1/2}$, R = 0.1, $\%OL$ = 50.

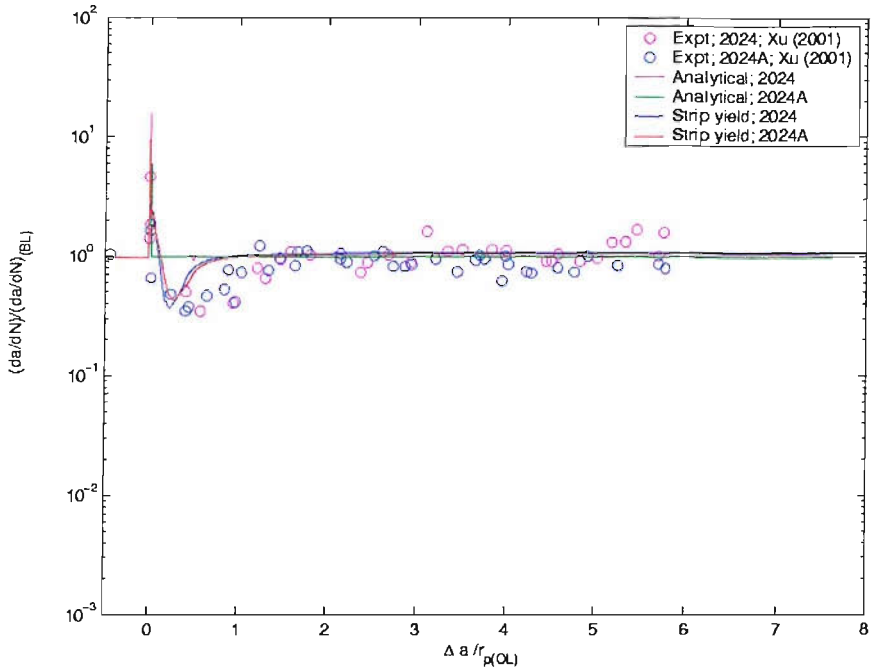

Figure 4.58: Comparison of normalised experimental (Xu, 2001) and predicted growth rates (da/dN), $\Delta K_{(BL)}$ = 8.0 MPa m$^{1/2}$, R = 0.1, $\%OL$ = 50.

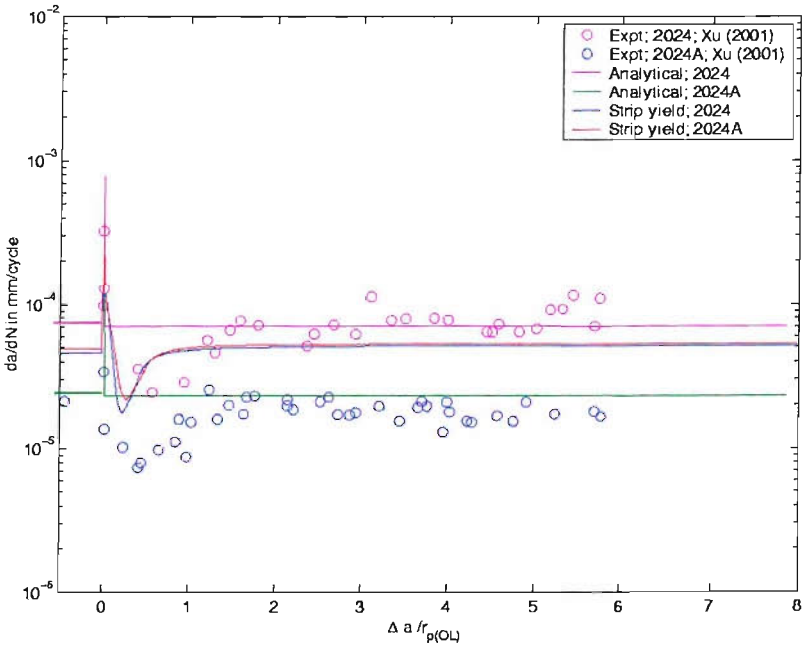

Figure 4.59: Comparison of experimental (Xu, 2001) and predicted growth rates (da/dN), $\Delta K_{(BL)}$ = 8.0 MPa m$^{1/2}$, R = 0.1, $\%OL$ = 50.

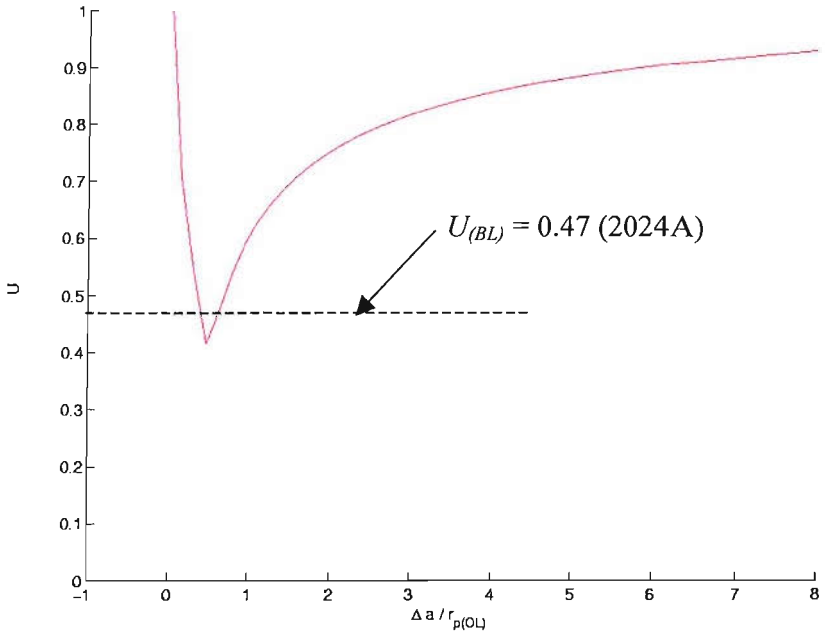

Figure 4.60: Analytical (RICC model) closure variation, $\Delta K_{(BL)}$ = 8.0 MPa $m^{1/2}$, R = 0.1, $\%OL$ = 50, β_{II} = 2.0, $L \geq 0.5\ r_{p(OL)}$, $\theta = 40^{\circ}$.

Chapter 5

5 Finite element analyses of closure due to double/multiple overloads

In the previous chapter, FE, strip yield and analytical investigations of both PICC and RICC for cracks subjected to single overload conditions have been shown. In this chapter the investigations are extended considering both double and multiple overload conditions. In particular, attempts are made to study the effects of overload spacing on closure levels and growth rates. Comparisons are then made with the relevant experimental results.

5.1 Introduction

When successive (or periodic) overloads are applied between constant amplitude fatigue loading, there arises a potential for overload interaction. Closely packed overloads may of course ultimately lead to acceleration rather than retardation of crack growth, since crack acceleration at each overload may exceed the retardation in the subsequent baseline cycles. In cases of remotely applied overloads, interaction between overloads may of course become trivial. However, there may be a range of overload spacing for which retardation effects are reported to be enhanced [e.g. Tur and Varder, 1996, Jonas and Wei, 1971, Wei *et al.*, 1973, Rice and Stephens, 1973, Mills and Hertzberg, 1976, Fleck, 1985, Geary, 1992, Hammouda *et al.*, 1998, Simoes *et al.*, 1999, McMaster and Smith, 1999, Meggiolaro and Castro, 2001, Klysz, 2001, Heper and Varder, 2003]. Based on experiments in Al 2024-T3, Mills and Hertzberg [1976] reported that the maximum interaction (and thus minimum overall growth rates) between single peak overloads resulted when two equal peak load cycles were separated by a distance, $a'_{min,}$ corresponding to the distance to the minimum fatigue crack propagation rate after the application of single overload. Experiments on a 7075-T6 Al alloy [Varder and Yildirim, 1990] and a 2024-T3 Al alloy [Tur and Varder, 1996] suggested that interaction is greatest when overloads are applied at a separation of $0.5N_D^*$ cycles, where N_D^* is the number of cycles of retarded growth in a single-peak overload test. For constant $\Delta K_{(BL)}$ tests on Al 2024-T3, it has been observed that peak interaction effects may in fact cover a range of overload spacing

values (expressed in terms of crack extension) [Tur and Varder, 1996]. Experimental and FE studies on fatigue crack growth on an unspecified 'commercial aluminium alloy' due to two successive single overloads have been reported by Hammouda *et al.*, [1998], noting that if the ratio of second to first overload is greater than or equal to one, fatigue crack growth rates followed closely predictions based on the second overload alone, otherwise, the following scenarios are identified: 1) when two overloads were closely applied, the second overload caused an initial crack growth acceleration followed by behaviour controlled by the first overload, 2) when the second overload was applied after crack growth rates had reached a minimum rate due to the first overload, enhanced retardation in growth was evident (consistent with Mills and Hertzberg's [1976] observation). Experimental (e.g. Vargas and Stephens, 1973, Klysz, 2001) and numerical (e.g. Meggiolaro and Castro, 2001) studies have also suggested an optimum number of baseline loading cycles interval between overloads at which the crack growth retardation is maximum. In spite of the various investigations reported, to the best of our knowledge there remains a lack of systematic study on the effect of overload spacing on closure levels. In this chapter, attempts will be made to investigate the effects of spacing on closure levels during repeated overloads using FE, strip yield type and analytical modelling approaches. Comparisons will also be made with relevant available results. The work at present only considers repetitive (identical) overloads, as illustrated in Figure 5.1 (Δa_s = overload spacing distance; and ΔN_s = loading cycles separating overloads).

5.2 Double overloads

5.2.1 FE modelling

The procedures used for FE modelling of undeflected fatigue cracks subjected to two successive overloads (double overloads) are essentially identical to those discussed in Chapter 3. Table 5.1 shows the matrix of key model parameters assessed to date *viz.*, $\Delta K_{(BL)}$, $\%OL$ and Δa_s (overload spacing, shown schematically in Figure 5.1). The spacings (Δa_s) are normalised by Irwin's plastic zone size ($r_{p(BL)}$, see Equation A.6). In the first instance the analyses were performed for $\Delta K_{(BL)}$=10.0, 12.0 and 15.0 MPa

$m^{1/2}$, R = 0.1, and $\%OL$ = 50, 75 and 100 (but identical for each OL). Overload spacing ranged from 0.136 $r_{p(BL)}$ to 25.97 $r_{p(BL)}$.

5.2.1.1 Crack profiles

Figure 5.2 and 5.3 shows crack profiles subjected to double overloads with Δa_s = 0.612 and 25.97 $r_{p(BL)}$ respectively at K/K_{max} = 0.612 ($\Delta K_{(BL)}$=12.0 MPa $m^{1/2}$, R = 0.1, and $\%OL$ = 100). Crack profiles due to the first (OL_1) and second (OL_2) overloads on their own are also plotted at the same load level (i.e. results for two single overload models). It may be seen from Figure 5.2 (closely spaced overloads) that there is an enhanced residual deformation wedge in the double overload case, i.e. there is an increase of residual wedge height by an amount $\Delta h_{rw,}$ suggesting an interaction between the two overloads in this case. The enhanced h_{rw} leads to an increased in closure level (further discussion follows in the subsequent section). However, as the spacing between OLs is increased to Δa_s = 25.97 $r_{p(BL),}$ the wedges due to OL_1 and OL_2 no longer appear to interact, as can be seen in Figure 5.3 (i.e. the single overload OL_1 and OL_2 peaks corresponds closely to those of the double overload model).

5.2.1.2 Crack closure - overload spacing effects

Variations of U with crack length are plotted against normalised crack length ($\Delta a/r_{p(BL)}$) in Figure 5.4 for various overload spacings (Δa_s) at $\Delta K_{(BL)}$ = 12.0 MPa $m^{1/2}$, R = 0.1, $\%OL$ = 75.0. The single overload (OL_1 only) case is also plotted for comparison. The first overload is applied at $\Delta a/r_{p(BL)}$ = 0.0. The behaviour of closure following a second overload then resembles closely the single overload case, although it can be observed that there is an increased severity of closure transient, identified by a minimum in U values at a $\Delta a/r_{p(BL)}$ of ~ 2. When the second overload very closely coincides with the first, transient interaction effects clearly diminish. Thus there appears to exist a maximum OL interaction zone for which the severity of overload closure effect is at its greatest (and hence maximum crack growth retardation should occur). Figure 5.5 plots the corresponding variation of $\alpha_{SOL\text{-}max}$ (=$[K_{cl}/K_{max}]_{DOL\text{-}max}/[K_{cl}/K_{max}]_{SOL\text{-}max}$) which is the ratio of maximum closure for the double OL (DOL) case to that of an equivalent single overload (SOL)), versus normalised overload spacing ($\Delta a_s/r_{p(OL)}$). It can be seen that as the overload spacing is increased there is an initial increase of $\alpha_{SOL\text{-}max}$ values up to a maximum value of ~1.2 when the overload

spacing is of the order of 0.2-0.5 $r_{p(OL)}$. At general $\Delta a_s/r_{p(OL)}$ levels, $\alpha_{SOL\text{-}max}$ diminishes with no overload interaction occurring for $\Delta a_s/r_{p(OL)} \geq 2.5$. The existence of such an interaction zone would then appear consistent with experimental results of by Mills and Hertzberg [1976] and Tur and Varder [1996]. It is interesting to note that whilst the study made on structural steel by Ramos *et al.*, [2003] indicated that the larger the interval of overload separation, the higher the fatigue crack growth retardation (or lower the fatigue crack growth), the studies made by Wei *et al.*, [1973] on Ti-6Al-4V alloy and Simoes *et al.*, [1999] on 7150 Al alloy reported that the retardation increases with the decrease in overloads separation distance. Comparing the overloads spacing distances in these works, it can be seen that the maximum Δa_s considered by Ramos *et al.*, is about 0.04 $r_{p(OL)}$ and the minimum Δa_s adopted by Simoes *et al.*, was about $0.52r_{p(OL)}$. Hence it appears that the results from Ramos *et al.*, and Simoes *et al.*, fall on the left (where maximum closure labels rise) and right hand side (where maximum closure labels drop) of the maximum interaction zone in Figure 5.5 respectively, i.e. qualitatively consistent with the present modelling.

5.2.1.3 Crack closure - OL ratio effects

The effect of overload ratio on maximum crack closure response is shown in Figure 5.6 and 5.7 for overloads ratios of 50%, 75% and 100%, for $\Delta K_{(BL)}$ = 12 MPa $m^{1/2}$, R = 0.1. $[K_{cl}/K_{max}]_{DOL\text{-}max}$ is plotted against overload spacing ($\Delta a_s/r_{p(OL)}$) in Figure 6.6. A maximum interaction zone can be identified for all the *%OL* considered, which is seen to lie between an overload spacing of 0.12 and 0.72 $r_{p(OL)}$ for 50% OL, and 0.23 to 0.40 $r_{p(OL)}$ for 100% OL. It should be noted that the exact apparent width of the overload interaction zone is of course dependent on the load step resolution of the FE models. In Figure 5.7 the response of $\alpha_{SOL\text{-}max}$ (i.e. a normalised indication of double overload severity) to changes in *%OL* is shown for different overload spacings ($\Delta K_{(BL)}$ = 12 MPa $m^{1/2}$, R = 0.1). It can be observed that there is an increase of about 20%, in the maximum closure levels (maximum $[K_{cl}/K_{max}]_{DOL\text{-}max}$) when compared to the single overload cases ($[K_{cl}/K_{max}]_{SOL\text{-}max}$) for all these results, suggesting only slightly greater interaction with increasing *%OL*. It can be seen that $\alpha_{SOL\text{-}max}$ values reach unity at $\Delta a_s$of the order of $2\text{-}3r_{p(OL)}$.

5.2.1.4 Crack closure - $\Delta K_{(BL)}$ ratio effects

Figure 5.8 shows broadly similar trends in maximum closure response in varying $\Delta K_{(BL)}$ (= 10, 12, 15 MPa $m^{1/2}$) at 100% OL. A similar zone of maximum overload interaction is evident, with Figure 5.9, showing an absence of overload interaction beyond a separation distance of 4 $r_{p(OL)}$.

5.2.2 Strip yield modelling

Strip yield type modelling is carried out for cracks subjected to two identical consecutive overloads, following the method discussed in Section 4.4 for single overload.

5.2.2.1 Crack closure – overload spacing effects

Figure 5.10 shows the variation of U plotted against normalised crack length ($\Delta a/r_{p(BL)}$) for $\Delta K_{(BL)}$ = 12 MPa $m^{1/2}$, R = 0.1, $\%OL$ = 75. In this figure, plots corresponding to five overload spacings (Δa_s = 0.05, 0.22, 0.53, 0.89 and 7.2 $r_{p(OL)}$) are shown. The first overload is located at ($\Delta a/r_{p(OL)}$) = 0.0. As in the FE results (see Figure 5.4) it can be observed that there is an increase in the maximum closure levels associated with the second overload being a short distance (~ 0.22 $r_{p(OL)}$) from the first overload location.

In Figure 5.11, the maximum closure levels corresponding to the second overload ($[K_{cl}/K_{max}]_{DOL\text{-}max}$) are plotted for $\%OL$ = 50, 75 and 100 ($\Delta K_{(BL)}$ = 12 MPa $m^{1/2}$, R = 0.1). $[K_{cl}/K_{max}]_{DOL\text{-}max}$ is plotted against $\Delta a_s/r_{p(OL)}$. An increase in $[K_{cl}/K_{max}]_{DOL\text{-}max}$ values with increase in %OL is again seen. In contrast to the FE results (see Figure 5.6) which suggests an increasing zone of maximum retardation span with decreasing $\%OL$, strip yield models predict a consistent maximum retardation point at approximately Δa_s = 0.29 $r_{p(OL)}$ for all the overloads modelled. Figure 5.12 shows the variation of $\alpha_{SOL\text{-}max}$ with $\Delta a_s/r_{p(OL)}$. It can be observed from Figure 5.12 that there is an increase of approximately 6%, 9.5% and 12.5% in the maximum closure levels when compared to the single overload conditions (expressed in terms of $\alpha_{SOL\text{-}max}$) for 50%, 75% and 100% OL respectively: i.e. somewhat lower than the corresponding FE

results but of a similar order. For the OLs considered, $\alpha_{SOL\text{-}max}$ drops to unity after at about 2 $r_{p(OL)}$, i.e. at the lower end of the range suggested by the FE models.

5.2.2.2 Crack closure - $\Delta K_{(BL)}$ ratio effects

The response of $[K_{cl}/K_{max}]_{DOL\text{-}max}$ and $\alpha_{SOL\text{-}max}$ to changes in $\Delta K_{(BL)}$ is shown in Figure 5.13 and 5.14 for different OL spacings ($\%OL$ = 100, R = 0.1). A negligible effect of baseline loading is identifiable in these results when $\Delta K_{(BL)}$ is increased from 10 to 15 MPa $m^{1/2}$.

5.2.3 Analytical modelling – dual overloads

From the FE studies it was seen from Figure 5.2 and 5.3 that an enhanced residual deformation wedge is evident when two OLs are closely spaced, thereby leading to an increased in transient closure levels. Similar interactions in overload displacement profiles has been reported by Heper and Varder [2003]. They suggested that the main mechanism of interaction of dual overloads is dependant on the 'spring effect' of deformation at the crack surface during closure, with 'spring effect' of the first overload inhibiting the reversed plastic deformation of the second overload, thereby leading to the creation of larger residual hump. This 'spring effect' is expected to become weaker as the overload spacing increases. The second overload hump size changes were found to be equivalent to those of a single overload with a higher K_{min} value, indicating a rise in effective R. The behaviour of such an 'R effective' overload interaction mechanism is interrogated here by modifying the analytical model discussed in Section 4.3. In the first instance Figure 5.15 shows the predicted variation of closure levels (K_{cl}/K_{max}) with crack propagation following an overload, expressed as ($\Delta a/r_{p(OL)}$) for $K_{(BL)}$ = 12 MPa $m^{1/2}$, R = 0.1, $\%OL$ = 100 using the approach of Section 4.3. The overload is applied at $\Delta a/r_{p(OL)}$ = 0.0. In the first instance, it is then assumed that if a second overload is applied after that at $\Delta a/r_{p(OL)}$ = 0.0, it is assumed that at the point of the second overload, the effective R ratio (R_{eff}) is determined by the previous overload closure level at that point, i.e.,

$$R_{OL2} = fn\left(R_{eff}\right)_{OL1} \tag{5.1}$$

where R_{OL2} is the R ratio due to the second overload, OL_2, and is expressed as a function of the $(R_{eff})_{OL1}$ due to the application of the first overload, OL_1. $(R_{eff})_{OL1}$ is

equated to the closure due to the first overload, $(K_{cl}/K_{max})_{OL1}$. In order to check the influence of such an effective R on residual wedge profile, FE studies have been conducted at various R ratios. Figure 5.16 shows variation of residual wedge profile for R = 0.0, 0.1, 0.3, 0.5 and 0.7 for K_{max} = 13.3 MPa $m^{1/2}$. It can be seen that there is indeed an increase in the maximum wedge height ($h_{rw(max)}$) with increasing R, consistent with the results from Heper and Varder [2003], consistent with a decreased reversed deformation effect on residual lump size. Figure 5.17 compares the FE and analytical (Equation 4.2b) variation of $h_{rw(max)}$ with R, for $\Delta K_{(BL)}$ = 12 MPa $m^{1/2}$, $\%OL$ = 100. It can be seen that whilst the FE results show an increased sensitivity to R-ratio, the analytical model provides a good first order approximation.

5.2.3.1 Crack closure – overload spacing effects

Variations of predicted U with crack length are plotted against normalised crack length ($\Delta a/r_{p(OL)}$) in Figure 5.18 for $\Delta K_{(BL)}$ = 12 MPa $m^{1/2}$, R = 0.1, $\%OL$ = 100. The first overload is applied at $\Delta a/r_{p(OL)}$ = 0.0. Second overloads are applied following the first overload at various spacing as noted in the plot. It can be seen that there is an increase in the maximum closure levels following the second overload, when overload spacing is increased from 0.09 $r_{p(OL)}$ to 0.50 $r_{p(OL)}$, then a decrease for spacings greater than 0.50 $r_{p(OL)}$. It may be noted that the location of maximum overload interaction is of necessity is fixed by λ (see Section 4.3), which is taken to be 0.50 as discussed earlier. In the first instance reasonably consistent trends may be identified between the analytical, FE and strip yield models for double overload crack closure behaviour.

The overload effects on maximum closure response are further shown in Figure 5.19 and 5.20 for overload ratios of 50%, 75% and 100%, for $\Delta K_{(BL)}$ = 12 MPa $m^{1/2}$, R = 0.1. Maximum $[K_{cl}/K_{max}]_{DOL\text{-}max}$ occurs at $\Delta a_s/r_{p(OL)}$ = 0.50 for all the overload ratios (as noted before), and decreases with decreasing overload ratios. Figure 5.20 shows the response of $\alpha_{SOL\text{-}max}$ to changes in overload ratios for varying spacing ($\Delta K_{(BL)}$ = 12 MPa $m^{1/2}$, R = 0.1). It can be seen that there is a closure level increase of approximately 18%, 26% and 32% respectively for 50%, 75% and 100% overloads when compared to the single overload case.

5.2.3.2 Crack closure - $\Delta K_{(BL)}$ ratio effects

The effect of $\Delta K_{(BL)}$ on maximum crack closure response is shown in Figure 5.21 and 5.22 for $\Delta K_{(BL)}$ = 10, 12 and 15 MPa $m^{1/2}$ ($\%OL$ = 100, R = 0.1). It can be seen that there is no significant change in the $[K_{cl}/K_{max}]_{DOL\text{-}max}$ values for the changes in $\Delta K_{(BL)}$ considered. In Figure 5.22, variation of $\alpha_{SOL\text{-}max}$ with $\Delta K_{(BL)}$ is plotted, for varying overload spacing. It can be observed that for all the $\Delta K_{(BL)}$ considered, there is an increase of ~32% in the maximum closure levels when compared to the single overload case.

5.2.4 Comparison of FE, strip yield type and Analytical modelling

Comparison of FE, strip yield and analytical models of maximum closure levels, identified by $[K_{cl}/K_{max}]_{DOL\text{-}max}$ and $\alpha_{SOL\text{-}max,}$ are shown in Figure 5.23-5.26 for both $\%OL$ and $\Delta K_{(BL)}$ variations. Following the discussion in Section 5.2.3, and from Figure 5.23-5.26 it can be seen that the simple analytical model with the R_{eff} mechanism concept is indeed able to approximate qualitatively the results from the FE and strip yield models for variation in $[K_{cl}/K_{max}]_{DOL\text{-}max}$ with overloads spacing (for both changes in $\%OL$ and $\Delta K_{(BL)}$). The implication that the primary effect of a previous load transient on a subsequent load event may be expressed through the instantaneous crack closure levels (and the consequent influence on forward and reverse deformation processes) is clearly of interest as this may provide a valuable simplification of any engineering design approach that may be developed. In the first instance it is clearly valuable to further consider the current modelling results in relation to available experimental data.

5.2.5 Growth rate interaction

In the previous sections, closure response during double overloads excursion have been studied using in plane strain various numerical modelling approaches viz., FE, strip yield and analytical, however to the best of author's knowledge corresponding experimental closure studies have not been widely reported previously. Experimental work carried out by Mills and Hertzberg [1977] on 2024-T3 aluminium alloy [1976] and A514F steel alloy [1977] may however show a valuable insight into the growth

rate interaction of double overloads. Figure 5.27 shows experimental crack growth variation following a pair of overloads for a 2024 alloy ($\Delta K_{(BL)}$ = 19.8 MPa $m^{1/2}$, R = 0.1, $\%OL$ = 75, plane stress conditions). It can be seen that the maximum interaction (i.e. minimum growth rate) between two single equal overloads occurs when the overloads are separated (a' is the increment of crack extension separating overloads in this work) by a small distance a'_{min} (~ 0.13 $r_{p(OL)}$), where the fatigue crack propagation rate resulting from a *single* overload reached a minimum.

The crack closure results from FE, strip yield type and analytical models have been used to predict crack growth rates using the method described in Section 4.7.2 (i.e. using previously determined da/dN vs ΔK_{eff} curves from constant amplitude tests). Predicted plane strain growth rates for single overload and double overloads are plotted, $\Delta K_{(BL)}$ = 12.0 MPa $m^{1/2}$, R = 0.1, $\%OL$ = 75, for FE, strip yield and analytical methods in Figure 5.28, 5.29 and 5.30 respectively (minor discontinuities in the predicted da/dN curves are due to the approximations in the curve fitting approach for da/dN vs ΔK_{eff}). It is seen that for all the models, the minimum in 2nd overload growth rates (and hence maximum interaction) occur when the two overloads are separated by a'_{min} (i.e. the amount of crack extension to reach the minimum growth rate during a single overload), consistent with the finding from Mills and Hertzberg. The predicted a'_{min} values are approximately 0.25 $r_{p(OL)}$, 0.19 $r_{p(OL)}$ and 0.50$r_{p(OL)}$ for FE, strip yield type and analytical models respectively. The incidence of the maximum double overload interaction effect occurring when the 2nd overload is applied at the growth rate minimum of the first transient can of course be seen as simply consistent with the previous consideration of 'R_{eff}' influences in the analytical model. If closure is the controlling process in these transients, then the minimum da/dN point of the single overload will correspond to the maximum closure condition of the first overload: any transient applied now will experience the least reversed plastic deformation during unloading and leave the largest residual lump in the crack wake. In terms of the quantitative comparison of the experimental results with the present models, it must be noted that the results of Mills and Hertzberg should be distinctly plane stress dominated, and as such, comparisons with the work of Khor [2004] on side grooved thick samples is required. Figure 4.53 shows examples of da/dN transient curves for 2024-types alloys under such plane strain dominated conditions. It may be seen that

an enhanced overload growth rate transient indeed occurs as overload spacings are reduced (see Figure 5.31).

It has been mentioned in the previous chapter that with $\beta_I = 1.3$, the current analytical model is able to predict experimental peak closure levels and minimum growth rates for cracks subjected to single overloads reasonably well. However for the dual overload models, the analytical model is tested for β_I values of 1.0, 1.1, 1.2 and 1.3 for comparison with experimental results from Khor [2004]. Figure 5.31 shows the plot of minimum normalised growth rates $((da/dN)/(da/dN)_{(BL)})$ versus normalised overloads spacing $(\Delta a_s/r_{p(OL)})$, for $\Delta K_{(BL)} = 12$ MPa $m^{1/2}$, $R = 0.1$, $\%OL = 100$. It can be seen that FE models predict higher minimum $(da/dN)/(da/dN)_{(BL)}$ values as compared to the experiments, however the trends in minimum $(da/dN)/(da/dN)_{(BL)}$ values appear to be reasonably well captured. Practical limitations prevented the experimental data covering small overloads spacing tests [Khor, 2004]. Analytical modelling with $\beta_I = 1.1$ gives a closer prediction to the experimental results, however analytical modelling is observed to over predict overload interactions for $\beta_I = 1.2$ and 1.3: for a range of intermediate overload spacing (~ 0.01 – 2 $r_{p(OL)}$ for $\beta_I = 1.3$ and ~0.03 – 1 $r_{p(OL)}$ for $\beta_I = 1.2$) crack arrest is in fact predicted. In the first instance there is therefore some conflict in optimum β_I values to fit the experimental data, with the reduced β_I required for the double overload results suggesting an attenuation in closure effect.

5.3 Multiple overloads

In moving towards an understanding on fatigue crack response during realistic service loads, the effects of periodic overloads (dual or multiple, isolated or block) have been investigated (e.g. Wei *et al.*, 1973, Mills and Hertzberg, 1976, 1977, Hammouda *et al.*, 1998, Tur and Vardar, 1996, Celik *et al.*, 2004, Klysz, 2001, Heper and Vardar, 2003, Ramos *et al.*, 2003, Fleck, 1985, Skorupa *et al.*, 1999, Petit *et al.*, 1988, Blom and Holm, 1987, Ohrloff *et al.*, 1988, Porter, 1972, Bretz, *et al.*, 1984, Chang et al., 1981, Jonas and Wei, 1971, Newman, 1997, 1999, Rice and Stephens, 1973, Park and Song, 1999, Zhang *et al.*, 1987, Trockels, *et al.*, 1994, 1996, Kiese *et al.*, 1990, Stephens, *et al.*, 1977, Iwasaki et al., 1982, Wei and Shih, 1974, Corbly and Packman,

1973, Yang and Li, 1991, Bathias and Vancon, 1978, Lang and Marci, 1999, Phillips, 1999, Dawicke, 1997, Kermandis and Pantelakis, 2001, Kim and Song, 1994). Jonas and Wei [1971] for example observed an apparent dependance of interactions between *repeated* overloads on the interval between the overloads. In the literature, the separation between periodic single overloads is almost invariably reported in terms of baseline cycles separating consecutive overloads, ΔN_s (e.g. Portar, 1972, Rice and Stephen, 1973, Fleck, 1985, Zhang *et al.*, 1987, Klysz, 2001, Ramos *et al.*, 2003, Celik *et al.*, 2004), with few expressing this in terms of separation distances, Δa_s (e.g., Stephens, *et al.*, 1977, Tur and Vardar, 1996, Khor, 2004). ΔN_s has been a favoured choice particularly due to the ease at which overload periodicity can be controlled during fatigue experiments, rather than using Δa_s as the controlling parameter, which requires accurate monitoring of crack length. The physical significance of using ΔN_s as a controlling parameter in multiple overload tests is clearly unsatisfactory as length scales relating the location of a given overload to previous deformation fields are required to appreciate the micromechanical processes involved. It has also been observed experimentally that equal ΔN_s need not necessarily yield equal Δa_s as the crack propagates, even for constant $\Delta K_{(BL)}$ tests (Khor, 2004). Experimental results reported by Porter [1972] (for 7075-T6 and 2024-T3 aluminium alloys), Rice and Stephens [1973] (for Mn-Steel alloy), Iwasaki *et al.*, [1982] (for SM50B steel alloy), Zhang et al., [1987] (for 7475-T7351 aluminium alloy), Trockels *et al.*, [1994, 1996] (for a modified 7075 aluminium alloy), Skorupa [1999] and Ramos *et al.*, [2003] (a 'low carbon steel' alloy) showed increasing crack growth retardation with increasing ΔN_s (up to ~ 1000, 20,000, 50,000, 100, 20,000, 100 and 20,000 cycles respectively). Similar observations have also been made by Fleck [1985], Ohrloff *et al.*, [1988] and Kiese *et al.*, [1990]. Yildrim and Vardar [1990] (7075-T6 aluminium alloy), Tur and Vardar [1996] (2024-T3 aluminium alloy), Klysz [2001] (PA7 aluminium alloy) and Celik *et al.*, [2004] (2024-T3 and 7075-T6 aluminium alloy) observed an optimum value of overload separation at which retardation is maximum, i.e., retardation initially increases with overload spacing (ΔN_s or Δa_s) and reaches a peak value, and then decreases to a value corresponding to single overload conditions, In the limiting case, i.e. when ΔN_s or $\Delta a_s = 0$, growth rate must correspond to constant amplitude growth at ΔK_{OL}, which will be faster than of $\Delta K_{(BL)}$. Celik *et al.*, [2004] and Tur and Vardar [1996] reported that for

constant applied stress tests (i.e. $\Delta\sigma_{(BL)}$ = constant) maximum retardation was observed at $\Delta N_s/N_d \approx 0.5$; however for constant stress intensity factor tests ($\Delta K_{(BL)}$ = constant) the maximum retardation exhibited a plateau, with the plateau extending from $\Delta N_s/N_d \approx 0.5$ to 1.0. In terms of separation distances, for $\Delta K_{(BL)}$ = constant tests, maximum crack growth retardation (exhibiting a plateau) occurred at $\Delta a_s/r_{p(OL)} \approx 0.07$ to 0.40; while for $\Delta\sigma_{(BL)}$ = constant tests, maximum retardation (peak) occurred at $\Delta a_s/r_{p(OL)} \approx 0.2$.

Whilst most studies made on reported periodic overloads are based on experimental approaches, a few FE studies exist, particularly for plane stress situations, e.g., Blom and Holm [1987], Park and Song [1999] and Heper and Vardar [2003]. Blom and Holm [1987] and Park and Song [1999] suggest an increase in crack closure levels with ongoing crack propagation, which then appears to stabilise to a 'plateau' level. Heper and Vardar [2003] studied deformation characteristics of periodic overloads and found that differential surface profiles (differences in crack surface displacements after and before overloads) increased with decreasing separation of overloads. It is appropriate to note to the best of author's knowledge no report has been found on plane strain FE analyses subjected to periodic overloads. Hence in the subsequent sections attempts will be made to address plane strain modelling in particular (using strip yield, FE and analytical methods) of fatigue cracks subjected to periodic overloads of equal magnitudes separated by equal spacings. Similar strip yield, FE and analytical methods described above are used. Figure 5.32 shows schematically the nomenclature adopted for periodic overloads analyses. In the first instance analyses are conducted for $\Delta K_{(BL)}$ = 12 MPa m$^{1/2}$ and R = 0.1 and $\%OL$ = 50, 75 and 100.

5.3.1 Strip yield type modelling

Figure 5.33 shows variations of U with normalised crack length ($\Delta a/r_{p(OL)}$) for $\Delta K_{(BL)}$ = 12 MPa m$^{1/2}$, R = 0.1, $\%OL$ = 50. The first overload is located at $\Delta a/r_{p(OL)}$ = 0.0 and subsequent periodic overloads are applied at a spacing, $\Delta a_s = 0.233\ r_{p(OL)}$. Increasing severity of peak closure levels can be observed for approximately 1.0 $r_{p(OL)}$ from the location of the first overload, after which 'saturation' appears to occur. In the first instance an envelope passing through maximum closure levels can be defined as a

measure of closure severity as the crack propagates. The variation of maximum closure envelopes for $\%OL$ = 50, 75 and 100 are plotted in Figure 5.34 for equal overload spacing of $\Delta a_s \sim 0.22\ r_{p(OL)}$ in all the 3 cases. It can be seen from Figure 5.34 that there is a rise in the maximum closure envelope as $\%OL$ increases, however the envelopes appear to saturate ('saturation effect') at $\Delta a = 1.0\ r_{p(OL)}$ in all 3 cases, suggesting that the saturation process is primarily controlled by overload deformation. The present results agree qualitatively with the experimental findings of Kim and Song [1994] on 2024 aluminium alloy subjected to periodic overloads (varying $\%OL$ and ΔN_s), where the authors reported a stabilized value of crack opening loads as crack growth proceeds.

5.3.2 Analytical modelling

The analytical model for periodic overloads follows the double overload model as discussed in Section 5.2.3. When an overload is applied, the closure level of the previous overload transient at the overload location is taken as the R_{eff}. Variation of U with normalised crack length ($\Delta a/r_{p(OL)}$) for $\Delta K_{(BL)}$ = 12 MPa m$^{1/2}$, R = 0.1, $\%OL$ = 75 is shown in Figure 5.35 for $\Delta a_s = 0.323\ r_{p(OL)}$. The saturation effect of the peak closure levels is observed and occurred at approximately $\Delta a = 1.0\ r_{p(OL)}$. Figure 5.36 shows the overload level effect on the maximum closure envelope ($\Delta a_s \sim 0.32\ r_{p(OL)}$). It can be seen from Figure 5.36 that there is a rise in maximum closure envelope with increasing $\%OL$. The findings from analytical model agree, at least functionally, with the results from strip yield model (see Section 5.3.3).

5.3.3 FE modelling

Figure 5.37 shows crack profiles subjected to both constant amplitude and periodic overloads ($\Delta K_{(BL)}$ = 12 MPa m$^{1/2}$, R = 0.1) after the crack has propagated for about 31.5 $r_{p(BL)}$: periodic overloads of $\%OL$ = 100 were applied at a spacing of $\Delta a_s = 0.595\ r_{p(OL)}$. The periodic overload crack profile is plotted at the onset of closure (K_{cl}/K_{max} = 0.68), and the constant amplitude crack profile is plotted at the same load level (K/K_{max} = 0.68) for comparison. Apparent interaction of the periodic residual lumps is observed with each lump starting near the overload locations. Such periodic lumps in

the crack wake are also seen in the plane stress FE analyses conducted by Heper and Vardar [2003] for similar loading patterns. It can be seen that the first contact occurs at the overload lump closest to the crack tip.

Variation of U with crack length is plotted against normalised crack length, $\Delta a/r_{p(OL)}$, in Figure 5.38 for the conditions mentioned above. The initial variation of U with crack length is seen to follow the results from the strip yield and analytical models. An increase of peak closure level is seen: this is however followed by a decrease to a lower saturation level ('peak and saturation effect'). The presence of the 'peak and saturation effect' in the maximum closure envelope is not shown by either the strip yield and analytical models (both approaches only show a 'saturation effect'). Figure 5.39 shows the variation of maximum closure envelopes for $\%OL$ = 50, 75 and 100 ($\Delta a_s \sim 0.3\ r_{p(OL)}$). A rising pattern of maximum closure levels is seen with increasing $\%OL$, which is consistent with the findings from strip yield and analytical models. 'Peak and saturation effect' on maximum closure envelope are however seen consistently for all $\%OL$s. In all cases, the peak of the maximum closure levels appear to occur at about 1.0 $r_{p(OL)}$ from the location of the first overload.

In assessing the presence of the 'peak and saturation effect' in the FE results a distinct evolution in the overload plastic zone sizes was noted. Variation of Von Mises plastic strain with (0.2% plastic strain as the limiting plastic boundary) is shown in Figure 5.40a, ($\Delta K_{(BL)}$ = 12 MPa $m^{1/2}$, R = 0.1, $\%OL$ = 100 and $\Delta a_s \sim 0.595\ r_{p(OL)}$. Interaction of the periodic OL plastic zone sizes can be readily seen for the conditions considered, with OL plastic zone sizes diminishing as propagation progresses. Figure 5.40b shows for comparison the baseline growth plastic zone behaviour ($\Delta K_{(BL)}$ = 12 MPa $m^{1/2}$, R = 0.1). An initial transient in plastic zone size can be seen in Figure 5.40b that is similar in relative magnitude to the change in periodic overload plastic zone sizes in Figure 5.40a. In Chapter 3, an initial closure transient (discontinuous closure near the pre-crack tip) in constant amplitude plane strain models has been noted, which is not present for the plane stress case and has been linked to the build up of in-plane constraint. To the best of author's knowledge, there are no reports in the literature on such changes in plastic zone size with ongoing crack propagation,

however, such a decreasing plastic zone size is clearly consistent with increasing constraint.

Figure 5.41a and 5.41b show the Von-Mises plastic plastic strain plot for static tearing (non-cyclic loding) and fatigue crack growth for similar loading conditions (K_{max} = 13.3 MPa $m^{1/2}$, R = 0.1). It can be seen from both Figure 5.41a and 5.41b that evolution of plastic zones behaviour takes place both in static tearing and fatigue crack propagation which is again consistent with increasing constraint. To validate the present FE model in relation to tearing cracks, which has been considered to some detail in the literature, comparison is made with the result from Sham [1983]. Figure 5.42 shows the variation of normalised crack opening ($\delta/(J/\sigma_y)$) with normalised distance behind the crack tip ($\Delta a/(K_{max}/\sigma_y)^2$), where K_{max} = 13.3 MPa $m^{1/2}$. Whilst the present models have a coarser mesh than that of Sham, both the results appear to agree well, suggesting that present FE modelling approach is indeed meaningful. The appearance of a 'peak and saturation effect' in the peak closure levels due to periodic overloads in plane strain may then be explained by understanding the material movement during fatigue crack propagation. It has been noted in Chapter 3 for constant amplitude plane strain conditions, material cannot move in the thickness direction and the discontinuous contact near the pre-crack tip results from the transverse (in plane) movement of material near the pre-crack tip (causing a transient lump), see Figure 3.10 and 3.11. It may be noted that diminishing closure effects (approaching saturation) following peak closure levels may then arise from the requirement to keep the material moving forward, in plane. For subsequent overloads: it may be intuitively noted that having drawn material forward along the crack wake for one overload, a closely spaced additional overload will encounter increased resistance in drawing more material forward from the crack wake. This follows through to the logical 'end point' where the overload spacing becomes vanishingly small and growth is simply occurring at a consistent $\Delta K_{(OL)}$: for plane strain conditions results in chapter 3 indicate that closure levels must tend towards zero under sustained crack growth (after an initial transient at the undeformed pre-crack tip). The requirement for transverse movement of material does not arise for plane stress conditions (materials movement occurs through thickness), and hence a 'peak and saturation' effect should not occur for plane stress cracks subjected to periodic

overloads if the above explanation is correct. Figure 5.43 plots the variation of U with normalised crack length ($\Delta a/r_{p(OL)}$), for sustained periodic overloads under plane stress conditions ($\Delta K_{(BL)}$ = 12 MPa m$^{1/2}$, R = 0.1, $\%OL$ = 100,) $\Delta a_s \sim 0.196\ r_{p(OL)}$). A simple saturation of peak closure levels is seen, consistent with proposed dependence of plane strain periodic transient behaviour on transverse material movement. It may then be seen that the evolution of multiple transient effects in plane strain requires consideration of at least two phenomena, *viz:* 1) the 'effective R-ratio' influence of previous transient, and, 2) increasing transverse constraint. These act in opposing senses in terms of the severity of ongoing closure transients. Whilst this has not been explored as part of this thesis, it may be seen that the formulation of the analytical overload models did not include the in-plane constraint effect, hence the fact that β_I needed to be lowered for consistency with experimental data is consistent with not including the constraint effect. The absence of 'peak + saturation' effect in the strip yield modelling may also be seen as entirely consistent with the model's fundamental plane stress character, where in-plane constraint effects must be minimal.

5.3.4 Growth rate predictions: Airbus test data

Due to the lack of detailed experimental results for closely applied periodic overloads, the present model results cannot be exactly verified. Attempts made by Khor [2004] yielded ambiguous and unreliable results when closely spaced periodic overloads were applied, due to the difficulty in controlling small OL separations. Data was alternatively volunteered by Airbus, UK [McMaster, 1997] as a 'blind' test of the overload modelling understanding obtained on this work. Figure 5.44 illustrates the crack growth data in question, where fatigue was occurring in 2024 –T351 aluminium alloy over a $\Delta K_{(BL)}$ varying from 12-35 MPa m$^{1/2}$, with 3 overloads of 75% being applied at $\Delta K_{(BL)}$ MPa m$^{1/2}$ ~ 18, 20 and 24 MPa m$^{1/2}$. The thickness of the specimen was 14 mm, so test conditions would be considered to be predominantly in plane strain. As the experimental $\Delta K_{(BL)}$ varies over quite high ΔK levels, in order to predict da/dN from analytical U values, an extended da/dN vs ΔK_{eff} curve was required. The available experimental da/dN vs ΔK_{eff} result (Figure 4.53) from Xu [2001] are valid up to $\Delta K_{eff} \cong$ 12 MPa m$^{1/2}$, whilst constant amplitude growth results from McMaster [1997] showed da/dN vs ΔK for higher ΔK (i.e. > 10 MPa m$^{1/2}$). From Figure 4.45 it

can however be seen that for high ΔK levels (say > 12 MPa $m^{1/2}$), $U > 0.90$ for plane strain conditions, suggesting negligible closure effect. For negligible closure levels, ΔK_{eff} may of course be approximated by ΔK_{app}. Figure 5.45 shows a plot of da/dN vs ΔK_{eff} curves from both Xu [2001] and McMaster [1997] where there indeed appears to be a seamless transition from one curve to the other, supporting the assumption that baseline closure becomes negligible (in plane strain) at higher ΔK values. In the previous Chapter 4, it has been identified that PICC should be the main mechanism controlling the transient overload, hence the PICC analytical model with $\beta_I = 1.3$ is adopted to predict the growth rate. Furthermore, it is assumed that the overloads do not interact as the spacing is found to be greater than $\sim 5r_{p(OL)}$ (i.e. beyond the interation distance suggested by the present modelling). Figure 5.46 shows the comparison of predicted analytical growth rate results and the experimental results from McMaster [1997]. It appears that the analytical predictions are indeed fairly good. It may be seen that the brief growth rate acceleration immediately following an overload is not predicted by analytical model as there is no baseline closure to alleviate. The predicted retardations are slightly less than those measured; but it may be noted that the experimental conditions were not for pure plane strain conditions (non-side groove samples), so there will always be a plane stress region at the surfaces which undergoes greater closure effect (for the OL K used here, the surface plastic zone size would be of ~2 mm, over a total section thickness of 14 mm). Overall it may be noted that the present closure understanding has been successfully used to predict the supplied data with no modification or re-calibration of the procedures and understanding obtained at lower K levels.

5.4 Conclusions

1. Double OL closure behaviour is functionally similar for all three modelling (i.e. FE, simple analytical and strip yield models) approaches used:
    - the analytical approach suggest much of the double OL effect is linked to closure influence of a first OL upon the second OL
    - under repeated overloads, an important functional difference is seen between FE and the analytical and strip yield models. This has been

linked to the absence of in-plane constraint in the non-FE models, which is seen to have a distinct decreasing influence on on-going closure effects.

2. Clear experimental validation of data is often complicated by experimental problems:
    - for high $\Delta K_{(BL)}$ periodic OL data supplied by Airbus [McMaster, 1997], reasonable correlation was achieved via simple analytical models (large OL spacing)
    - for intermediate $\Delta K_{(BL)}$ double OL data from Southampton, FE models produce reasonable trend information
    - analytical (PICC) modelling is shown to over-predict retardation effects, although this may be identified with the current lack of constraint effects in the model

$\Delta K_{(BL)}$	%OL	$\Delta a_s/r_{p(BL)}$								
		0.136	0.272	0.612	0.952	1.632	4.692	7.752	13.94	25.975
12.0	50.0	♣	♣	♣	♣	♣	♣	♣	♣	
	75.0	♣	♣	♣	♣	♣	♣	♣	♣	♣
	100.0	♣	♣	♣	♣	♣	♣	♣	♣	♣

♣ Analyses performed

Table 5.1: Analysis matrix for undeflected cracks subjected to double overload loads separated by various $\Delta a_s/r_{p(BL)}$ spacings ($R = 0.1$).

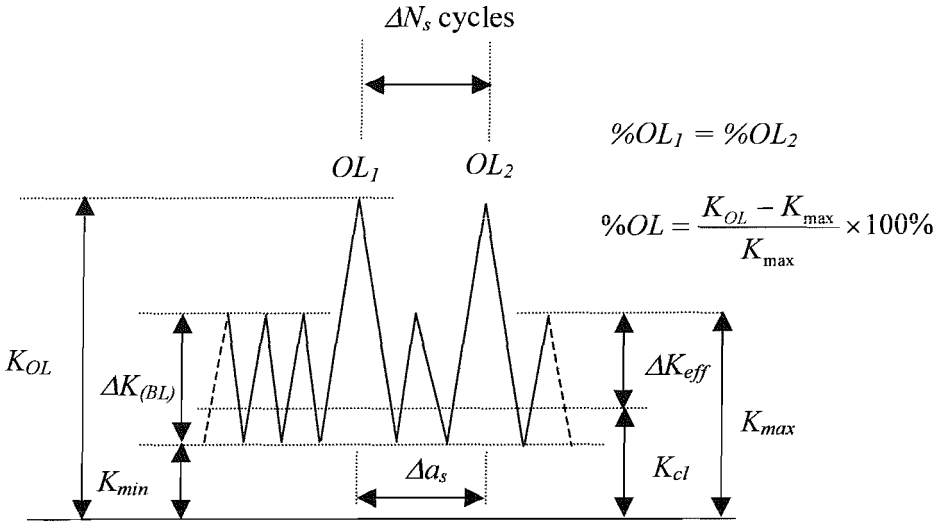

Figure 5.1: Schematic illustration of the nomenclature adopted for double overloads analyses.

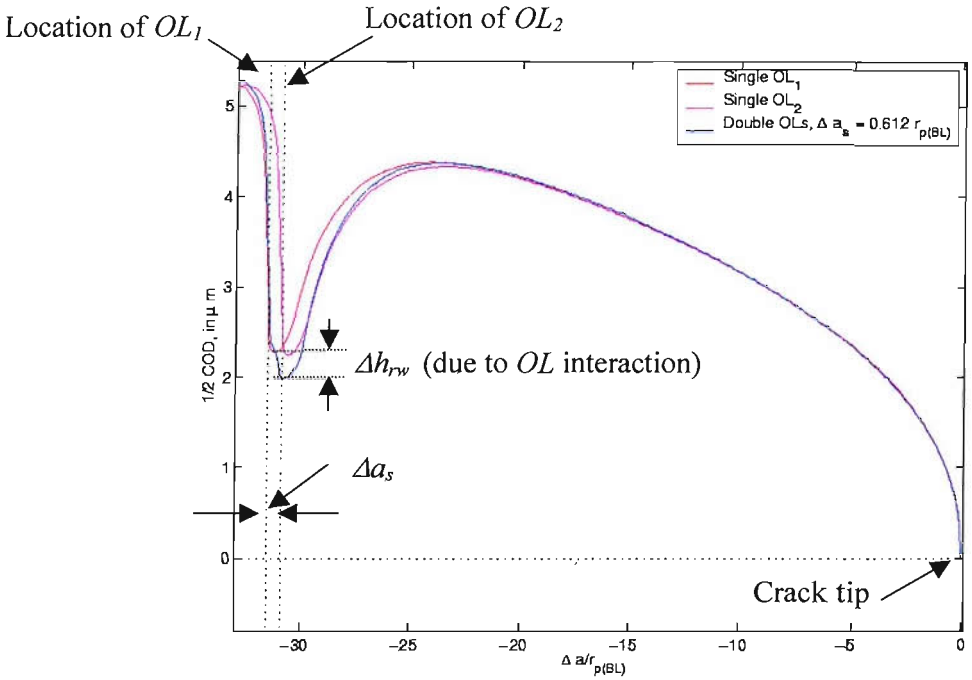

Figure 5.2: Crack profiles predicted by FE modelling for single and double overloads (Δa_s = 0.612 $r_{p(BL)}$) at K/K_{max} = 0.612 ($\Delta K_{(BL)}$ = 12.0 MPa m$^{1/2}$, R = 0.1, $\%OL$ = 100.0).

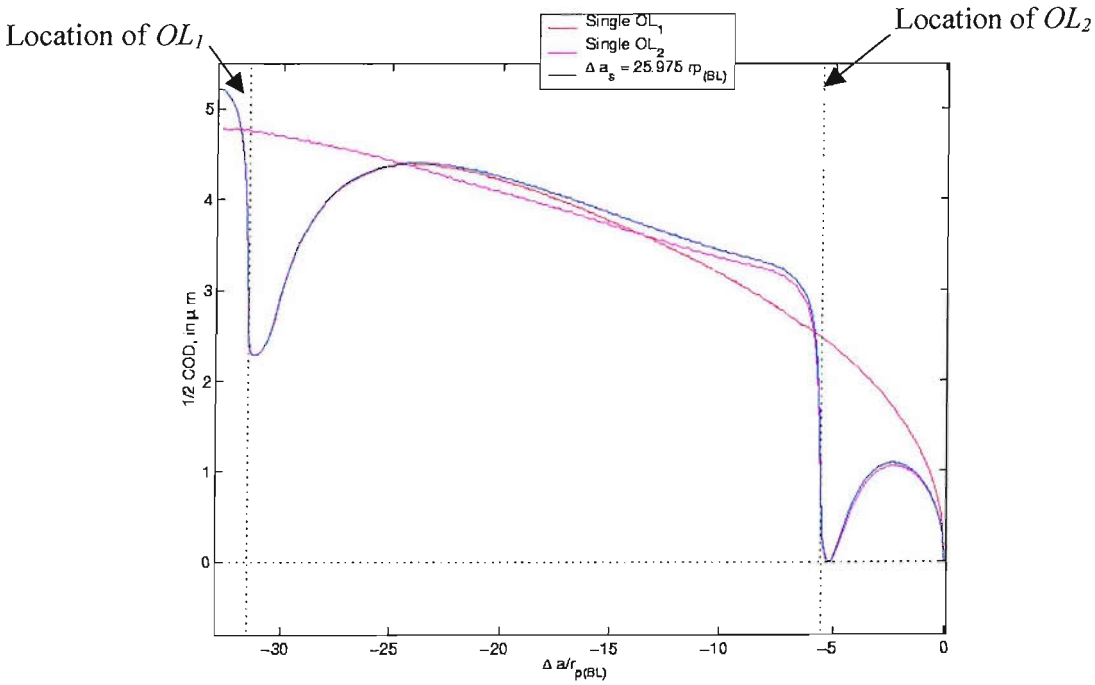

Figure 5.3: Crack profiles predicted by FE modelling for single and double overloads (Δa_s = 25.97 $r_{p(BL)}$) at K_{cl}/K_{max} = 0.612 ($\Delta K_{(BL)}$ = 12.0 MPa m$^{1/2}$, R = 0.1, $\%OL$ = 100.0).

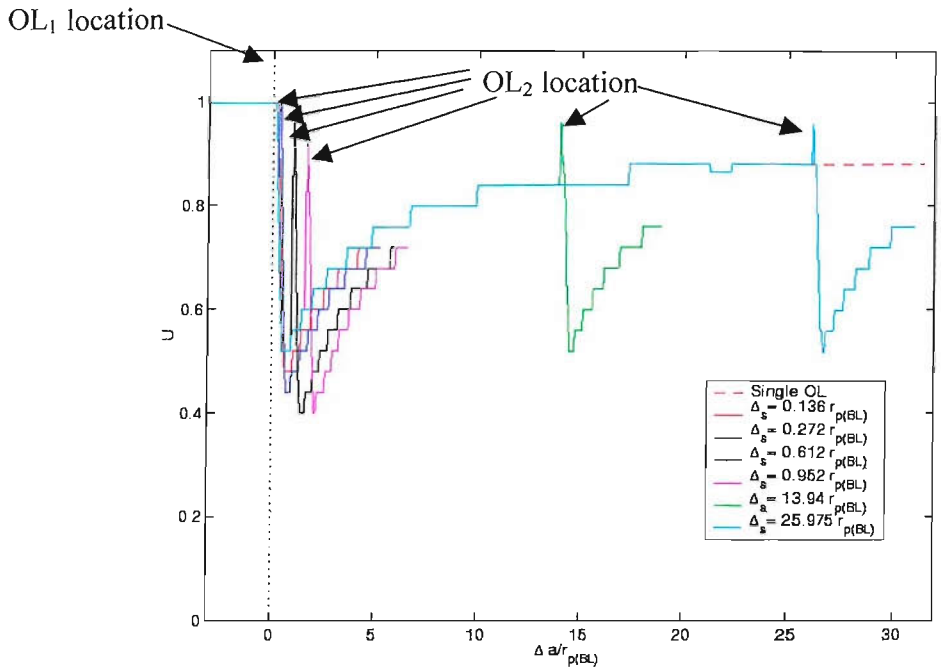

Figure 5.4: Effect of overload spacing on closure predicted by FE modelling ($\Delta K_{(BL)}$ = 12.0 MPa m$^{1/2}$, $R = 0.1$, $\%OL = 75.0$).

$$\alpha_{SOL-\max} = \frac{\left[\frac{K_{cl}}{K_{\max}}\right]_{DOL-\max}}{\left[\frac{K_{cl}}{K_{\max}}\right]_{SOL-\max}}$$

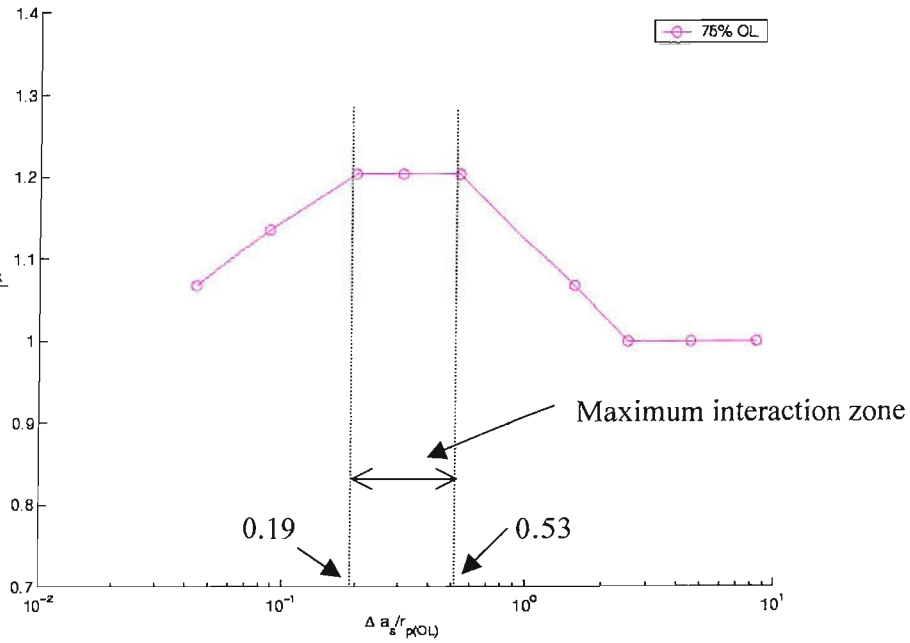

Figure 5.5: Variation of $\alpha_{SOL-max}$ with OL spacing for different OL ratios predicted by FE modelling ($\Delta K_{(BL)}$ = 12 MPa m$^{1/2}$, $R = 0.1$, $\%OL = 75$).

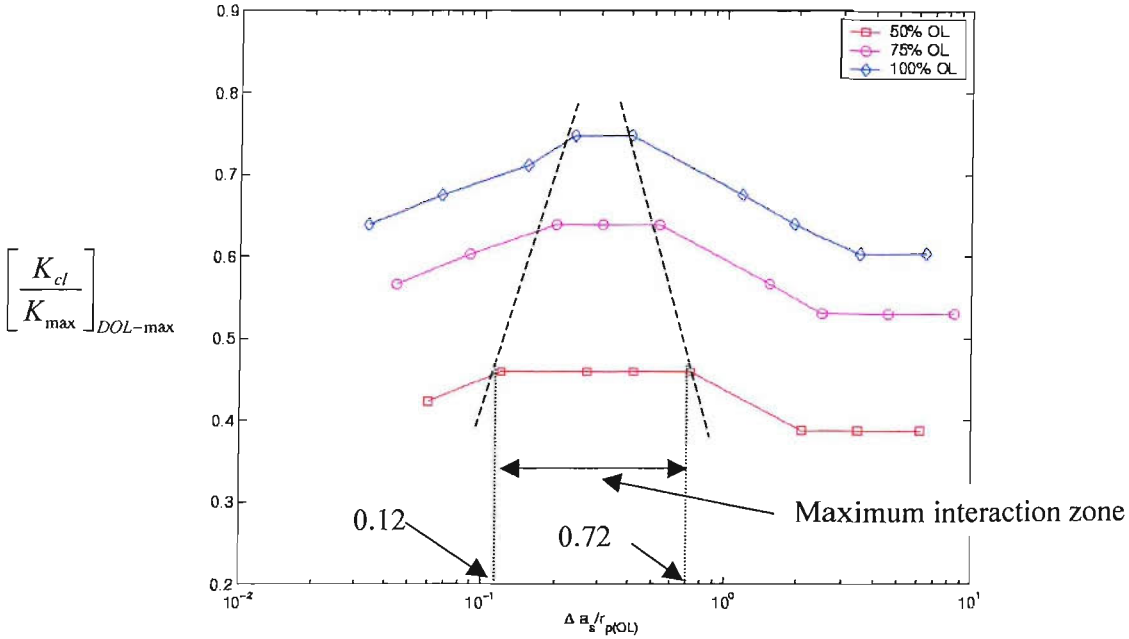

Figure 5.6: Variation of maximum closure levels with OL spacing predicted by FE modelling ($\Delta K_{(BL)}$ = 12.0 MPa m$^{1/2}$, R = 0.1).

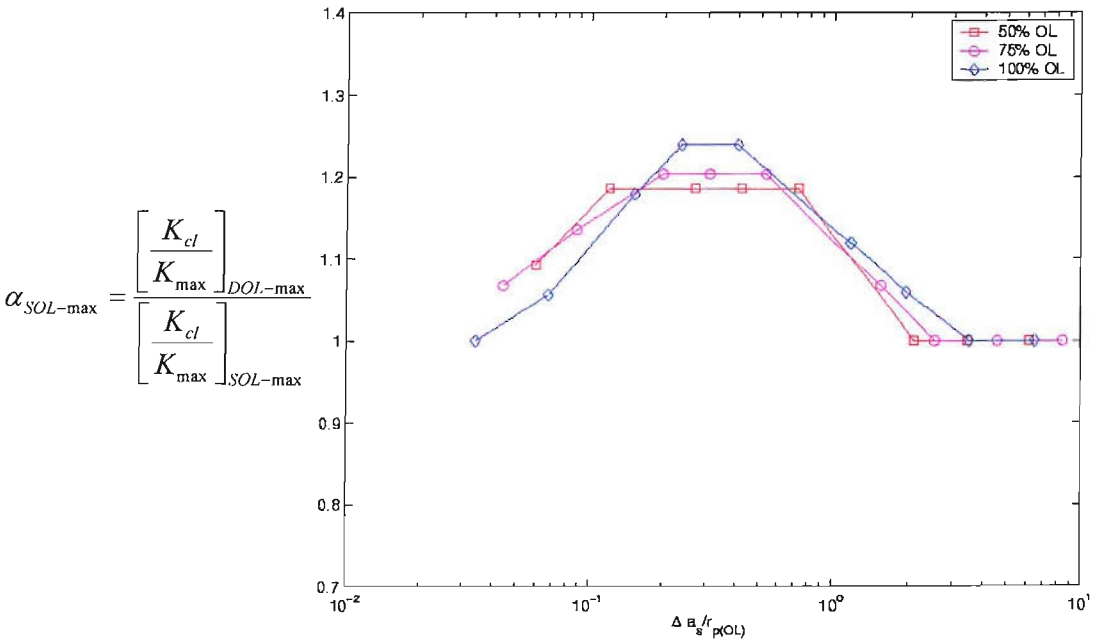

Figure 5.7: Variation of $\alpha_{SOL-max}$ with OL spacing for different OL ratios predicted by FE modelling ($\Delta K_{(BL)}$ = 12 MPa m$^{1/2}$, R = 0.1).

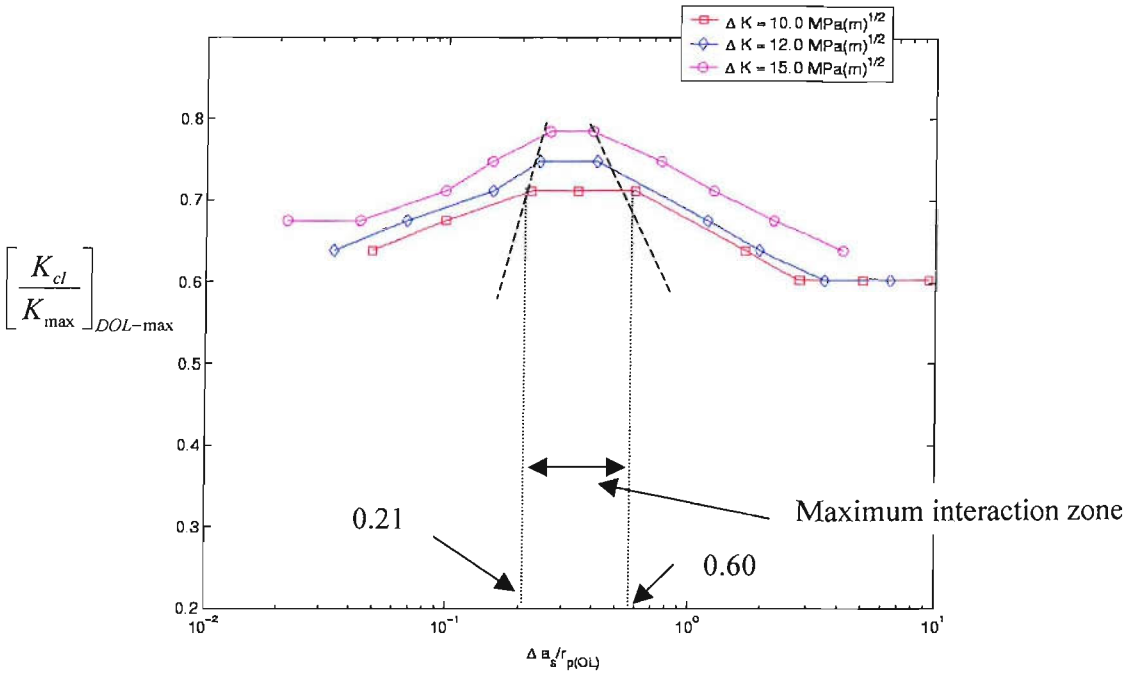

Figure 5.8: Variation of maximum closure levels with $\Delta K_{(BL)}$ predicted by FE modelling, $\%OL = 100$, $R = 0.1$.

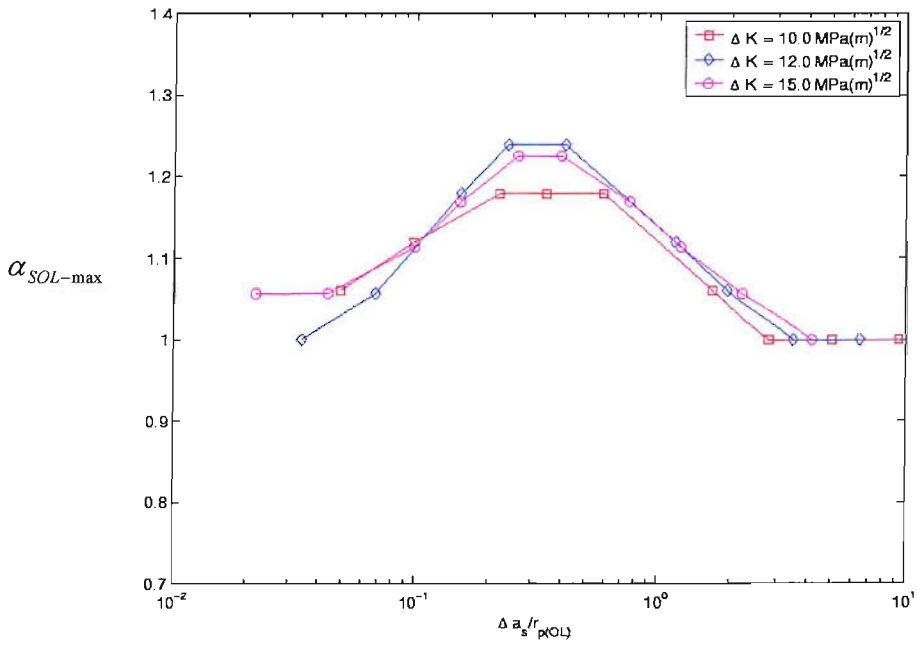

Figure 5.9: Variation of $\alpha_{SOL\text{-}max}$ with $\Delta K_{(BL)}$ predicted by FE modelling, $\%OL = 100$, $R = 0.1$.

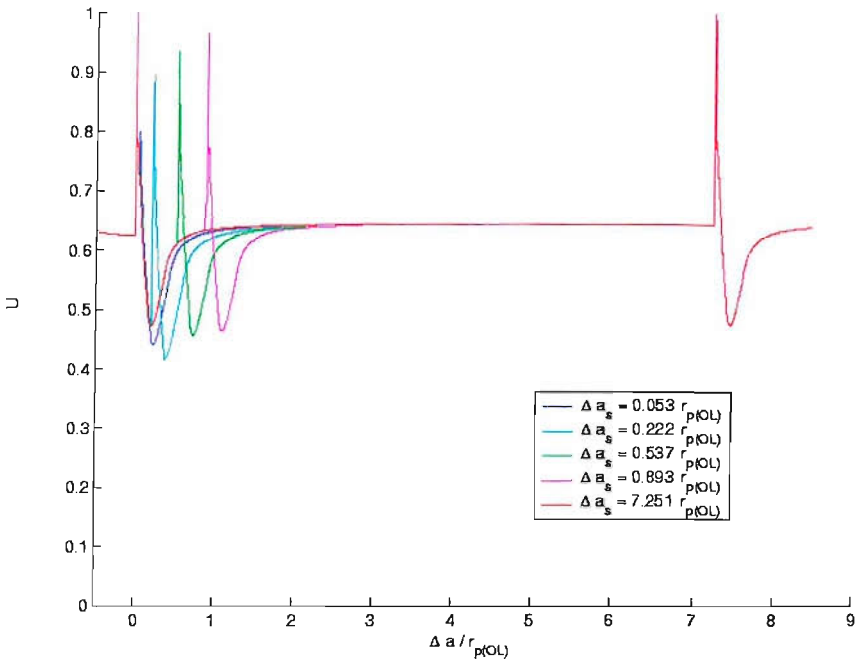

Figure 5.10: Effect of overload spacing on closure predicted by strip yield approach, $\Delta K_{(BL)}$ = 12 MPa m$^{1/2}$, R = 0.1.

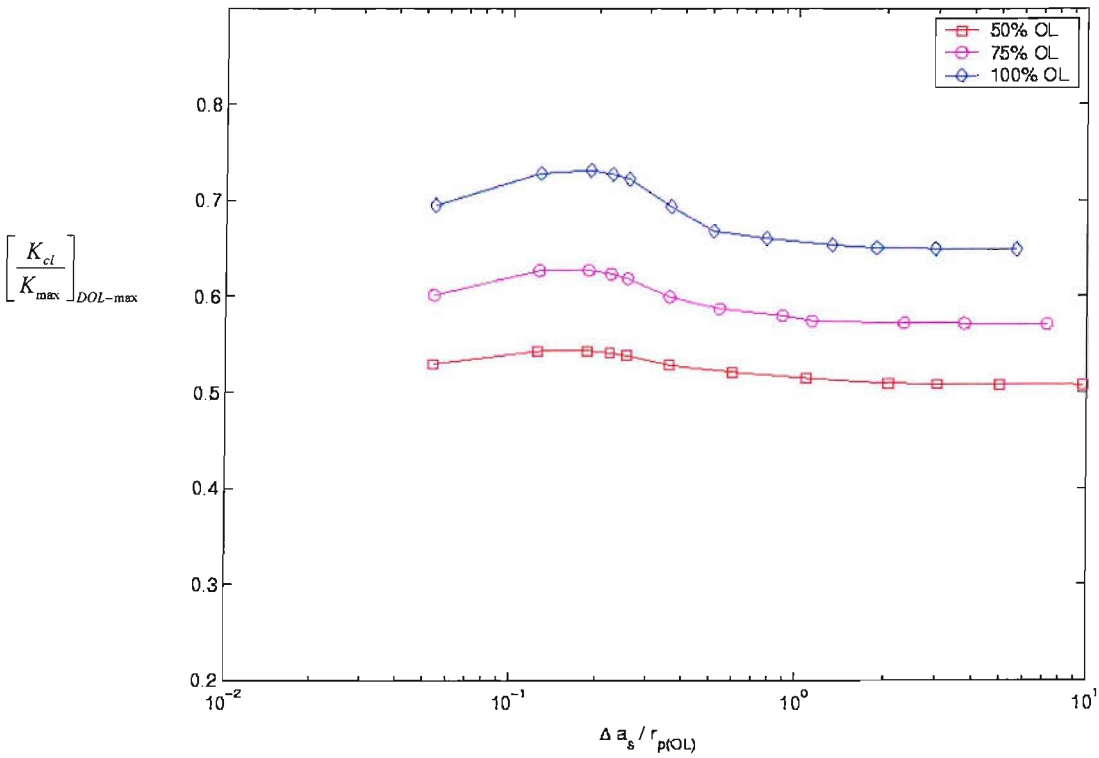

Figure 5.11: Variation of maximum closure levels with OL spacing for different OL ratios predicted by strip yield approach ($\Delta K_{(BL)}$ = 12 MPa m$^{1/2}$, R = 0.1).

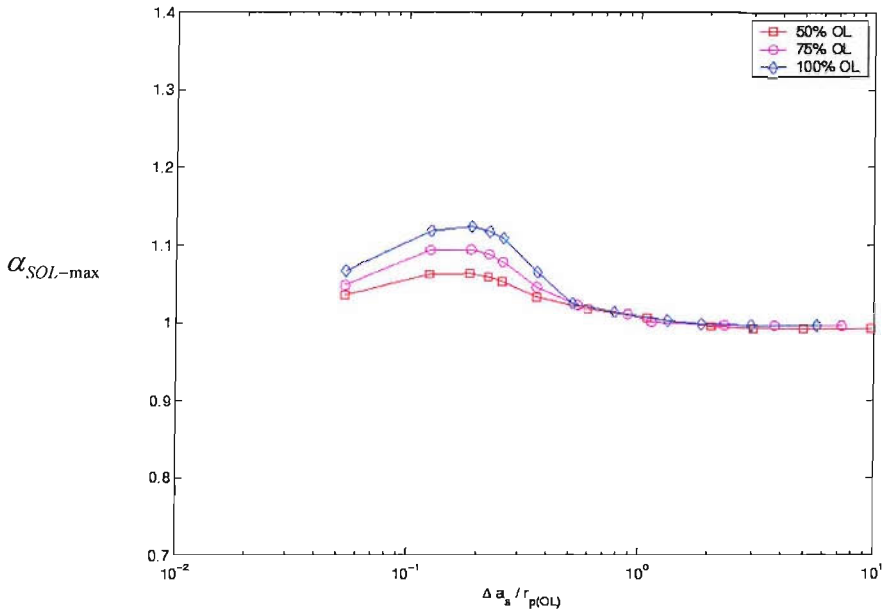

Figure 5.12: Variation of $\alpha_{SOL\text{-}max}$ with OL spacing for different $\Delta K_{(BL)}$ predicted by strip yield approach ($\Delta K_{(BL)}$ = 12 MPa m$^{1/2}$, $R = 0.1$).

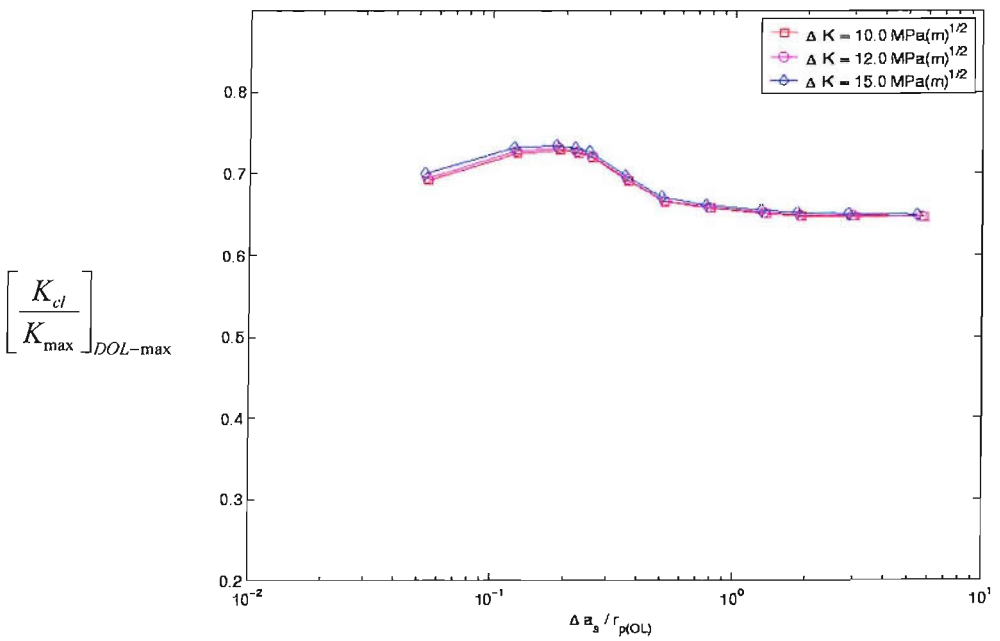

Figure 5.13: Variation of maximum closure levels with OL spacing for different OL ratios predicted by strip yield approach ($\%OL$ = 100, $R = 0.1$).

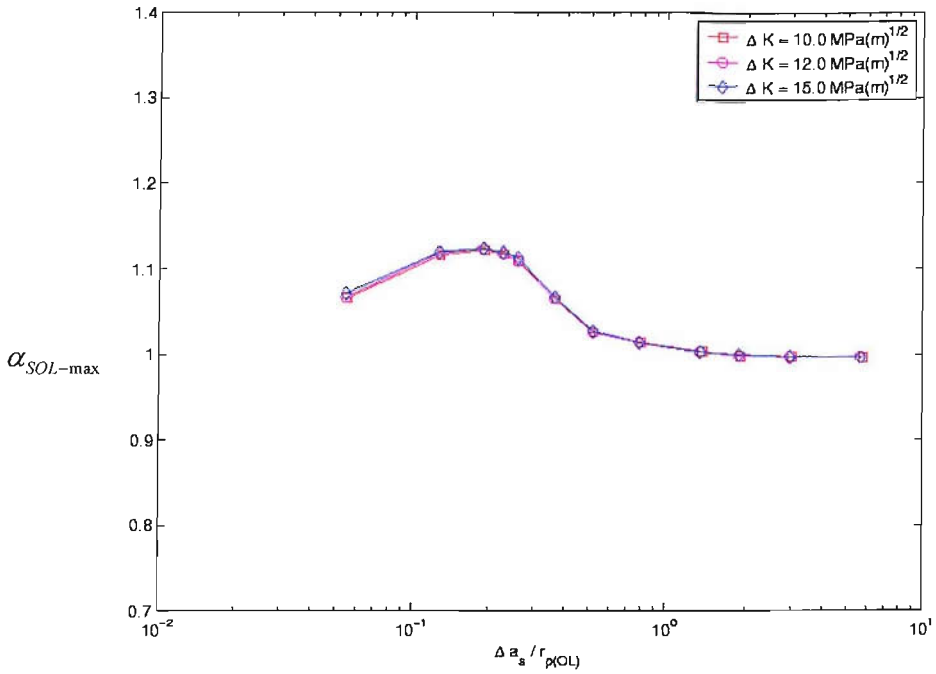

Figure 5.14: Variation of $\alpha_{SOL\text{-}max}$ with OL spacing for different $\Delta K_{(BL)}$ predicted by strip yield approach ($\%OL$ = 100, R = 0.1).

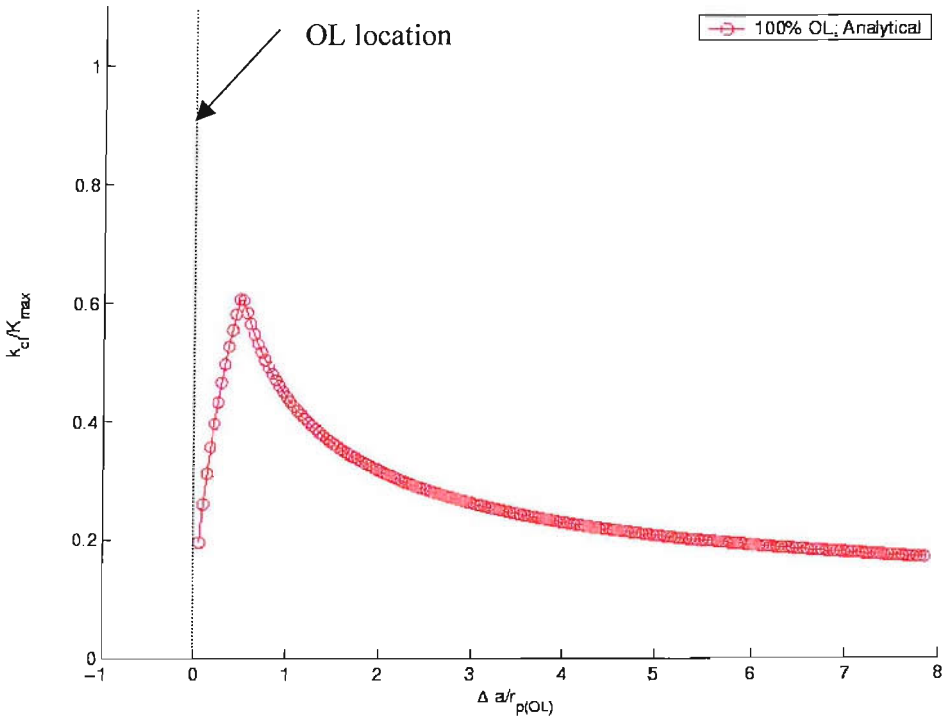

Figure 5.15: Variation closure levels for single OL predicted by analytical modelling ($\Delta K_{(BL)}$ = 12 MPa m$^{1/2}$, R = 0.1, $\%OL$ = 100).

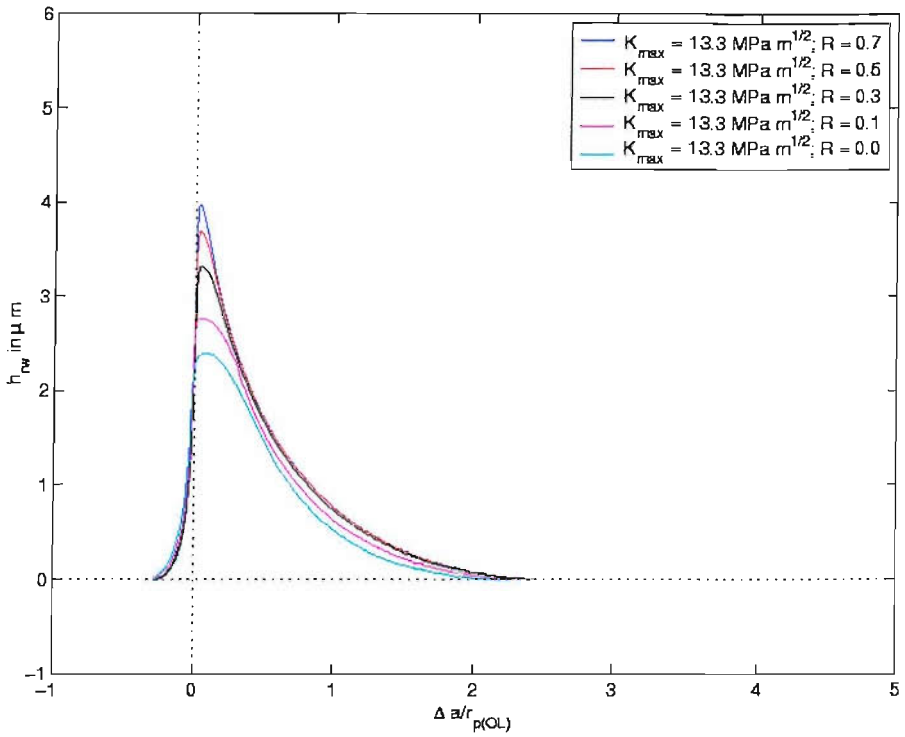

Figure 5.16: Variation of wedge profiles (h_{rw}) with R (fixed K_{max}) predicted by FE modelling, $\%OL$ = 100.

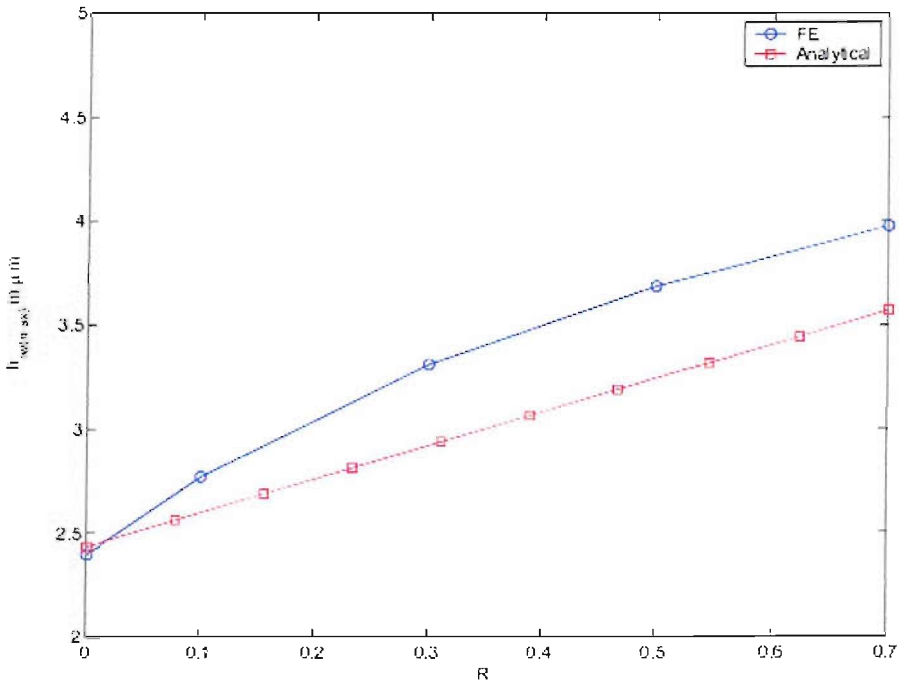

Figure 5.17: Normalised $h_{rw(max)}$ variation, $\Delta K_{(BL)}$ = 12 MPa m$^{1/2}$, $\%OL$ = 100.

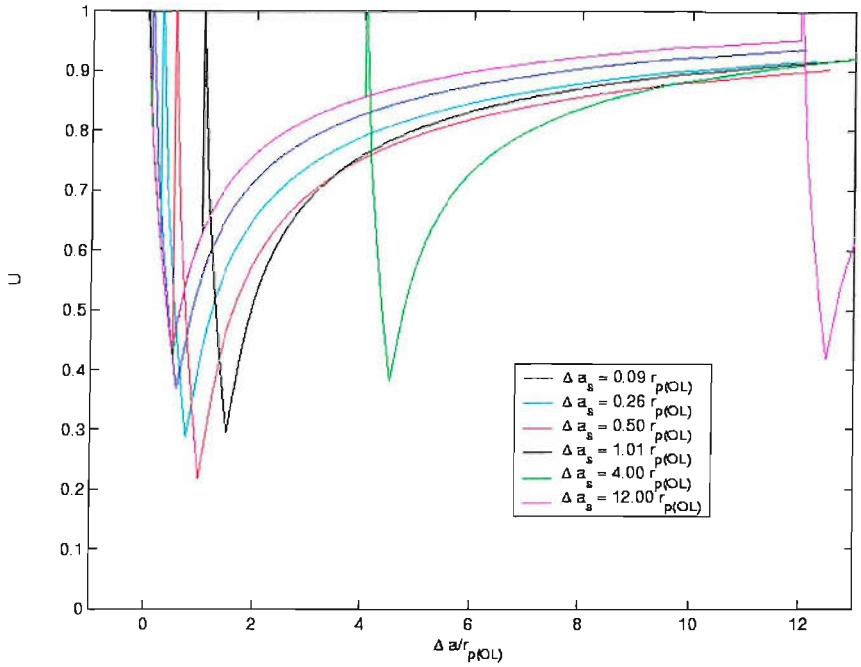

Figure 5.18: Effect of overload spacing on closure predicted by analytical modelling ($\Delta K_{(BL)}$ = 12 MPa m$^{1/2}$, R = 0.1, $\%OL$ = 100).

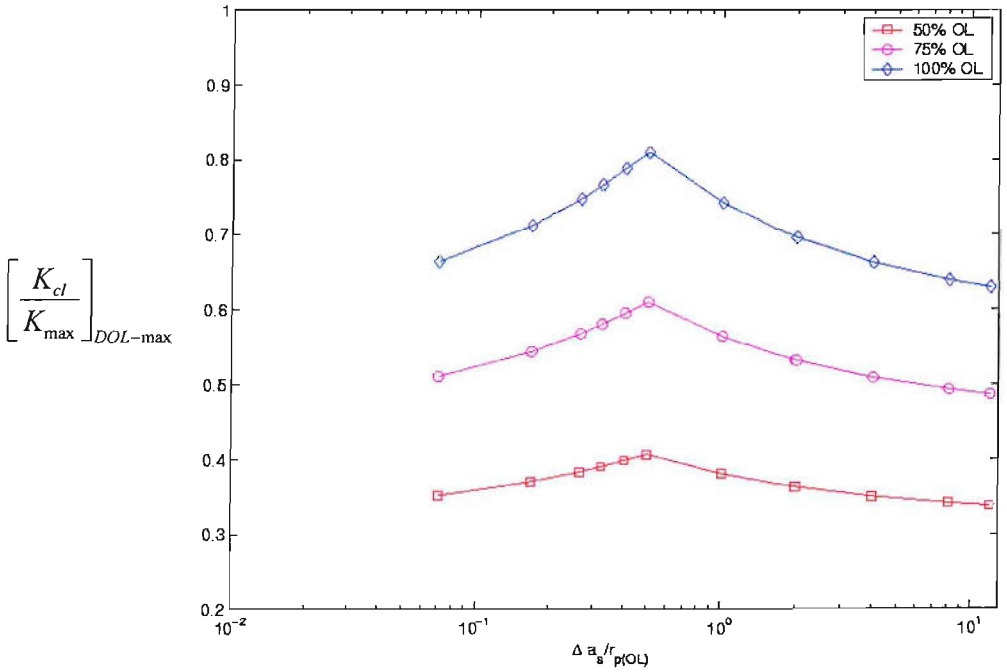

$$\left[\frac{K_{cl}}{K_{\max}}\right]_{DOL-\max}$$

Figure 5.19: Variation of maximum closure levels with OL spacing for different OL ratios predicted by analytical modelling ($\Delta K_{(BL)}$ = 12 MPa m$^{1/2}$, R = 0.1).

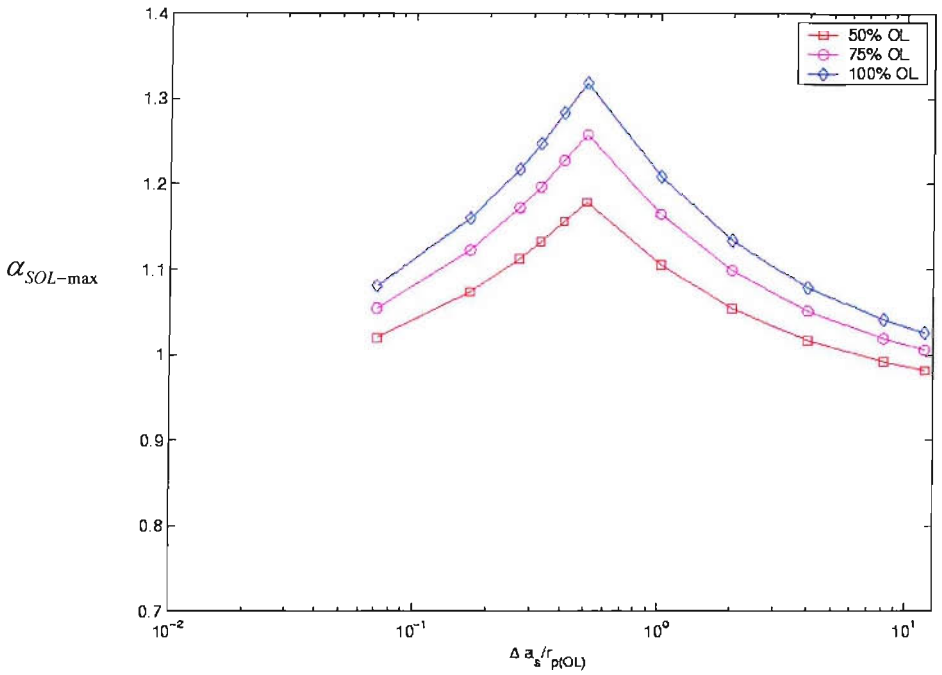

Figure 5.20: Variation of $\alpha_{SOL\text{-}max}$ with OL spacing for different OL ratios predicted by analytical modelling ($\Delta K_{(BL)}$ = 12 MPa m$^{1/2}$, $R = 0.1$).

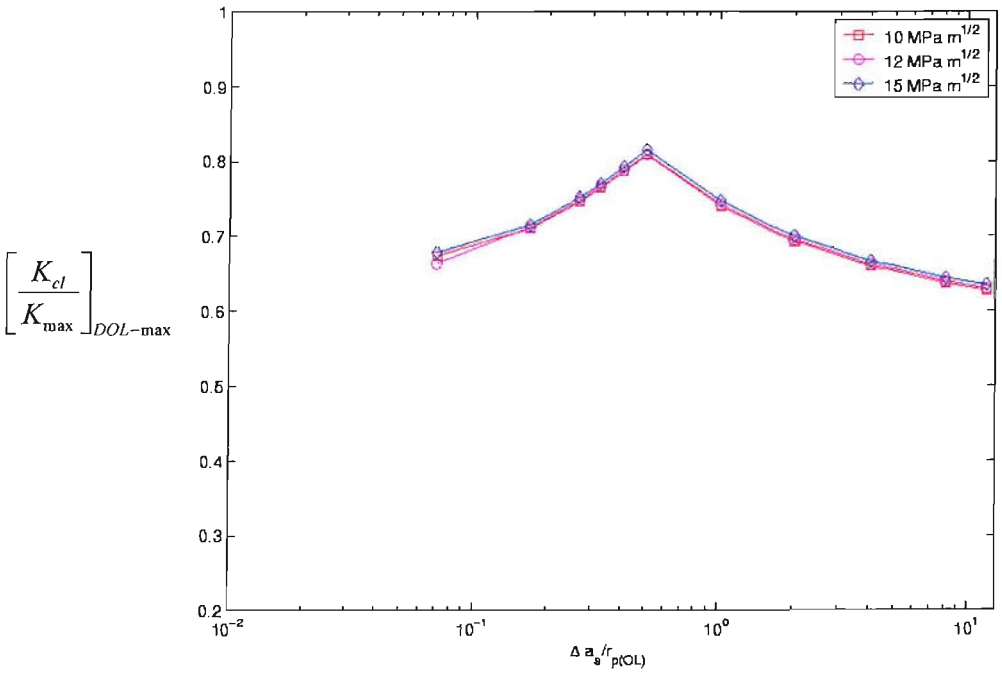

Figure 5.21 Variation of maximum closure levels with OL spacing for different $\Delta K_{(BL)}$ predicted by analytical modelling ($\%OL$ = 100, $R = 0.1$).

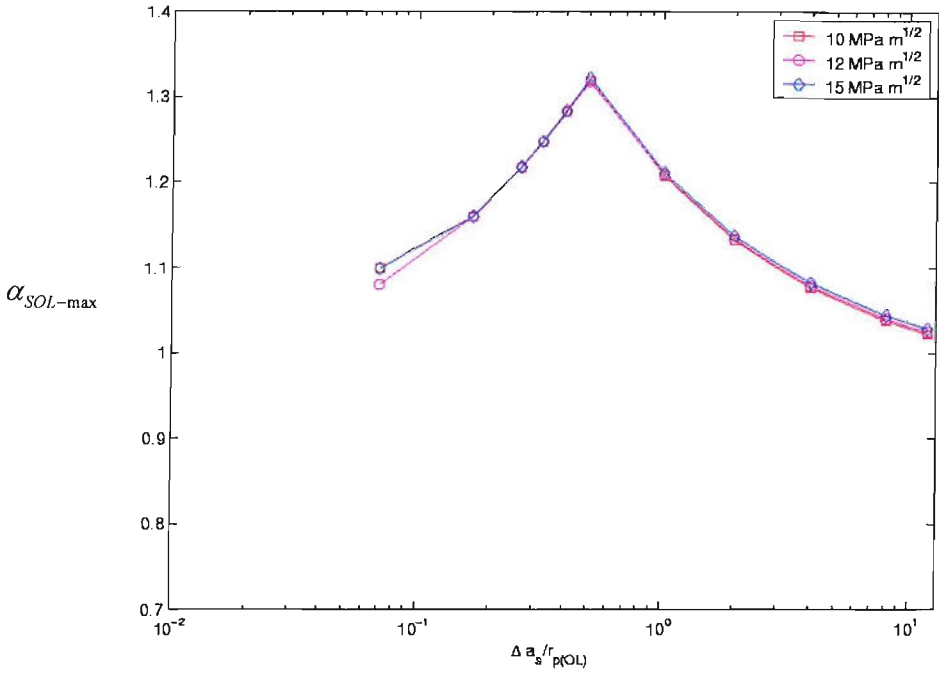

Figure 5.22: Variation of $\alpha_{SOL\text{-}max}$ with OL spacing for different $\Delta K_{(BL)}$ predicted by analytical modelling ($\%OL$ = 100, R = 0.1).

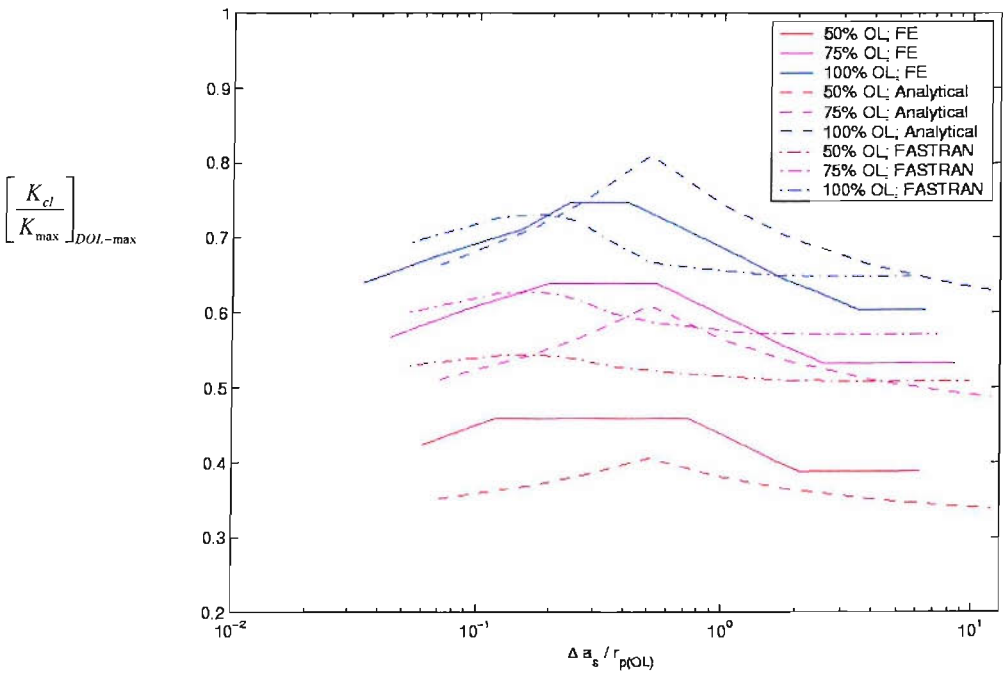

Figure 5.23: Variation of maximum closure levels with OL spacing for different OL ratios ($\Delta K_{(BL)}$ = 12 MPa m$^{1/2}$, R = 0.1).

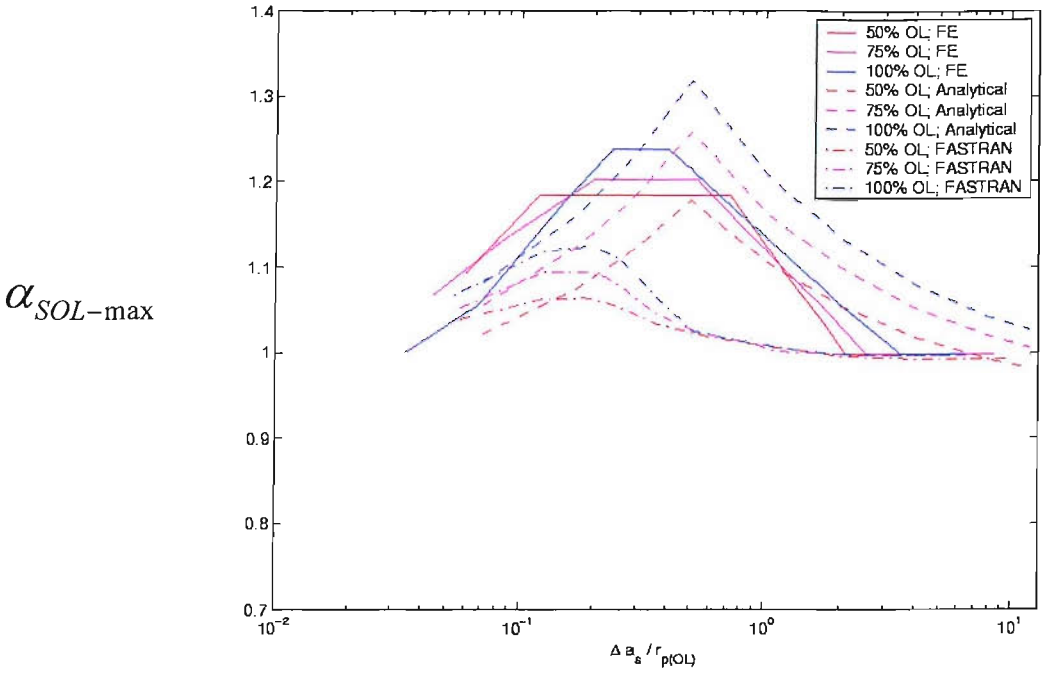

Figure 5.24: Variation of $\alpha_{SOL\text{-}max}$ with OL spacing for different OL ratios ($\Delta K_{(BL)}$ = 12 MPa m$^{1/2}$, R = 0.1).

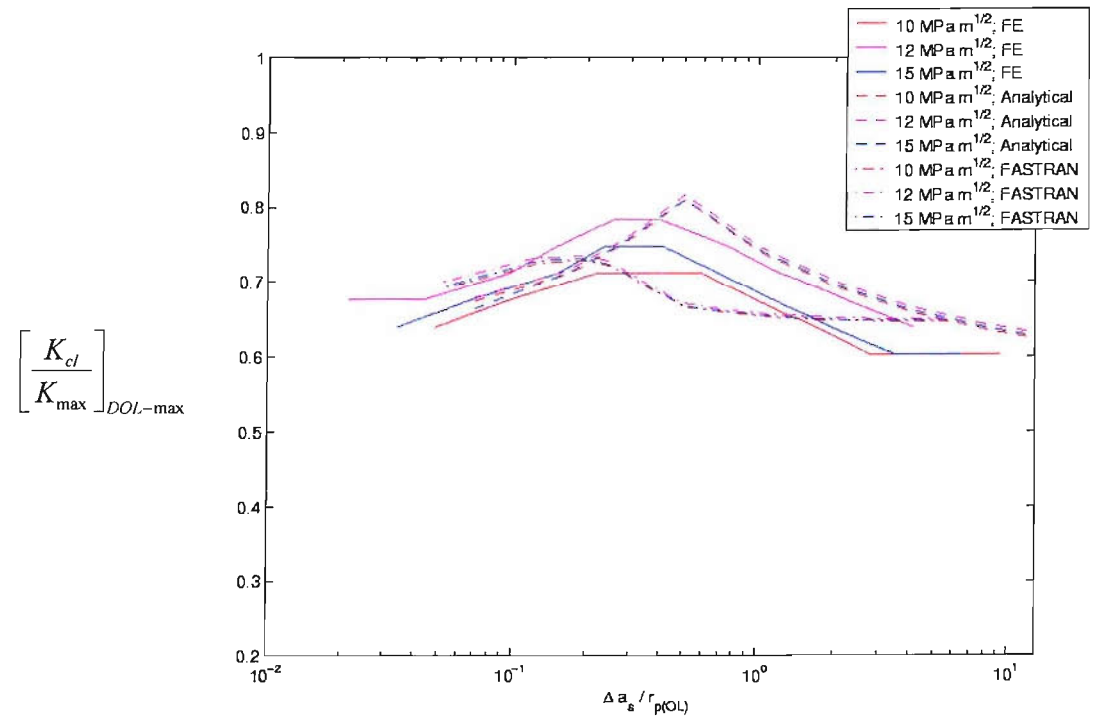

Figure 5.25: Variation of maximum closure levels with OL spacing for different OL ratios ($\Delta K_{(BL)}$ = 12 MPa m$^{1/2}$, R = 0.1).

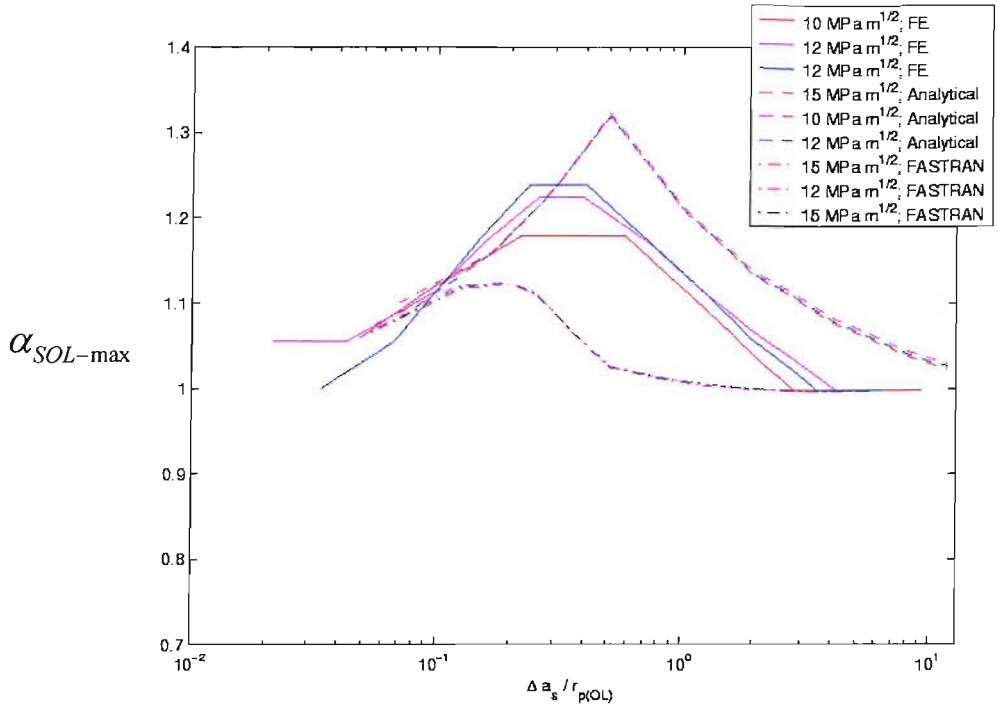

Figure 5.26: Variation of $\alpha_{SOL\text{-}max}$ with OL spacing for $\Delta K_{(BL)}$ ($\%OL$ = 100, R = 0.1).

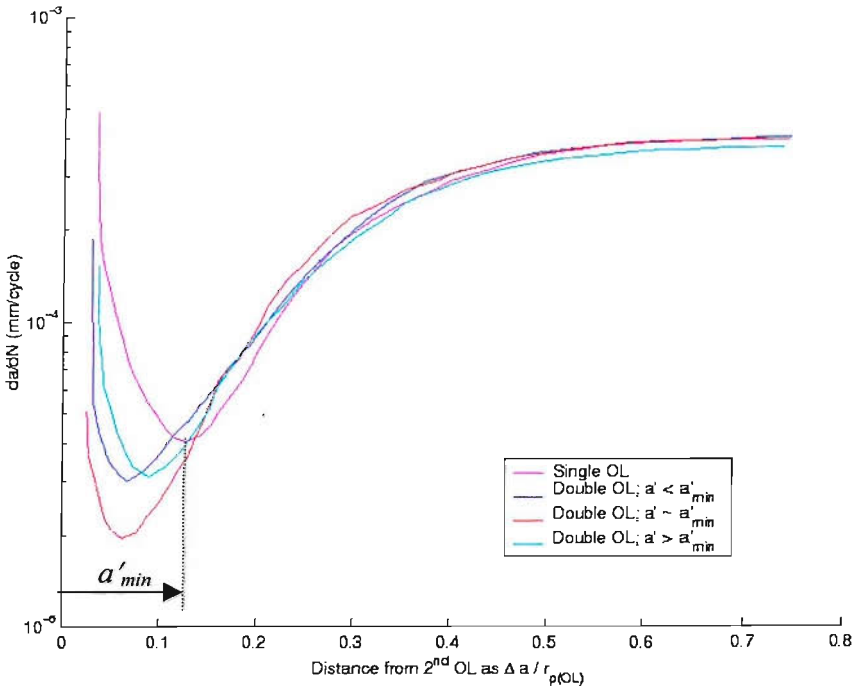

Figure 5.27: Experimental crack growth rate variations following 2 Ols separated by a distance a'. Lines are shown for a sinele overload transient along with transient curves for second overload (identified as 'double OL') where the point of applying the second overload is offset back to $\Delta a/r_{p(OL)}$ = 0.0 point on the x-axis, $\Delta K_{(BL)}$ = 19.8 MPa $m^{1/2}$, R = 0.1, %OL = 75 (Mills and Hertzberg, 1976).

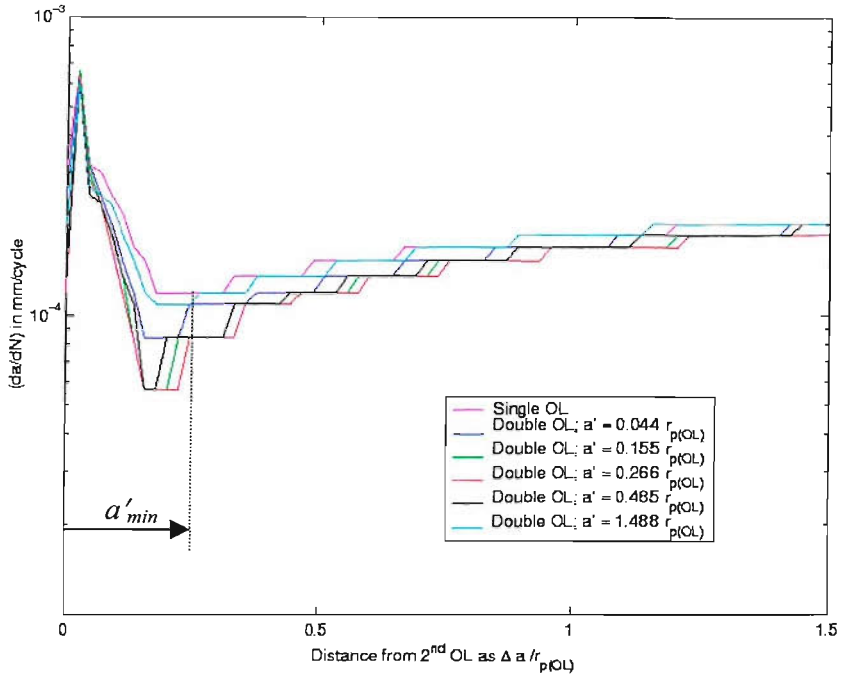

Figure 5.28: Predicted crack growth rate variations following 2 OLs , $\Delta K_{(BL)}$ = 12.0 MPa $m^{1/2}$, R = 0.1, %OL = 75 (FE method), plotted in an equivalent manner to Figure 5.27.

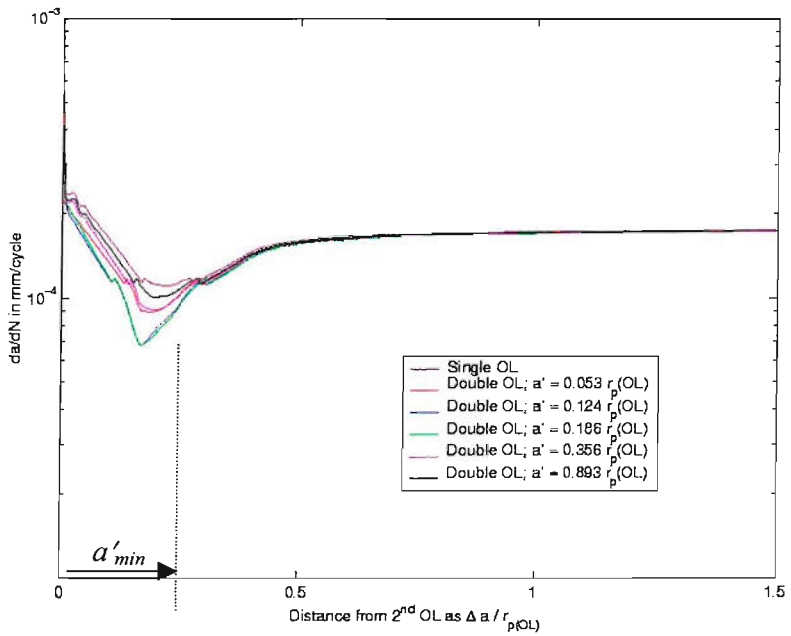

Figure 5.29: Predicted crack growth rate variations following 2 OLs , $\Delta K_{(BL)}$ = 12.0 MPa $m^{1/2}$, R = 0.1, %OL = 75 (strip yield method), plotted in an equivalent manner to Figure 5.27.

.

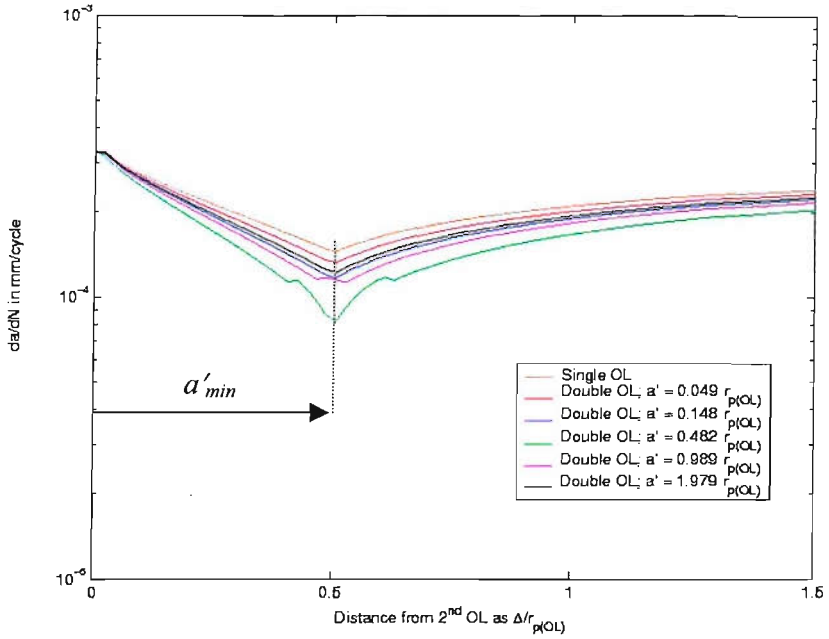

Figure 5.30: Predicted crack growth rate variation following 2 OLs, $\Delta K_{(BL)}$ = 12.0 MPa $m^{1/2}$, R = 0.1, %OL = 75 (Analytical method), plotted in an equivalent manner to Figure 5.27..

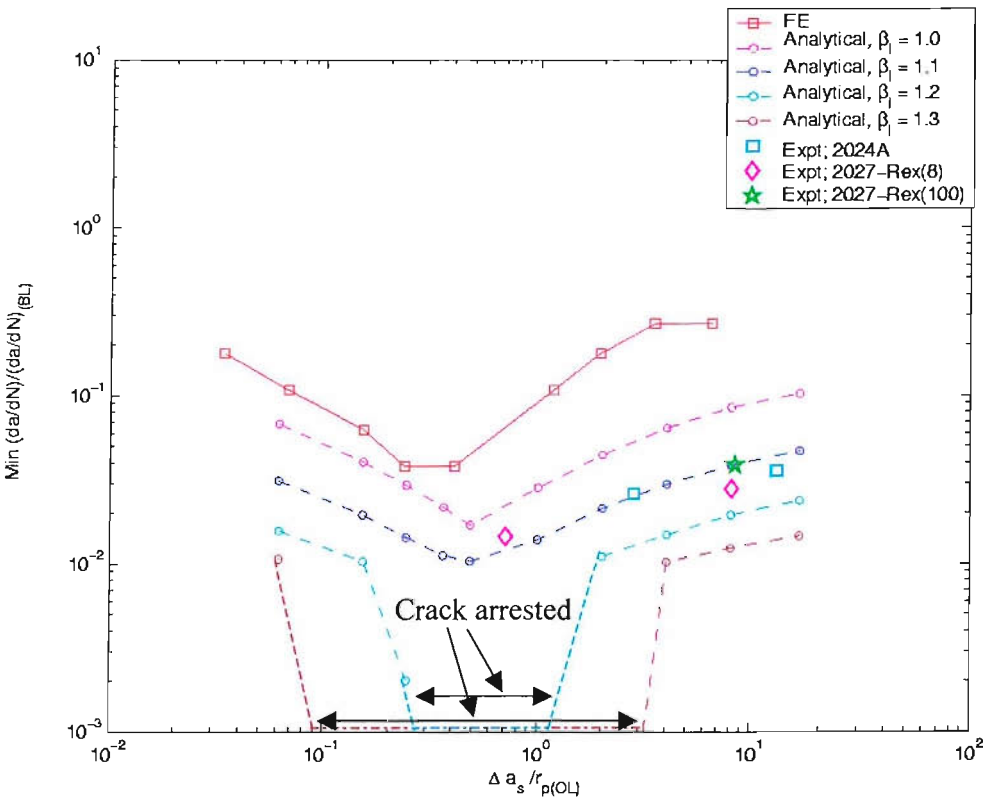

Figure 5.31: Comparison of experimental and predicted growth rates for crack subjected to dual overloads, ($\Delta K_{(BL)}$ = 12 MPa $m^{1/2}$, R = 0.1, $\%OL$ = 100).

$$\%OL = \frac{K_{OL} - K_{\max}}{K_{\max}} \times 100\% \qquad \%OL_1 = \%OL_2 = \%OL_3 \ldots$$

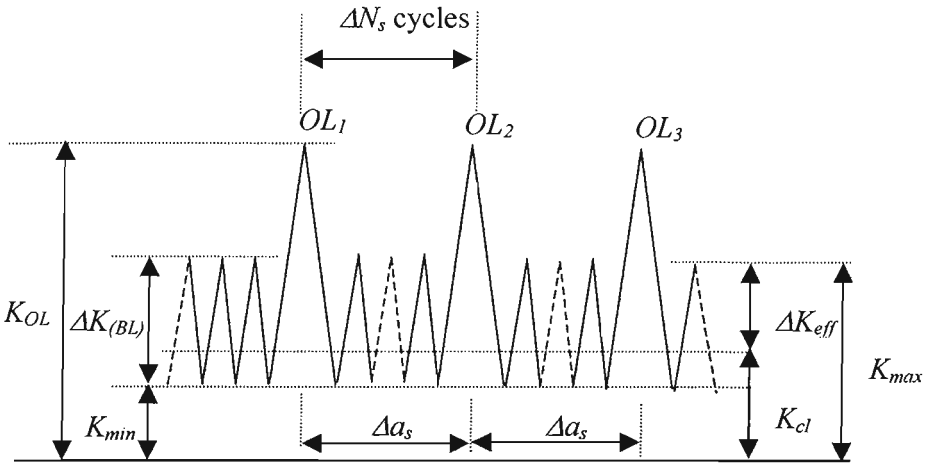

Figure 5.32: Schematic illustration of the nomenclature adopted for periodic/periodic overloads analyses.

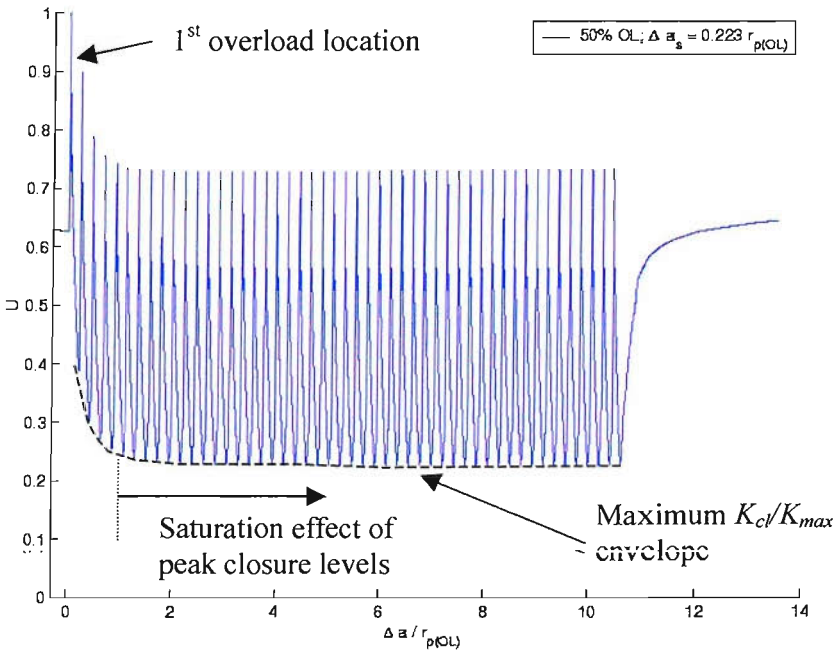

Figure 5.33: Typical closure variation of a crack subjected to periodic overloads, $\Delta K_{(BL)}$ = 12 MPa m$^{1/2}$, R = 0.1, $\%OL$ = 50 (Strip yield method)

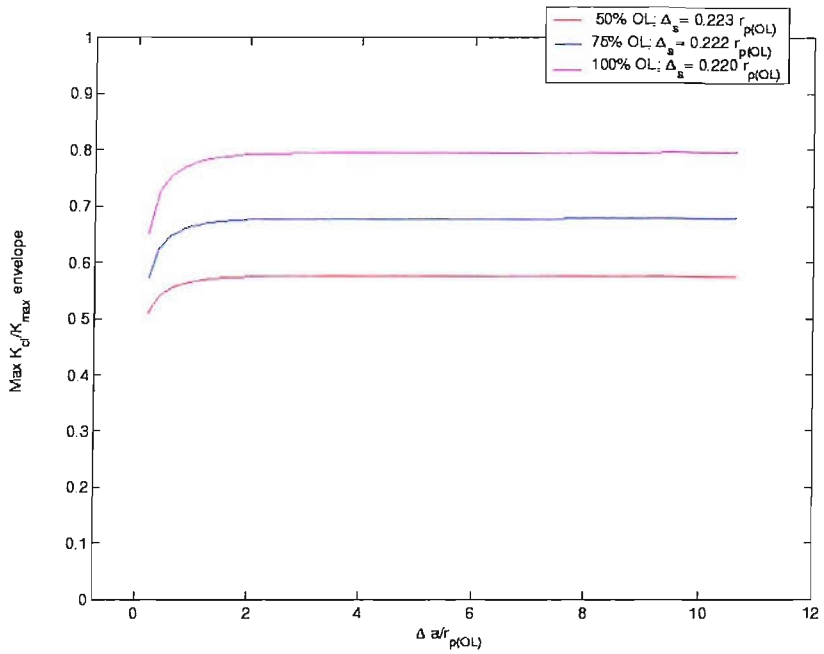

Figure 5.34: Variation of maximum closure envelope with OL spacing for different OL ratios, $\Delta K_{(BL)}$ = 12 MPa m$^{1/2}$, R = 0.1, $\%OL$ = 100 (Strip yield method).

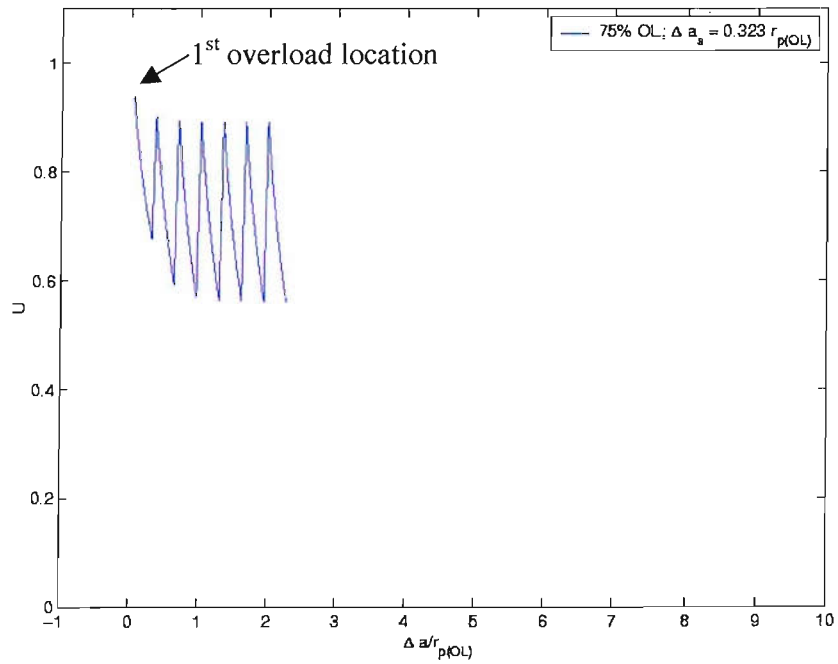

Figure 5.35: Typical closure variation of a crack subjected to periodic overloads, $\Delta K_{(BL)}$ = 12 MPa m$^{1/2}$, R = 0.1, $\%OL$ = 75 (Analytical method).

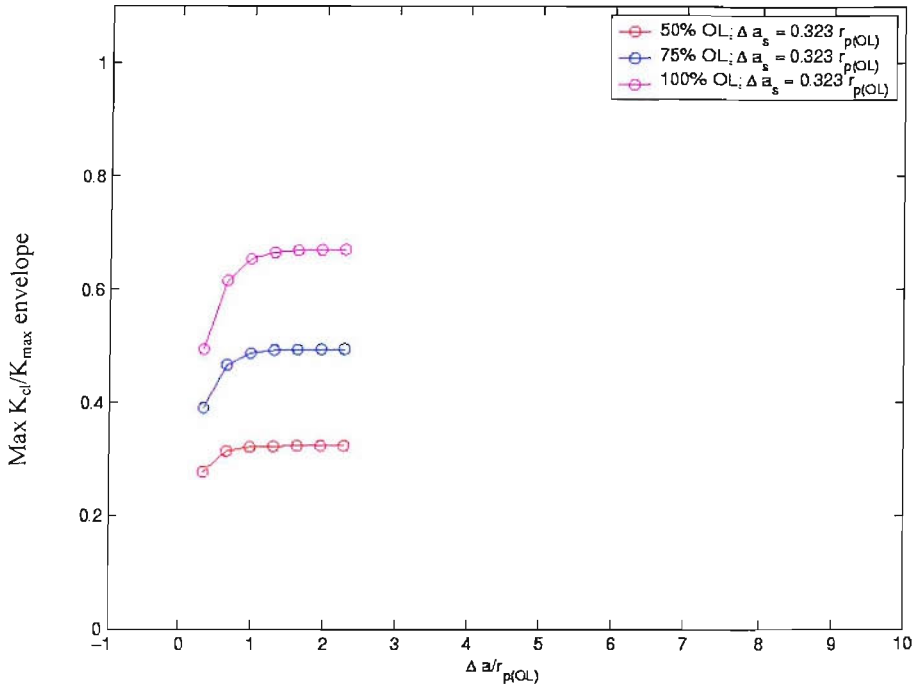

Figure 5.36: Variation of maximum closure envelope with OL spacing for different OL ratios, $\Delta K_{(BL)}$ = 12 MPa m$^{1/2}$, R = 0.1 (Analytical method).

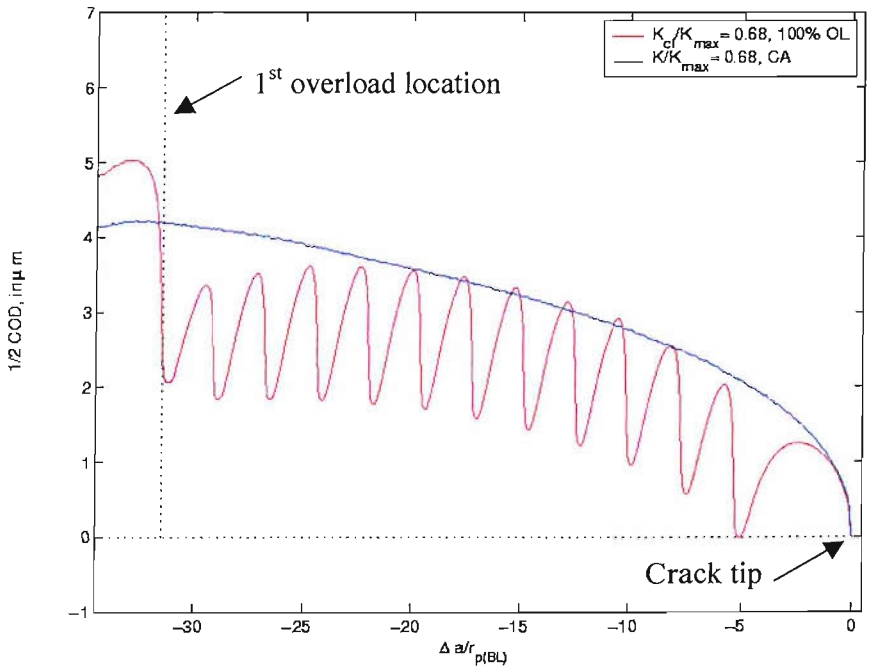

Figure 5.37: Typical crack profile of a crack subjected to periodic overloads, $\Delta K_{(BL)}$ = 12 MPa m$^{1/2}$, R = 0.1, $\%OL$ = 100, Δas = 0.595 $r_{p(OL)}$ (FE method).

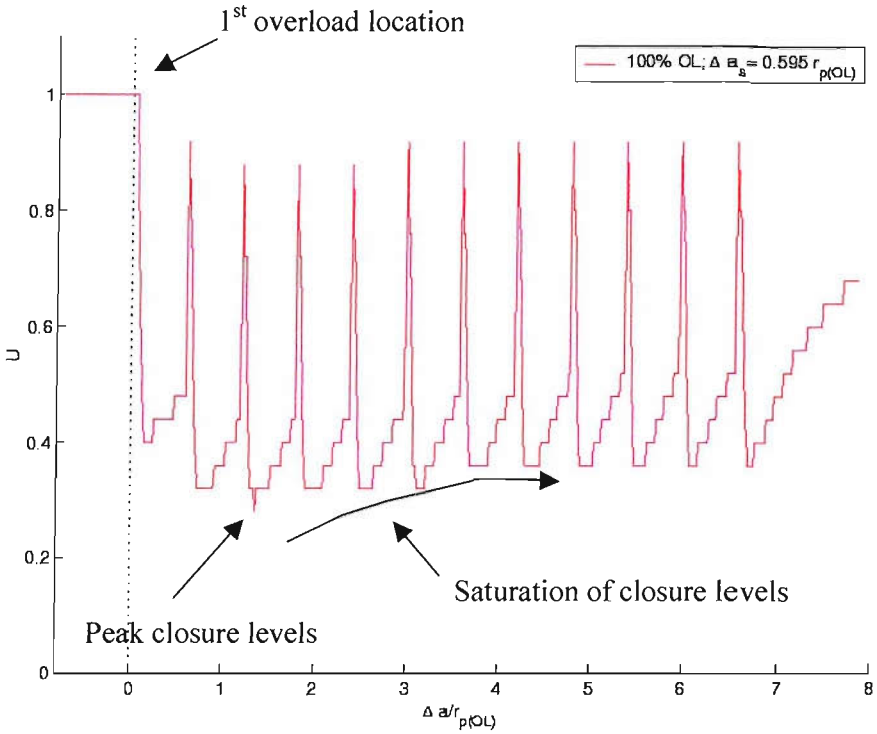

Figure 5.38: Typical closure variation of a crack subjected to periodic overloads, $\Delta K_{(BL)}$ = 12 MPa m$^{1/2}$, R = 0.1, $\%OL$ = 100 (FE method).

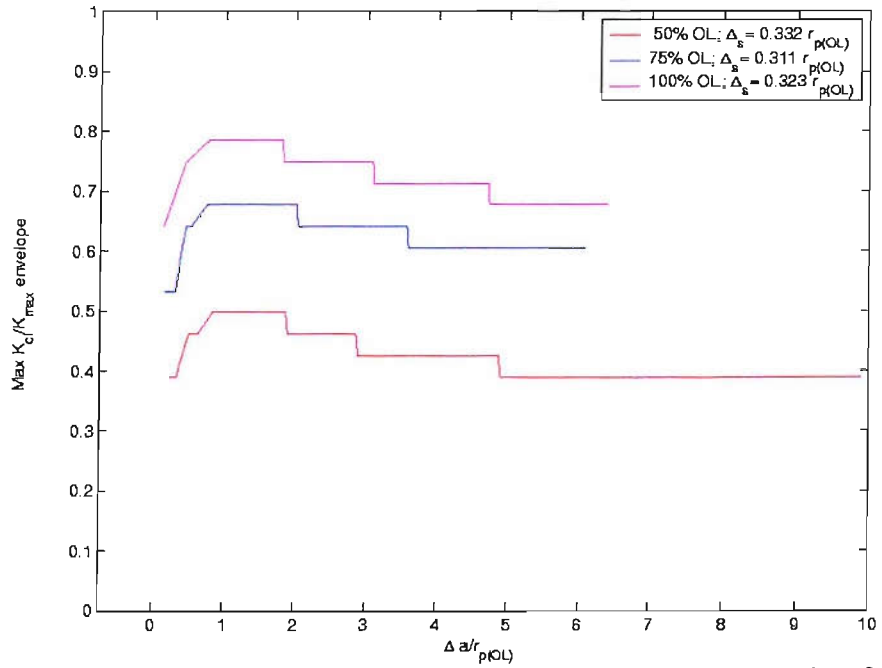

Figure 5.39: Variation of maximum closure envelope with OL spacing for different OL ratios, $\Delta K_{(BL)}$ = 12 MPa m$^{1/2}$, R = 0.1, $\%OL$ = 100 (FE method).

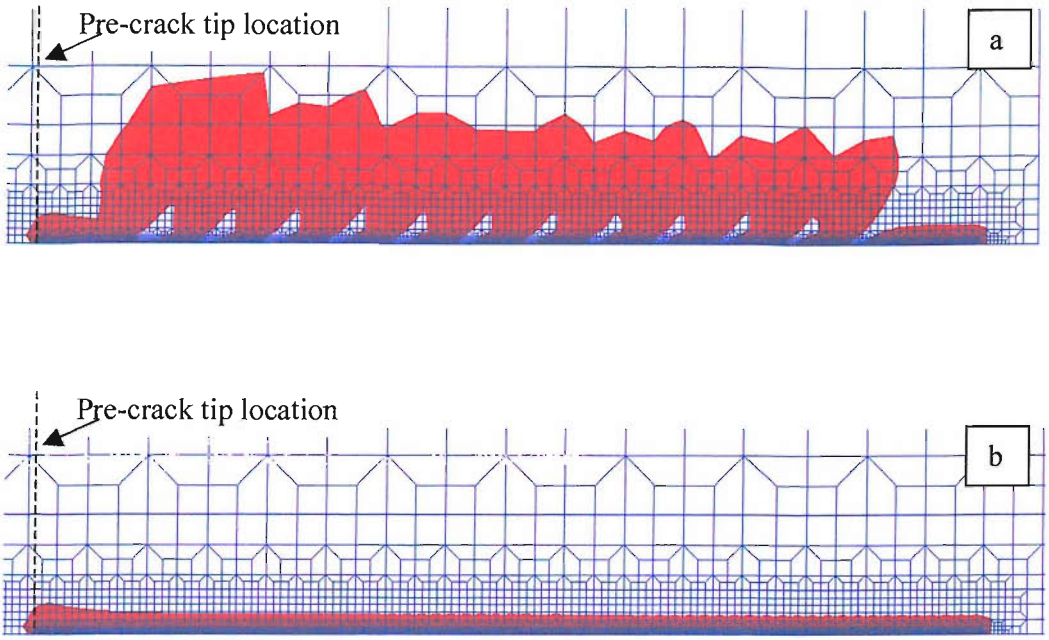

Figure 5.40: Variation of Von-Mises plastic strain (0.2% plastic strain), $\Delta K_{(BL)}$ = 12 MPa $m^{1/2}$, R = 0.1, for a) periodic overloads and b) CA loading.

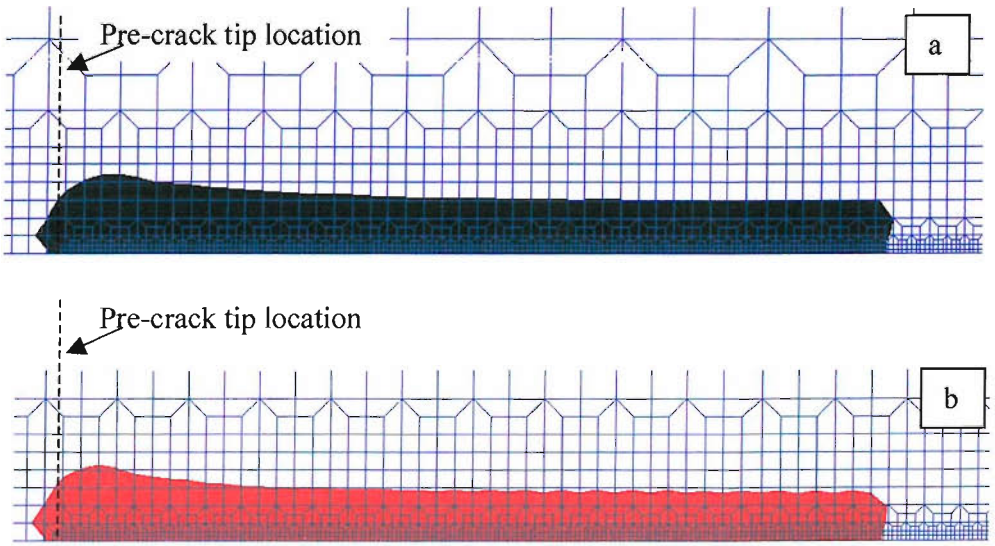

Figure 5.41: Variation of Von-Mises plastic strain (0.2% plastic strain), K_{max} = 13.33 MPa $m^{1/2}$, for a) static tearing and b) fatigue propagation.

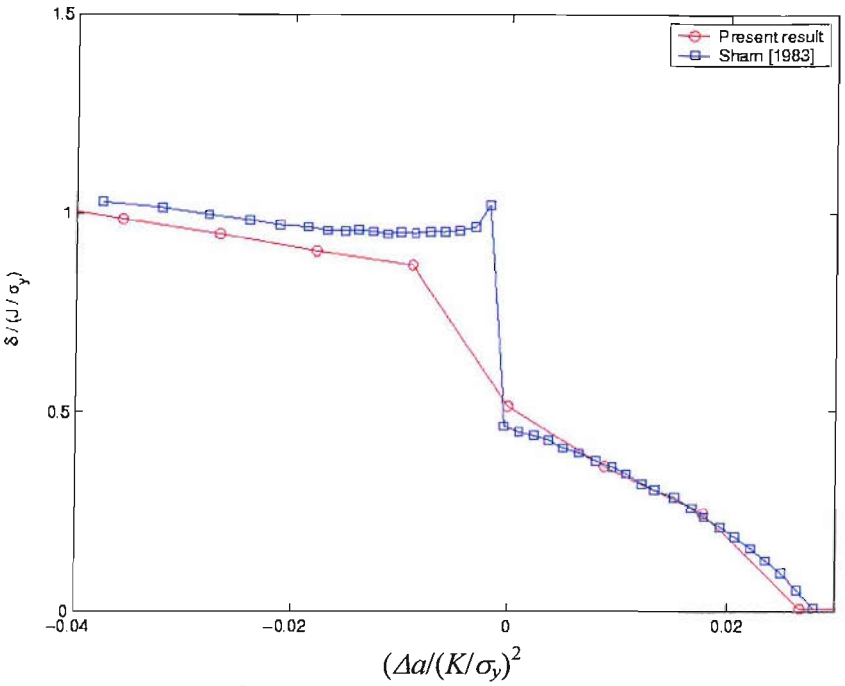

Figure 5.42: Comparison of stable growth COD profiles between present and Sham's [1983] result.

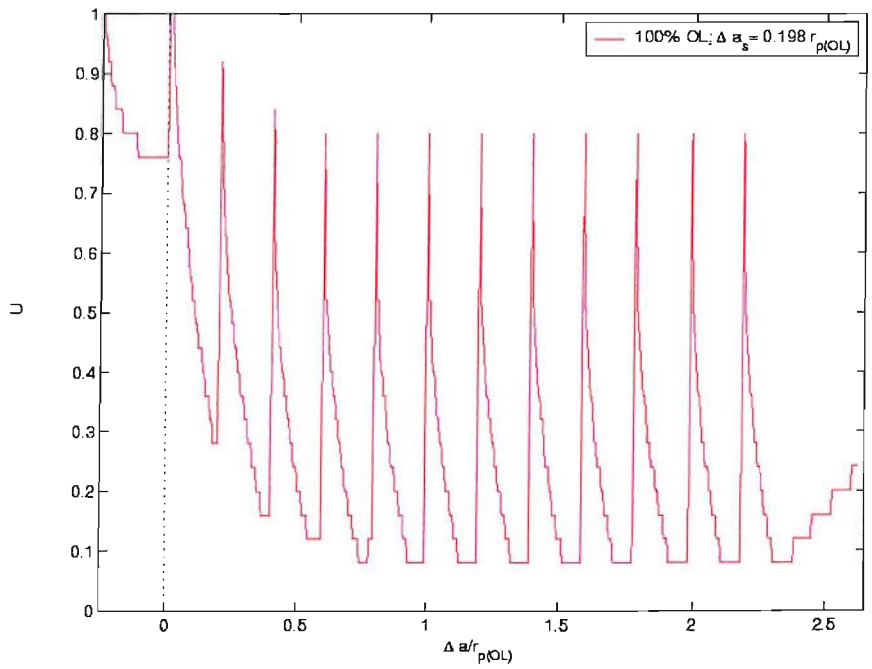

Figure 5.43: Typical closure variation of a crack subjected to periodic overloads, $\Delta K_{(BL)}$ = 12 MPa m$^{1/2}$, R = 0.1, $\%OL$ = 100, plane stress (FE method).

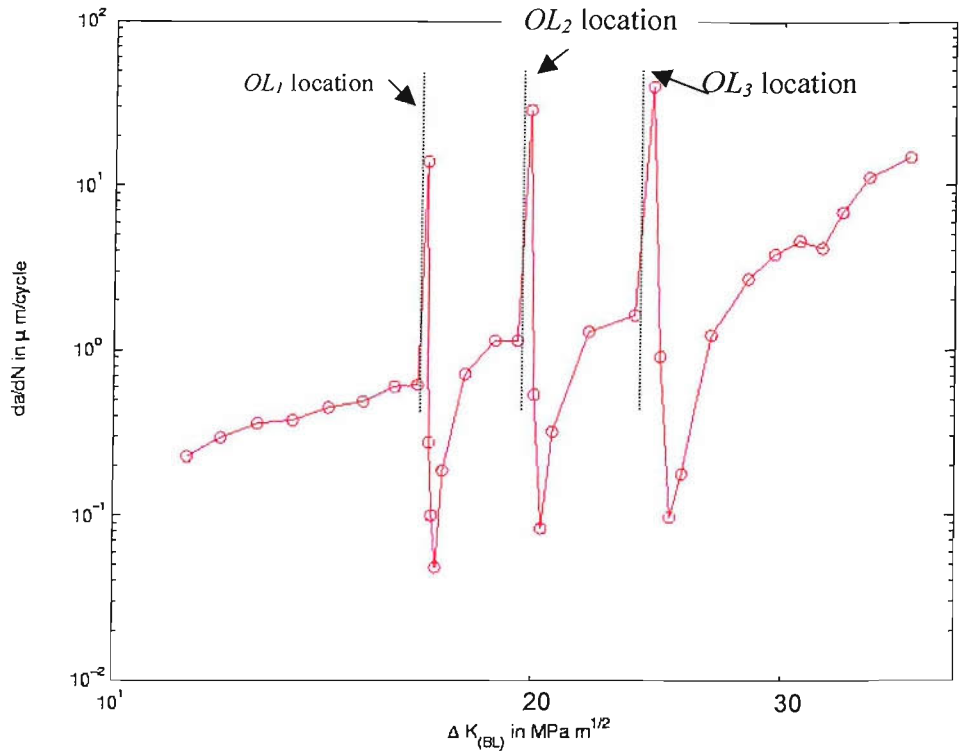

Figure 5.44: Experimental growth rate variation of 2024 under three equal overload transients (OL_1, OL_2 and OL_3), $\Delta P_{(BL)}$ = 83.97 KN, R = 0.1, $\%OL$ = 75, (McMaster, 2004)

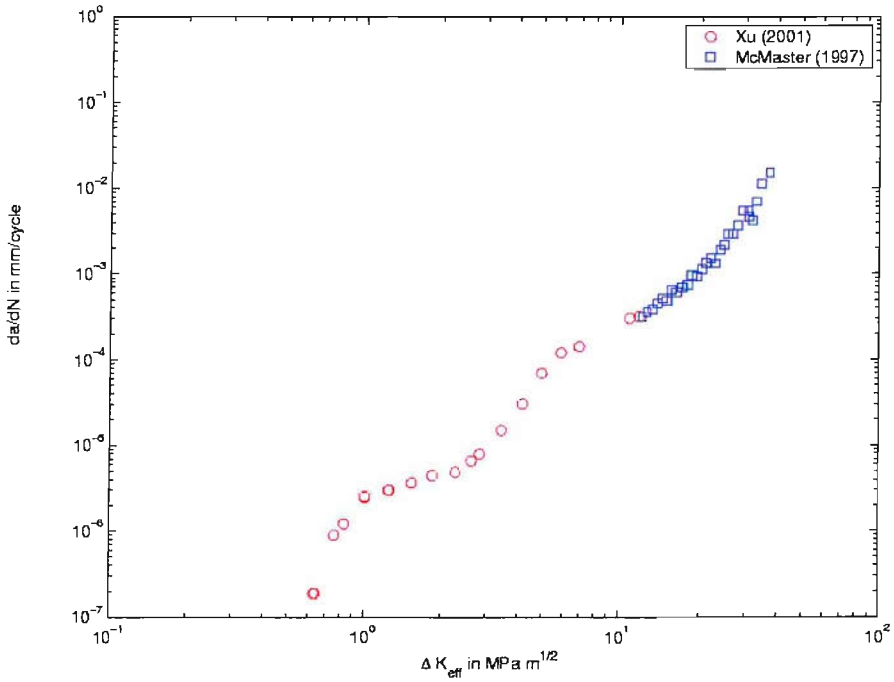

Figure 5.45: Experimental crack growth behaviour of 2024, $\Delta K_{(BL)}$ = 12 MPa $m^{1/2}$, R = 0.1 (Xu, 2001 and McMaster, 2004)

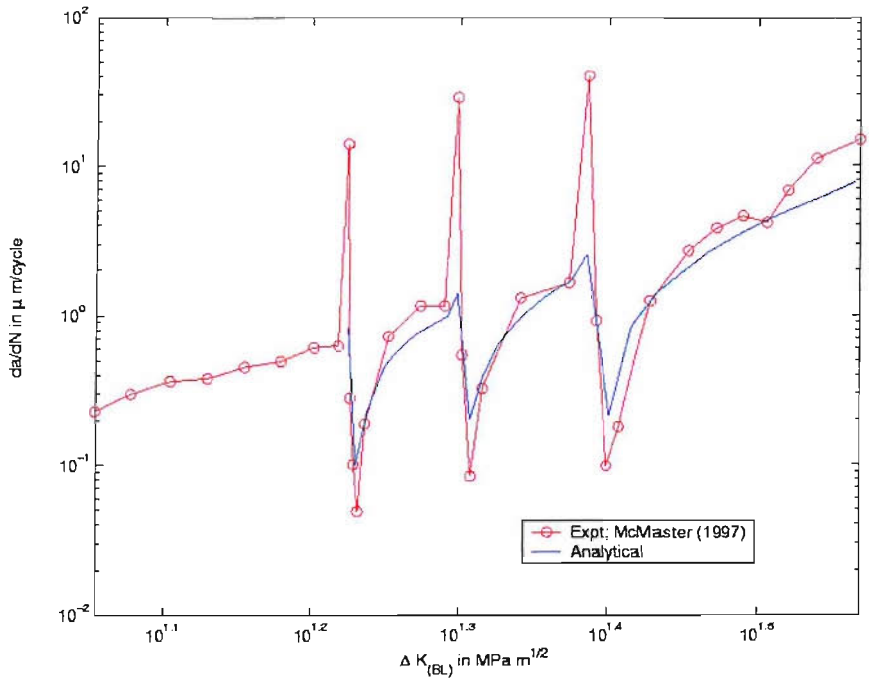

Figure 5.46: Comparison of experimental and predicted growth rates, $\Delta P_{(BL)}$ = 83.97 KN, R = 0.1, $\%OL$ =75.

Chapter 6 Summary and conclusions

Finite element, strip yield and simple analytical fracture mechanics modelling efforts have been made to enhance the understanding of PICC and RICC in high strength Al alloys for both constant amplitude and variable amplitude loading conditions. Each of the methods was particularly used to gain understanding of the micromechanistic processes of crack closure. Notwithstanding the inherent limitations of the modelling approaches, it has been observed that key functional aspects of the various FE models are reproducible in simple analytical representations of RICC and PICC, paving a promising route to improve, computationally efficient, mulitmechanistic fatigue lifing methods involving crack closure. Specific conclusions are summarised below.

Based on the FE and analytical modelling under constant amplitude loading conditions the following conclusions have been made:

1. Anomalous near-tip closure in FE models has been identified to occur under both plane stress and plane strain conditions and is seen to vary with baseline load levels and crack propagation algorithm.
2. Anomalous near-tip closure is favoured by: (i) use of the LDU crack propagation algorithm, (ii) plane strain loading, and (iii) isotropic work hardening or elastic-perfect plastic hardening. When using LDULU crack propagation, it is the additional loading and unloading of the current cycle that particularly alleviates near-tip closure, consistent with this being an artifact of the unrealistic step-wise node release process, even when a smooth spring release scheme is used.
3. The use of LDU or LDULU propagation algorithms is also seen to influence closure at the pre-crack in the plane strain models.
4. Plane stress FE models are found to exhibit 'rational' distributed closure along crack length: R-ratio and baseline load level effects are found to be consistent with predictions of Hutchinson and Budiansky (for the values relevant to this work at least).
5. Extended FE assessment of closure levels in regularly deflecting crack profiles confirms and extends the regime over which normalized asperity size (expressed as L/r_p) is seen to control RICC influences. Modification of the

analytical modeling of RICC to account for small a^* and L/r_p values is shown to be in good functional agreement with the present FE models.

6. 2D analytical modelling of RICC has been extended to represent a simplified 3D crack surface and associated tilt (θ) and twist (ϕ) effects on closure and is found to support the experimental findings from Xu [2001] and Khor [2004].

In terms of the FE, analytical and strip yield modelling under variable amplitude (single overload) loading conditions, the following conclusions have been drawn

1. The post-peak closure behaviour of deflected cracks subjected to changes in both $\%OL$ and $\Delta K_{(BL)}$ is generally similar to that of equivalent undeflected cracks, except a zone well away from the overload location where cyclic variations of closure due to deflections come into effect. Effects of L/r_p ratios on deflected cracks during overloads are seen to be functionally similar to RICC under constant amplitude loading (particularly in the 'saturation' of RICC influence for $L/r_{p(OL)} > 1$)
2. A simple model for competitive influences of RICC and PICC effects during overloads has been developed and seen to be functionally similar to the FE results.
3. The present work is seen to map out regimes of loading where RICC and PICC effects may be expected to operate. In conjunction with CA closure understanding, a particularly complete description of overload behavior is produced, with quantitative improvement in overload transient and baseline growth rate predictions over the popular strip yield approach.

In terms of the FE, analytical and strip yield modelling under variable amplitude (dual and periodic overloads) loading conditions, the following conclusions have been drawn

1. FE, simple analytical and strip yield models produce functionally similar behaviour for double and periodic OLs:
    - Analytical approaches suggest much of double OL effect linked to closure influence of first OL upon the second OL

- The potential role of flow constraint is identified in multiple overloads in plane strain

2. Clear experimental validation of data is often complicated by experimental problems:
    - For high $\Delta K_{(BL)}$ periodic OL data supplied by Airbus [McMaster, 1997], reasonable correlation was achieved via simple analytical models (large OL spacing)
    - For intermediate $\Delta K_{(BL)}$ double OL data from Southampton, FE models produce reasonable trend information
    - analytical (PICC) models are shown to over-predict retardation effects, however simplifications of the analytical model are known to be most critical at the small OL spacing tested.

Chapter 7 Recommendations for future work

In terms of the FE modelling, the following areas may be identified for future work:

- Incorporating crack surface frictional effects may improve the modelling accuracy, particularly the effect on near-tip conditions for loads below the closure levels,
- Studying the effect of crack angles for variable amplitude loading conditions (including underloads).
- Examining mixed mode crack closure effects.
- A detailed 3D FE modelling approach may be performed to compare with the 3D analytical results, particularly the effect of tilt (θ) and twist (ϕ) angles.

In terms of the strip yielding modelling, the following areas may be beneficial to extend:

- Implementation of RICC-PICC interaction understanding from FE analyses as an improvement over the empirical RICC model integrated previously by Xu [2001].
- Treatment of the propagating plane strain cracks as observed in the FE model.
- Extension of the 2D approach to 3D modelling of crack closure to address the through the thickness stress state that occurs in engineering components.

This work has shown that RICC and OL phenomena may be treated via simple residual deformation concepts: this is not an engineering tool as yet, but can form the basis for implementing physical understanding:

- A key point that is raised is the treatment of in-plane constraint in propagating plane strain cracks: it is clear that some description of this effect would be needed for a comprehensive treatment of plane strain crack behaviour. Some relation of current crack tip position and length scales of prior plastic deformation may help treat this effect, but would require future investigation.
- There is also a clear need to address underloads and possible asperity crushing, as that is not treated in the present work.

References

ABAQUS (1998). *ABAQUS Theory Manual* Version 5.8, Hibbiit, Karlson and Sorensen, Inc., Pawtucket, RI, USA.

Aerospaceweb (2003). http://www.aerospaceweb.org/aircraft/jetliner/comet /index.shtml

Albert, W.A.J. (1838). Uber Treibseile am Harz. *Archive fur Mineralogie, Geonosie, Bergbau und Huttenkunde* 10, 215-234.

Alexander, D.J. and Knott, J.F. (1987). Fatigue crack retardation in Aluminium alloys. In *Proceedings of third International Fatigue Conference*, Charlottesville, Virginia, 395-406.

Allison, J.E., Ku, R.C. Pompetzki, M.A. (1988). A comparison of measurement methods and numerical procedures for experimental characterization of fatigue crack closure. ASTM STP 982, 171-185.

Allison, J.E. (1979). Measurement of crack-tip stress distributions by x-ray diffraction, ASTM STP 677, 115-562.

Alzos, W.X., Skat, A.C. Jr. and Hillberry, B.M. (1976). Effect of single overload/underload cycles on fatigue crack propagation. ASTM STP 595, 4160.

Andersson, H., Persson, C. and Hansson, T. (2001). Crack growth in IN718 at high temperature, *International Journal of Fatigue* **23**, 817-827.

Andersson, H., Persson, C., Hansson, T., Melin, S. and Jarvstrat, N. (2004). Constitutive dependence in finite-element modelling of crack closure during fatigue, *Fatigue and Fracture of Engineering Materials and Structures* **27**, 75-87.

Anderson, T.L. (1995). *Fracture Mechanics. Fundamentals and Applications*. Boca Raton: CRC Press LLC.

Antunes, F.V., Borrego, L.F.P., Costa, J.D. and Ferreira, J.M. (2004). A numerical study of fatigue crack closure induced by plasticity, *Fatigue and Fracture of Engineering Materials and Structures* **27**, 825-835.

Anquez, L. and Baudin, G. (1988). Correlation between numerically predicted crack opening load and measured load history dependent crack growth threshold, ASTM STP 982, 380-397.

Arkema, W.J. and Schijve, J. (1976). Observation on the prediction of fatigue crack growth under variable amplitude loading, ASTM STP 595, 3-23.

Asaro, R.J., Hermann, L., and Baik, J.M. (1981). Transitions in fatigue crack closure in 2048 aluminium. *Metalurgical Transaction* **12A**, 1133-1135.

Ashbaugh, N.E., Dattaguru, B., Khobaib, M., Nicholas, T., Prakash, R.V., Ramamurthy, T.S., Seshadri, B.R. and Sunder, R. (1997). Experimental and analytical estimates of fatigue crack closure in an aluminium-copper alloy. Part II: A finite element analysis. *Fatigue and Fracture of Engineering Materials and Structures* **20**, 963-974.

ASM Speciality Handbook (1994). Aluminium and aluminium alloys. ASM International.

ASTM E647 (2003). Annual book of Special Technical Publication standards, 615-657, American Society for Testing and Materials, Philaldelphia, PA.

Bateman, D.A., Bradshaw, F.J. and Rooke, D.P. (1964). Some observations on surface deformation around cracks in stressed sheets. *Royal Aircraft Establishment*, Farnborough, TN-CPM 63.

Banasaik, D.H., Grandt, A.F. and Montulli, L.T. (1977). Fatigue crack retardation in polycarbonate. *Journal of Applied Polymer Science* 21, 1297-309.

Bao, H. and McEvily, A.J. (1995). The effect of an overload on the rate of fatigue crack propagation under plane stress conditions. *Metallurgical and Materials Transactions* A **26A**, July 1725-1733.

Bathias, C. and Pelloux, R.M. (1974). Fatigue crack propagation in martensitic and austenitic steels. *Metallurgical Transactions* **4**, 1265-1273.

Bathias, C. and Vancon, M. (1978). Mechanisms of overload effect on fatigue crack propagation in aluminium alloys. *Engineering Fracture Mechanics* **10**, 409-424.

Barenblatt, G.I. (1962). The mathematical theory of equilibrium cracks in brittle fracture, *Advances in Applied Mechanics*, VIII, Academic press, 55-129.

BBC. (1954). Metal fatigue caused Comet crashes. http://news.bbc.co.uk/onthisday /hi/dates/stories/october/19 /newsid_3112000/3112466.stm

Beevers, C.J., Bell, K, Carlson, R.L. and Starke, E.A. (1984). A model of fatigue crack closure. *Engineering Fracture Mechanics* **19**, 93-100.

Bernard, P.J., Lindley, T.C. and Richards, C.E. (1976). Mechanisms of overload retardation during fatigue crack propagation. In *Fatigue Crack Growth Under Spectrum Loads*, ASTM STP 595, 78-97.

Bernard, P.J., Lindley, T.C., and Richard, C.E. (1977). The effect of single overloads on fatigue crack propagation in steels. *Metal Science*, 390-398.

Betegon, C. and Hancock, J.W. (1991). Stress intensity factors at the tips of kinked and forked cracks. *Journal of Applied Mechanics* **58**, 104-110.

Bichler, C. and Pippan, R. (1999). Direct observation of the residual plastic deformation caused by a single tensile overload. In *Advances in Fatigue Crack Closure Measurement and Analysis*, ASTM STP 1343, 191-206.

Bilby, B.A. Cottrell, A.H. and Swinden, K.H. (1963). The spread of plastic yield from a notch. In *Proceeding of Royal Society of England* A **272**, 304-310.

Bilby, B.A. and Swinden, K.H. (1965). Representation of plasticity at notches by linear dislocation arrays. *Proceeding of Royal Society of England* **A 275**, 22-30.

Bilby, B.A., Cardew, G.E., Goldthrope, M.R. and Howard, I.C. (1986). A finite element investigation of the effects of specimen geometry on the fields of stress and strain at the tip of stationary cracks. In *Size Effects in Fracture*, 37-46, London: Institute of Mechanical Engineers.

Bilby, B.A., Cardew, G.E. and Howard, K.H. (1977). Stress intensity factors at the tips of kinked and forked cracks. In *Fracture* 1977 **3**, Pergamon press, Yew York, 197-200.

Biner, S.B., Buck, O. and Spitzig, W.A. (1994). Plasticity induced crack closure in single and dual phase materials. *Engineering Fracture Mechanics* **47**, 1-12.

Blandford, R.S., Daniewicz, S.R. and Skinner, J.D. (2002). Determination of the opening load for a growing fatigue crack: evaluation of experimental data reduction techniques and analytical models. *Fatigue and Fracture of Engineering Materiuals and Structures* **25**, 17-26.

Blom, A, Wang G. and Chermahini, R.G. (1990). Comparison of crack closure results obtained by 3D elastic-plastic FEM and modified Dugale Model. In *Localised Damage: Computer-Aided Assessment and Control.* (Editors. M.H. Aliabadi et al.) 57-68, Berlin: Springer-Verlag.

Blom, A.F. (1984). Near threshold fatigue crack growth and crack closure in 17-4 PH stell and 2024-T3 aluminium alloy. In *Fatigue Crack Growth Threshold Concepts*, Edited by Davidson, D.L. and Suresh, S, TMS-AMIE, Warrendale, PA, 263-279.

Blom, A.F. and Holm, D.K. (1985). An experimental and numerical study of crack closure. *Engineering Fracture Mechanics* **22**, 997-1011.

Blom, A.F. and Holm, D.K. (1987). Load interaction effects on fatigue crack propagation in steels of varying strength. In *Role of Fracture Mechanics in*

Modern Technology, (Editors. Sih, C.C, Nisitani, H. and Ishihara, T.), Elsevier Science Publishers B.V., Holland.

Blom, A.F., Hadrboletz, A. and Weiss, B. (1983). Effect of crack closure on near-threshold crack growth behaviour in a high strength Al-alloy up to ultrasonic frequencies. In *Fourth Internatinal Conference on Mechanical Behaviour of Materials*, Oxford: Pergamon Press Ltd, 755-762.

Booth, D.P.P. (2003). Fatigue of friction stir welded AA2024-T351 plate. PhD Thesis, University of Southampton, UK.

Borrego, L.P., Ferreira, J.M., Pinho da Cruz, J.M., and Costa, J.M. (2003). Evaluation of overload effects on fatigue crack growth and closure. *Engineering Fracture Mechanics* **70**, 1379-1397.

Brahma, K.K., Dash, P.K., and Dattaguru, B. (1989). Observation of crack closure using a crack mouth opening displacement gauge. *International Journal of Fatigue* **11**, 37-41.

Bray, G.H. Reynolds, A.P. and Starke, E.A. (1992). Mechanisms of fatigue crack retardation following single tensile overloads in powder metallurgy aluminium alloys. *Metallurgical Transactions* **23A**, 3055-3066.

Bretz, P.E., Vasudevan, A.K., Bucci, R.J. and Malcolm, R.C. (1984). Fatigue crack growth behaviour of 7XXX aluminium alloys under simple variable amplitude loading. In *Fracture Mechanics: Fifteenth Symposium*, ASTM STP 833, 242-265.

Broek, D. (1999). Elementary fracture mechanics. Kluwer academic publishers, Netherlands.

Brown, R.D. and Weertman, J. (1978). Effects of tensile overloads on crack closure and crack propagation rates in 7050 aluminium. *Engineering Fracture Mechanics* **10**, 867-878.

Bucci, R.J., Thakker, A.B., Sandares, T.H., Sawtell, R.R. and Staley, J.T. (1980). *Ranking 7XXX aluminium alloy fatigue crack growth resistance under constant amplitude and spectrum loading*. ASTM STP 714, 41-78.

Budiansky, B. and Hutchinson, J.W. (1978). Analysis of closure in fatigue crack growth. *Journal of Applied Mechanics* **45**, 267-276.

Burdekin, F.M. and Stone, D.E.W. (1966). The crack displacement approach to fracture mechanics in yielding materials. *Journal of Strain Analysis* **1**, 145-153.

Carlson, R.L. and Beevers, C.J. (1985). A mixed mode fatigues crack closure model. *Engineering Fracture Mechanics* **22**, 651-660.

Carnhan, B., Luther, A.H., and Wilkes, J.O. (1969). Applied numerical methods. Wiley, New York.

Carter, R.D., Lee, E-W., Starke, E.A. and Beevers, C.J. (1984). Effect of microstructure and environment on fatigue crack closure in 7475 aluminium alloy. *Metallurgical Transactions* **15A**, 555-563.

Celik, C.E., Vardar, O. and Kalenderoglu, V. (2004). Comaprison of retardation behaviour of 2024-T3 and 7075-T6 Al alloys. *Fatigue and Fracture of Engineering Materials and Structures*, **27**, 713-727.

Chaki, T.K. and Li, J.C.M. (1984). Overload effect and fatigue crack propagation in amorphous metallic alloys. *Scripta Metallurgica* **18**, 1675-1678.

Chanani, G.R. (1977). Effect of thickness on retardation behaviour of 7075 and 2024 aluminium alloys, In *Flaw Growth and Fracture* ASTM STP 631, 365-387.

Chanani, G.R. and Mays, B.J. (1971). Observation of crack closure behaviour after single overload cycles in 7075-T6 single edge-notched specimens. *Engineering Fracture Mechanics* **9**, 65-73.

Chang, J.B., Engle, R.M. and Stolpestad, J. (1981). Fatigue crack growth behaviour and life predictions for 2219-T851 aluminium subjected to variable-amplitude loadings. In *Fracture Mechanics: Thirteenth Symposium*, ASTM STP 3, 242-27.

Chen, D.L., Weiss, B. and Stickler, R. (1996). A model for crack closure. *Engineering Fracture Mechanics* 53, 493-509.

Chermahini, R.G. and Blom, A.F. (1991). Variation of crack-opening stresses in three dimensions: finite thickness plate. *Theoretical and applied fracture mechanics* **15**, 267-276.

Chermahini, R.G., Shivakumar, K.N. and Newman, J.C. (1988). Three dimensional elastic-plastic finite element analysis of fatigue crack growth closure. Mechanics of Fatigue Crack Closure, ASTM STP **982**, 398-413.

Cherpanov, G.P. (1967). Crack propagation in continuous media. *Journal of Applied Mathematics and Mechanics* (USSR) 31, 504.

Cherpanov, G.P. (1969). On crack propagation in solids. *International Journal of solids and structures* **5** , 863-871.

Christensen, R.H. (1959). Metal Fatigue, New York. McGraw-Hill.

Collins, R.A. (2001). Private communication, Damage Tolerance Department (ESAD), Filton, Airbus, UK.

Corlby, D.M. and Packman, P.F. (1973). On the influence of single and multiple peak overloads on fatigue crack propagation in 7075-T6511 aluminium. *Engineering Fracture Mechanics* 5, 479-497.

Damri, D. and Knott, J.F. (1991). Transient retardations in fatigue crack growth following a single peak overload. *Fatigue and Fracture of Engineering Materials and Structures* **14**, 709-719.

Daniewicz, S.R., and Bloom, J.M. (1996]). An assessment of geometry effects on plane stress fatigue crack closure using modified strip-yield model. *International Journal of Fatigue* **18**, 483-490.

Davidson, D.L. (1988). Determination of local driving force for fatigue crack growth under variable amplitude loading. In *Fatigue Crack Growth Under Variable Amplitude Loading*, Elsevier Applied Science, 1-11.

Davidson, D.L. and Lankford, J. (1976). Plastic strain distribution at the tips of propagating fatigue cracks. *Journal of Engineering Materials and Technonology* 24-29.

Dawicke, D.S. (1997). Overlaod and underload effects on fatigue crack growth behaviour of 2024-T3 aluminium alloy, NASA CR 201668.

Dawicke, D.S., Grandt, A.F., and Newman Jr, J.C. (1990a). Three dimensional crack closure behaviour. *Engineering Fracture Mechanics* **36**, 1, 111-121.

Dawicke, D.S. Newman, J.C. and Grandt, A.F. (1990b). Through-the-thickness fatigue crack closure behaviour in an aluminium alloy. In *Fatigue 90*, Bermingham, 1283-1288.

de Castro, J.T.P. and Parks, D.M. (1982) Decrease in closure and delay in fatigue crack growth in plane strain. *Scripta Metallurgica* **16**, 1442-1446.

Dias, A., Lebrun, J.L. and Bignonnet, A. (1999). X-ray diffraction studies on fatigue crack plastic zones developed under plane strain state conditions. *Fatigue and Fracture of Engineering Materials and Structures* **22**, 133-144.

Dill, H.D. and Saff, C.R. (1976) Spectrum Crack Growth Prediction Methods Based on Crack Surface Displacement and Contact Analyses. ASTM STP 595, 306-319.

Dixon, J.R. (1965). Stress and strain distributions around cracks in sheet materials having various wirk hardening characteristics. *International Journal of Fracture Mechanics* **1**, 224-243.

Dodds, R.H., Anderson T.L. and Kirk M.T. (1991) A framework to correlate a/W ratio effects on elastic plastic fracture toughness (J_c). *International Journal of Fracture* **48**, 1-22.

Donahue, R.J., Clark, H.M., Atanmo, P., Kumble, R., and McEvily, A.J., (1972). Crack opening displacement and the rate of fatigue crack growth. *International Journal of Fracture* **8**, 209-219.

Donald, J.K. (1988). A procedure for standardising crack closure model. ASTM STP 982, 222-229.

Dougherty, J.D., Padovan, J., and Srivatsan, T.S. (1997). Fatigue crack propagation and closure behaviour of modified 1070 steel: finite element study. *Engineering Fracture Mechanics* **56**, 189-1997.

Dover, V.D. and Boutle, N.F. (1976). Crack closure at positive stresses during random load fatigue crack growth. *Journal of Strain Analyses*, **11**, 32-38.

Dugdale, D.S. (1960). Yielding of steel sheets containing slits. *Journal of Mechanics and Physics of solids* **8** , 100-108.

Elber, W. (1970). Fatigue crack closure under cyclic tension. *Engineering Fracture Mechanics* **2**, 37-45.

Elber, W. (1971). The significance of fatigue crack closure. In Damage Tolerance in Aircraft Structures, ASTM STP 486, 230-242.

Ellyin, F. and Wu, J. (1999). A numerical investigation on the effect of an overload on fatigue crack opening and closure behaviour. *Fatigue and Fracture of Engineering Materials and Strutures* 22, 835-847.

Eshelby, J.D. (1956). The continuum theory of lattice defects. *Solid State Physic* , 3 (Editors: Seitz, F. and Turnbull, D.), Academic, New York, 55-129.

Evan, A.G. and Hutchinson, J.W. (1989). Effects of non-planarity on the mixed mode fracture resistence of bimaterial interfaces. *Acta Metallurgica* **37**, 909-916.

Ewalds, H.L. and Furnee, R.T. (1978). Crack closure measurement along the fatigue crack front of center cracked specimens. *International Journal of Fracture* **14**, R53-R55.

FAA (1997). Damage-tolerance and fatigue evaluation of structure. AC 25.521-IB, U.S. Department of Transportation, 1-17.

Faber, K.T. and Evans, A.G. (1983). Crack deflection processes – I. Theory. *Acta Metallullurgica* 31, 565-576.

Fleck, N.A. (1984). Plane strain crack closure. PhD thesis, University of Cambridge, England.

Fleck, N.A. (1985). Fatigue crack growth due to periodic underloads and overloads. *Acta Metallurgica* **33**, 1339-1354.

Fleck, N.A (1986). Finite element analysis of plasticity-induced crack closure under plane strain conditions. *Engineering Fracture Mechanics* **25**, 441-449.

Fleck, N.A. (1988). Influence of stress state on crack growth retardation. In *Basic Questions in Fatigue I*, ASTM STP 924, 157-183.

Fleck, N.A. and Newman, J.C. (1988). Analysis of crack closure under plane strain conditions. In *Mechanics of Fatigue Crack Closure*, ASTM STP 982, 319-341.

Fleck, N.A. and Shercliff, H.R. (1989). Overload retardation due to plasticity-induced crack closure. In *Proceedings of the 7th International Conference on Fracture ICF7*, Houston, Texas, USA, 1405-1415.

Fleck, N.A., and Smith, R.A. (1982). Crack closure-is it a surface phenomenon? *International Fracture Fatigue* **4**, 157-160.

Fleck, N.A., Smith, I.F.C. and Smith, R.A. (1983). Closure behaviour of surface cracks. *Fatigue and Fracture of Engineering Materials and Structures* **6**, 225-239.

Foreman, R.G. (1965). Effect of plastic deformation on the strain energy release rate in a centrally notched plate subjected to uniaxial tension. ASME, paper 65-WA/MET-9.

Foreman, R.G., Keary, V.E., and Engle, R.M. (1967). Numerical analysis of crack propagation in cyclic-loaded structures. *Journal of Basic Engineering* **89**, 459-464.

Forsyth, P.J.E. (1953). Exudation of material from slip bands at the surface of fatigued crystals of an aluminium-copper alloy. *Nature* **171**, 172-173.

Forsyth, P.J.E. (1962). A two stage process of fatigue crack growth. In *Crack Propagation: Proceedings of Cranfield Symposium*, London, 76-94.

Fuhring, H. and Seeger, T. (1979). Dugdale crack closure analysis of fatigue cracks under constant amplitude loading. *Engineering Fracture Mechanics* **11**, 99-122.

Gan, D. and Weertman, J. (1981). Crack closure and crack propagation rates in 7050 aluminium. *Engineering Fracture Mechanics* **15**, 87-106.

Gangloff, R.P., Piascik, R.S., Dicus, D.L. and Newman, J.C. (1994). Fatigue crack propagation in aerospace alloys. *Journal of Aircraft* **31**, 720-729.

Garcia A.M. and Sehitoglu, H. (1997). Contact of the crack surfaces during fatigue: Part I. Formulation of the model. *Metallurgical and Materials Transactions* **28A**, 2263-2275.

Geary, W. (1992). A review of some aspects of fatigue crack growth under variable amplitude loading. *International Journal of Fatigue* **14,** 377-386.

Goel, H.S. and Chand, S. (1994). A fatigue crack growth model for single overload tests. *Journal of Engineering Materials Technology, Transactions of ASME* **116**, 168-172.

Griffith, A.A. (1920). The phenomena of rupture and flow in solids. *Philosophical Transactions* A **221**, 163-198.

Hahn, G.T., Hoagland, R.G. and Rosenfield, A.R. (1972). Local yielding attending fatigue crack growth. *Metallurgical Transactions*, **3**, 1189-1196.

Hahn, G.T. and Rosenfield, A.R. (1965). Local yielding and extension of a crack under plane stress. *Acta Metallurgica*, **3**, 1189-1196.

Halliday, M.D. and Beevers, C.J. (1981). Some aspects of closure in two titanium alloys. *Journal of Testing and Evaluation* **9**, 195-201.

Halliday, M.D., Zhang, J.Z., Poole, P., and Bowen, P. (1997). In situ SEM observations of the contrasting effects on an overload on small fatigue crack growth at two different load ratios in 2024-T351 aluminium alloy. *International Journal of Fatigue* **19**, 4, 273-282.

Hammouda, M.M.I., Ahmed, S.S.E., Seleem, M.H., and Sallam, H.E.M. (1998). Fatigue crack growth due to two successive single overloads. *Fatigue and Fracture of Engineering Materials and Structures* **21**, 1537-1547.

Harter, J.A. (1999). Comparison of contemporary FCG life prediction tools. *International Journal of Fatigue,* **21**, S181-S185.

Herper, R. Varder, O. (2003). Elasto-plastic material response of fatigue crack surface profiles due to overload interactions. *International Journal of Fatigue*, **25**, 801-810.

Hertzberg, R.W., and Mills, W.J. (1976). Character of fatigue fracture surface micromorphology in ultra-low growth rate regime. In *Fractography– Microcospic Cracking Processes*, ASTM STP 600, 220-234.

Himmelein, M.K. and Hillberry, B.M. (1976). Effects of stress ratio and overload ratio on fatigue crack delay and arrest behaviour due to single peak overloads. In *Mechanics of Crack Growth*, ASTM STP 590, 321-330.

Hornbogen, E., and Zum Gahr, K.H. (1976). Microstructure and fatigue crack growth in a Fe-Ni-Al alloy. *Acta Metallurgical.* **24**, 581-592.

Hopkins, S.W., Rau, C.A. Leverant, G.R. and Yuen, A. (1976). Effects of various program overloads on threshold for high frequency fatigue crack growth. In *Fatigue Crack under Spectrum Loads*, ASTM STP 595, 125-141.

Hudak, S. J. Jr. and Davidson, D. L. (1988). The dependence of crack closure on fatigue loading variables. In *Mechanics of Fatigue Crack Closure*, ASTM STP 982, 121-138.

Hutchinson, J.W. (1968). Singular behaviour at the end of a tensile crack tip hardening material. *Journal of the Mechanics and Physics of Solids* **16**, 13-31.

Irwin, G.R. (1948). Fracturing of metals, American Society of Metals, Cleveland, 147-166.

Irwin, G.R. (1957). Analysis of stresses and strains near the end of a crack traversing a plate. *Journal of Applied Mechanics* **24**, 361-364.

Irwin, G.R. (1960). Plastic near a crack and fracture toughness. In Proceedings of the Seventh Sagamore Ordance Materials Conference IV, New York, Syracus University, 63-78.

Irwin, G.R. (1961). Plastic zone near a crack and fracture toughness. Sagamore Research Conference, **4** , 1961.

Iwasaki, T., Katoh, A. and Kawafara, M. (1982). Fatigue crack growth under random loading. *Naval Architecture and Ocean Engineering (Japan),* **20**, 194-216.

James, M.N., Pacey, M.N., Wei, L.W. and Patterson, E.A. (2003). Characterisation of plasticity-induced crack flank contact force versus plastic enclave. *Engineering Fracture Mechanics* **70**, 2473-2487.

Jonas, O. and Wei, R.P. (1971). An exploratory study of delay in fatigue-crack growth. *International journal of fracture*, **7**, 116-118.

Jones, R.E. (1973). Fatigue crack growth retardation after single overload in Ti-6Al-4V titanium alloy. *Engineering Fracture Mechanics* **5**, 585-604.

Kemp, N. Parry, M.R., Singh, K.D. and Sinclair, I. (2004). Analytical and finite element modelling of roughness induced crack closure. *Acta Materialia* **52**, 343-353.

Kanninen, M. F., and Popelor, C. H., (1985). Advanced fracture mechanics. Oxford University Press, New York.

Katcher, M. (1973). Crack growth retardation under aircraft spectrum loads. *Engineering Fracture Mechanics* **5**, 793-818.

Kermanidis. Al. Th. And Pantelakis. Sp. G. (2001). Fatigue crack growth analysis of 2024 T3 aluminium specimens under aircraft spectra. *Fatigue and Fracture of Engineering Materials and Strutures* **21**, 699-710.

Khor, K.H. (2004). Materials assessment and optimisation of aluminium alloys for fatigue resistance. PhD thesis under preparation, University of Southampton.

Kibey, S., Sehitoglu, H. and Peckard, D.A. (2004) Modeling of fatigue crack closure in inclined and deflected cracks. *International Journal of Fracture* 129, 279-308.

Kiese, J., Gysler, A. and Lutjering, G. (1990). Fatigue crack propagation mechanism in al-alloys under variable amplitude loading. In Proceedings of the *Fourth International Conference on Fatigue and Fatigue Thresholds*, Birmingham, UK, 1523-1528.

Kim, S.S. and Shin, K.S. (1999). Closure-affected fatigue crack propagation behaviours of powder metallurgy-processed Al-Li alloys in various environments. *Metallurgical and Materials Transactions* **30A**, 2097-2102.

Kim, C.Y. and Song, J.H. (1994). Fatigue crack closure and growth behaviour under random loading. *Engineering Fracture Mechanics* **49**, 105-120.

Kitagawa, H., Yuuki, R. and Ohira, T. (1975). Crack-morphological aspects in fracture mechanics. *Engineering Fracture Mechanics* **7**, 515-529.

Klesnil, M. and Lukas, P. (1972). Influence of strength and stress history on growth and stablisation of fatigue cracks. *Engineering Fracture Mechanics* **4**, 77-92.

Klysz, S. (2001). Pecularities of fatigue crack growth and modifications of the wheeler retardation model. In *VII Summer School of Fracture Mechanics*, Pokrzywna, Poland, 85-104.

Knott, J.F. and Packard, A.C. (1977). Effects of overloads on fatigue crack propagation: Aluminium alloys. *Metal Science* **11**, 399-404.

Kumai, S. and Higo, Y. (1996). Effects of delamination on fatigue crack growth retardation after single tensile overloads in 8090 Al-Li alloys. *Materials Science and Engineering* **A221**, 154-162.

Kumar, R. (1992). A review on crack closure for single overload, programmed and block loadings. *Engineering Fracture Mechanics* **42(1)** 151-158.

Kumar, R. and Garg, S.B.L. (1989). Effect of prestrain on material and single tensile overload on crack closure. *Engineering Fracture Mechanics*, **32**, 833-843.

Laird, C. (1979). Mechanism and theories of fatigue. In *Fatigue and Microstructure*, Papers presented at the 1978 ASM Materials Science Seminar, Ohio: American society of Metals, 149-203.

Lafarie-Frenot, M.C. and Gasc, C. (1983). The influence of age-hardening of fatigue crack propagation behaviour in 7075 aluminimum alloy in vacuum. *Fatigue and Fracture of Engineering Materials and Structures* **6**, 329-344.

Lalor, P.L., Sehitoglo, H., and McClung., R.C. (1986). Mechanics aspects of small crack growth from notches-the role of crack closure. In *The Behaviour of Short Fatigue Cracks*, EGF 1, Mechanical engineering publications, London, 369-379.

Lalor P.L. and Sehitoglo, H. (1988). Fatigue crack closure outside a small scale yielding regime. In *Mechanics of Fatigue Crack Closure*, ASTM STP 982, 342-360.

Landgraf, R.W. (1979). Control of fatigue resistance through microstructure- ferrous alloys. In *Fatigue and Microstructure*, Proceeding of the 1978 ASM Materials Science Seminar, Ohio: American Society of Metals, 439-466.

Lang, M. and Marci, G. (1999). The influence of single and multiple overloads on fatigue crack propagation. *Fatigue and Fracture of Engineering Materials and Structures*, 22, 257-271.

Lankford, J. and Davidson, D.L. (1976). Fatigue crack tip plasticity associated with overloads and subsequent cycling. *Journal of Engineering Materials Technology*, Transaction of ASME **98**, 17-23.

Lankford, J. and Davidson, D.L. (1981). The effect of overloads upon fatigue crack tip opening/closing loads in aluminium alloys. In *Advances in Fracture Research* **2**, Pergamon press, Oxford, 899-906.

Lankford, J., Davidson, D.L. and Chan, K.S. (1984). The influence of crack tip plasticity in the growth of small fatigue cracks. *Metallurgical Transactions* 15A, 1579-1588.

Larsson, S.G. and Carlsson, A.J. (1973). Influence of non-singular stress terms and specimen geometry on small scale yielding at crack tip in elastic-plastic solids. *Journal of Mechanics and Physics of solids* **21**, 263-277.

Lawson, L., Chen, E.Y. and Meshii, M. (1999). Near-threshold fatigue: a review. *International Journal of Fatigue* **21**, S15-S34.

Legris, L., Ei Haddad, M.H., and Topper, T.H. (1981). *The effect of cold rolling on the fatigue properties of a SAE 1010 Steel.* In *Fatigue '81.* Society of Environmental Engineers Conference, Westbury House.

Levy, N.J., Marcal, P.V. Ostergren, V.J. and Rice, J.R. (1971). Small scale yielding near a crack in plane strains – A finite element analysis. International Journal of Fracture **7**, 143-156.

Li, C. (1990). Vector CTD analysis for crystallographic crack growth. *Acta Metallurgical et Materiala* **38**, 2129-2134.

Li, S., Sun, L., Zang, Q., and Wang, Z., (1992) A geometric model for fatigue crack closure induced by fracture roughness under mode I displacements. *Material Science and Engineering* A150, 209-212.

Liebowitz, H. and Moyer, Jr., E.T. (1989). Finite element methods in fracture mechanics. *Computer and Sructures* **31**, 1, 1-9.

Lindgkeit, J., Gysler, A., and Lutjering, G. (1981). The effect of microstructure on the fatigue crack propagation behaviour of an Al-Zn-Mg-Cu alloys. *Metallurgical Transactions* A **12A**, 1613.

Lindley, T.C., and Richards, C.E. (1974). The relevance of crack closure to fatigue crack propagation. *Material Science and Engineering* **14**, 281-293

Llorca, J. and Sanchez-Galvez, V. (1990). Modelling plasticity-induced fatigue crack closure. *Engineering Fracture Mechanics* **37**, 185-196.

Llorca, J. (1992). Roughness induced fatigue crack closure: a numerical study. *Fatigue and Fracture of Engineering Materials and Structures* 15, 655-669.

Llorca, J. and Sanchez-Galvez, V. (1989). Dynamic analysis of plasticity-induced fatigue crack closure. In *Advances in Fatigue Science and Technology.* Kluwer Academic Press, Denventer, 809-819.

Lo, K.K. (1978). Analysis of branched cracks. *Journal of Applied Mechanics* **45**, 797-802.

Lo, K.K. (1980). Fatigue crack closure following a step-increase load. *Journal of Applied Mechanics* **47**, 811-814.

Louat, N., Sadananda, K., Duesbury, M. and Vasudevan, A.K. (1993). Theoretical evaluation of crack closure. *Metallurgical Transactions* **24A**, 2225-2232.

Loye, C., Bathias, C, Retali, D. and Devaux, J.C. (1983). The plastic zone ahead of a fatigue crack in 316 stainless steel. In *Fatigue Mechanisms: Advances in Quantitative Measurement of Physical Damage.* ASTM STP 811, 427-444.

Mahulikar, D.S., Slage, W.P. and Marcus, H.L. (1979). Edge effects on fatigue crack closure of aluminium alloys. *Scripta Metallurgica* **13**, 867-870.

Mathews, W.T., Baratta, F.I., and Driscoll, G.W. (1971). Experimental observation of a stress intensity history effect upon fatigue crack growth rate. *International Journal of Fracture* **7**, 224-228.

McClintock, F.A. (1963). On the plasticity of the growth of fatigue cracks. In *Fracture of Solids* (Editors: Drucker, D.C. and Gilman, J.J.) **20** , New York, Wiley, 65-102.

McClung, R.C. (1991). Crack closure and plastic zone sizes in fatigue. *Fatigue and Fracture of Engineering Materials and Structures* **14**, 455-468.

McClung, R.C. (1991a). The influence of applied stress, crack length, and stress intensity factor on crack closure. *Metallurgical Transactions* **22A**, 1559-1571.

McClung, R.C. (1994). Finite element analysis of specimen geometry effects on fatigue crack closure. *Fatigue Fracture Engineering Materials Structures* **17**, 8, 861-872.

McClung, R.C. (1999). Finite element analysis of fatigue crack closure: a historical and critical review. In *Proceedings of Seventh International Fatigue Crack Conference*, Beijing, China, **1**, 495-502.

McClung, R.C. and Sehitoglu, H. (1989). On the finite element analysis of fatigue crack closure – 1. Basic modelling issues. *Engineering Fracture Mechanics* **33**, 2 237-252.

McClung, R.C. and Sehitoglu, H. (1989a). On the finite element analysis of fatigue crack closure – 2. Numerical results. *Engineering Fracture Mechanics* **33**, 2 253-272.

McClung, R. C. and Davidson, D.L. (1991). High resolution numerical and experimental studies of fatigue cracks. *Engineering Fracture Mechanics*. **39** 1, 113-130.

McClung, R.C., Thacker, B.H. and Roy, S. (1991). Finite element visualisation of fatigue crack closure in plane stress and plane strain. *International Journal of Fracture* **50** 27-49.

McClung, R.C. and Newman, J.C. (1999) Overview. In *Advances in Fatigue Crack Closure Mesurement and Analysis*, ASTM STP 1343, 11-14.

McEvily, A.J. (1988). On closure in fatigue crack growth. In *Mechanics of Fatigue Crack Closure*, ASTM STP 982 , 35-43.

McEvily, A.J. and Ishihara, S. (2002). On the retardation in fatigue crack growth rate due to an overload; a review. International Conference on Fatigue, SAE Brasil, 145-150.

McEvily, A.J. and Ishihara, S. (2002). On the development of crack closure at high R levels after an overload. *Fatigue Fracture Engineering Materials Structures* **25**, 993-998.

McEvily, A.J. and Yang, Z. (1990). The nature of the two opening levels following an overload in fatigue crack growth. *Metallurgical Transactions* A **21A**, 2717-2727.

McMaster, F. J. (1997). Load interaction effects in fatigue life prediction. Final Report, University of Bristol, UK.

McMaster, F. J., and Smith, J.S. (1999). Effect of load excursions and specimen thickness on crack closure measurements. In *Advances in Fatigue Crack Closure Measurements and Analysis*, ASTM STP 1343, 246-264.

McMeeking, R.M. (1977). Finite deformation analysis of crack-tip opening in elastic-plastic materials and implications for fracture. *Journal of Physics and Solids* **25**, 357-381.

McMeeking, R.M. and Parks, D.M. (1979). On the criteria for *J* dominance of crack tip fields in large scale yielding. In *Elastic-Plastic Fracture*, ASTM STP **668** , 175-194.

Meggiolaro, M.A., and Castro, J.T.P. (2001). An evaluation of Elber-type crack retardation models. *II Seminário Internacional de Fadiga* (SAE-Brasil), São Paulo, SAE no. 2001-01-4063, 207-216,

Mendelsohn, D.A., Gross, T.S. and Zhang, Y. (1995). Fracture surface interference in shear-I A model based on experimental surface characterizations. *Acta Metallurgica et Materialia* **43**, 893-906.

Mille, P. (1979). Closure phenomena at crack tips in steels (in French), PhD thesis, University of Technology of Compiegne.

Miller, K.J. (1991). Metal fatigue-past, current and future. In *Proceedings of the Institution of Mechanical Engineers* **205** , 291-304.

Miller, K.J. (1993). Material science perspective of metal fatigue resistance. *Materials Science Technology* **9**, 453-462.

Mills, W.J., and Hertzberg, R.W. (1975). The effect of sheet thickness on fatigue crack retardation in 2024-T3 aluminium alloy. *Engineering Fracture Mechanics* **7**, 705-708.

Mills, W.J., and Hertzberg, R.W. (1976). Load interaction effects on fatigue crack propagation in 2024-T3 aluminium alloy. *Engineering Fracture Mechanics* **8**, 657-667.

Mills, W.J., and Hertzberg, R.W. and Roberts, R. (1977). Load interaction effects on fatigue crack growth in A514 steel alloy. In *Cyclic Stress-Strain and Plastic Deformation Aspects of Fatigue Crack Growth*. ASTM STP 637, 192-208.

Minakawa, K., and McEvily, A.J. (1981). On crack closure in the near-threshold region. *Scripta Metallurgica* **15**, 633-636.

Minakawa, K., Levan, G. and McEvily, A.J. (1986). The influence of load ratio on fatigue crack growth in 7090-T6 and IN9021-T4 P/M aluminium alloys. *Metallurgical Transactions* **17A**, 1787-1795.

Mishra, S.C. and Parinda, B.K. (1985). A study of crack-tip plastic zone by elastoplastic finite element analysis. *Engineering Fracture Mechanics*, **22**, 951-956.

Miyamoto, H., Miyoshi. T., and Fukuda, S. (1973). An analysis of crack propagation in welded structures. Significance of Defects in Welded Structures. In *Proceedings of Japan-U.S. Seminar*, Tokyo Press, 189-202.

Miyamoto, H. (1974). The mechanics of crack propagation. In *Proceedings of symposium on mechanical behaviour of materials*, Kyoto, 37-47.

Molent, L. and Aktepe, B. (2000). Review of fatigue monitoring of agile military arcraft. *Fatigue and Fracture of Engineering Materials and Structures* **23**, 767-785.

MSC/PATRAN (1999). User's Manual. Version 9.0, MSC.Software Corporation, Santa Anna, CA, USA.

Nagtegaal, J.C., Parks, D.M., and Rice, J.R. (1974). On numerically accurate finite element solutions in the fully plastic range. *Computer Methods in Applied Mechanics and Engineering* **4**, 153-177.

Nakagaki, M. and Atluri, S.N., (1979). Fatigue crack closure and delay effects under mode I spectrum loading: an efficient elastic-plastic procedure. *Fatigue Engineering Material Structure* **1**, 421-429.

Nakagaki, M. and Atluri, S.N., (1980). Elasto-plastic analysis of fatigue crack closure in modes I and II. *AIAA* **18**, 1110-1117.

Nakamura, H. and Kobayashi, H. (1988). Analysis of fatigue crack closure caused by asperities using the modified Dugdale model. In *Mechanics of Fatigue Crack Closure*, ASTM 982, 459-474.

Nakamura, H., Kobayashi, H. Yanase, S. and Nakazawa, H. (1983). Finite element analysis of fatigue closure in compact specimen. In *Mechanical Behaviour of Materials*, Proceedings ICM4 **2**, 817-823.

Nayeb-Hashemi, H. McClintock, F.A. and Ritchie, R.O. (1983). Influence of overloads and block loading in mode III fatigue crack propagation in A469 rotor steel. *Engineering Fracture Mechanics* **18**, 736-743.

Newman, J.A., Riddell, W.T. and Piascik, R.S. (2003). A threshold fatigue crack closure model: Part I – model development. *Fatigue and Fracture of Engineering Materials and Structures* **26**, 603-614.

Newman, J.C. (1976). A finite element analysis of fatigue crack closure. In *Mechanics of Crack Growth*, ASTM STP **590**, 281-301.

Newman, J.C., (1977). Finite element analysis analysis of crack growth under monotonic and cyclic loading. In *Cyclic Stress-Strain and Plastic Deformation Aspects of Fatigue Crack Growth*, ASTM STP **637**, 56-80.

Newman, J.C., (1981). A crack closure model for predicting fatigue crack growth under aircraft spectrum loading. In *Methods and Models for Predicting Fatigue Crack Growth under Random Loading*, ASTM STP 748, 53-84.

Newman, J.C. (1992). FASTARN II: A fatigue crack growth structural analysis program. NASA TM 104159.

Newman. J.C. (1997). Prediction of crack growth under variable-aplitude loading in thin-sheet 2024-T3 aluminium alloys. *In* Engineering against fatigue, University of Sheffield. March 1997.

Newman. J.C. (1997a). The merging of fatigue and fracture mechanics concepts: a historical perspective. In *Fatigue and Fracture Mechanics*, ASTM STP 1321, 3-5.

Newman, J.C. (1998). Prediction of crack growth under variable-amplitude loading in thin cheet 2024-T3 aluminimum alloys. In *Engineering Against Fatigue*, Proceedings of International Conference on the Importance of Understanding the fundamentals of the Fatigue Process, Rotterdam: A.A. Balkema, 261-268.

Newman, J.C. (1998a). An evaluation of the plasticity-induced crack-closure concept and measurement methods. NASA TM 208430.

Newman, J.C. (1998b). The merging of fatigue and fracture mechanics concepts: a historical perspective. *Progress in Aerospace Sciences* **34**, 347-390.

Newman, J.C. (1999). Analyses of fatigue crack growth and closure near threshold conditions for large-crack behaviour. NASA TM 209133.

Newman, J.C. (1999a). Analyses of fatigue and fatigue-crack growth under constant- and variable-amplitude loading. *In* XVI Meeting of the Spanish Group of Fracture, Malaga, Spain.

Newman, J.C. and Armen, H. (1975). Elastic-plastic analysis of a propagating crack under cyclic loading. *AIAA Journal*, **13**, 1017-1023.

Newman, J.C., Bigelow, C.A. and Sivakumar, K.N. (1993). Three-dimensional elastic-plastic finite element analysis of constraint variations in cracked bodies. *Engineering fracture mechanics*, **46**, 1-13.

Newman, J.C. and Elber W. (1988). *Mechanics of Fatigue crack closure*. ASTM STP 982.

Ngangga, S.P., and James, M.N. (1996). Variable amplitute loading in En8(080M40) steel: a detailed experimental study of crack growth. *Fatigue and Fracture of Engineering Materials and Structures* **19**, 207-216.

Nguyen, O. Repetto, E.A. Oritz, M. Radovitzky, R.A. (2001). A cohesive model of fatigue crack growth. *International Journal of Fracture* **110**, 351-369.

Nicholas, T. Palazotto, A. and Bednarz, E. (1988). An analytical investigation of plasticity induced closure involving short cracks. In *Mechanics of Fatigue Crack Closure*, ASTM STP **982**, 361-379.

Nicoletto, G. (1987). Fatigue crack tip strains in 7075-T6 aluminium alloy. *Fatigue Fracture of Engineering Materials and Structures* **10**, 37-49.

Nicoletto, G. (1989). Plastic zones about fatigue cracks in metals. *International Journal of Fatigue* **11**, 107-115.

Nowack, H., Trautmann, K.H., Schulte, K. and Lutjering, G. (1979). Sequence effects on fatigue crack propagation; mechanical and microstructural contributions. In *Fracture Mechanics*, ASTM STP 677, 36-53.

Nowell, D. (1998). A boundary element model of plasticity-induced fatigue crack closure. *Fatigue Fracture of Engineering Materials and Structures* **21**, 857-871.

Ogura, K., Ohji, K. and Ohkubo, Y. (1974). Fatigue crack growth under biaxial loading. *International Journal of Fracture* 10, 609-610.

Ogura, K., Ohji, K. and Honda, K. (1977a). Influence of mechanical factors on the fatigue crack closure. In *Fracture 1977* (Editor: D.M.R. Taplin), **2**, 1035-1047. New York: Pergamon Press.

Ogura, K., and Ohji, K. (1977b). FEM analysis of crack closure and delay effect in fatigue crack growth in variable amplitude loading. *Engineering Fracture Mechanics* **9**, 471-480.

Ohji, K., Ogura, K and Ohkubo, Y. (1974). On the closure of fatigue cracks under cyclic tensile loading. *International Journal of Fracture* **10**, 123-124.

Ohji, K., Ogura, K and Ohkubo, Y. (1975). Cyclic analysis of a propagating crack and its correlation with fatigue crack growth. *Engineering Fracture Mechanics* **7**, 457-464.

Ohrloff, N., Gysler, A. and Lutjering, G. (1988). Fatigue crack propagation behaviouor under variable amplitude loading. In In *Fatigue Crack Growth Under Variable Amplitude Loading.* (Editors. Petit, J., Davidson, D.L., Suresh, S. and Rabbe, P.), 24-34.

Orowan, E. (1948) Fracture and strength of solids. Reports on Progress in Physics, **XII**, 185.

Palaniswamy, K. and Knauss, W.G. (1978). On the problem of crack extension in brittle solids under general loading. In *Mechanics Today*, Pergamon press, New York, 87-148.

Palazotto, A., Bendnarz, E. (1989). A finite element investigation of viscoplastic-induced closure of short cracks at high temperatures. In *Fracture Mechanics: Perspectives and Directions*, ASTM STP 1020, 530-547.

Palazotto, A., and Mercer, J.C. (1990). A finite element comparison between short and long within a plastic zone due to notch. *Engineering Fracture Mechanics* **35**, 967-986.

Paris, P.C. (1960). The growth of cracks due to variations in loads. PhD. Thesis. Bethlehem, Lehigh University.

Paris, P.C. Gomez, M.P. and Anderson, W.P. (1961). A rational analytic theory of fatigue. *The trend in engineering* **13**, 9-14.

Paris, P.C. and Erdogan, F. (1963). A critical analysis of crack propagation laws, *Basic Engineering* **85** , 528-534.

Paris, P.C. (1998). Fracture mechanics and fatigue: a historical perspective. *Fatigue and Fracture of Engineering Materials and Structures* **21**, 535-540.

Paris, P.C. and Hermann, L. (1982). *Twenty years of reflection on questions involving fatigue crack growth, Part II.* Some observations on crack closure. In Fatigue Thresholds, Fundamental and Engineering Applications **1**, 11-33, EMAS, UK.

Park, S.-J., Earmme, Y.-Y. and Song, J.H. (1997). Determination of most appropriate mesh size for a 2-D finite element analysis of fatigue crack closure behaviour. *Fatigue and Fracture of Engineering Materials and Structures* **20**, 533-545.

Park, S.-J., and Song, J.H. (1999). Simulation of fatigue crack closure behaviour under variable-amplitude loading by a 2D finite element analysis based on the most appropriate mesh size concept. In *Advances in Fatigue Crack Closure Measurements and Analysis*, ASTM STP 1343, 337-348.

Parry, M.R. (1999). Numerical modelling of combined roughness and plasticity induced fatigue crack closure effects in fatigue. Mphil/PhD Transfer thesis, Report no. PG/RA/MP/99/01/275, School of Engineering Sciences, University of Southampton. Southampton, UK.

Parry, M.R. (2000). Finite element and analytical modelling of roughness induced fatigue crack closure. PhD thesis, University of Southampton. Southampton, UK.

Parry, MR., Syngellakis, S. and Sinclair, I. (2000a). Numerical modelling of combined roughness and plasticity induced crack closure in fatigue. *Material Science and Engineering A.* **A291**, 224-34.

Parry MR. Syngellakis S. Sinclair I. (2000b). Numerical. Modelling of roughness and plasticity induced crack closure effects in fatigue, *Material Science Forum*, **331-337**, 1473-1478.

Parry MR. Syngellakis S. Sinclair I. (2000c). Investigation of roughness induced crack closure effects in fatigue. *Damage and Fracture Mechanics* **VI**, (Editors: Selvadurai, A.P.S and Brebbia C.A.), 313-322., WIT press, Southampton, Boston.

Parry, M.R. (2003). Private communications, Airbus UK, Bristol.

Pelloux, R.M., Faral, M. and McGee, W.M. (1979). Assesment of crack tip closure in an aluminium alloy by electron microscopy. *Fatigue and Fracture of Engineering Materials and Sructures*, **1**, 21-35.

Petit, J., Renuad, P., and Violan, P. (1982). Effect of microstructure on crack growth in a high strength aluminium alloy. In *Proceedings of the 4th European Conference on Fracture*, EMAS Leobon, Austria, 426-433.

Petit, J., Tintiller, R., Ranganathan, N., Ait Abdedaim, M. and Chalant, G. (1988), Influence of microstructure and environment on fatigue crack propagation

affected by single or repeated overloads in a 7075 alloy. In *Fatigue Crack Growth Under Variable Amplitude Loading.* (Editors. Petit, J., Davidson, D.L., Suresh, S. and Rabbe, P.), 162-179.

Phillips, E.P. (1999). Periodic overload and transport spectrum fatigue crack growth tests of Ti62222STA and Al2024T3 sheet. NASA TM 208995, 1-39.

Pineau, A.G. and Pelloux, R.M. (1974). Influence of strain-induced martensitic transformations on fatigue crack growth in stainless steels. *Metallurgical Transactions* **5**, 1103-1112.

Pipan, R., Kolednik, O. and Lang, M. (1994). A mechanism of plasticity induced crack closure under plane strain conditions. *Fatigue and Fracture of Engineering Materials and Structures* **17**, 721-726.

Pitonaik, F.J., Grandt, A.F., Montulli, L.T., and Packman, P.F. (1974). Fatigue crack retardation and closure in polymethylmethacrylate. *Engineering Fracture Mechanics* **6**, 663-670.

Polmear, I.J. (1995). Light alloys, metallurgy of the light metals. Butterworth-Heinemann, Oxford.

Pommier, S. (2002). Plane strain crack closure and cyclic hardening. *Engineering Fracture Mechanics* **69**, 25-44.

Pommeir, S and Bompard, P.H. (2000). Bauschinger effect of alloys and plasticity-induced crack closure: a finite element analysis. *Fatigue and Fracture of Engineering Materials and Structures* **23**, 129-139.

Porter, T.R. (1972). Method of analysis and prediction for variable amplitude fatigue crack growth. *Engineering Fracture Mechanics* **4**, 717-736.

Powell, P.M., Forsyth, P.J.E. and Williams, T.R.G. (1981). The effect of overloading on fatigue crack propagation in two aluminium alloys and an austenitic stainless steel. In *Proceedings of 5th International Conference on Fracture*, Cannes, France, Pergamon Press, Oxford, UK, 1781-1788.

Ramos, M.S., Pereira, M.V., Darwish, F.A., Motta, S.H. and Carneiro, M.A. (2003). Effect of single and multiple overloading on the residual fatigue life of a structural steel. *Fatigue and Fracture of Engineering Materials and Structures* **26**, 115-121.

Ray, S.K. and Grandt, A.F. (1988). Comparison of methods for measuring fatigue crack closure in a thick specimen. In *Mechanics of Fatigue Crack Closure*, ASTM STP 982, 197-213.

Ravichandran, K.S. (1990). A theoretical model for roughness induced crack closure. *International Journal of Fracture* **44**, 97-110.

Riemelmoser, F.O. and Pippan, R. (1996). Plasticity induced crack closure under plain strain condition in terms of dislocation arrangement. In *Proceedings Fatigue '96*. Edited by Lutjering, G. and Nowwack, H., 363-368.

Riemelmoser, F.O. and Pippan, R. (1998a). Mechanical reasons for plasticity-induced crack closure under plane strain conditions. *Fatigue and Fracture of Engineering Materials and Structures* **21**, 1425-1433.

Riemelmoser, F.O. and Pippan, R. (1998b). Discussion of error in the analysis of the wake dislocation problem. *Material Transactions A*, **29A**, 1357-1359.

Rice, J.R. (1967). Mechanics of Crack Tip Deformation and Extension by Fatigue. In *Fatigue Crack Propagation*, ASTM STP 415, 247-309.

Rice, J.R. (1968a). Mathematical analysis in the mechanics of fracture. *Fracture-An Advanced Treatise*. II , (Editor: Leibowitz, H.), Academic, New York, 191-308.

Rice, J.R. (1968b). A path independent integral and the approximate analysis of strain concentrations by notches and cracks. *Journal of Applied Mechanics* 68, 379-386.

Rice, J.R. (1973). Paper I-441. In *Proceedings of Third International Congress on Fracture* , (Editor: Kochendorfer, A.), II , Verein Deutscher Eisenhuttenleute, Dsseldorf.

Rice, J.R. (1974). Limitations to the small scale yielding approximation for crack tip plasticity. *Journal of the Mechanics and Physics of Solids* **22** , 17-26.

Rice, J.R. and Rosengren, G.F. (1968). Plane strain deformation near a crack tip in a power law hardening material. *Journal of the Mechanics and Physics of Solids* 16, 1-12.

Rice, R.C. and Stephens, R.I. (1973). Overload effects on subcritical crack growth in austenitic manganese steel. In *Progress in Flaw Growth and Fracture Toughness Tesing,* ASTM STP 536, 95.

Ritchie, R.O. (1988). Mechanisms of fatigue crack propagation in metals, ceramics and composites: Role of crack tip shielding. *Materials Science and Engineering* **A103**, 15-28.

Ritchie, R. O. and Suresh, S. (1982). Some considerations on fatigue crack closure at near threshold stress intensities die to fracture morphology. *Metallurgical Transactions* **13A**, 937-940.

Ritchie, R. O., Suresh, S. and Moss, C.M. (1980). Near-threshold crack growth in 21/4 Cr-1 Mo pressure vessel steel in air and hydrogen. *Journal of Engineering Materials and Technology* 102, 293-199.

Ritchie, R.O., Yu., W., Blom, A.F. and Holm, D.K. (1987). An analysis of crack tip shielding in aluminium alloy 2124: a comparison of large, small, through-thickness and surface fatigue cracks. *Fatigue and Fracture of Engineering Materials and Structures* **10**, 343-363.

Robin, C., Louah, M. and Pluvinage, G. (1983). Infulence of an overload on the fatigue crack growth in steels. *Fatigue and Fracture of Engineering Materials and Structures* **6**, 1-13.

Roe, K. Siemund, T. (2001). Simulation of fatigue crack growth via a fracture process zone model. In *First MIT Conference on Computational Fluid and Solid Mechanics*, MA, USA.

Roychowdhury, S., and Dodds Jr., R.H. (2003). A numerical investigation of 3-D small-scale yielding fatigue crack growth. *Engineering Fracture Mechanics* **70**, 2363-2383.

Roychowdhury, S., and Dodds Jr., R.H. (2003a). Three dimensional effects on fatigue crack closure in the small scale-yielding regime. *Fatigue and Fracture of Engineering Materials and Structures* **8**, 663-673.

Roylance, D. (2001). Introduction to fracture mechanics. Department of Materials Science and Engineering, MIT, Cambridge, MA 02139, 1-17.

Sanders, J.L. (1960). On the Griffith-Irwin fracture theory. *Journal of Applied Mechanics* **27**, 352-353.

Schijve, J. (1974). Fatigue damage accumulation and incompatible crack front orientation. *Engineering Fracture Mechanics* **6**, 245-252.

Schijve, J. (1976). The effect of pre-strain on fatigue crack growth and crack closure. *Engineering Fracture Mechanics* **8**, 575-581.

Schijve, J. (1994). Fatigue of aircraft materials and structures. *International Journal of Fatigue*, 16, 21-32.

Schijve, J. and Broek, D. (1962). The results of a test programme based on a gust spectrum with variable amplitude loading. *Aircraft Engineering* **34**, 314-316.

Schutz, W. (1996). A history of fatigue. *Engineering Fracture Mechanics* ***54***, 263-300.

Sehitoglu, H. and Garcia A.M. (1997). Contact of the crack surfaces during fatigue: Part 2. Simulation. *Metallurgical and Materials Transactions* **28A**, 2277-2289.

Sehitoglu, H. and Sun, W. (1989). Mechanisms of crack closure in plain strain and plane stress. In *3rd conference on biaxial/multiaxial fatigue*, Struttgart, Germany.

Sehitoglu, H. and Sun, W. (1991). Modelling of plane strain fatigue crack closure. Transactions of ASME. *Journel of Engineering Materials and Technology* **113**, 31-40.

Sham, T.L. (1983). A finite element study of the asymptotic near-tip fields for mode I plane strain cracks growing stably in elastic ideally plastic solids. In *Elastic-Plastic Fracture*, ASTM STP 803, 52-79.

Shercliff, H.R. and Fleck, N.A. (1990). Effect of specimen geometry on fatigue crack growth in plane strain II. Overload response. *Fatigue and Fracture of Engineering Materials and Structures* **3**, 297-310.

Shih, C.F. (1974). Small scale yielding analysis of mixed mode plane strain crack problems. In *Fracture Analysis* , ASTM STP 560, 187-210.

Shih, C.F. (1976). J-Integral estimates for strain hardening materials in antiplane shear using fully plastic solution. In *Mechanics of Crack Growth*. ASTM STP 590, 3-26.

Shih, T.T. and Wei, R.P. (1974) A Study of fatigue crack growth. *Engineering Fracture Mechanics* **6**, 19-32.

Shin, C.S. and Fleck, N.A. (1987). Overload retardation in a structural steel. *Fatigue and Fracture of Engineering Materials and Structures* **9**, 379-393.

Shin, C.S. and Fleck, N.A. (1989). Fatigue and fracture of a zinc die casting alloy. *International Journal of Fatigue* 11, 341-346.

Shin, C.S. and Hsu, S.H. (1993). On the mechanisms and behaviour of overload retardation in AISI 304 stainless steel. *International Journal of Fatigue* **15**, 181-192.

Shutter, D.M. and Geary, W. (1996). Some aspects of fatigue crack growth retardation in AISI 304 stainless steel. *International Journal of Fatigue* **15**, 181-192.

Simoes, A.F., Pereira, M. and Godefroid, L. (1999). Effect of overloading on fatigue crack growth retardation in a 7150 aluminium alloy. In *Proceedings of the 7th International Fatigue Congress*, IFC-7, Beijing, China, 1069-1074.

Sinclair, I. and Gregson, P.J. (1998). Microstructural Control of Fatigue in High Strength Aluminium Alloys. In *Proceedings 6th International Conference on Al-Alloys* , Tokyo: JILM, 4 -85.

Sneddon, I.N. (1946). The distribution of stress in the neighbourhood of a crack in a elastic solid. In *Proceedings of Royal Society of London*, **A-187**, 229-260.

Socie, D.F. (1977). Prediction of fatigue crack growth in notched members under variable amplitude loading histories. *Engineering Fracture Mechanics* 9, 849-865.

Solanki, K., Daniewicz, S.R. and Newman, J.C. (2003). Finite element modelling of plasticity-induced crack closure with emphasis on geometry and mesh refinement effects. *Engineering Fracture Mechanics* **70**, 1475-1489.

Solanki, K., Daniewicz, S.R. and Newman, J.C. (2003a). Finite element analysis of plasticity-induced fatigue crack closure: an overview. *Engineering Fracture Mechanics* **71**, 149-171.

Stephens, R.I., Sheets, E.C. and Njus, G.O. (1977). Fatigue crack growth and life predictions in Man-Ten steel subjected to single and intermittent tensile overloads, ASTM STP 637, 176-191.

Skorupa. M. (1998). Load interaction effects during fatigue crack growth under variable amplitude loading – a literature reviews. Part I: empirical trends. *Fatigue and Fracture of Engineering materials and Structures* **21**, 987-1006.

Skorupa. M. (1999). Load interaction effects during fatigue crack growth under variable amplitude loading – a literature reviews. Part II: qualititative interpretation. *Fatigue and Fracture of Engineering materials and Structures* **22**, 905-626.

Starink, M.J., Gao, N. and Yan, J.L. (2004) The origins of room temperature hardeing of Al-Cu_Mg alloys. *Materials Science and Engineering* A, 222-226.

Sukumar, N, Chopp. D.L. and Moran, B. (2003). Extended finite element method and fast marching method for three-dimensional fatigue crack propagation. *Fatigue and Fracture of Engineering Materials and Structures* **70**, 29-48.

Sun, W. and Sehitoglu, H. (1992). Residual Stress Fields During Fatigue Crack Growth. *Fatigue and Fracture of Engineering Materials and Structures* **15**, 115-128.

Sunder, R. and Desh, P.K. (1982). Measurement of fatigue crack closure through electron microcospy. *International Journal of Fatigue*, **97**, 97-103.

Suresh, S. (1982). Crack growth retardation due to microroughness: a mechanism for overload effects in fatigue. *Scripta Mettalurgica* **16**, 995-999.

Suresh, S. (1983). Micromechanisms of fatigue crack growth retardation following overloads. *Engineering Fracture Mechanics* **18**, 577-593.

Suresh, S. (1983a). Crack deflection: implications for growth of long and short fatigue cracks. *Metallurgical Transactions* A **14A**, 2375-2385.

Suresh, S., (1985). Fatigue crack deflection and fracture surface contact: Micromechanical models. *Metallurgical Transactions* **16A**, 249-260.

Suresh, S. (1988) Micro-mechanisms of variable amplitude load effects during fatigue crack growth in metals and ceramics. In *Fatigue Crack Growth Under Variable Amplitude Loading*. Elsevier Science Publishers, England, 146-161

Suresh, S. (1998). Fatigue of Materials, Cambridge University Press, UK.

Suresh, S. and Ritchie, R.O. (1982a). A geometric model for fatigue crack closure induced by fracture surface morphology. *Metallurgical Transactions* **13A**, 1627-1631.

Suresh, S. and Ritchie, R.O. (1982b). Mechanistic dissimilarities between environmentally-influenced fatigue-crack propagation at near-threshold and higher growth rates in lower strength steels. *Metal Science* **16**, 529-538.

Suresh, S., and Vasudevan, A.K. (1984). Application of fatigue threshold concepts to variable amplitude crack propagation. In *Fatigue Crack Growth Threshold Concepts*. The Matallurgical Society of AIME, Warrendale, PA, 361-378.

Suresh, S., and Vasudevan, A.K., and Bretz, P.E. (1984). Mechanisms of slow fatigue crack growth in high strength aluminium alloys: Role of microstructure and environment. *Metallurgical Transactions* **15A**, 369-379.

Suresh, S., Zamiski, G.F. and Ritchie, R.O. (1981). Oxide-induced crack closure: an explanation for near-threshold corrosion fatigue crack growth behaviour. *Metallurgical Transactions* **12A**, 1435-1443.

Swedlow, J.L., Williams, M.L. and Yang, W.H. (1965). *Elastic-plastic stresses and strains in cracked plates*. In *Proceedings of the 1st International Conference on Fracture*, Sendai.

Swift, T. (1996). Damage tolerance certification of commercial aircraft. In: ASM Handbook volume **19**: *Fatigue and Fracture*, Ohio: American society of Metals, 566-576.

Tada, H., Paris, P.C. and Irwin, G.R. (2000). The stress analysis of cracks handbook. ASME, New York.

Tanaka, K., Matsuoka, S., Schmidt, V and Kuna, M. (1981). Influence of specimen geometry on delayed retardation phenomena of fatigue crack growth in HT80 steel and A5083 aluminium alloy. In *Proceedings of 5th International Conference on Fracture*, Cannes, France (Advances in Fracture Research 4, Pergamon Press, Oxford, UK), 1789-1798.

Taira, S. and Tanaka, K. (1979). Local residual stress near fatigue crack tip. Transactions, Iron and Steel Institute of Japan **19**, 411-418.

Taylor, D. and Knott, J.F. (1982). *Unpublished results cited as Reference [21]*, ASTM STP 924, 157-183.

Toda, H., Sinclair, I., Buffiere, J-Y., Maire, E. Connolley, T., Joyce, M., Khor, K.H., Gregson, P. (2003). Assesment of fatigue crack closure phenomenon in damage tolerant aluminium alloy by in-situ high-resolution synchroton X-ray microtomography. *Philosophical Megazine A* **83**, 2429-2448.

Tokaji, K., Ando, Z. and Kojima, T. (1984). Fatigue crack retardation in low carbon steel in salt plant. *Journal of Materials Technology*, Transactions of ASME **106**, 38-42.

Trebules, V.W., Jr., Roberts, R., and Hertzberg, R.W., Effect of multiple overloads on fatigue crack propagation in 2024-T3 aluminium alloy. In *Progress in Flaw Growth and Fracture Toughness Testing*. ASTM STP 536, 115-146.

Trockels, I., Gysler, A. and Lutjering, G. (1994). Effects of periodically applied overloads on the fatigue crack propagation behaviour of high-strength al-alloys. In *Fourth International Conference on Aluminium Alloys*, Atlanta, Georgia, USA, 717-723.

Trockels, I., Lutjering, G. and Gysler, A. (1996). Fatigue crack propagation behaviour of an aluminium alloy under variable amplitude loading conditions. In *Sixth International Conference on Aluminium Alloys*, Berlin, Germany, 571-576.

Tsukunda, H., Ogiyama, H. and Shiraishi, T. (1996). Transient fatigue crack growth behaviour following single overloads at high stress ratios. *Fatigue and Fracture of Engineering Materials and Structures* **19**, 879-891.

Tur, Y.K. and Varder, O. (1996). Periodic tensile overloads in 2024-T3 Al-Alloy. *Engineering Fracture Mechanics* **53**, 69-77.

Underwood, J.H. and Kendall, D.P. (1969). Measurement of plastic strain distributions in the region of a crack tip. *Experimental Mechanics*, 296-304.

Varder, O. and Yildirium, N. (1990). Crack growth retardation due to intermittent overloads. *International Journal of Fatigue* **12**, 283-287.

Vargas, L.G. and Stephen, R.I. (1973). Subcritical crack growth under imtermittent overloading in cold-rolled steel. In 3rd International Conference on Fracture, Munich, Germany, 1-5.

Vasudevan, A.K. and Doherty, R.D. (1989). Aluminium alloys-contemporary research and applications. Harcourt Brace Jovanovich Ltd, London.

Vasudevan, A.K., Sadananda, K. and Louat, N. (1994). A review of crack closure, fatigue crack threshold and related phenomena. *Materials Science and Engineering* **A188**, 1-22.

Vecchio, R.S., Hertzberg, R.W. and Jaccard, R. (1983). Overload induced fatigue crack growth rate attenuation behaviour in aluminium and steel alloys. Scripta Mettalurgica **17**, 343-346.

Vecchio, R.S., Hertzberg, R.W. and Jaccard, R. (1984). On the overload induced fatigue crack crack propagation behaviour in aluminium and steel alloys. *Fatigue and Fracture of Engineering Materials and Structures*, **7**, 181-194.

Venkateshwara Rao, K.T. and Ritchie, R.O. (1988). Mechanisms for the retardation of fatigue cracks following single tensile overloads: behaviour in aluminium-lithium alloys. *Acta Mettalurgica* **36**, 2849-2862.

Venkateshwara Rao, K.T. and Ritchie, R.O. (1988a). Micromechanisms of transient fatigue crack growth behaviour in aluminium-lithium alloys following single tensile overloads. In *Fatigue Crack Growth Under Variable Amplitude Loading*. (Editors: Petit, J., Davidson, D.L., Suresh, S., Rabbe, P.), Elsevier Applied Science, 134-145.

Venkateshwara Rao, K.T. and Ritchie, R.O. (1992). Fatigue of aluminium-lithium alloys. *International Materials Reviews* **37**, 153-185.

Von Euw, E.J.F., Hertzberg, R.W. and Roberts, R. (1972). Delay effects in fatigue crack propagation. In *Stress Analysis and Growth of Cracks*, Part I, ASTM STP 513, 230-259.

Walker, N. and Beevers, C.J. (1979). A fatigue crack closure mechanism in titanium. Fatigue of Engineering Materials and Structures **1**, 135-148.

Wang, G.S. and Blom, A.F. (1991). A strip model for fatigue crack growth predictions under general load conditions. *Engineering Fracture Mechanics* **40**, 507-533.

Wang, S-H., Muller, C., and Exner, H.E. (1998). A model for roughness-induced fatigue crack closure. *Metallurgical and Materials Transactions* A, **29A**, 1933-1939.

Wang, C.H., Rose, L.R.F. and Newman, J.C. (2002). Closure of plane-strain cracks under large-scale yielding conditions. *Fatigue and Fracture of Engineering Materials and Structures*, **25**, 127-139.

Wanhill, R.J.H. (2002). Milestones case histories in aircraft structural integrity. NLR-TP-2002-521, National Aerospace Laboratory, Netherlands, 1-25.

Ward-Close, CM. Blom, A.F. and Ritches, R.O. (1989). Mechanisms associated with transient fatigue crack growth under variable-amplitude loading: an experimental and numerical study. *Engineering Fracture Mechanics* **32** 613-638.

Ward-Close, C.M. and Ritchie, R.O. (1988) On the role of crack closure mechanisms in influencing fatigue crack growth following tensile overloads in a titanium alloy: Near threshold versus higher ΔK behaviour. In *Mechanics of Fatigue Crack Closure*, ASTM STP 982, 93-111.

Wasen, J., Hamberg, K. and Karlsson, B. (1988). The influence of grain size and fracture surface geometry on the near-threshold fatigue crack growth in ferritic steels. *Materials Science Engineering* **A102**, 217-226.

Wei, R.P., Fenelli, N.E., Unangst, K.D., and Shih, T.T. (1980). Fatigue crack growth response following a high-load excursion in 2219-T851 aluminium alloy. *Journal of Engineering Materials Technology*, Transactions of ASME **102**, 280-292.

Wei, L.W. and James, M.N. (2000). A study of fatigue crack closure in polycarbonate CT specimens. *Engineering Fracture Mechanics* **66**, 223-242.

Wei, R.P. and Shih, T.T. (1974). Delay in fatigue crack growth. *International Journal of Fracture* **10**, 77-85.

Wei, R.P., Shih, T.T. and Fitzgerald, J.H. (1973). Load interaction effects on fatigue crack growth in Ti-6Al-4V alloy. NASA CR-2239.

Wells, A.A. (1961). Unstable crack propagation in metals: cleavage and fast fracture. Proceedings of the Crack Propagation Symposiums, **1**, Paper 84, Cranfield, UK.

Weertman, J. (1966). Rate of growth of fatigue cracks calculated from the theory of infinitesimal disloactions distributed on a plane. *International Journal of Fracture Mechanics* **2**, 460-467.

Westergaard, H.M. (1939). Bearing pressures and cracks. *Journal of Applied Mechanics* **61**, A49-A53.

Wheatley, G., Hu, X.Z. and Estrin, Y. (1999). Effect of a single tensile overload on fatigue crack growth in a 316L steel, *Fatigue and Fracture of Engineering Materials and Structures*, **22**, 1041-1051.

Wheeler, O.E. (1972). Spectrum loading and crack growth. *Basic Engineering*, Transaction of ASME. 181-186.

Willenberg, J., Eagle, R.M. and Wood, H. (1971). *A crack growth retardation model using an effective stress concept.* AFFDL-TM-71-1-BFR, Los Angeles, North America.

Williams, M.L. (1957). On the stress distribution at the base of a stationary crack. *Journal of Applied Mechanics* **24**, 109-114.

Wu, J. and Ellyin F. (1996) A study of fatigue crack closure by elastic-plastic finite element analysis for constant amplitude loading. *International Journal of Fracture* 82, 43-65.

Xu, Y.G. (2000). Variable amplitude loading effects on damage tolerant airframe materials. Mphil/PhD Transfer Thesis, University of Southampton, PG/RA/YX/00/1/285.

Xu, Y.G., Gregson, P.J. and Sinclair, I. (2000). Systematic assessment and validation of compliance based crack closure measurements in fatigue. *Materials Science and Engineering* A **284**, 114-125.

Xu, Y. (2001). Closure assessment and overload transient behaviour in damage tolerant airframe materials. PhD Thesis, School of Engineering Sciences, University of Southampton. Southampton, UK.

Yang, S. and Li, H. (1991). Interaction of overloads on fatigue crack growth for 40CrNi steel. *Fatigue and Fracture of Engineering Materials and Structures*, **14**, 907-913.

Yokobori, T., Sato, K. and Yaguchi, H. (1973). Observations of microcospic plasict zone and slip band zone at the tip of fatigue crack. *Reports of the Research Institute for Strength and Fracture of Materials* **9**, 1-10, Tohoku University, Sendau, Japan.

Zepatero, J., Moreno, B. and Dominguez, J. (1997). On the use of the strip-yeild model to predict fatigue crack growth under irregular loading. *Fatigue and Fracture of Engineering Materials and Structures* **20**, 759-770.

Zhang, J.Z. and Bowen, P. (1998). On the finite element simulation of three-dimensinoal semi-circular fatigue crack growth and closure. *Engineering Fracture Mechanics* **60**, 341-360.

Zhang, J.Z., Halliday, M.D., Bowen, P. and Poole, P. (1999). Three dimensional elastic-plastic finite element modelling of small fatigue crack growth under a single tensile overload. *Engineering Fracture Mechanics* **63**, 3, 229-251.

Zhang, X., Chang, A.S.L. and Davies, G. A. O. (1992). Numerical simulation of fatigue crack growth under complex loading sequences. *Engineering Fracture Mechanics* **42**, 305-321.

Zhang, S., Marissen, R., Schulte, K., Trautmann, K.H. and Schijve, J. (1987). Crack-propagation studies on Al-7475 on the basis of constant amplitude and selective variable amplitude loading histories. *Fatigue and Fracture of Engineering Materials and Structures* **10**, 315-332.

Zhao, L.G., Tong, J. and Byrne, J. (2004). The evolution of the stress-strain fields near a fatigue crack tip and plasticity-induced crack closure revisited. *Fatigue and Fracture of Engineering Materials and Structures* **27**, 19-29.

Appendix A Fracture mechanics concepts

Fatigue crack growth analyses inevitably demand a comprehension of the assumptions, significance and limitations associated with the various crack parameters. Attention here will be particularly focussed on linear elastic and small scale yielding (SSY) conditions.

- *Modes of crack loading*

A crack in a solid can be loaded in three fundamental modes, as illustrated in Figure A.1: normal stresses give rise to the *opening mode,* or mode I loading. Mode I loading causes the crack surfaces to be displaced perpendicular to the plane of the crack. The *sliding mode,* or mode II, results from in-plane shear, causing the crack surfaces to be displaced in the plane of the crack, perpendicular to the leading edge of the crack. The *tearing mode* or mode III, is caused by out-of-plane shear of the crack, parallel to the leading edge of the crack. A general crack loading case may always be considered to be a superposition of the three modes. In keeping with the general literature on fracture and fatigue the present work concentrates on macroscopic mode I loading as the most damaging in common structural applications.

A.1 The Energy balance concept

Griffith [1920] applied the First Law of Thermodynamics to formulate the criteria for unstable crack extension of brittle solids in terms of a balance between changes in surface and mechanical energies. It was postulated that, for the occurrence of unit crack extension under the influence of an applied load, the decrease in potential energy of the system (by virtue of the displacement of the outer boundaries and the change in the stored elastic energy) must at least equal the increase in surface energy due to extension of the crack. Then, for a crack to propagate, the *elastic strain energy release rate*, G, which may be considered as the crack *driving force* (defined as elastic strain energy released per unit crack area) must be at least equal to the energy consumed in crack propagation, R', the *crack resistance*. If R' is a constant, G must

exceed a certain critical value G_{IC}, and hence may be considered a material property. Griffith assumed that R' consisted of surface energy only, however in ductile materials, such as metals, plastic deformation occurs at the crack tip. Irwin [1948] and Orowan [1948] modified the Griffith expression independently to account for materials that are capable of plastic flow by introducing a term to represent the plastic work per unit area to create crack surface. However it is to be noted that the Griffith model is only strictly applicable when the global behaviour of the structure is elastic; extension of the approach to include nonlinear effects, such as plasticity, requires non-linearity to be confined to a region near the crack tip that is 'small' in relation to the elastic stress fields (described as 'small scale yielding condition', discussed further in Section A.3).

A.2 Stress intensity factors

It is possible to derive accurately closed form solutions for the near crack tip fields for certain classes of linear elastic cracked bodies subjected to external forces, e.g. see Westergaard [1939], Sneddon [1946], Irwin [1957] and Williams [1957]. If a polar coordinate system is defined with the crack tip as origin, the near tip stresses may be shown to be expressed by (e.g. Larsson and Carlsson, 1973);

$$\sigma_{ij}(r,\theta) = \frac{K}{\sqrt{2\pi r}} f_{ij}(\theta) + \begin{bmatrix} T & 0 & 0 \\ 0 & 0 & 0 \\ 0 & 0 & \nu T \end{bmatrix} + \text{vanishing terms at crack tip} \qquad \text{(A.1)}$$

where $\sigma_{ij}(r,\theta)$ is the stress tensor at a point, r and θ are the polar coordinates about the crack tip, and f_{ij} is a dimensionless function of θ. K is the *stress intensity factor,* which represents the elastic stress field magnitude, and is a function of the applied stress, crack length, and specimen geometry. In general terms, K is given by;

$$K = \sigma\sqrt{\pi a}\, f(\text{geometry}) \qquad \text{(A.2)}$$

where σ, is the remote applied stress on a body, a is the crack length and f(geometry) is a geometrical factor reflecting the shape of the cracked body and the form of loading. In Equation A.1, the first term is the leading singular term, exhibiting a $1/\sqrt{r}$ singularity. The second term, generally referred to as the 'T-term' or 'T-stress',

containing the non-singular stress T which is independent of r. The 'T-stress ' is a constant stress term acting along the x direction (the crack growth direction) for plane stress conditions, whilst for plane strain conditions it additionally causes a stress νT (in the z-direction), where ν is the relevant material Poisson's ratio [Williams, 1957, Irwin, 1960, Larsson and Carlsson, 1973, Rice, 1974]. Whilst the leading singular term in the Equation A.1 is considered adequate for characterising classical linear elastic fatigue crack growth problems, significant errors can be introduced if the T-term is neglected in certain fatigue situations, such as: 1) short fatigue cracks, 2) cracks subjected to mixed mode loading where in-plane shear stresses are substantially larger than the tensile stresses [Suresh, 1998]. Stresses within the plastic zone and plastic zone shape can be affected significantly by the T-term [Bilby *et al.*, 1986, Betegon and Hancock, 1991].

For linear elastic materials, the three modes of loading may be expressed as a function of separate stress intensity factors, K_I, K_{II} and K_{III}. In the general three-dimensional case involving plane and anti-plane loading, K's and G are related as;

$$G = \frac{1-\nu^2}{E}(K_I^2 + K_{II}^2) + \frac{1+\nu}{E}K_{III}^2 \tag{A.3}$$

whilst for plane stress conditions;

$$G = \frac{(K_I^2 + K_{II}^2)}{E} \tag{A.4}$$

where E is the Young's modulus. From Equation A.3 and A.4 it may then be seen that, for uniaxial loading at least, there is a simple direct relationship between using K_c (critical stress intensity factor) to define fracture resistance and using G_c (critical energy release rate) [Suresh, 1998].

A.3 Small scale yielding condition

The *stress intensity factor*, K defined by Equation A.1, is a measure of the near tip stress fields under linear elastic conditions. In the immediate vicinity of the crack tip there may be considered to exist an annular region where the leading terms of

Equation A.1 are the most significant, known as the K-dominant region, represented by region D in Figure A.2. The outer boundary of the annular zone is determined by the radial distance at which the asymptotic singular solution consisting only the first leading term in Equation A.1 deviates 'significantly' from the full elasticity solutions which include the higher order terms (*viz.* the T-term and the non-singular terms). Due to the singular nature of the elastic stress field, there may then exist an inelastic (plastic) region engulfing the crack tip where microscopic failure processes such as void nucleation, growth, and coalescence may occur. A representative dimension r_p of the inelastic region may be computed for mode I loading under plain stress conditions e.g. using the approximate expression[1] of Irwin [1960];

$$r_p = \frac{1}{\pi}\left(\frac{K_I}{\sigma_y}\right)^2 \tag{A.5}$$

where σ_y is the yield stress. Linear elastic expressions are invalid within region r_p. It is thus not possible to characterise the fracture process directly via a linear elastic formulation. However when r_p is small compared to D, and any other geometrical dimension, linear elastic conditions (and, in particular, K values) may be considered to *control* behaviour in region r_p. Such a situation is referred to as *small scale yielding*. When the small scale yielding condition exists, *linear elastic fracture mechanics* (LEFM) may be used to analyse the behaviour of cracks in ductile solids.

A.4 The Plastic zone

- *Monotonic loading*

Irwin [1960] indicated that the plastic zone, r_p ahead of a crack tip, is proportional to the square of the stress intensity factors and for Mode I loading under plane stress conditions r_p may be given by Equation A.5, whilst for the plane strain;

$$r_p = \frac{1}{3\pi}\left(\frac{K_I}{\sigma_y}\right)^2 \tag{A.6}$$

[1] r_p, is in fact based on a second order estimate of plastic zone size, as discussed further in Section A.4

where r_p is the diameter of the plain strain plastic zone (assumed circular). Other simple approaches to find the extent of the plastic zone at a crack tip are provided by Dugdale [1960] and Barenblatt [1962]. In the Dugdale model, the plastic zone is envisioned as narrow strip of yielded material of negligible height extending a distance of r_p ahead of the crack tip, loaded by the traction $\sigma_{yy} = \sigma_y$ over the length r_p. The estimated extent of plastic zone based on the balance of stresses about the crack tip is then given by;

$$r_p = \frac{\pi}{8}\left(\frac{K_I}{\sigma_y}\right)^2 \tag{A.7}$$

The analysis of continuous distributions of dislocations (adopted by Bilby *et al.*, [1963] and Bilby and Swinden [1965]), yields similar results. More detailed solutions for crack tip plasticity are provided by Hutchinson [1968] and Rice and Rosengren [1968] (see Section A.6.1), and numerous experimental [e.g. Bateman *et al.*, 1964, Underwood and Kendall, 1969, Hahn and Rosenfield, 1965, Hahn *et al.*, 1972] and finite element analyses exist [e.g. Swedlow *et al.*, 1965, Levy *et al.*, 1971, Mishra and Parinda, 1985, McClung and Sehitoglu, 1989a, Dodds *et al.*, 1991, Pommier, 2002]. Using x-ray diffraction studies on fatigue crack plastic zones developed under plane strain conditions, Dias *et al.*, [1999] suggested that the coefficient of $(K_{max}/\sigma_y)^2$ in the calculation of maximum monotonic plastic zone size, increases as the yield strength of the material increases, in the pattern $0.196[\sigma_y/(129+0.928\sigma_y)]^2$ instead of a fixed function of π. However, it may be noted that it is difficult to compare with experimental results as elastic and plastic strains cannot easily be distinguished and measurements are usually confined to specimen surfaces.

- *Cyclic loading*

When an elastic-plastic crack under small scale yielding conditions is unloaded from a far field tensile load, there exists within the monotonic plastic zone a region of reversed flow, also known as the *cyclic plastic zone,* in which compressive yielding occurs (due to the constraint of the surrounding elastic material). The existence of such a cyclic plastic zone ahead of a fatigue crack has long been recognised [Paris,

1960, McClintock, 1963, Rice, 1967]. In the absence of closure of the crack faces ('crack closure' is discussed in Section 2.3), a simple superposition principle may be used to estimate the extent of the cyclic plastic zone [Rice, 1967]. When a cracked elastic-perfectly plastic solid, is unloaded from K_{Imax} by ΔK_I (where K_{Imax} is the maximum mode I stress intensity and ΔK_I the cyclic stress intensity range), the stress within the cyclic plastic zone should be equal to the flow stress in compression, $-\sigma_y$. The size of r_c is then given by;

$$r_c = \frac{1}{3\pi}\left(\frac{\Delta K_I}{2\sigma_y}\right)^2 \qquad \text{for plane strain} \qquad \text{(A.8)}$$

$$r_c = \frac{1}{\pi}\left(\frac{\Delta K_I}{2\sigma_y}\right)^2 \qquad \text{for plane stress} \qquad \text{(A.9)}$$

on the premise that going into reversed flow from the peak applied load is equivalent to causing yielding in a material of double the yield stress (the near tip material goes from $+\sigma_y$ to $-\sigma_y$ on unloading). For zero-tension-zero loading, $\Delta K = K_{Imax}$ and $r_c = r_p/4$. For materials which harden or soften cyclically, σ_y may be replaced by the cyclic yield strength σ'_y. These simple calculations of cyclic plastic zone size have the following general assumptions and limitations:

1. although both monotonic and cyclic plastic zone sizes are estimated to be lesser for plane strain as compared to plane stress, by a factor of about 3, the r_p/r_c ratio is considered to remain unaffected with state of stress,
2. plastic zone size is measured along the crack line, although the shape of plastic zone (further discussion follows) is a complex one which will depend on the stress state and geometry

When strain hardening takes place less stress redistribution is expected, resulting in smaller plastic zone size. To take care of the strain hardening effect, a multiplicative correction factor of $(n - 1)/(n + 1)$ has been suggested, where n is the strain hardening exponent (see Section A.6.1) [Shih, 1976], resulting in $r_c = [(n-1)/(n+1)]r_p/4$ [McClung, 1991].

For a plane stress analysis reported by Budiansky and Hutchinson [1978] the reversed plastic zone for an extending fatigue crack was identified as less than 10% of the Dugdale monotonic plastic zone size, a result attributable to the incidence of crack flank closure during unloading, as considered in further detail in Section 2.3. Based on finite element simulation under plane stress conditions McClung [1991a] and McClung and Sehitoglu [1989] reported that for stationary cracks (which do not experience crack closure) $r_c = r_p/5$, which is slightly less than the Rice's estimate of one-fourth the size of forward plastic zone. However for fatigue cracks (considering crack closure) they found r_c no greater than $r_p/6.6$ and approaching $r_p/10$ at lower stress levels (for load ratio, $R = K_{min}/K_{max} = 0$, where K_{min} and K_{max} are the minimum and maximum stress intensity factors in any load cycle). They reasoned that the decrease is due to crack closure which impedes the reversed plastic flow when the crack tip closes and effectively eliminates the crack tip singularity. Solanki *et al.*, [2003a] reported plane strain FE analyses and found that $r_c = r_p/10$ (for $R = 0$), suggesting that stress state conditions apparently do not affect r_c/r_p. Various experimental values of r_c/r_p have been reported, *viz.* 0.20-0.25 [Hahn *et al.*, 1972 (using an etching technique), Bathias and Pelloux, 1974, Pineau and Pelloux, 1974, Loye *et al.*, 1983 (using microhardness measurements), Nicoletto, 1987, 1989 (using optical techniques)] and 0.09-0.13 [Davidson and Lankford, 1976 (using selected area electron channelling patterns), Yokobori *et al.*, 1973 (using an X-ray microbeam technique)] for $R = 0.0$. In the first instance, such variations are consistent with possible crack closure influences, particularly with the various value being $\leq \sim 0.2$ In terms of large scale yielding Zhang *et al.*, [2001] found (based on 3D FE modelling) that there is a trend of decreasing r_c/r_p values with decreasing crack length, however this is beyond the scope of the present projects interests.

- *Plastic zone shape*

The shape of a crack tip plastic zone may be roughly assessed via a study of elastic crack tip stresses for varying angles around the crack tip using yield criteria such as Tresca and Von Mises. The extent of the plastic zone as a function of θ may be estimated using the Von Mises criterion as [Broek, 1999];

$$r_p(\theta) = \frac{K^2}{4\pi\sigma_y^2}\left[\frac{3}{2}\sin^2\theta\ (1-2\nu)^2(1+\cos\theta)\right] \qquad \text{for plane strain} \qquad \text{(A.10)}$$

$$r_p(\theta) = \frac{K^2}{4\pi\sigma_y^2}\left[1+\frac{3}{2}\sin^2\theta+\cos\theta\right] \qquad \text{for plane stress} \qquad \text{(A.11)}$$

Similar analyses may also be made for modes II and III cracks. Figure A.3 shows the boundary of the mode I plastic zone predicted by Von Mises and Tresca for both plane stress and plain strain conditions. A key point is the particular "dual-lobe" form of the mode I plane strain condition, where the maximum extent of plasticity actually occurs at an angle to the plane of maximum tensile loading ahead of the crack tip. More accurate elastic-plastic power law analyses are discussed in Section A.6.1, with Rice and Rosengren [1968] for example finding that whilst the plastic zone size is to some extent affected by strain hardening rate, the farthest boundary of the zone always occurs at $\theta \cong 100°$ for plane strain conditions (θ being measured from the plane of the crack). Shih [1974] further computed the contours of plastic zones for mixed mode cracks subjected to small scale deformation with power-law plasticity: the plastic zone contours for different strain hardening exponents for both mode I and mode II under plain stress and plane strain conditions are illustrated in Figure A.4. Similar shapes of plastic zone were obtained through experimental [e.g. Hahn and Rosenfield, 1965] and finite element methods [e.g. Anderson, 1995, McClung, 1991]. The effect of cyclic hardening on plastic zone shape was studied by Pommier [2002] using finite element analysis on a plane strain stationary fatigue crack, and that found when the amount of hardening is increased for a given yield stress and rate of hardening, the zone containing high residual compressive stress is rotated about the crack tip from the front to the wake of the crack tip, but the size stays approximately unchanged. This effect is explained by a redistribution of yielding from previously deformed and work hardened material to softer, undeformed material.

As noted previously the state of stress has an effect on the plastic zone. For a loaded plate free of surface traction ($\sigma_{zz} = 0$), even if the plane strain state exists in the

interior of the plate, plane stress conditions will exist at the surfaces, with the stress σ_{zz} gradually increasing from zero at the surface, to the plane strain value in the interior [Dixon, 1965]. As a result, a decrease of plastic zone size is observed from the plane stress size at the surface to the plane strain size in the interior of the plate. The ratio of plastic zone size to thickness of the plate is an important factor for the state of stress. Plane stress conditions may be expected to develop through the thickness of a plate if the size of the zone is of the order of the plate thickness i.e. if r_p/B approaches unity, where B is the plate thickness. For plane strain to be dominant, the ratio must be appreciably less than unity [Broek, 1999].

A.5 Crack tip opening displacement

Wells [1961] first proposed the opening at the crack tip as a measure of fracture toughness after observation of the movement of crack faces prior to fracture. Since then, *crack tip opening displacement* (CTOD), has been used to provide a measure of the blunting at an initially sharp crack where plastic deformation is significant. The CTOD provides a physical length scale for deformation at the very tip of a crack, which may then be convenient to characterise near-tip crack behaviour.

Following Irwin's analysis [1961], CTOD can be expressed for plane stress as;

$$\delta = \frac{4}{\pi}\frac{K_I^2}{\sigma_y E} \tag{A.12}$$

where δ is the CTOD .

A similar expression can be derived from a strip yield model [Burdekin and Stone, 1966] giving;

$$\delta = \frac{K_I^2}{\sigma_y E} \tag{A.13}$$

Various expressions for plane strain CTOD have been reported through experimental, analytical and numerical studies (e.g. McMeeking, 1977). In general, plane strain CTOD can be expressed as;

$$\delta = m' \frac{K_I^2}{\sigma_y E} \tag{A.14}$$

where m' is a dimensionless constant that is approximately equal to 0.5 [Rice, 1973].

For cyclic variation in the stress intensity factor, ΔK_I (i.e. ΔK (= K_{max}-K_{min}) for mode I), Rice's reverse plasticity approach (see Section A.4) can be used to express cyclic CTOD as;

$$\Delta\delta \approx \frac{\Delta K_I^2}{2\sigma_y E} \qquad \text{for plane stress} \tag{A.15}$$

$$\Delta\delta \approx 0.5\frac{\Delta K_I^2}{2\sigma_y E} \qquad \text{for plane strain} \tag{A.16}$$

i.e. giving values that are one half of the displacements associated with monotonic loading.

A.6 The J integral and elastic-plastic fracture mechanics

The energy release rate G cannot be determined from the elastic stress fields if there is appreciable plasticity at the crack tip, since G may be effected by the crack tip plastic zone [Forman, 1965]. When, plasticity effects are non-negligible, the J -integral provides a means for determining energy release rate with certain limitation. Rice [1968a, 1968b] was apparently the first to recognise the potential use of this energy integral in fracture mechanics, although Eshelby [1956] was the first to derive the integral. Some of the features of this integral were also discussed independently by Sanders [1960] and Cherpanov [1967, 1969]. The basic relationship of the J -integral is;

$$J = \int_{\Gamma}\left(w dy - T_i \frac{\partial u_i}{\partial x} ds \right) \tag{A.17}$$

Where Γ is a curve surrounding the crack tip, T_i the components of the traction vector, u_i is the displacement vector components, and ds is a length increment along the contour Γ; w is the strain energy density defined as;

$$w = \int_0^{\varepsilon_{ij}} \sigma_{ij} d\varepsilon_{ij} \tag{A.18}$$

where σ_{ij} and ε_{ij} are the stress and strain tensors, respectively. J may be shown to be path-independent for materials showing linear or nonlinear elastic behaviour. J gives the rate of change of potential energy with respect to crack advance for a nonlinear elastic solid, and reduces to the energy release rate G for the linear elastic case; J cannot strictly be used to described elastic-plastic behaviour, particularly for unloading cases as, in the first instance plasticity is not equivalent to non-linear elasticity.

A.6.1 Hutchinson-Rice-Rosengran (HRR) fields

The monotonic stress-strain behaviour of ductile solids under uniaxial tension can be generally represented by the Ramberg-Osgood relationship;

$$\varepsilon = \frac{\sigma}{E} + \left(\frac{\sigma}{A}\right)^n \tag{A.19}$$

where, A is a constant called the monotonic strength coefficient, ε is the uniaxial strain, and n is the strain hardening exponent. Equation A.19 can be approximated near the crack tip (as elastic strains become negligible) by the pure power law;

$$\frac{\varepsilon}{\varepsilon_y} = \upsilon\left(\frac{\sigma}{\sigma_o}\right)^n \tag{A.20}$$

where σ_o is a reference stress value that is usually equal to yield strength, $\varepsilon_y = \sigma_y / E$. υ is a dimensionless constant, and n is the strain hardening exponent. Hutchinson [1968] and Rice and Rosengren (1968c) showed that for nonlinear elastic solids undergoing monotonic, small strain deformation, the strength of the near-tip fields scale with the J-integral, with the stresses, strains and displacements exhibiting $r^{-1/(n+1)}$, $r^{-n/(n+1)}$ and $r^{1/(n+1)}$ singularities respectively. Their relationships may be written as;

$$\sigma_{ij} = \sigma\left(\frac{J}{\alpha\sigma_y\varepsilon_y I_n r}\right)^{1/(n+1)} \tilde{\sigma}_{ij}(\theta, n) \tag{A.21}$$

$$\varepsilon_{ij} = \alpha\varepsilon_y\left(\frac{J}{\alpha\sigma_y\varepsilon_y I_n r}\right)^{n/(n+1)} \tilde{\varepsilon}_{ij}(\theta, n) \tag{A.22}$$

$$u_{ij} = \alpha\varepsilon_y\left(\frac{J}{\alpha\sigma_y\varepsilon_y I_n}\right)^{1/(n+1)} r^{n/(n+1)}\tilde{u}_i(\theta, n) \tag{A.23}$$

where $\tilde{\sigma}_{ij}(\theta, n)$, $\tilde{\varepsilon}_{ij}(\theta, n)$, and $\tilde{u}_i(\theta, n)$ are universal functions that vary with the polar angle θ, the strain hardening exponent n and the state of stress. The integration factor I_n depends mildly on the strain hardening exponent n. The fields represented by the Equations A.21, A.22 and A.23 are generally known as 'HRR fields'.

A.6.2 Regions of K and J dominance

Figure A.5(a) shows schematically the condition of small scale yielding in fracture mechanics, where J and K may be used to characterise the crack tip conditions. At a short distance from the crack tip, relative to the characteristic length, L, which corresponds to the size of the structure, the stress is proportional to $1/\sqrt{r}$. This zone is called the K-dominated region. Well inside the plastic zone, where the elastic singularity no longer applies, a J dominated region occurs in which the HRR solution is approximately applicable and stresses vary as $r^{1/n+1}$. Finite strain effects are found to be significant over a distance $\leq$3CTOD from the crack tip (based on finite element and flow theory model calculations of the crack-tip fields) [McMeeking, 1977 and McMeeking and Parks, 1979] and in this zone, the HRR solutions lose validity. In small scale yielding, K may be used to uniquely characterise crack tip conditions, although the $1/\sqrt{r}$ singularity does not exist all the way to the crack tip. Also, J may be considered to uniquely characterise crack tip conditions, even though the deformation plasticity and small strain assumptions are not valid within the finite strain zone. The elastic-plastic fracture condition is illustrated in Figure A.5 (b), where J is still approximately valid, but there is no longer a significant K field. Here,

the plastic zone is increased in size, relative to L, leading to the disappearance of the K dominated zone, but in some geometries a J dominated zone may be considered to persist. Figure A.5 (c) illustrates large scale yielding where the plastic zone size becomes significant relative to L and there is no longer a region reasonably characterised by J. For such cases, plastic zones may fully engulf the uncrack ligament of the body in question and the scale of J dominance is as small as 1 % of the uncracked ligament length for a center-cracked tension specimen, or 7 % of the length of the uncracked ligament for a deeply cracked bend bar or a compact tension specimen [McMeeking and Parks, 1979].

A.6.3 Mixed mode fracture aspects

For pure elastic conditions, and considering only mode I and mode II loading in the first instance the near-tip stress components for a crack remotely subjected to tensile opening and sliding stress intensity factors may be shown to be given by;

$$\sigma_{ij} = \frac{1}{\sqrt{2\pi r}}\left(K_I f_{ij}^{I}(\theta) + K_{II} f_{ij}^{II}(\theta)\right) \tag{A.24}$$

where $f_{ij}^{I}(\theta)$ and $f_{ij}^{II}(\theta)$ are simple trigonometric functions (see Suresh, 1998).

Mixed mode near tip fields in an elastic-plastic solid based on the HRR-type approach may be given by [Shih, 1974];

$$\sigma_{ij} = \sigma_y K_M^P r^{-1/(n+1)} \tilde{\sigma}_{ij}(\theta, M^P, n) \tag{A.25}$$

$$\varepsilon_{ij}^{p} = \frac{\alpha\sigma_Y}{E}(K_M^P)^n r^{-n/(n+1)} \tilde{\varepsilon}_{ij}^{p}(\theta, M^P, n) \tag{A.26}$$

where the dimensional functions $\tilde{\sigma}_{ij}$, $\tilde{\varepsilon}_{ij}$ depend only on the polar angle θ, the mixed mode plastic stress intensity factor K_M^P and the near-tip plastic mixity parameter, M^P, which is given by;

$$M^P = \frac{2}{\pi}\tan^{-1}\left\{\lim_{n\to 0}\frac{\sigma_{\theta\theta}(r,\theta=0)}{\sigma_{r\theta}(r,\theta=0)}\right\} \tag{A.27}$$

$$= \frac{2}{\pi} \tan^{-1} \left\{ \frac{\tilde{\sigma}_{\theta\theta}(\theta = 0, M^P)}{\tilde{\sigma}_{r\theta}(\theta = 0, M^P)} \right\} \tag{A.28}$$

M^P is equal to 0 for pure mode II, 1 for pure mode 1, and $0 < M^P < 1$ for different mixity levels. K_M^P can be related to the J integral via M^P as;

$$J = \frac{(1-\nu^2)}{E}(K_I^2 + K_{II}^2) = \frac{\alpha \sigma_y^2}{E} I_n(M^P)(K_M^P)^{n+1} \tag{A.29}$$

where $I_n(M^P)$ is a numerical constant which is a function of strain hardening exponent n and the plastic mixity factor M^P. Thus the parameters, K_M^P and M^P completely specify the near tip fields for a given value of n; Shih [1974] preformed finite element analysis of mixed mode loading under small scale yielding conditions and computed the relationship between M^e ($= 2/\pi \tan^{-1} |K_I / K_{II}|$) and M^P for values of $n = 1 - 99$, finding that, for $n = 1$, $M^e = M^P$, and $M^P > M^e$ for $n > 1$.

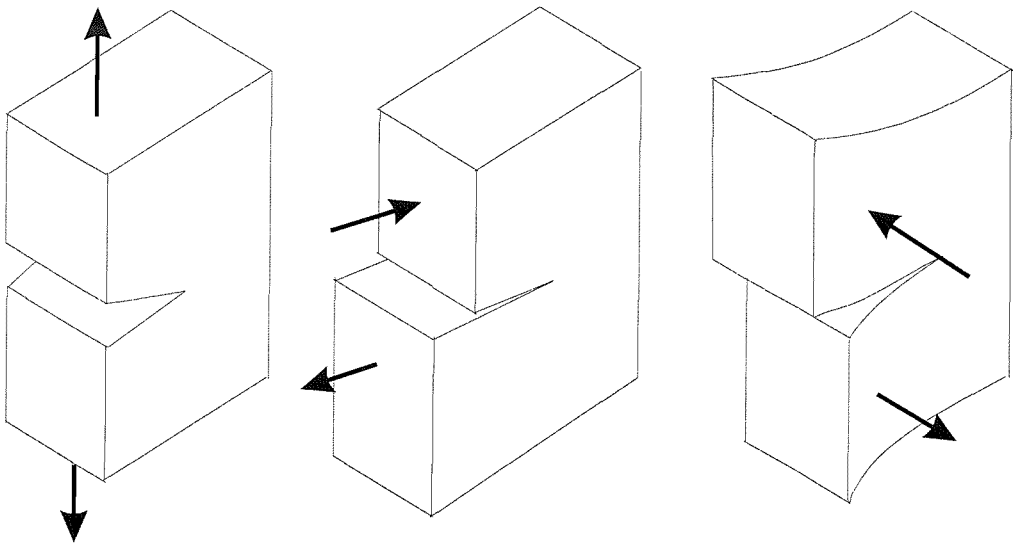

Figure A.1: The three fundamental modes of fracture.

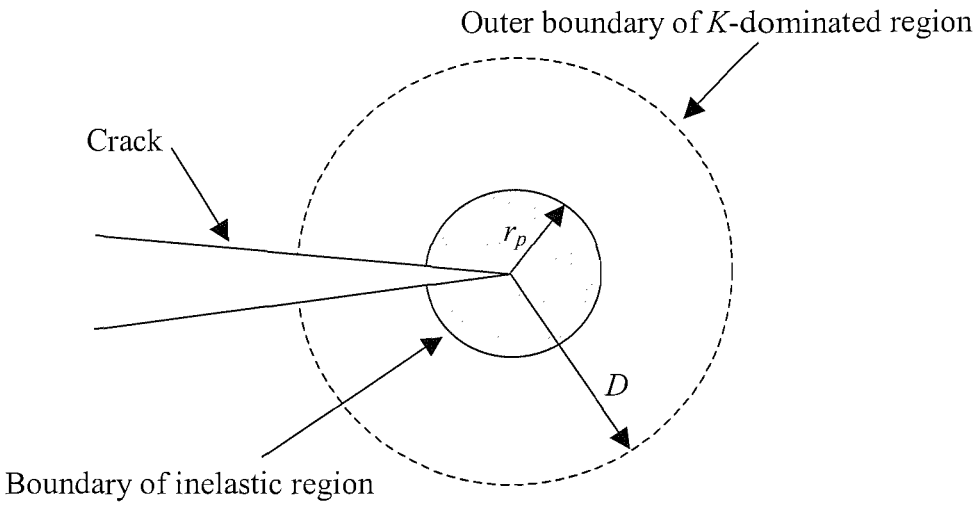

Figure A.2: Schematic representation of the basis of linear elastic fracture mechanics and small scale yielding conditions.

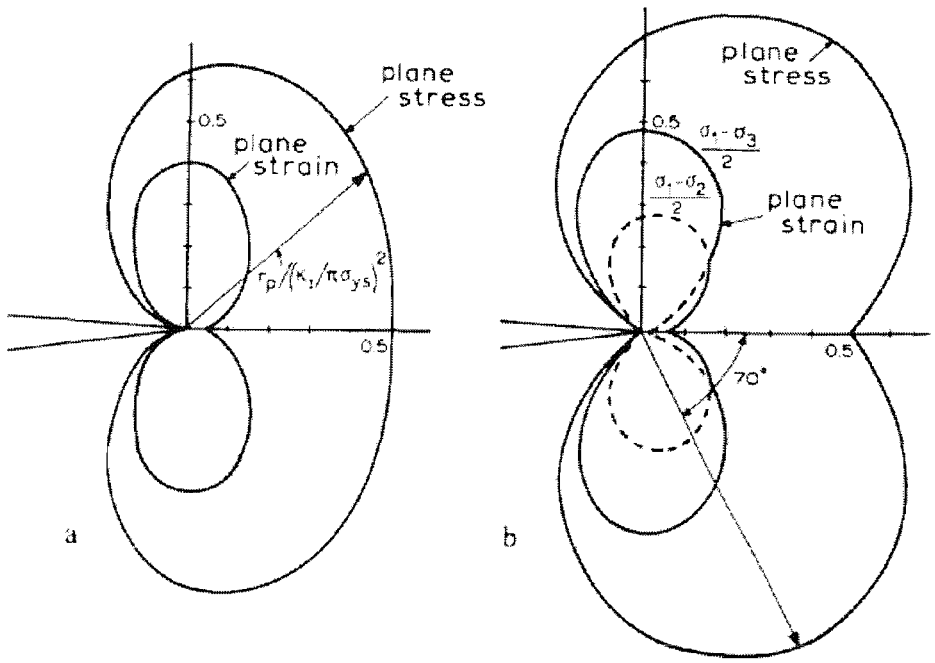

Figure A.3: Shapes of plastic zone derived from elastic crack tip fields according to Von Mises and Tresca yield criteria, a) Von Mises; b) Tresca criterion [Broek, 1999].

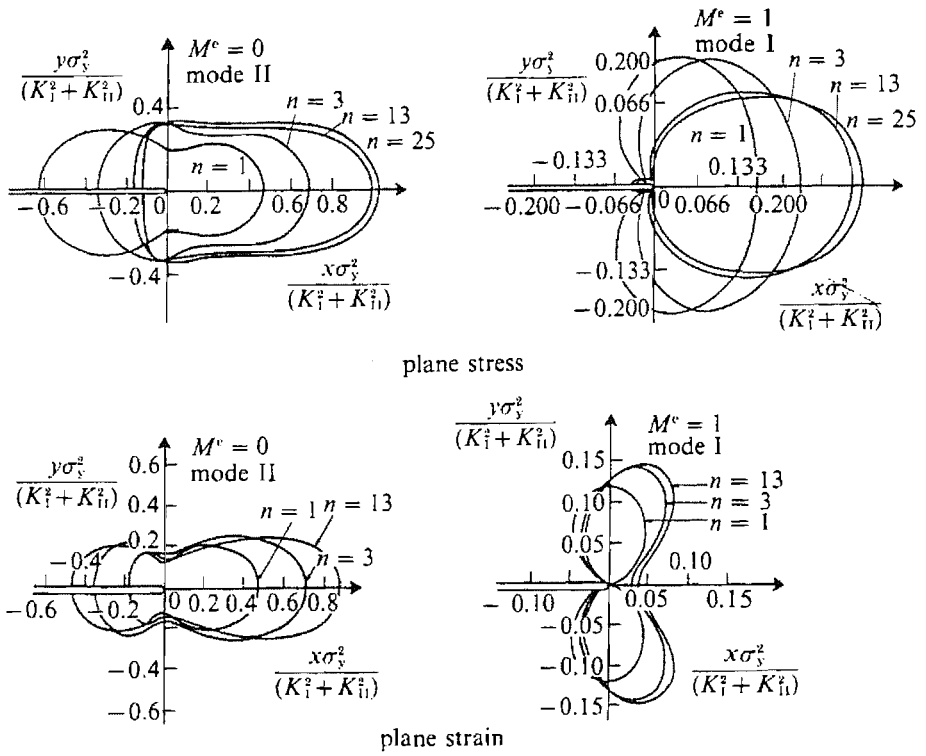

Figure A.4: Plastic zone contours for different strain hardening exponent (n) values for mode I and mode II cracks subjected to plane strain and plane stress conditions [Shih, 1974].

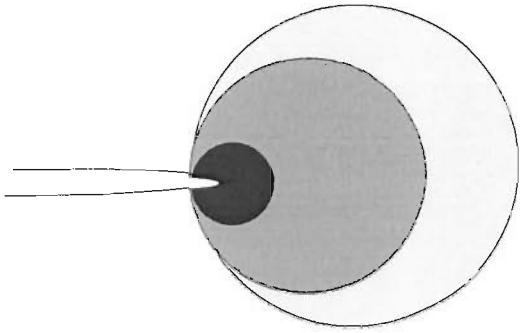

(a) Small scale yielding

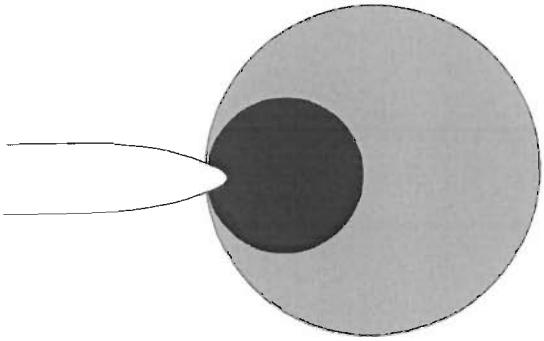

(b) Elastic-plastic condition

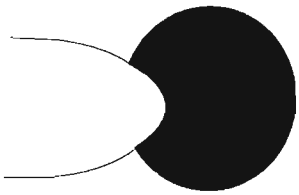

(c) Large scale yielding

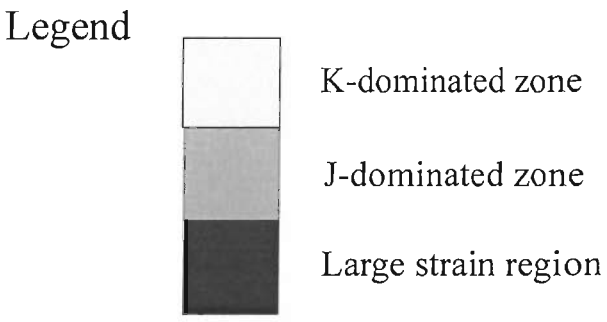

Figure A.5: Schematic illustration of effects of plasticity on crack tip fields: (a) small scale yielding, (b) elastic-plastic condition, and (c) large scale yielding [after Anderson, 1995].

Appendix B Input preparation of the FE model

Following the work of Parry [2000], further FE modelling for undeflected and deflected fatigue cracks under constant and variable amplitude loading histories have been studied. The present FE models are essentially similar to that of Parry's work. Chapter 3 discusses most of the key model designs and their implementation. Some additional modelling details are highlighted in this Appendix.

B.1 Loads and boundary conditions

Although loads are usually applied on both top and bottom edges of CCP specimen in experiments, in the present simulated FE models loads are applied on top face and boundary conditions (rollers or hinges depending on the degrees of freedom to be constrained) are applied on the bottom face. Figure B.1a and B.1b shows schematically the geometry and simulated loading pattern. As the present studies are performed in terms of stress intensity factor range (ΔK), ΔK's are converted into equivalent total load (P) to be applied on the top face as follows (after Anderson 1995):

$$P = \frac{K_I B\sqrt{W'}}{f\left(a/W'\right)} \tag{B.1}$$

where

$$f\left(a/W'\right) = \sqrt{\frac{\pi a}{4W'}\sec\frac{\pi a}{2W'}}\left[1 - 0.025\left(\frac{a}{W'}\right)^2 + 0.06\left(\frac{a}{W'}\right)^4\right] \tag{B.2}$$

For example, for K_{Imax} = 4.6 MPa $m^{1/2}$ and a ~ 7.99 mm (corresponding to ΔK = 4.6 MPa $m^{1/2}$ and R = 0.0), P = 15878.3 N to be applied over a face of length $2W'$ and width B. P is then lumped on the nodes depending on the area of the elements on the top face. For instance, if the top face consists of n'' (say 8) elements of equal size, then each element would be loaded with P/n'' (= 1984.79 N). Half of the load (i.e. $P/(n''/2)$ = 992.393 N) on each elements on either side of a node is added up and lumped on the load to form nodal forces. Hence the edge nodes are loaded with $P/(n''/2)$. It may be noted that it is possible to apply distributed load (and hence as stress,

σ) using DLOAD option in ABAQUS, however not significant differences are expected between the two approaches as equal size Q4 elements are used and loads (uniform) are applied remotely not to affect the near-tip region.

B.2 Material properties

In the FE models, 1 mesh unit was taken to be 1 μm, hence the coordinates and material parameters (σ_o = 370 MPa, E = 74GPa and $H = 0.07E$) were expressed in terms of mesh units. Hence for the elastic part, E = 2.664 N/ (mesh unit)^2. For the plastic part two sets of points (corresponding to yield stress and plastic strain) are chosen at a convenient spacing (= 0.01) of plastic strain (with the first plastic strain taken as zero) to define the linear stress-plastic strain behaviour. Hence, for the first point, yield stress = 0.01332 N/(mesh unit)^2 and plastic strain = 0; for the second point yield stress = 0.0151848 N/(mesh unit)^2 and plastic strain = 0.01.

B.3 Element properties

In order to realise the FE models several types of elements have been used. To model the solid part of the specimen isoparametric Q4 elements with selective reduced integration method to model plasticity were used as discussed in Section 3.3. To model plane strain and plane stress conditions CPE4 (4-node bilinear plane strain quadrilateral) and CPS4 (4-node bilinear plane strain quadrilateral) elements in ABAQUS were used.

To affect the changing boundary conditions during crack propagation and crack face contact, line spring elements were used. In the undeflected crack modelling SPRING1 elements were used, whereas SPRING2 and SPRINGA elements were used for deflected cracks. Spring elements are allowed to act as tension and compression spring elements by forcing to respond only on tensile and compressive forces respectively as discussed in Section 3.4.

a) SPRING1 element

SPRING1 element connects between a node and a ground (Figure B.2a), acting in a fixed direction, thus the line of action is along the line joining node and the ground point. In undeflected crack models, only one quarter of the specimen was modelled and hence the springs have each one node to be connected to the Q4 nodes whilst the other nodes need to be connected to the support boundary conditions (~ ground).

The relative displacement induced in a SPRING1 element is the i^{th} component of displacement of the spring's node:

$$\Delta u = u_i \tag{B.3}$$

Nonlinear spring behaviour is achieved by including the NONLINEAR parameter on the *SPRING option and providing pairs of force-relative displacement values. In the present case, as the springs are assumed to be linear, by providing two pairs of force-relative displacement values, the NONLINEAR parameter yields in a linear behaviour.

b) SPRING2 element

SPRING2 element connects between two nodes (Figure B.2b), acting in a fixed direction, acting in a fixed direction, the line of action being along the line joining the two nodes. The relative displacement induced in SPRING2 element is given by the difference between the i^{th} compoment of displacement of the spring's first node and the j^{th} component of displacement of the second node of the spring:

$$\Delta u = u_i^1 - u_j^2 \tag{B.3}$$

c) SPRINGA element

SPRINGA element connects between two nodes (Figure B.2c), acting in a fixed direction, acting in a fixed direction, the line of action being along the line joining the two nodes. The line of action may be allowed to rotate in large-displacement analysis. When geometrically nonlinear analysis is considered, the relative displacement

induced in SPRINGA element is the chance in length in the spring between the initial and the current configuration:

$$\Delta u = u - u_o \tag{B.4}$$

where

$$l = \sqrt{\left(X^1 - X^2\right)\left(X^1 - X^2\right)} \tag{B.5}$$

is the current length of the spring and l_o is the value of the l in the initial configuration and X^1 and X^2 are the current positions of the nodes of the spring. Although this allows large strains to be developed but one must be cautious so as not to influence the accuracy of the results. The ability of the SPRINGA element to rotate its line of action helps in modelling of the predefined deflected cracks, where the springs are connected perpendicular to the inclined crack surfaces.

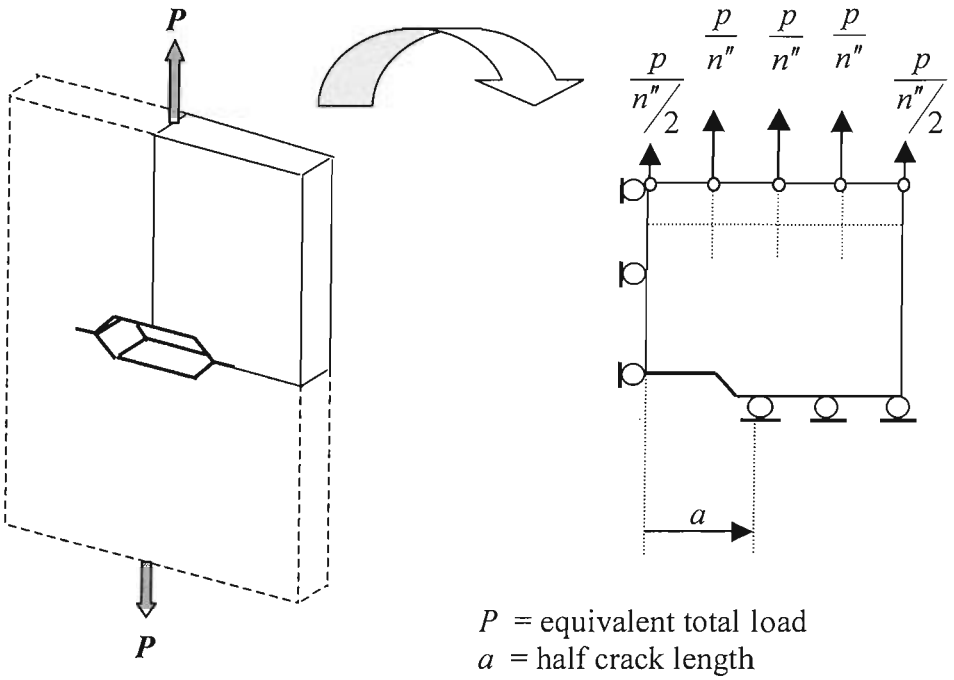

Figure B.1: Schematic diagram showing application of loads a) full CCP specimen with equivalent total load (P) applied on top and bottom and b) quarter CCP specimen with nodal loads applied. Not to scale.

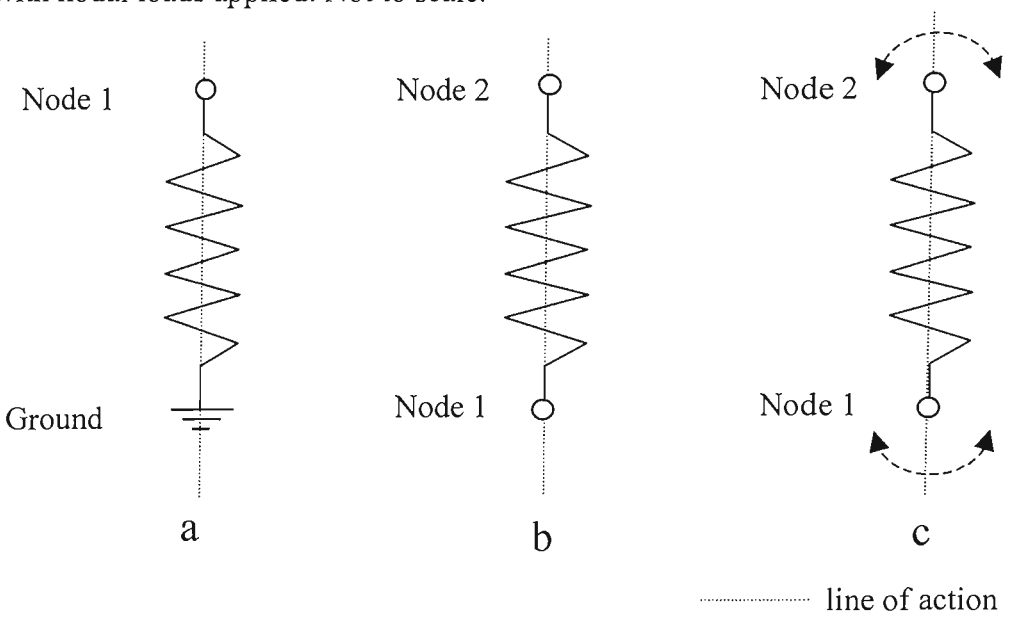

Figure B.2. Schematic diagram showing a) SPRING1 (fixed line of action), b) SPRING2 (fixed line of action), and c) SPRINGA (line of action allowed to rotate) (after ABAQUS, 1998).

B.4 Typical ABAQUS (version 5.8) input files (annotated)

1. Main file

```
*HEADING, SPARSE                                        (Print a heading (title) on the output)
CCP, Del K = 4.6Mpa m^1/2, R = 0, Plane strain          (Title)
*PREPRINT,CONTACT=NO,ECHO=NO,HISTORY=NO,MODEL=NO        (Suppress large volume of output)
*INCLUDE, INPUT=nod.inp                                 (Include node file)
*INCLUDE, INPUT=elm.inp                                 (Include element file)
*INCLUDE, INPUT=ten.inp                                 (Include tension spring file)
*INCLUDE, INPUT=com.inp                                 (Include compression spring file)
*INCLUDE, INPUT=mat.inp                                 (Include material property file)
*INCLUDE, INPUT=bcs.inp                                 (Include boundary conditions file)
*INCLUDE, INPUT=out.inp                                 (Include output file)
*INCLUDE, INPUT=hst.inp                                 (Include load history file)
```

1.1 nod.inp (node input file[1])

```
*NODE                                                   (specifying nodal coordinates)
       1,         -1250.,        20833.3
       2,          312.5,        20833.3
       :
       :
    5921,        251.719,             0.
```

1.2 elm.inp (element input file)

```
*ELEMENT, TYPE=CPE4 , ELSET=CONTINUA                    (specifying elements and their connectivity)
       1,        4,       14,       15,        5
       2,        3,       13,       14,        4
       :
```

[1] Length dimensions in mesh unit (1 mesh unit = 6μm)

```
      :
    5570,     4933,     5921,     2228,     4932
```

1.3 ten.inp (tension spring input file)

```
*SPRING,ELSET=TENS1,NONLINEAR                    (specifying spring element behaviour)
 2,2                                             (dof associated with 1st and 2nd node of spring element)
 0,0                                             (force, relative displacement)
 266.4E5,1000                                    (force, relative displacement)
*ELEMENT, TYPE=SPRING1, ELSET=TENS1              (specifying spring elements and their connectivity)
    6092,     5452
    6093,     5453
       :
       :
    6561,     5921
```

1.4 com.inp (compression spring input file)

```
*SPRING,ELSET=COMP1,NONLINEAR                    (specifying spring element behaviour)
 2,2                                             (dof[2] associated with 1st and 2nd node of spring element)
-266.4E5,-1000                                   (force, relative displacement)
 0,0                                             (force, relative displacement)
*ELEMENT, TYPE=SPRING1, ELSET=COMP1              (specifying spring elements and their connectivity)
    5571,      155
    5572,      367
       :
       :
    6091,     5921
```

1.5 mat.inp (material definition input file)

```
*MATERIAL, NAME=AL2024                           (specifying material name)
*ELASTIC                                         (specifying elastic material properties)
2.664,0.33                                       (Young's modulus, Poisson's ratio)
```

[2] degrees of freedom

```
*PLASTIC,HARDENING=KINEMATIC                          (specifying a plasticity model)
0.01332,0                                             (yield stress, plastic strain)
0.0151848,0.01                                        (yield stress, plastic strain)
*SOLID SECTION, ELSET=CONTINUA, MATERIAL=AL2024       (specifying element properties for solid)
 1250                                                 (element thickness)
```

1.6 bcs.inp (boundary definition input file)

```
*NSET, NSET=SIDE                                      (assigning nodes to node sets)
       1,   6,  11,  16,  21,  26,  31,  36,
       :
       :
       41, 46,  51,  56, 101, 104,  107, 206
*NSET, NSET=BOTTOM
     132, 133, 134,  35, 136, 137,  138, 139,
       :
       :
    4967, 4970, 4973
*BOUNDARY                                             (specifying boundary conditions on node sets)
 BOTTOM,2                                             (fixed along y-axis)
 SIDE,1                                               (fixed along x-axis)
```

1.7 out.inp (output request input file)

```
*NSET,NSET=CRACK,UNSORTED                             (assigning nodes to node sets for output at nodes)
155,  611,  849,  435,  870 . .
*NSET,NSET=CRACK,GENERATE
5452,5921,1
:
:
```

1.8 hst.inp (loading history input file)

```
*NSET,NSET=LOADFULL,GENERATE
       2,       4,       1
*NSET,NSET=LOADHALF
```

```
      1,        5
**========== Loading Step ==========
*STEP,INC=1000,NLGEOM                    (begin a load step, max no. of increments, geometric nonlinearity)
*STATIC                                  (begin static load step)
 0.1, 1, 0.0001, 1                       (initial increment, time period of step, min and max increments)
*OUTPUT,HISTORY,FREQUENCY=0              (suppress output to odb (output database) file)
*CLOAD                                   (specify concentrated loads at nodes)
 LOADFULL,2,   1984.79                   (node set, dof, load magnitude)
 LOADHALF,2,   992.394
*EL FILE,FREQUENCY=1                     (output element results to .fil file every increment)
S,E,PE                                   (stresses, strains, plastic strains)
*EL PRINT,FREQUENCY=0                    (output element results to .dat file)
*NODE FILE,FREQUENCY=0                   (output node results to .fil file)
*NODE PRINT,FREQUENCY=100                (output node results to .dat file at 100th or max (higher)increment)
U                                        (displacement)
*END STEP                                (end a load step)
**========== Debonding Step ==========
*STEP,INC=1000,NLGEOM
*STATIC
 0.33, 1, 0.0001, 0.4
*MODEL CHANGE,REMOVE                     (changing model by removing tension spring elements)
 6092                                    (tension spring element to be removed to propagate crack)
*EL FILE,FREQUENCY=0
*EL PRINT,FREQUENCY=0
*NODE FILE,FREQUENCY=0
*NODE PRINT,FREQUENCY=0
*END STEP
**========== Unloading Step ==========
*STEP,INC=1000,NLGEOM
*STATIC
 0.04, 1, 0.0001, 0.04                   (unload to min load in a minimum of 25 increments)
*CLOAD
 LOADFULL,2,  0.0000000E+00
 LOADHALF,2,  0.0000000E+00
*EL FILE,FREQUENCY=0
*EL PRINT,FREQUENCY=1,ELSET=COMP1        (output compression spring element results)
```

```
 S11                                          (stress)
*NODE FILE,FREQUENCY=0
*NODE PRINT,FREQUENCY=0
*END STEP
:
:
*STEP,INC=1000,NLGEOM
*STATIC
 0.02, 1, 0.0001, 0.02
*CLOAD
 LOADFULL,2,  0.0000000E+00
 LOADHALF,2,  0.0000000E+00
*EL FILE,FREQUENCY=0
*EL PRINT,FREQUENCY=1,ELSET=COMP1
 S11
*NODE FILE,FREQUENCY=0
*NODE PRINT,FREQUENCY=1, NSET=CRACK
 U
*END STEP
```